STABILITY OF THE COMPRESSIBLE REACTING MIXING LAYER

By
D. S. Shin and J. H. Ferziger

Prepared with the support of the
NASA-Ames Research Center and
NASA-Stanford Center for Turbulence Research

Report No. TF-53

Thermosciences Division
Department of Mechanical Engineering
Stanford University
Stanford, California 94305

March 1992

STABILITY OF THE COMPRESSIBLE REACTING MIXING LAYER

by

D. S. Shin and J. H. Ferziger

Prepared with the support of the
NASA-Ames Research Center and
NASA-Stanford Center for Turbulence Research

Report No. TF-53

Thermosciences Division
Department of Mechanical Engineering
Stanford University
Stanford, California 94305

March 1992

Abstract

Linear stability analysis is used to understand the behavior of compressible reacting mixing layers. The chemistry model is a single step, irreversible, finite rate reaction between the fuel in the upper stream and oxidizer in the lower stream. Laminar flows calculated from the compressible boundary-layer equations serve as inputs to the stability study, and illustrate the structure of laminar diffusion flames.

For incompressible free shear layers with density variation, new inflectional modes of instability—outer modes—occur in the outer part of the mixing layer when there is significant heat release. Heat release stabilizes the center mode—Kelvin-Helmholtz mode—but hardly affects the outer modes. For heat release typical of combusting flows, the outer modes are more amplified than the center mode. However, the outer modes do not cause the flow to roll up in the manner of an incompressible non-reacting mixing layer, so the mixing between fuel and oxidizer is reduced.

In compressible free shear layers, supersonic unstable modes can exist, provided there is a region of the laminar flow supersonic relative to the disturbance phase velocity. The most unstable modes are the center modes at low Mach numbers, but the outer modes at high Mach numbers. The growth rate of the mixing layer drops with increasing Mach number and approaches an asymptotic value at high Mach numbers. Heat release destabilizes high-speed flows. Pressure contours demonstrate the radiative nature of supersonic disturbances; radiation of energy is one reason for the decreased growth rates. Supersonic disturbances do not mix the reactants very well because they are largely confined to one side of the flow. For reacting flows, the most unstable modes are two-dimensional outer modes even at high Mach numbers.

Reflection of supersonic disturbances by the walls makes the confined supersonic mixing layer more unstable than the unconfined free shear layer. Decreasing the distance between the walls makes the flow more unstable. However, subsonic disturbances are relatively unaffected by the walls. Heat release and Mach number hardly change the growth rates of supersonic disturbances. The most unstable supersonic disturbances are two-dimensional in rectangular channel flows, but three-dimensional in partially confined flows. Finally, the reactants are not strongly mixed by supersonic instabilities which mainly disturb one side of the layer.

Acknowledgements

There are many people we would like to thank for their help, guidance and support through the course of this work. We are truly grateful to Professor Godfrey Mungal for valuable discussions, insights and suggestions throughout this work. We also wish to thank Professor Brian Cantwell for his careful reading of the manuscript and many helpful suggestions.

Dr. Michele Macaraeg of NASA Langley Research Center and Professor Thomas Jackson of Old Dominion University provided valuable discussions during a visit of one of the authors (DSS). In their student days, Professors Shankar Mahalingam and Chris Rutland were very helpful in the early stages of this work, and Professor William C. Reynolds and Mr. Olivier Planché provided many important ideas and directions.

Financial and computational support by NASA-Ames Research Center and the NASA-Stanford Center for Turbulence Research is gratefully acknowledged.

Table of Contents

List of Tables and Figures

NOMENCLATURE

Roman Symbols

a	Speed of sound, Section 2.1.2.
a	Stretching parameter, Section 2.2.1.
a	Amplitude of the disturbance, Section 4.3.8.
$\hat{A}_j, \hat{B}_j, \hat{C}_j$	Block matrices, Section 2.2.2.
$A, \ldots, O$	Matrix elements, Section 3.1.
B	Breadth of the rectangular channel, Section 6.1.
c	Complex wave velocity, Section 3.1.
c_2, c_4, c_4'	Constants, Section 2.2.2.
c_i	Imaginary part of the wave velocity, Section 4.2.
c_l	Sonic phase speed of a disturbance relative to the lower stream, Section 3.2.
c_p	Specific heat at constant pressure, Section 2.1.2.
$c_{p,i}$	Specific heat at constant pressure for i-th species, Section 2.1.2.
c_r	Real part of the wave velocity, Section 3.2.
c_u	Sonic phase speed of a disturbance relative to the upper stream, Section 3.2.
c_v	Specific heat at constant volume, Section 2.1.2.
C_1, C_2	Constants, Section 3.3.
D	Mass diffusivity, Section 2.1.1.
D	Operator d/dy, Section 4.2.
Da	Damköhler number, Section 2.1.1.
E	Activation energy of the reaction, Section 2.1.2.
f	General dependent variable, Section 3.1.
$\bar{f}$	Mean of a general dependent variable, Section 3.1.
f'	Fluctuation of a general dependent variable, Section 3.1.
$\hat{f}$	Eigenfunction of general dependent variable, Section 3.1.
$\hat{f}_s$	Eigenfunction of the slow mode, Section 4.3.8.
$\hat{f}_f$	Eigenfunction of the fast mode, Section 4.3.8.
F	Fuel, Section 2.1.1.

F	Function appearing in Newton/Raphson method, Section 3.3.
h	Specific enthalpy, Section 2.1.2.
h_i	Specific enthalpy of i-th species, Section 2.1.2.
h'	Metric in mapping, Section 2.2.1.
H	Half of the channel height, Section 6.1.
i	Square root of -1, Section 3.1.
j, n	Indices along the y and x direction, Section 2.2.2.
m	Spanwise wavenumber, Section 6.1.
m, n	Indices of the matrix elements, Section A.2.
M_1	Mach number of the upper stream, Section 2.1.2.
M_2	Mach number of the lower stream, Section 2.1.2.
M_c	Isentropic convective Mach number, Section 2.3.1.
$\hat{M}_c$	Convective Mach number based on the most unstable mode, Section 5.7.1.
M_f	Flame convective Mach number, Section 5.7.1.
M_r	Relative Mach number, Section 3.2.
O	Oxidizer, Section 2.1.1.
P	Pressure, Section 2.1.1.
P	Product, Section 2.1.1.
$p^{(0)}$	Zeroth order pressure, Section 4.1.
$p^{(1)}$	First order pressure, Section 4.1.
p_1	Pressure of the upper stream, Section 3.3.
p_2	Pressure of the lower stream, Section 3.3.
Pr	Prandtl number, Section 2.1.2.
q	Exponent in an asymptotic solution, Section 3.2.
Q	Non-dimensional heat release parameter, Section 2.1.2.
R	Gas constant, Section 2.1.2.
R	Normalized growth rates, Section 5.7.2.
Re	Reynolds number, Section 2.1.2.
$\hat{R}_j$	Vector, Section 2.2.2.
R_u	Universal gas constant, Section 2.1.2.
$[RXN1], [RXN2]$	Density variation terms in the stability equation, Section 3.1.
S_c	Schmidt number, Scetion 2.1.2.
t	Time, Section 2.1.2.

t_0	Initial time, Section 4.3.9.
T	Temperature, Section 2.1.1.
T_{ad}	Non-dimensional adiabatic flame temperature, Section 2.1.2.
T_f	Temperature at the falme sheet, Section 5.7.1.
T_{max}	Non-dimensional maximum temperature, Section 2.3.4
u	Velocity component in the x direction, Section 2.1.2.
u_f	Velocity at the flame sheet, Section 5.7.1.
u_s	Mean velocity at an inflection point, Section 4.2.
U_1	Velocity of the upper stream, Section 2.1.2.
U_2	Velocity of the lower stream, Section 2.1.2.
U_c	Convective velocity of the large structure, Section 5.7.1.
v	Velocity component in the y direction, Section 2.1.2.
v^*	Complex conjugate of v, Section 4.2.
V	Velocity vector, Section 7.2.
V	Velocity component in the y direction, Section 7.2.
w	Velocity component in the z direction, Section 3.1.
$w_{i,j}$	Matrix elements of the Jacobian $\partial W/\partial \Phi$, Section A.1.
W	Velocity component in the z direction, Section 7.2.
W_i	Molecualar weight of i-th species, Section 2.1.2.
x	Streamwise coordinate, Section 2.1.2.
x_0	Initial x position, Section 4.3.9.
y	Normal coordinate, Section 2.1.2.
y_0	Initial y position, Section 4.3.9.
y_i	Mass fraction of the i-th speices, Section 2.1.2.
y_s	Inflection point, Section 4.2.
Y_F, Y_O	Free stream fuel and oxidizer mass fractions, Section 2.3.3.
z	Spanwise coordinate, Section 3.1.

Greek Symbols

α, β	Streamwise and spanwise wavenumbers, Section 3.1.
α_i	Imaginary part of the streamwise wavenumber, Section 3.1.
α_r	Real part of the streamwise wavenumber, Section 3.1.
β'	Non-dimensional activation energy, Section 2.1.2.

β_u	Velocity ratio, Section 2.1.2.
γ	Specific heat ratio, Section 2.1.2.
δ	Mixing layer thickness, Section 4.3.10.
δ_1	1% product thickness, Section 2.3.1.
δ_ω	Mixing layer vorticity thickness, Section 2.1.2.
$\delta_{\omega o}$	Inital mixing layer vorticity thickness, Section 2.1.2.
δ_P	Integral product thickness, Section 2.3.1.
Δt	Time step, Section 3.2.1.
ΔT	Temperature rise, Section 4.3.10.
ΔT_{max}	Maximum temperature rise, Section 4.3.10.
Δx	Grid spacing in the x direction, Section 2.2.2.
$\Delta \eta$	Grid spacing in the η direction, Section 2.2.2.
$\Delta \bar{\rho}$	Mean density reduction, Section 4.3.10.
ϵ	Small parameter in expansion in terms of Mach number, Section 4.1.
η	Mapped coordinate in the y direction, Section 2.2.1.
$\eta_{1,2}$	1% points of the mean temperature profile on the high- and low-speed sides, Section 4.3.10.
θ	Propagation angle of disturbance, Section 3.1.
κ	Thermal diffusivity, Section 2.1.1.
μ	Molecular viscosity, Section 2.1.1.
μ	Mach angle, Section 6.2.4.
ν_i	Stoichiometric coefficients for the i-th species, Section 2.1.1.
ρ	Density, Section 2.1.2.
$\bar{\rho}$	Integrated mean density, Section 4.3.10.
ρ_1	Density of the upper stream, Section 2.3.3.
ρ_2	Density of the lower stream, Section 2.3.3.
ϕ	Equivalence ratio, Section 2.3.
Φ	A general variable, Section 2.2.2.
ω	Frequency, Section 3.1.
ω_i	Reaction rate of i-th species, Section 2.1.2.
ω_i	Imaginary part of the frequency, Section 3.1.
ω_o	Complex frequency which makes the group velocity $d\omega/d\alpha$ zero, Section 4.3.3.

ω_{oi}	Imaginary part of ω_o, Section 4.3.3.
ω_T	Rate of heat release, Section 2.1.2.
ω_z	Spanwise vorticicy, Section 4.3.8.

Other Symbols

$()^*$	Dimensional quantity, Section 2.1.2.
$()^\circ$	Reference quantity, Section 2.1.2.
$()^{-1}$	Inverse of a matrix, Section 3.3.
$\widehat{()}$	Eigenfunction of a fluctuating quantity, Section 3.1.
$\overline{()}$	Mean quantity, Section 3.1.
$()'$	Disturbance quantity, except where explicitly labeled as a derivative, Section 3.1.
$\|()\|$	Magnitude, Section 3.2.
$\Re$	Real part of a fluctuating variable, Section 4.3.8.

Chapter 1

Introduction

Reacting free shear layers occur in many systems, including gas turbine combustors and rockets. Chemical reaction can occur only when the reactants are molecularly mixed. However, short residence times require efficient mixing between the fuel and oxidizer. This is especially important for air-breathing ramjets. Fast mixing requires the flow to be vigorously turbulent, which requires the laminar flow to be unstable.

The usual reacting mixing layer consists of two-fluid streams, one containing the fuel and the other, the oxidizer. The large temperature change caused by the combustion alters the thermodynamic properties of the flow considerably and produces dilatation; both of these effects cause a strong interaction between the hydrodynamics and the chemistry, making the study of reacting flows difficult.

Mixing in shear layers depends on the development of flow instabilities. Hence, understanding of the stability characteristics of reacting free shear layers may lead to techniques for enhancing mixing or controlling the flow. Stability analysis can also predict some characteristics of the turbulent reacting mixing layer. The conclusions may be expected to apply, with quantitative modifications, to other shear flows, eg., jets.

1.1 Historical Background

1.1.1 *Stability Theory*

The study of linear instability of mixing layers in incompressible, parallel, inviscid flows was initiated by Helmholtz [1868] and Kelvin [1871]. They assumed that the disturbances of the flows were infinitesimally small, and derived the linearized hydrodynamic equations. They found what is now called the Kelvin-Helmholtz instability mode, the growing wavy disturbance of a surface across which the initial velocity distribution is discontinuous. Rayleigh [1880] studied the instability of incompressible, parallel, inviscid flows with continuous velocity profiles. He showed that if the velocity profile has an inflection point, the flow is unstable. Tollmien [1935] enhanced this finding, showing that the existence of an inflection point is not only a necessary

but also a sufficient condition for instability. Other workers showed that the dominant unstable waves are two-dimensional in incompressible flows (Squire [1933]) and suggested that for large Reynolds numbers the instability is inviscid, as viscosity has just a slight damping influence (Lin [1955]).

For incompressible flows, Michalke [1965] solved the linearized equation numerically using hyperbolic-tangent velocity profiles for temporally as well as spatially growing disturbances. His spatial case results agreed well with the experiments. The effects of the mean velocity profile were studied by Monkewitz & Huerre [1982]. They found that the amplification rate for the Blasius mixing layer velocity profile agreed well with the experimental results. Morkovin [1988] suggested that only stability analyses based on mean profiles derived from the boundary-layer equations should be compared with the results of experiments.

Due to the increasing importance of high-speed flows, linear stability theory has been extended to include the effects of compressibility. Lees & Lin [1946] investigated the stability of compressible mixing layers to infinitesimal disturbances. Depending on the Mach number of the disturbance relative to the free stream, they classified the disturbances as subsonic, sonic and supersonic. They also pointed out the possibility that such disturbances can produce transition to turbulence. Lessen *et al.* studied inviscid temporal stability of two- and three-dimensional neutral subsonic [1965] and supersonic [1966] disturbances. They found unstable supersonic disturbances whose amplification rates are much smaller than those of unstable subsonic disturbances. They also suggested that the three-dimensional waves are more unstable than two-dimensional ones at high Mach numbers. Gropengiesser [1970] carried out inviscid spatial stability calculations using laminar solutions of the compressible boundary-layer equations as the base flow, rather than hyperbolic-tangent profiles. He found a second mode of instability to two-dimensional disturbances at high Mach numbers and that the most unstable modes are three-dimensional at high Mach numbers. Blumen [1970] and Drazin *et al.* [1977] studied the stability problem of a compressible, inviscid, free mixing layer and showed that two-dimensional disturbances are unstable at all Mach numbers, and that there exists a second unstable supersonic mode. Ragab & Wu [1988] studied the stability of the compressible mixing layer and found that the instability is basically inviscid with the viscosity having a damping effect. They also found that non-parallel effects are negligible in compressible mixing layers. Sandham & Reynolds [1989] solved the linearized inviscid compressible stability equation and

found maximum amplification at the frequency at which vortices are found in the laboratory. They compared the linear theory with direct numerical simulations and showed that linear theory can be very useful in understanding the physics of mixing layers. They also found that three-dimensional effects are important at high Mach numbers. Jackson & Grosch [1989] carried out inviscid spatial stability calculations and found two sets of unstable modes if the Mach number exceeds a critical value, which is consistent with the findings of other researchers (Gropengiesser [1970], Blumen [1970] and Drazin *et al.* [1977]). They also found that three-dimensional modes have higher amplification rates than two-dimensional modes.

For compressible boundary-layers, Mack [1984] studied the linear stability and demonstrated the existence of non-inflectional supersonic modes. He also noted that the three-dimensional waves have higher growth rates than two-dimensional ones at high Mach numbers.

Huerre & Monkewitz [1985] introduced the concept of convective and absolute instabilities for mixing layers. They proposed that the spatial stability theory should be used for convectively unstable flows, whereas temporal stability theory should be used for absolutely unstable flows. They found that when there is significant counterflow, the mixing layer is absolutely unstable and should be described in terms of temporally growing disturbances.

For reacting mixing layers, most researchers have used constructed mean velocity and temperature profiles. These are not consistent with the governing equations and may be unrealistic. Menon *et al.* [1984] developed inviscid compressible stability equations and applied them to premixed chemically reacting supersonic free shear layers. They included the chemical reaction rate terms in their analysis. Trouvé & Candel [1988] analyzed linear stability of the inlet jet in a ramjet dump combustor using hyperbolic-tangent velocity and temperature profiles and ignored chemical reaction in the stability. They found that the density gradient has an important effect on the instability. For the reacting subsonic jet, Mahalingam *et al.* [1989] found that heat release stabilizes coflowing, chemically reacting jets. Using analytical velocity profiles and the flame sheet concept, Jackson & Grosch [1990] studied the effect of heat release on the spatial stability of supersonic reacting mixing layers. They found that sufficient heat release could make the flow absolutely unstable.

Most stability analyses have been carried out for unbounded flows, while most experiments are conducted in enclosed test sections. Recently, Tam & Hu [1989]

showed that coupling between a mixing layer and acoustic modes in a rectangular channel produces a new type of spatially growing instability wave. For a confined temporal compressible mixing layer, Greenough *et al.* [1989] showed that there are two types of instabilities, confined Kelvin-Helmholtz modes and supersonic wall modes. Macaraeg & Streett [1991] found highly amplified waves supersonic relative to the free streams at high wavenumbers for high-speed, temporally growing bounded mixing layers. Spatially growing mixing layers between parallel walls were studied by Zhuang *et al.* [1990]. They considered a two-dimensional case and found that reflection of the compression/expansion waves by the walls provides a feedback mechanism that renders the bounded shear layers more unstable than the corresponding free shear layers. Morris & Giridharan [1991] examined the effect of wall location on instability waves in confined supersonic shear layers. They showed that the growth rates of Kelvin-Helmholtz instability waves are independent of wall height but the growth rate of the unstable acoustic mode has a maximum as a function of the ratio of duct width to height.

1.1.2 *Related Numerical Simulations*

Linear stability theory can provide input to accurate numerical simulations of free-shear layers; the numerical simulations may confirm the predictions of linear stability theory and be used to study non-linear behavior. In order to identify important mechanisms and develop a successful model in mixing layers, numerical simulations are important because they can provide complete data, both time-dependent and statistical. Mansour *et al.* [1978] and Cain *et al.* [1981] performed the first numerical simulations of time-developing mixing layers with large-eddy simulation which uses a model for the smallest scales of turbulence. Riley & Metcalfe [1980] performed the first direct numerical simulations of time developing mixing layers. Recent direct numerical simulations of time developing mixing layers (Rogers & Moser [1989]) showed the phenomena of primary roll-up and secondary streamwise vortices. Simulations of spatially developing mixing layers (Lowery & Reynolds [1986]; Sandham & Reynolds [1989]) showed the large entrainment asymmetry observed experimentally.

Direct numerical simulations of compressible mixing layers (Lele [1988, 1989]; Sandham & Reynolds [1989]) showed that the rate of growth of the mixing layer thickness decreases as the convective Mach number increases. Lele also showed that the wavelength of the primary roll-up becomes longer as the convective Mach number

increses, which agrees well with the prediction of linear stability theory. Sandham & Reynolds found that the most amplified waves are three-dimensional at high Mach numbers.

For reacting flows, Givi *et al.* [1986] simulated two-dimensional temporal mixing layers with the constant density approximation and finite rate chemistry. They found extinction in regions of high scalar dissipation in the later stages of evolution of the vortex structures. McMurtry *et al.* [1985] carried out direct numerical simulations of reacting mixing layers using the low Mach number approximation. They observed that mixing-layer growth, product formation and entrainment rate all decrease with increasing heat release. Mahalingam *et al.* [1989] performed direct numerical simulations to study the effect of heat release on jet diffusion flames. They found strong stabilization by heat release due to momentum reduction in the region where the shear layer is trying to roll up. Planché & Reynolds [1991] performed temporal direct simulations of compressible reacting mixing layers. They observed that mixing of the fuel and oxidizer by large-scale entrainment of fluid from both sides is not likely to occur and proposed that a two-step mixing mechanism in which fluid from each of the free streams is first mixed with product and then diffuses into the reaction zone.

1.1.3 *Related Experimental Works*

Although the transition to turbulence may be the most critical issue for supersonic combustion technology, most experiments have studied turbulent mixing layers. A major finding about the mixing layer is due to Brown & Roshko [1974] who first showed that two-dimensional large-scale coherent structures, which had been considered as transition phenomena, persisted in high Reynolds number turbulent flows. The large-scale instabilities, subsequently found by many other investigators (Dimotakis & Brown [1976]; Oster & Wygnansky [1982]), were considered to enhance macro-scale mixing or stirring of the two fluids by violent lateral motions of vortices even without turbulence (randomization of the flow). Knowledge of large-scale structures in the incompressible mixing layers has led to the development of the models that predict both entrainment and mixing (Broadwell & Breidenthal [1982]; Dimotakis [1986]; Broadwell & Mungal [1988], [1991]).

For compressible mixing layers, Birch & Eggers [1973] reviewed the available experimental data and demonstrated a trend of decreasing growth rate with increasing the free stream Mach number. Brown and Roshko [1974] suggested that the reduction

in growth rates in compressible mixing layers, results not from density variation but from compressibility. Chinzei *et al.* [1986] and Papamoschou & Roshko [1986, 1988] demonstrated suppression of large scale structures in two-dimensional supersonic turbulent mixing layers. Elliott *et al.* [1990] and Goebel & Dutton [1990] conducted experiments at high Reynolds numbers in compressible free shear layers and reported reduced turbulence levels at high Mach numbers. Clemens & Mungal [1990] and Hall *et al.* [1991] found that compressible mixing layers are generally devoid of large-scale structures at high Mach numbers, which suggests that turbulence, rather than the large-scale instability itself, might provide the primary mixing mechanism. Demetriades & Brower [1990] investigated transition of laminar free shear layers between two parallel high-speed streams. They reported that transition of the mixing layer from the laminar to the turbulent state occurred via instability in a relatively short region of the flow, and suggested that, turbulence remains the principal mixing mechanism.

Bogdanoff [1983] first proposed the convective Mach number as a parameter for characterizing the effect of compressibility. A similar definition of convective Mach number was proposed by Papamoschou & Roshko [1988]. The latter suggested that the growth rate of a compressible shear layer normalized by the incompressible growth rate might be expressible as a function of the convective Mach number over a wide range of velocity and density ratios. They suggested that the growth rate decreases with increasing convective Mach number for subsonic convective Mach numbers, and reaches an asymptotic value at supersonic convective Mach numbers. Recently, Papamoschou [1989] measured the convective velocities of large scale structures from experimental Schlieren images and found that the isentropic convective Mach number (Papamoschou & Roshko [1988]) does not collapse all experimental data. He proposed an alternative two-dimensional large-scale structure, in which shock waves are located on one side of the mixing layer.

For reacting mixing layers, most experiments studied incompressible turbulent flows. Experimental data for compressible reacting mixing layers are badly needed. Mungal & Dimotakis [1984] studied mixing and product formation in a gas-phase shear flow with hydrogen-fluorine reaction. They suggested that, for two-dimensional shear layers, mixing and combustion are dominated by the dynamics of the large-scale structures. Mungal *et al.* [1985] and Mungal & Frieler [1988] addressed the effects of Reynolds number and chemical reaction rate, and Masutani & Bowman [1986] examined the structure of a gas-phase chemically reacting mixing layer prior

to the mixing transition using the nitric oxide-ozone reaction. Those studies were all conducted under conditions of low-heat release, with little coupling between heat release and fluid mechanics.

The effect of heat release on the mixing and combustion in a reacting shear layer was investigated by Wallace [1981] with a maximum adiabatic flame temperature about 400 K; he reported a slight decrease in layer growth rate with increasing heat release. Keller & Daily [1985] performed an experimental study of the effect of a highly exothermic chemical reaction (about 1400 K temperature rise) on a two-stream mixing layer. They reported that the chemical reaction did not affect the large spanwise vortex structures that dominated the flow. Hermanson & Dimotakis [1989] studied the effects of large heat release (about 1240 K temperature rise) in a planar, turbulent shear layer at high Reynolds numbers. They reported a slight decrease of the growth rate of the shear layer and a reduction of large-scale structure spacing with increasing heat release, which suggests that heat release may inhibit the mechanisms of large-structure coalescence. To date, no experimental measurements of the stability of reacting mixing layers have been reported.

1.2 Focus of Present Work

1.2.1 *Objectives*

The primary objective of this work is to understand the stability of a simple chemically reacting flow in order to understand the coupling of the chemical reaction and the fluid mechanics, and to lead to techniques for enhancing mixing or controlling this flow.

From the previous work in this area, several questions arise. The first issue is to ascertain the effect of heat release on the stability of reacting shear layers. The reacting shear layer might behave very differently than the non-reacting shear layer. To answer this question, we shall consider a plane mixing layer in which the fuel and oxidizer are initially unmixed. The chemistry is a finite-rate single-step irreversible reaction with Arrhenius kinetics, which is more realistic than the infinite-rate chemistry of the flame sheet model. We derive and investigate linearized perturbation equations that include chemical reaction.

Another major thrust of this work is to understand mixing between the fuel and oxidizer in reacting mixing layers. Do the large-scale structures found in incompressible flows provide the primary mixing mechanism in high Mach number reacting mixing layers, and if not, what is the primary mixing mechanism? Linear stability study analysis can help answer this question.

The effect of compressibility in reacting mixing layers raises many questions. Are three-dimensional modes the most unstable ones in high Mach number reacting mixing layers? Is the convective Mach number the principal parameter in determining the effect of compressibility in reacting mixing layers? What is the effect of walls on reacting mixing layers at high Mach numbers? In order to answer these questions, we shall study the stability of reacting mixing layers with embedded diffusion flames over a large range of the Mach number.

Laminar profiles obtained by solving the compressible boundary-layer (thin-shear layer) equations will provide an input to the linear stability analysis. We compare the results obtained from these profiles with those based on analytical profiles such as hyperbolic-tangent and error functions in order to investigate use of the latter. We also study the laminar flow profiles to understand the behavior of laminar reacting mixing layers including such effects as ignition, and the existence of premixed and diffusion flame regimes.

Because viscosity has a damping effect in free shear flows, inviscid theory is a reliable guide for understanding stability at moderate and large Reynolds numbers and is the basis for this work. Both temporally and spatially developing layers are considered; the former are easier to understand while the latter are preferred for comparison with experiment. For the spatially developing layer, we consider only convectively unstable cases.

In summary, the specific goals of this work are:

- To study the nature and origin of instabilities in laminar reacting mixing layers. To accomplish this, we shall derive and solve the linearized perturbation equations with finite-rate chemical reaction.

- To study the effects of a number of parameters on both the laminar flow and instability. Parameters included are heat release, Mach number, variable properties, density ratio of the free streams, equivalence ratio, and Damköhler number.

- To study the flow and flame structure in the linear regime. To do this, we study linear eigenfunctions and contours of flow variables obtained from them. We calculate streaklines as approximations of flow patterns, to see whether or not large-scale structures provide the primary mixing mechanisms.
- To study the validity of the convective Mach number as a universal parameter for characterizing compressible reacting flows. We shall compare normalized growth rates to see whether the convective Mach number is capable of collapsing the results.
- To study the effect of confining walls on the stability of supersonic mixing layers.
- To study the validity of using analytical flow profiles for studying stability. We shall compare stability results obtained from hyperbolic-tangent and error function profiles with ones based on boundary-layer solutions.
- To identify the ignition, premixed flame and diffusion flame regimes of a laminar reacting mixing layer. For this purpose, we shall simulate laminar flames with various activation energies and Mach numbers.

1.2.2 *Organization of This Work*

This work is divided into four main topics: laminar flows, instability of incompressible reacting free shear layers, instability of compressible reacting free shear layers and instability of confined compressible reacting shear layers. A chapter is devoted to each topic, arranged in order of increasing complexity. Chapter 2 deals with laminar mixing layers with chemical reaction. The governing equations for laminar flows are derived from the two-dimensional compressible boundary-layer equations, and the numerical method used to solve the problem is described. Simulations of laminar flows are presented to illustrate the structure of laminar diffusion flames in mixing layers, which is essential for understanding more complex flows. The calculated laminar flows serve as inputs to the stability study in later chapters. Chapter 3 formulates the fully compressible linear stability problem and describes the numerical solution technique at length. Chapter 4 presents the results of linear stability analysis of incompressible reacting mixing layers. A set of equations appropriate to low Mach numbers is described, along with a necessary condition for instability of the incompressible reacting plane mixing layers. A new set of inflectional modes of

instability is found and their characteristics described. Chapter 5 includes another complexity—compressibility—in the stability study on reacting mixing layers without walls. The nature of the supersonic modes of instability is described in non-reacting and reacting flows. We compare various definitions of the convective Mach number and check whether it is a universal parameter for expressing the effect of compressibility in non-reacting and reacting flows. Chapter 6 studies the effect of walls on supersonic disturbances by putting a mixing layer in a channel. The results include new supersonic unstable modes due to wave reflections from the walls. Conclusions and recommendations for future work are given in Chapter 7.

Chapter 2

Laminar Flows

In this chapter, we shall compute laminar flows in which mixing and chemical reaction takes place between parallel streams of reactive species. The computed laminar flows provide understanding of laminar diffusion flames and will serve as inputs to the linear stability studies in later chapters. The simplest model of a reacting mixing layer involves two uniform parallel streams containing the fuel and oxidizer. The chemistry is a finite rate single step irreversible reaction with Arrhenius kinetics. The physical processes considered are diffusion, reaction and thermal conduction. First, we derive the governing equations for laminar flows from the two-dimensional compressible boundary-layer equations and describe the numerical method used to solve them. We present the simulations of laminar flows to illustrate the structure of laminar diffusion flames.

2.1 Governing Equations for Laminar Flows

This section presents the equations describing a reacting flow in an Eulerian reference frame. We consider a plane mixing layer in which the fuel and oxidizer are initially unmixed. Density variations due to chemical heating or compressibility may affect the velocity field. For this reason, we use the two-dimensional compressible boundary-layer (or thin shear-layer) equations to calculate profiles.

A schematic of the flow configuration is shown in Fig. 2.1. To simplify matters, we assume that the fast stream contains the fuel and the slow stream, the oxidizer; U_1 and U_2 represent the free-stream velocities.

2.1.1 *Assumptions*

In what follows, we make several assumptions. We assume that static pressure is constant throughout the mixing layer even though total pressures are different, so that heat release does not increase static pressure but expands the flow. This assumption allows supersonic flow to be free of compression or expansion waves. We also assume the Prandtl and Lewis numbers are unity, which means that temperature and species

diffuse at the same rate as momentum. Changing the Prandtl number to 0.7 was found to produce only small quantitative differences. We assume the following power laws in temperature T and pressure P for the transport properties:

$$\mu \propto P^0\, T^{0.7}\ ; \quad \kappa \propto P^0\, T^{0.7}\ ; \quad D \propto P^{-1}\, T^{1.7} \tag{2.1}$$

where μ is the viscosity, κ is the thermal diffusivity, and D is the mass diffusivity. To emphasize the importance of using variable properties, we will compare otherwise identical constant and variable property cases. Chemistry is treated by a single step irreversible scheme, involving fuel F and oxidizer O reacting to yield a product P:

$$\nu_F\, F + \nu_O\, O \rightarrow \nu_P\, P \tag{2.2}$$

where ν_F, ν_O and ν_P represent the stoichiometric coefficients for the fuel, oxidizer and product, respectively. For the reaction rate, we assume the Arrhenius law (see below). This assumption is more realistic than those made in the fast chemistry or flame sheet model.

2.1.2 *Governing Equations*

The boundary-layer equations for the two-dimensional flow of a compressible perfect gas with zero streamwise pressure gradient and chemical reaction form the basis for the computation. The conservation equations for mass, momentum, energy and species can be written in the following forms (White [1974]; Williams [1985]), using the superscript $*$ for dimensional quantities:

$$\frac{\partial \rho^*}{\partial t^*} + \frac{\partial \rho^* u^*}{\partial x^*} + \frac{\partial \rho^* v^*}{\partial y^*} = 0 \tag{2.3}$$

$$\frac{\partial \rho^* u^*}{\partial t^*} + \frac{\partial \rho^* u^{*2}}{\partial x^*} + \frac{\partial \rho^* v^* u^*}{\partial y^*} = \frac{\partial}{\partial y^*}\left(\mu^* \frac{\partial u^*}{\partial y^*}\right) \tag{2.4}$$

$$\frac{\partial \rho^* h^*}{\partial t^*} + \frac{\partial \rho^* u^* h^*}{\partial x^*} + \frac{\partial \rho^* v^* h^*}{\partial y^*} = \frac{\partial}{\partial y^*}\left(\frac{\kappa^*}{c_p^*}\frac{\partial h^*}{\partial y^*}\right) + \mu^*\left(\frac{\partial u^*}{\partial y^*}\right)^2 \tag{2.5}$$

$$\frac{\partial \rho^* y_i}{\partial t^*} + \frac{\partial \rho^* u^* y_i}{\partial x^*} + \frac{\partial \rho^* v^* y_i}{\partial y^*} = \frac{\partial}{\partial y^*}\left(\rho^* D^* \frac{\partial y_i}{\partial y^*}\right) + \omega_i^* \tag{2.6}$$

The streamwise direction is x^* and the normal direction y^*. The velocity components in these directions are u^* and v^*, respectively. The density is denoted by ρ^*, the mixture specific enthalpy by h^*, and the mass fraction of the i-th species by y_i. The quantity μ^* is the viscosity, κ^* the thermal diffusivity, D^* the mass diffusivity, and c_p^* the specific heat at constant pressure which is assumed constant. The term ω_i^* is the reaction rate of i-th species and defined as follows:

$$\omega_i^* = \frac{W_i(\nu_i'' - \nu_i')}{W_F^{\nu_F} W_O^{\nu_O}} (\rho^* y_F)^{\nu_F} (\rho^* y_O)^{\nu_O} B T^{*\tilde{\alpha}} exp\left[-\frac{E^*}{R_u^* T^*}\right] \tag{2.7}$$

where W_i represents the molecular weight and ν_i' and ν_i'' represent the stoichiometric coefficients of the species when appearing as a reactant or product, respectively; thus ν_O' is ν_O, while ν_O'' is zero for the scheme in (2.2). The molecular weights of the reactants were taken to be equal, so that in the absence of heat release there is no effect of the reaction on the flow-field dynamics. E^* is the activation energy of the reaction, $BT^{*\tilde{\alpha}}$, the frequency factor and R_u^*, the universal gas constant. We assume $\tilde{\alpha}$=0. The pre-exponential factor is inversely related to the characteristic time associated with the chemical reaction. The specific enthalpy of species i, h_i^*, can be expressed in terms of $h_i^{\circ *}$, the standard heat of formation of species i at reference temperature $T^{\circ *}$, and $c_{p,i}^*$, the specific heat of species i:

$$h_i^* = h_i^{\circ *} + \int_{T^{\circ *}}^{T^*} c_{p,i}^* \, dT^* \tag{2.8}$$

h^* and h_i^* are related as follows:

$$h^* = \sum_i h_i^* \, y_i \tag{2.9}$$

Similarly, c_p^* and $c_{p,i}^*$ are related.

$$c_p^* = \sum_i c_{p,i}^* \, y_i \tag{2.10}$$

The perfect gas law is

$$P^* = \rho^* R^* T^* \tag{2.11}$$

where R^* is the gas constant, P^* the pressure and T^* the temperature.

The energy equation (2.5) contains no reaction terms. If the energy equation is written in terms of the temperature, a source term due to heat release appears. Using Eqs. (2.5), (2.6), (2.8), (2.9) and (2.10), we obtain this equation:

$$c_p^* \left(\frac{\partial \rho^* T^*}{\partial t^*} + \frac{\partial \rho^* u^* T^*}{\partial x^*} + \frac{\partial \rho^* v^* T^*}{\partial y^*} \right) = \frac{\partial}{\partial y^*} \left(\kappa^* \frac{\partial T^*}{\partial y^*} \right) + \mu^* \left(\frac{\partial u^*}{\partial y^*} \right)^2 - \sum_i h_i^{\circ *} \omega_i^* \tag{2.12}$$

We choose to non-dimensionalize the above equations by dividing each dimensional quantity by its corresponding value on the high-speed side of the mixing layer (subscript 1). Thus

$$\begin{aligned} u &= \frac{u^*}{U_1^*} \quad v = \frac{v^*}{U_1^*} \quad \rho = \frac{\rho^*}{\rho_1^*} \quad P = \frac{P^*}{P_1^*} \quad \mu = \frac{\mu^*}{\mu_1^*} \\ \kappa &= \frac{\kappa^*}{\kappa_1^*} \quad D = \frac{D^*}{D_1^*} \quad t = \frac{t^* U_1^*}{\delta_{\omega o}^*} \quad x = \frac{x^*}{\delta_{\omega o}^*} \quad y = \frac{y^*}{\delta_{\omega o}^*} \end{aligned} \tag{2.13}$$

The reference length scale is $\delta_{\omega o}^*$, the vorticity thickness of the initial velocity profile:

$$\delta_\omega^* = \frac{U_1^* - U_2^*}{|du^*/dy^*|_{max}} \tag{2.14}$$

The non-dimensional equations for continuity, momentum, energy and species are:

$$\frac{\partial \rho}{\partial t} + \frac{\partial \rho u}{\partial x} + \frac{\partial \rho v}{\partial y} = 0 \tag{2.15}$$

$$\frac{\partial \rho u}{\partial t} + \frac{\partial \rho u^2}{\partial x} + \frac{\partial \rho v u}{\partial y} = \frac{1}{Re} \frac{\partial}{\partial y} \left(\mu \frac{\partial u}{\partial y} \right) \tag{2.16}$$

$$\frac{\partial \rho T}{\partial t} + \frac{\partial \rho u T}{\partial x} + \frac{\partial \rho v T}{\partial y} = \frac{1}{Pr Re} \frac{\partial}{\partial y} \left(\kappa \frac{\partial T}{\partial y} \right) + \frac{M_1^2 (\gamma - 1)}{Re} \mu \left(\frac{\partial u}{\partial y} \right)^2 + Da\, \omega_T \tag{2.17}$$

$$\frac{\partial \rho y_i}{\partial t} + \frac{\partial \rho u y_i}{\partial x} + \frac{\partial \rho v y_i}{\partial y} = \frac{1}{Re Sc} \frac{\partial}{\partial y} \left(\rho D \frac{\partial y_i}{\partial y} \right) + Da\, \omega_i \tag{2.18}$$

and

$$\rho T = 1 \tag{2.19}$$

since the static pressure is assumed uniform.

The Reynolds number is defined by $Re = \rho_1^* U_1^* \delta_{\omega o}^* / \mu_1^*$, the Prandtl number by $Pr = c_p^* \mu_1^* / \kappa_1^*$, and the Schmidt number by $Sc = \mu_1^* / \rho_1^* D_1^*$, both of the latter are assumed to be 1. We set initial Reynolds number to 1000 to assure satisfaction of the boundary-layer approximation. Here, γ is the specific heat ratio and M_1 is the Mach number of the upper stream. They are defined by

$$\gamma = \frac{c_p^*}{c_v^*} \; ; \quad M_1 = \frac{U_1^*}{a_1^*} \tag{2.20}$$

where c_v^* is the specific heat at constant volume and a_1^* is the speed of sound in the upper stream; the speed of sound of a perfect gas with constant specific heat is

$$a^{*2} = \gamma R^* T^* \tag{2.21}$$

There is another Mach number based on the lower stream properties, namely, M_2, but this parameter is eliminated in favor of the velocity ratio $\beta_u = U_2/U_1$. The Damköhler number, Da, and the non-dimensional activation energy parameter, β', are defined by

$$Da = \frac{\delta_{\omega o}^*}{U_1^*} \Big/ \left[\frac{W_F \nu_F}{W_F^{\nu_F} W_O^{\nu_O}} B \rho_1^{*(\nu_F + \nu_O - 1)} exp(-\beta') \right]^{-1} \tag{2.22}$$

$$\beta' = \frac{E^*}{R_u^* T_1^*} \tag{2.23}$$

The Damköhler number is the ratio of a characteristic flow time to a characteristic chemical reaction time. ω_T and ω_i, the rate of heat release and the reaction rate of species i, respectively, are defined as follows:

$$\omega_T = \frac{Q}{W_F \nu_F} (\rho\, y_F)^{\nu_F} (\rho\, y_O)^{\nu_O} exp\left[-\beta' \left(\frac{1}{T} - 1 \right) \right] \tag{2.24}$$

$$\omega_i = \frac{W_i (\nu_i'' - \nu_i')}{W_F \nu_F} (\rho\, y_F)^{\nu_F} (\rho\, y_O)^{\nu_O} exp\left[-\beta' \left(\frac{1}{T} - 1 \right) \right] \tag{2.25}$$

The non-dimensional heat release parameter, Q, expressed in terms of dimensional variables is

$$Q = \frac{[h_F^{\circ *} W_F \nu_F + h_O^{\circ *} W_O \nu_O - h_P^{\circ *} W_P \nu_P]}{c_p^* T_1^*} \tag{2.26}$$

The non-dimensional adiabatic flame temperature, T_{ad}, is related to Q as follows:

$$T_{ad} = Q + 1 \tag{2.27}$$

In all cases reported here, the stoichiometric coefficients, ν_F and ν_O are equal to 1, the specific heat ratio, γ is equal to 1.4, and the non-dimensional activation energy parameter, β' is equal to 6 unless otherwise specified. Changing β' hardly alters the structure of laminar flows.

2.2 Numerical Method

This section describes the numerical method used to solve the governing equations for the laminar flow. The equations are parabolic in both the temporally and spatially developing layers. Here, we consider the spatially developing layer. The same approach can be applied to the temporally developing layer. In the spatially developing case, we assume that the flow is steady so that time derivatives are zero.

2.2.1 *Transformation*

In the normal direction (y), we use a mapping (Cain *et al.* [1984]) to transform an infinite physical domain into a finite computational one. The transformation is

$$y = h(\eta) = -a \cot(2\pi\eta) \tag{2.28}$$

where η is a mapped coordinate and a is a stretching parameter, chosen to be $32/\pi$ in the current work. Eq. (2.28) maps the original domain $-\infty < y < \infty$ into the finite domain $0 \leq \eta \leq 1/2$. This mapping allows us to invoke the appropriate free-stream boundary conditions at finite boundaries in the computational domain. If we define the metric

$$h' = \frac{dy}{d\eta} = \frac{2\pi a}{\sin^2(2\pi\eta)} \tag{2.29}$$

then the first derivative of a function f is

$$\frac{df}{dy} = \frac{1}{h'}\frac{df}{d\eta} \tag{2.30}$$

The transformed governing equations for spatially developing layers are

$$\frac{\partial \rho u}{\partial x} + \frac{1}{h'}\frac{\partial \rho v}{\partial \eta} = 0 \tag{2.31}$$

$$\frac{\partial \rho u^2}{\partial x} + \frac{1}{h'}\frac{\partial \rho v u}{\partial \eta} = \frac{1}{Reh'}\frac{\partial}{\partial \eta}\left(\frac{\mu}{h'}\frac{\partial u}{\partial \eta}\right) \tag{2.32}$$

$$\frac{\partial \rho u T}{\partial x} + \frac{1}{h'}\frac{\partial \rho v T}{\partial \eta} = \frac{1}{PrReh'}\frac{\partial}{\partial \eta}\left(\frac{\kappa}{h'}\frac{\partial T}{\partial \eta}\right) + \frac{M_1^2(\gamma-1)}{Reh'^2}\mu\left(\frac{\partial u}{\partial \eta}\right)^2 + Da\,\omega_T \tag{2.33}$$

$$\frac{\partial \rho u y_i}{\partial x} + \frac{1}{h'}\frac{\partial \rho v y_i}{\partial \eta} = \frac{1}{ReSch'}\frac{\partial}{\partial \eta}\left(\frac{\rho D}{h'}\frac{\partial y_i}{\partial \eta}\right) + Da\,\omega_i \tag{2.34}$$

2.2.2 *Finite-Difference Method*

For the boundary-layer equations, several good finite-difference methods are available (Anderson *et al.* [1984]). We use one of the implicit methods, Crank-Nicolson, which has second order accuracy with respect to both independent variables. We use indices n and j for the x and the y directions, respectively. Using an expansion point $(n+1/2, j)$, we obtain the following difference equations:

$$\frac{\rho_j^{n+1}u_j^{n+1} - \rho_j^n u_j^n + \rho_{j-1}^{n+1}u_{j-1}^{n+1} - \rho_{j-1}^n u_{j-1}^n}{2\Delta x} + \frac{\rho_j^{n+1}v_j^{n+1} - \rho_{j-1}^{n+1}v_{j-1}^{n+1}}{h'_{j-1/2}\Delta\eta} = 0 \tag{2.35}$$

$$\frac{(\rho_j^{n+1}u_j^{n+1} + \rho_j^n u_j^n)(u_j^{n+1} - u_j^n)}{2\Delta x} +$$

$$\frac{(\rho_j^{n+1}v_j^{n+1} + \rho_j^n v_j^n)[(u_{j+1}^{n+1} - u_{j-1}^{n+1}) + (u_{j+1}^n - u_{j-1}^n)]}{8h'_j\Delta\eta} =$$

$$\frac{1}{2Reh'_j(\Delta\eta)^2}\left[\frac{\mu_{j+1/2}}{h'_{j+1/2}}(u_{j+1}^{n+1} - u_j^{n+1}) - \frac{\mu_{j-1/2}}{h'_{j-1/2}}(u_j^{n+1} - u_{j-1}^{n+1}) +\right.$$

$$\frac{\mu_{j+1/2}}{h'_{j+1/2}}(u^n_{j+1}-u^n_j)-\frac{\mu_{j-1/2}}{h'_{j-1/2}}(u^n_j-u^n_{j-1})\Bigg] \tag{2.36}$$

$$\frac{(\rho^{n+1}_j u^{n+1}_j+\rho^n_j u^n_j)(T^{n+1}_j-T^n_j)}{2\Delta x}+$$

$$\frac{(\rho^{n+1}_j v^{n+1}_j+\rho^n_j v^n_j)[(T^{n+1}_{j+1}-T^{n+1}_{j-1})+(T^n_{j+1}-T^n_{j-1})]}{8h'_j\Delta\eta}=$$

$$\frac{1}{2PrReh'_j(\Delta\eta)^2}\left[\frac{\kappa_{j+1/2}}{h'_{j+1/2}}(T^{n+1}_{j+1}-T^{n+1}_j)-\frac{\kappa_{j-1/2}}{h'_{j-1/2}}(T^{n+1}_j-T^{n+1}_{j-1})+\right.$$

$$\left.\frac{\kappa_{j+1/2}}{h'_{j+1/2}}(T^n_{j+1}-T^n_j)-\frac{\kappa_{j-1/2}}{h'_{j-1/2}}(T^n_j-T^n_{j-1})\right]+$$

$$\frac{M_1^2(\gamma-1)}{2Re}\mu_j\left[\frac{(u^{n+1}_{j+1}-u^{n+1}_{j-1})^2+(u^n_{j+1}-u^n_{j-1})^2}{(h'_j\Delta\eta)^2}\right]+\frac{Da}{2}(\omega^{n+1}_{Tj}+\omega^n_{Tj}) \tag{2.37}$$

$$\frac{(\rho^{n+1}_j u^{n+1}_j+\rho^n_j u^n_j)(y^{n+1}_{Fj}-y^n_{Fj})}{2\Delta x}+$$

$$\frac{(\rho^{n+1}_j v^{n+1}_j+\rho^n_j v^n_j)[(y^{n+1}_{Fj+1}-y^{n+1}_{Fj-1})+(y^n_{Fj+1}-y^n_{Fj-1})]}{8h'_j\Delta\eta}=$$

$$\frac{1}{2ReSch'_j(\Delta\eta)^2}\left[\frac{(\rho D)_{j+1/2}}{h'_{j+1/2}}(y^{n+1}_{Fj+1}-y^{n+1}_{Fj})-\frac{(\rho D)_{j-1/2}}{h'_{j-1/2}}(y^{n+1}_{Fj}-y^{n+1}_{Fj-1})+\right.$$

$$\left.\frac{(\rho D)_{j+1/2}}{h'_{j+1/2}}(y^n_{Fj+1}-y^n_{Fj})-\frac{(\rho D)_{j-1/2}}{h'_{j-1/2}}(y^n_{Fj}-y^n_{Fj-1})\right]+\frac{Da}{2}(\omega^{n+1}_{Fj}+\omega^n_{Fj}) \tag{2.38}$$

$$\frac{(\rho^{n+1}_j u^{n+1}_j+\rho^n_j u^n_j)(y^{n+1}_{Oj}-y^n_{Oj})}{2\Delta x}+$$

$$\frac{(\rho^{n+1}_j v^{n+1}_j+\rho^n_j v^n_j)[(y^{n+1}_{Oj+1}-y^{n+1}_{Oj-1})+(y^n_{Oj+1}-y^n_{Oj-1})]}{8h'_j\Delta\eta}=$$

$$\frac{1}{2ReSch'_j(\Delta\eta)^2}\left[\frac{(\rho D)_{j+1/2}}{h'_{j+1/2}}(y^{n+1}_{Oj+1}-y^{n+1}_{Oj})-\frac{(\rho D)_{j-1/2}}{h'_{j-1/2}}(y^{n+1}_{Oj}-y^{n+1}_{Oj-1})+\right.$$

$$\left.\frac{(\rho D)_{j+1/2}}{h'_{j+1/2}}(y^{n}_{Oj+1}-y^{n}_{Oj})-\frac{(\rho D)_{j-1/2}}{h'_{j-1/2}}(y^{n}_{Oj}-y^{n}_{Oj-1})\right]+\frac{Da}{2}(\omega^{n+1}_{Oj}+\omega^{n}_{Oj}) \quad (2.39)$$

$$\rho^n_j T^n_j = 1 \quad (2.40)$$

These equations are algebraically non-linear in the unknowns $\Phi = [u, v, \rho, y_F, y_O]^T$, and are solved using a Newton quasi-linearization procedure. For example, the term $\rho^{n+1}_j u^{n+1}_j$ is expanded in a Taylor series about the value at the previous station n and is linearized by truncating the terms of order higher than (Δx):

$$\rho^{n+1}_j u^{n+1}_j = \rho^{n+1}_j u^n_j + \rho^n_j u^{n+1}_j - \rho^n_j u^n_j + O(\Delta x^2) \quad (2.41)$$

If we define $W = Da\,[0, 0, \omega_T, \omega_F, \omega_O]^T$, the vector of reaction rate terms at the station $n+1$, W^{n+1} can be linearized with the aid of the Jacobian $\partial W/\partial\Phi$, which is given in the Appendix. We get

$$W^{n+1}_j = \left(\frac{\partial W}{\partial \Phi}\right)^n_j (\Phi^{n+1}_j - \Phi^n_j) \quad (2.42)$$

The linearized equations can be written in block-tridiagonal form:

$$\hat{A}_j \Phi^{n+1}_{j-1} + \hat{B}_j \Phi^{n+1}_j + \hat{C}_j \Phi^{n+1}_{j+1} = R_j \quad (2.43)$$

where $\hat{A}_j, \hat{B}_j$ and $\hat{C}_j$ are 5×5 blocks and R_j is the vector obtained from the previous station (see Appendix).

We solve the above equations by using a general block-tridiagonal solver (Anderson *et al.* [1984]). T^{n+1} is evaluated from Eq. (2.40). Having obtained all the values at the station $n+1$, we advance to the next station. The step size, Δx, is chosen by reducing it until the change in the solution is in the fifth siginificant figure.

To check the accuracy of the method, we estimate the errors in Φ. If we denote the approximation $\Phi(\Delta x)$ that depends on the step size Δx, the approximation can be represented by a Taylor series in the small step size Δx:

$$\Phi(\Delta x) = \Phi + c_2(\Delta x)^2 + c_4(\Delta x)^4 + \cdots \tag{2.44}$$

where c_2, c_4, ... are constants. The odd order terms are missing because of the second order accuracy in the Crank-Nicolson method. The first term $c_2(\Delta x)^2$ represents the leading error. Now suppose that we have calculated $\Phi(\Delta x)$ with Δx replaced by $\Delta x/2$. Then we would obtain the value:

$$\Phi\left(\frac{\Delta x}{2}\right) = \Phi + \frac{1}{4}c_2(\Delta x)^2 + \frac{1}{16}c_4(\Delta x)^4 + \cdots \tag{2.45}$$

We estimate the leading error term by substracting Eq. (2.45) from Eq. (2.46):

$$c_2(\Delta x)^2 = \frac{4}{3}\left\{\Phi(\Delta x) - \Phi\left(\frac{\Delta x}{2}\right)\right\} + c_4'(\Delta x)^4 + \cdots \tag{2.46}$$

Fig. 2.2 shows the leading error of u velocity as a function of Δx. The logarithm of the error decreases linearly with the logarithm of Δx and the slope of the error, 2.09, confirms the second order accuracy of the Crank-Nicolson method.

2.2.3 *Boundary Conditions*

This subsection discusses the implementation of the boundary conditions. We specify u, ρ, y_F and y_O as constants as $y \to \pm\infty$. Those conditions can be written as follows:

$$u = \rho = y_F = 1 \quad y_O = 0, \quad \text{as} \quad y \to \infty$$

$$u = U_2, \quad \rho = \rho_2, \quad y_F = 0, \quad y_O = 1, \quad \text{as} \quad y \to -\infty \tag{2.47}$$

In the spatially developing layer, the boundary conditions for the normal velocity v, are difficult to determine. We tried Neumann conditions but found that v becomes so large that it violates the boundary-layer approximation. Instead, we improved the

integral boundary conditions used by Tzuoo *et al.* [1987] for incompressible flow. To develop these, consider the y-momentum equation with constant pressure, which is

$$\frac{\partial \rho u v}{\partial x} + \frac{1}{h'}\frac{\partial \rho v^2}{\partial \eta} = \frac{1}{Re h'}\frac{\partial}{\partial \eta}\left(\frac{\mu}{h'}\frac{\partial v}{\partial \eta}\right) \tag{2.48}$$

Integrating the above equation between 0 and 1/2 over the η-axis, we obtain the integral relation.

$$\int_0^{1/2} h' \frac{\partial \rho u v}{\partial x}\, d\eta + (\rho v^2)_{\eta=1/2} - (\rho v^2)_{\eta=0} = 0 \tag{2.49}$$

At each step, v is specified at the boundaries and is iterated until it satisfies the above equation up to the error of 10^{-4}. The fact that the magnitude of the normal velocity is always less than 1% of the streamwise velocity validates the boundary-layer approximation.

2.2.4 *Initial Conditions*

We need to specify the initial flow field. For a non-reacting compressible mixing layer, we can use self-similar solutions (Sandham & Reynolds [1989]) to initialize the flow field. The initial reactant mass fraction profiles are chosen to be normalized error functions. The disturbances resulting from the incompatibility between the specified initial flow field and the governing equations require a period of adjustment to decay. We include an averaging technique to assist in this adjustment. We use two points in making this adjustment: the initial station and a first station, a short distance downstream. Averaging the solutions at the initial and first stations eliminates most of the error and provides an improved initial condition. The calculation then restarts from a location midway between the initial and first stations, and a half step is taken in order to obtain a better solution at the first station. This averaging process is repeated three times. Each time, the location of the averaged solution is moved forward by half a step size. After this averaging process, we continue normally. It was found that this procedure eliminates nearly all the oscillations created by incorrect initial conditions.

2.3 Mean Flow Profiles

This section presents the results for steady laminar diffusion flames. These provide understanding of the effects of finite rate chemistry and serve as inputs to the linear stability theory. The non-dimensional adiabatic flame temperature, T_{ad}, is used to specify the heat release. The number of parameters is quite large and includes the adiabatic flame temperature, T_{ad}, density ratio, ρ_2/ρ_1, equivalence ratio, ϕ, Mach number, M_1 and Damköhler number, Da. The velocity ratio, U_2/U_1 is equal to 0.5 in all cases reported here. We present spatially developing cases unless otherwise specified. Temporal developing cases show no qualitative differences.

2.3.1 *Effect of Heat Release and Properties*

Fig. 2.3 shows the laminar flame structure at several streamwise locations for M_1=0 and T_{ad}=8. The reaction rate is defined as the consumption rate of fuel, $Da\,\omega_F/\rho$. The rate of increase of the centerline temperature decreases as does the peak reaction rate. Since finite rate chemistry is assumed, the reaction zone is thick and fuel and oxidizer co-exist in the reaction zone. If we normalize the laminar profiles in Fig. 2.3 by local vorticity thicknesses, the profiles become nearly similar.

To see the importance of variable properties, a constant property case is compared with the corresponding variable property one for the same inlet profiles. Fig. 2.4 compares the laminar flame structures of the two cases and Fig. 2.5 shows the vorticity thickness versus heat release at the same streamwise distance, x=7.7. The figures show that variable properties affect the profiles considerably and need to be included when there is large temperature variation. These flows may have significantly different Reynolds numbers, depending on the choice of characteristic shear layer thickness and viscosity.

Fig. 2.6 compares the structure of spatial layers with the same inlet profiles and different heat release parameters. The upper stream Mach number M_1 is 1 and the corresponding isentropic convective Mach number M_c (Papamoschou & Roshko [1988]) is 0.25. These structures are compared at a particular non-dimensional downstream distance x. Since the temperature increases with heat release, the rate of fuel consumption also increases.

Fig. 2.7 shows the variation of the maximum temperature and normalized product thickness with heat release. The maximum temperature of the layer at a given x changes almost linearly with the adiabatic flame temperature. The product thickness,

$$\delta_P(x) = \int_{-\infty}^{+\infty} y_P(x,y)\, dy \tag{2.50}$$

is a good measure of the size of the region occupied by reaction product. We normalize this product thickness with respect to 1% thickness of the layer at the same location, δ_1 (the distance between the points at which the mean product concentration is 1% of its maximum value); this has been used as a reference length by various researchers (Mungal and Dimotakis [1984]; Hermanson and Dimotakis [1989]; Heidarinejad & Ghoniem [1989]). Unlike the maximum temperature, the change δ_P/δ_1 with T_{ad} is not linear. At low heat release, product formation is strongly affected by T_{ad}. The effect is weaker at high heat release.

To study the stability of plane mixing layers, most researchers use analytical velocity profiles such as error function or hyperbolic-tangent profiles. However, when there is heat release, the density and property variations change the velocity profile. It is important to have consistent mean profiles. We next compare consistent mean profiles with analytical profiles. Their stability characteristics will be compared later. Fig. 2.8 compares the laminar solutions with analytic profiles of the same vorticity thickness. Fig. 2.8a compares a laminar solution with the corresponding hyperbolic-tangent profile for the spatial case and Fig. 2.8b compares it with the error function for the temporal case. In the temporal case, the error function is the exact boundary-layer solution when there is no heat release. We shall see that the profiles obtained by numerical simulation have very different stability properties from the analytic profiles.

2.3.2 *Effect of Damköhler Number*

This subsection considers the effect of the Damköhler number, Da, on the spatially developing layer. In Sec. 2.1.2, the Damköhler number was defined as the ratio of the convective flow time to the chemical reaction time. It is expected that as Da increases, the rate of product formation and heat release also increase. In Fig. 2.9, we show velocity and temperature profiles for M_1=0 and T_{ad}=8 for various Damköhler numbers. The effect of the Damköhler number is strongest for $Da < 1$, where the rate of product formation and heat release increases rapidly with the speed of the

chemical reaction; an asymptote is reached for $Da > 2$. Mungal & Frieler [1988] and Heidarinejad & Ghoniem [1989] reported similar results based on experiments and simulations (vortex method) respectively, but their results are limited to low heat release. We used a very high Da ($\sim$ 1000) to study the fast chemistry limit. For large Da, the reaction zone is very thin and the region in which the fuel and oxidizer co-exist is very small. When $Da \rightarrow \infty$, the fuel and oxidizer co-exist nowhere and the reaction zone becomes an infinitesimally thin flame sheet.

Fig. 2.10 shows the variation of the maximum temperature and normalized product thickness with Damköhler number for low speed and T_{ad}=8. The effect of Damköhler number on the maximum temperature is far from linear. Fig. 2.10b shows the normalized product thickness vs. Da for two Reynolds numbers, Re=500 and 1000, at the same x. At low Damköhler numbers, the rate of product formation and the growth of the layer thickness are strongly influenced by Da; the behavior is said to be reaction limited. At high Damköhler numbers, both rates approach asymptotic values. Fig. 2.10b also shows that the product thickness is only weakly dependent on Reynolds number. In Fig. 2.11, we plot the normalized product thickness, δ_P/δ_1, vs. streamwise coordinate x for M_1=0 and T_{ad}=8. At low Da, the thickness increases slowly with x, while at high Da, it approaches a plateau on which the growth is diffusion limited. Again, the change is not linear with Da. The reaction zone thickness, the distance between points at which the reaction rate is 10% of its maximum value, is expected to vary as $Da^{-1/3}$ for large values of the Damköhler number (Gibson & Libby [1972]). Fig. 2.12 shows that the flow exhibits the expected behavior.

2.3.3 *Effect of Mach Number, Density Ratio and Equivalence Ratio*

As the Mach number increases, the temperature increases further due to viscous dissipation (Fig. 2.13a). However, the effect of the Mach number on reaction rate is relatively weak at Da=10 and T_{ad}=8; i.e. compressibility hardly changes the structure of the laminar flame when there is sufficiently high heat release.

In real combustion systems, the fuel and oxidizer usually have different initial temperatures and densities. Most experiments on compressible mixing layers are done with unequal density free-stream conditions. We therefore consider the effects of free-stream density ratio. In Fig. 2.14, we show the temperature profiles and reaction rates for various density ratios at T_{ad}=8, M_1=1 and Da=10. The temperature profiles

have significant differences, which can be traced to the initial temperature difference. The reaction rate hardly changes, but the peak shifts toword the low temperature side because reaction is faster in a dense region and the diffusion is stronger at high temperature. The reaction rate at ρ_2/ρ_1=0.5 is large because the temperature is high.

The equivalence ratio of a diffusion flame can be defined by

$$\phi = \frac{(Y_F/Y_O)_{real}}{(Y_F/Y_O)_{ideal}} \tag{2.51}$$

where Y_F, Y_O represent the mass fractions of fuel and oxidizer in the free streams. We assume that $(Y_F/Y_O)_{ideal}$=1. If $\phi > 1$, the mixture is fuel rich, while if $\phi <$ 1 it is fuel lean. Fig. 2.15 shows the temperature and reaction rate for different equivalence ratios. The upper stream contains the fuel, the lower stream, the oxidizer. As expected, the stoichiometric case has the highest temperature and reaction rate. Any deviation from stoichiometric conditions decreases the heat release and the flame is shifted from the centerline of the mixing layer. When $\phi < 1$, the flame moves to the fuel-rich high speed flow; the reverse is true for $\phi > 1$.

2.3.4 *Ignition, Premixed Flame, and Diffusion Flame Regime*

By using activation energy asymptotics, Liñan & Crespo [1976] studied the structure of a diffusion flame. They showed that ignition, premixed flame, and diffusion flame regimes exist in the laminar flame. These were also found by Jackson & Hussaini [1988] in high speed flow by using activation energy asymptotics. We studied these regimes in the compressible reacting mixing layer, using two values of the nondimensional activation energy parameter, β'=6 and 20.

Fig. 2.16a shows the maximum temperature T_{max} in the profile as a function of streamwise location x for β'=6, T_{ad}=4, M_1=0 and Da=10. At this activation energy, T_{max} changes smoothly from the initial temperature at x=0 to the characteristic value of a diffusion flame (cf. Fig. 2.6a). Fig. 2.16b shows the results with the same parameters except now β'=20. There is a sudden change in the maximum temperature in a thin region around x=0.37, which defines a premixed flame ignition zone location. At the beginning of this ignition zone, the reactants have mixed but the temperature is low so there is little reaction. As reaction begins to takes place, the temperature rises and the reaction rate increases rapidly, creating a premixed flame. Premixed combustion continues until all the premixed gas is consumed. These

ignition and premixed flame regimes occupy a very small portion of the flow field. A diffusion flame is established just downstream of the premixed flame. This flame is similar to the ones calculated earlier and occupies the bulk of the mixing layer.

Figs. 2.17-18 show the similar results but for M_1=2.5 and 5. These figures show that the ignition regime exists in supersonic flows if the activation energy is high. In all cases, higher activation energy sharpens the transition to a diffusion flame. Note that at high Mach numbers the temperatures at x=0 increase considerably due to viscous heating.

Fig. 2.19 shows contours of temperature, reaction rate and the mass fractions for conditions of Fig. 2.16a. At this activation energy, it is hard to distinguish the ignition and premixed flame regimes. Supersonic flows with β'=6 do not produce qualitatively different results. However, Fig. 2.20a shows the rapid rise of the temperature over a narrow range of x at high activation energy ($\beta' = 20$); this is the premixed flame zone. The reaction rate contours show clearly the existence of the three regimes. Fig. 2.20b shows that ignition occurs at about x=0.37; this gives rise to an oblique premixed flamelet. This premixed flamelet propagates outward until all of the mixed reactant is consumed. The region of high reaction near the center of the layer just beyond the ignition region is the beginning of the diffusion flame. From there on, the diffusion flame behavior is dominant and the flame location is at the centerline of the flow. Fig. 2.20c shows contours of the mass fraction of the fuel. The mass fraction of the fuel varies from 1 at $y=+\infty$ to 0 at $y=-\infty$. Prior to ignition, the fuel diffuses from the upper stream into the lower stream. At the premixed flame (x=0.37), the premixed fuel is consumed. After the premixed flame, no fuel is found below y=0. Fig. 2.20d shows the contours of the mass fraction of the oxygen; its behavior is the reverse of the fuel. Fig. 2.21 shows similar results but for M_1=2.5. The behavior described M_1=0 also occurs for $M_1 > 0$. Fig. 2.22 shows the contours for M_1=5. The temperature contours do not show a sharp temperature rise. The reaction rate contours show that iginition occurs earlier due to the higher temperatures and the premixed flame is less oblique than at low Mach numbers. The mass fraction contours clearly show the existence of the premixed flame regime.

2.4 Chapter Summary

In this chapter, we derived the governing equations for laminar flows from the two-dimensional compressible boundary-layer equations and described the numerical method used to solve them. We computed the governing equations to illustrate the structures of laminar diffusion flames and serve as inputs to the linear stability study in later chapters. We found that property variations affect the laminar profiles considerably and need to be included when there are large temperature differences. The maximum temperature of a laminar reacting mixing layer is almost linear with the adiabatic flame temperature; the normalized product thickness depends strongly on the adiabatic flame temperature at low heat release, but only weakly at high heat release. Compressibility hardly changes the structure of the laminar layer when the heat release is high. Free-stream density ratios and equivalence ratios affect the temperature profiles considerably. Ignition, premixed flame, and diffusion flame regimes are found to exist in the laminar reacting mixing layer at high activation energy. Finally, at high Mach numbers, ignition occurs earlier due to the higher temperatures in the unburnt gas.

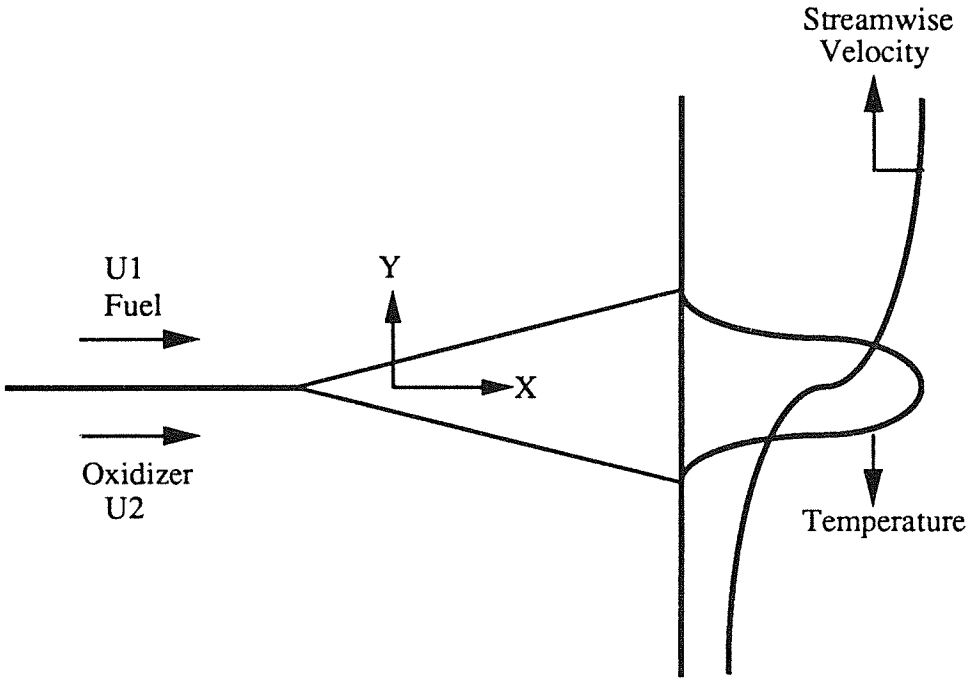

FIGURE 2.1. Schematic diagram of spatially developing mixing layer.

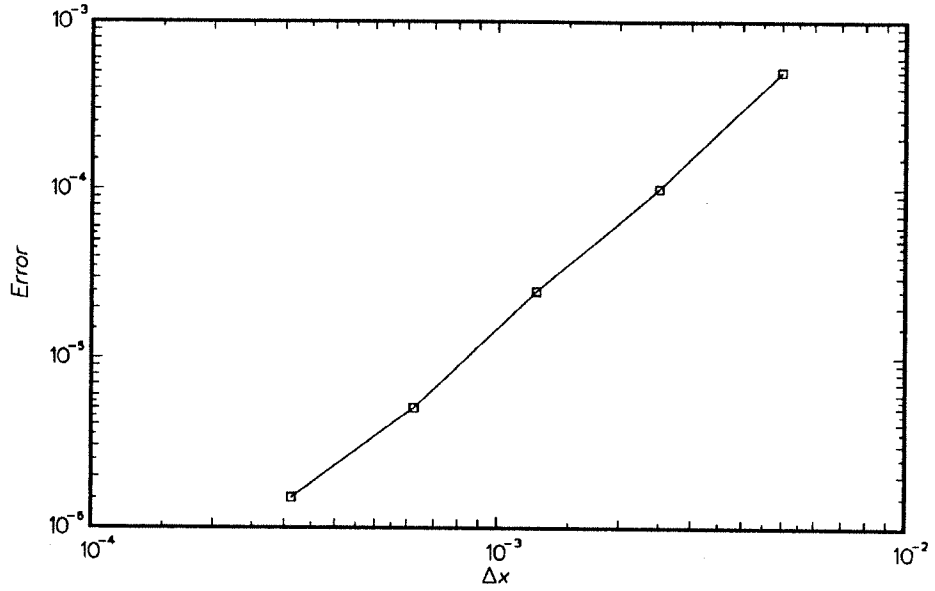

FIGURE 2.2. The error of u vlocity versus Δx. Da=10, M_1=0, T_{ad}=4.

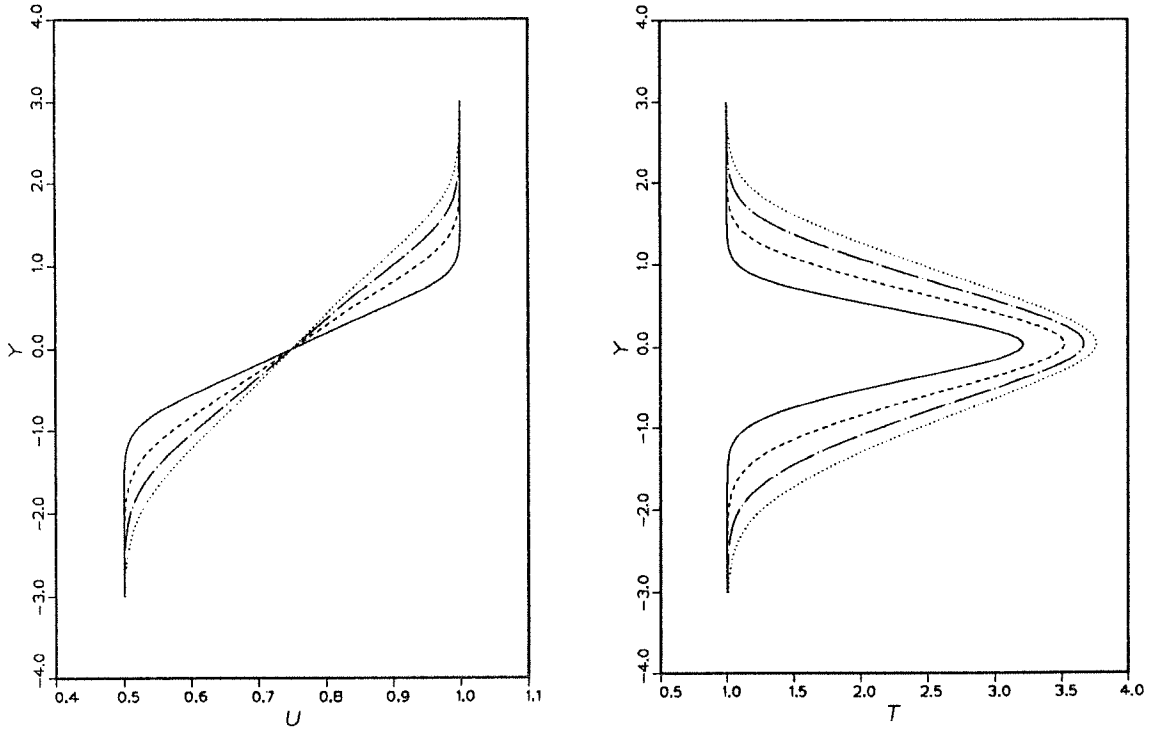

(a) (b)

FIGURE 2.3. Continued.

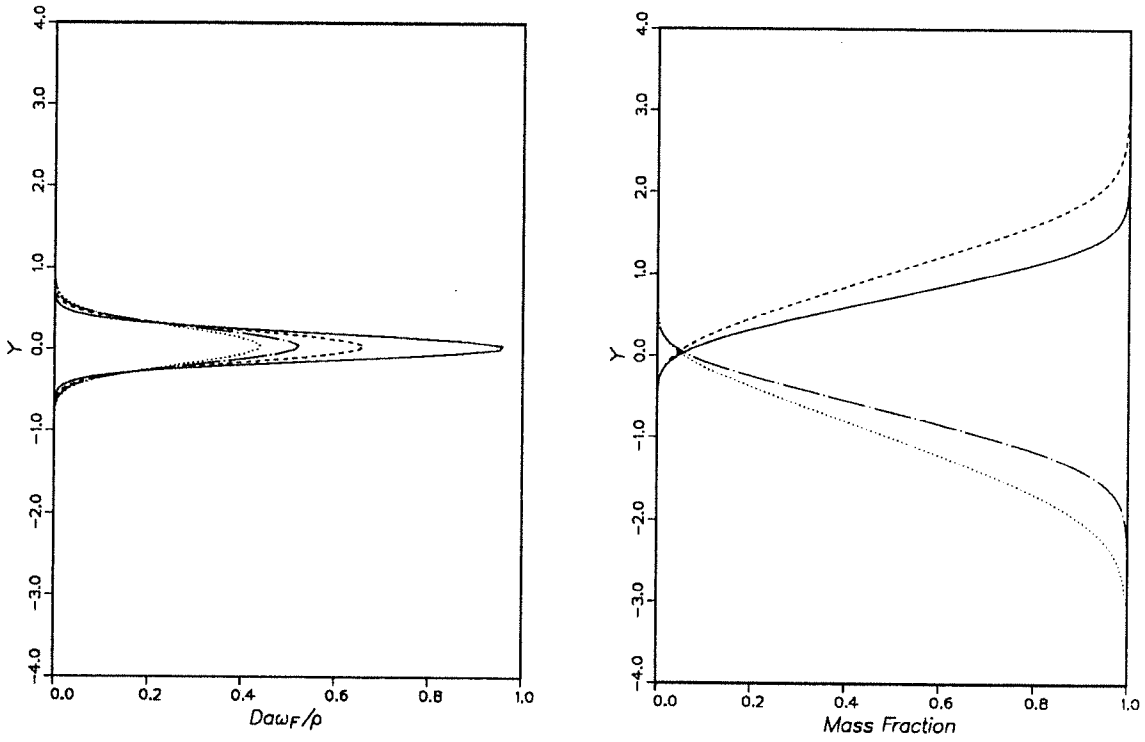

(c) (d)

FIGURE 2.3. Laminar flow structure. Da=10, M_1=0, T_{ad}=8. (a) velocity (b) temperature (c) reaction rate. —— , x=3.85; ---- , x=7.7; —·— , x=11.55; ····· , x=15.4. (d) mass fraction. —— , Y_F, x=7.7; ---- , Y_F, x=15.4; —·— , Y_O, x=7.7, ····· , Y_O, x=15.4.

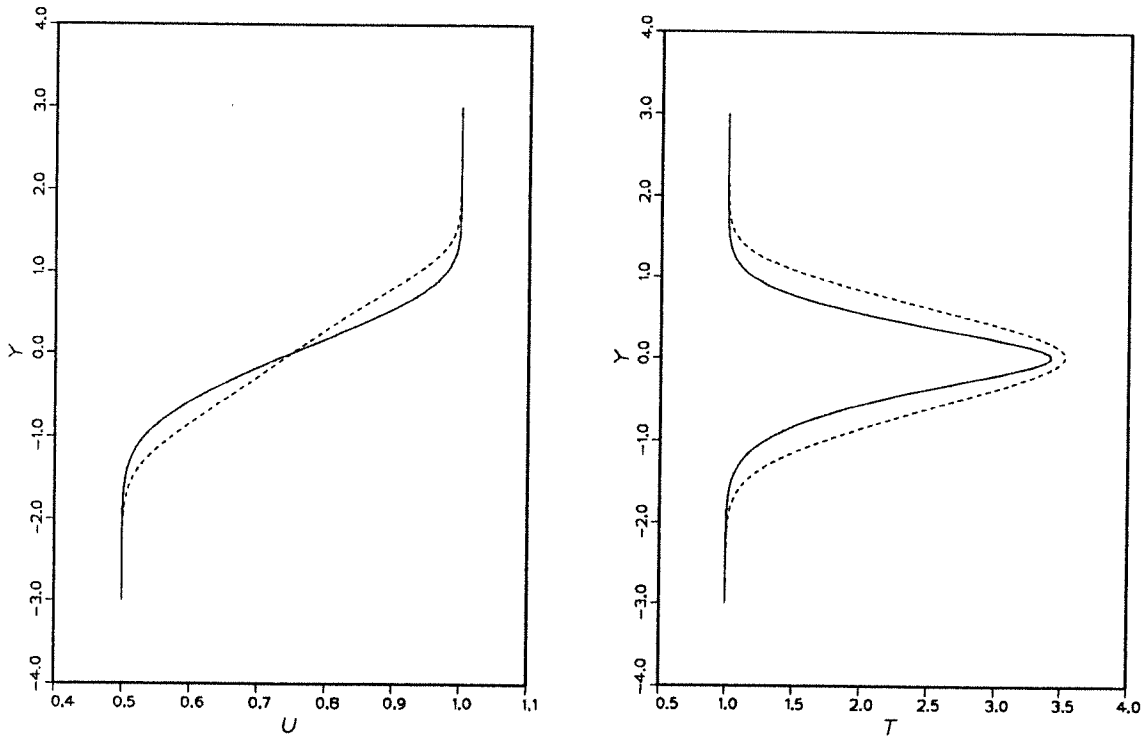

FIGURE 2.4. Effect of variable properties on (a) velocity (b) temperature profiles. Da=10, M_1=0, T_{ad}=8, x=7.7. —— , constant property; ---- , variable property.

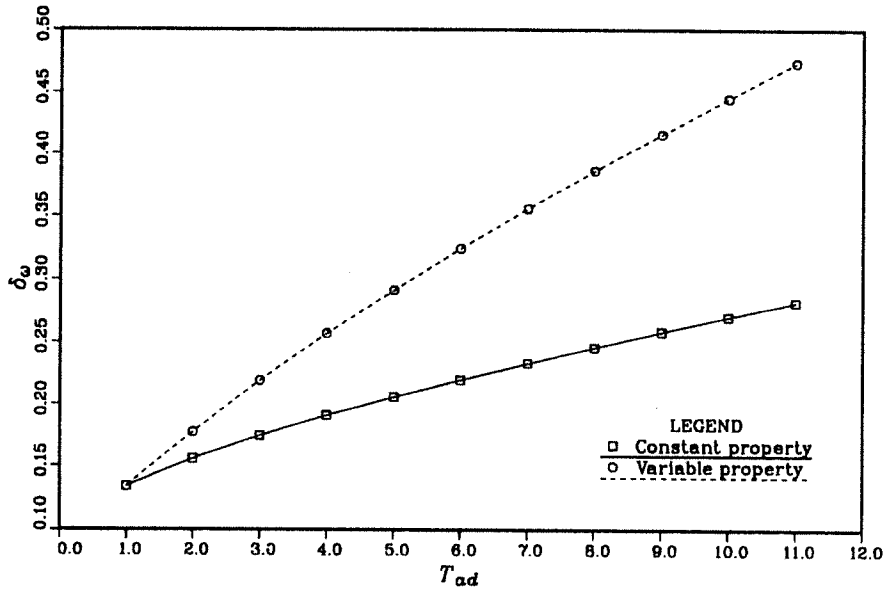

FIGURE 2.5. The growth of vorticity thickness versus T_{ad}. Da=10, M_1=0, x=7.7. ▫ , constant property; ○ , variable property.

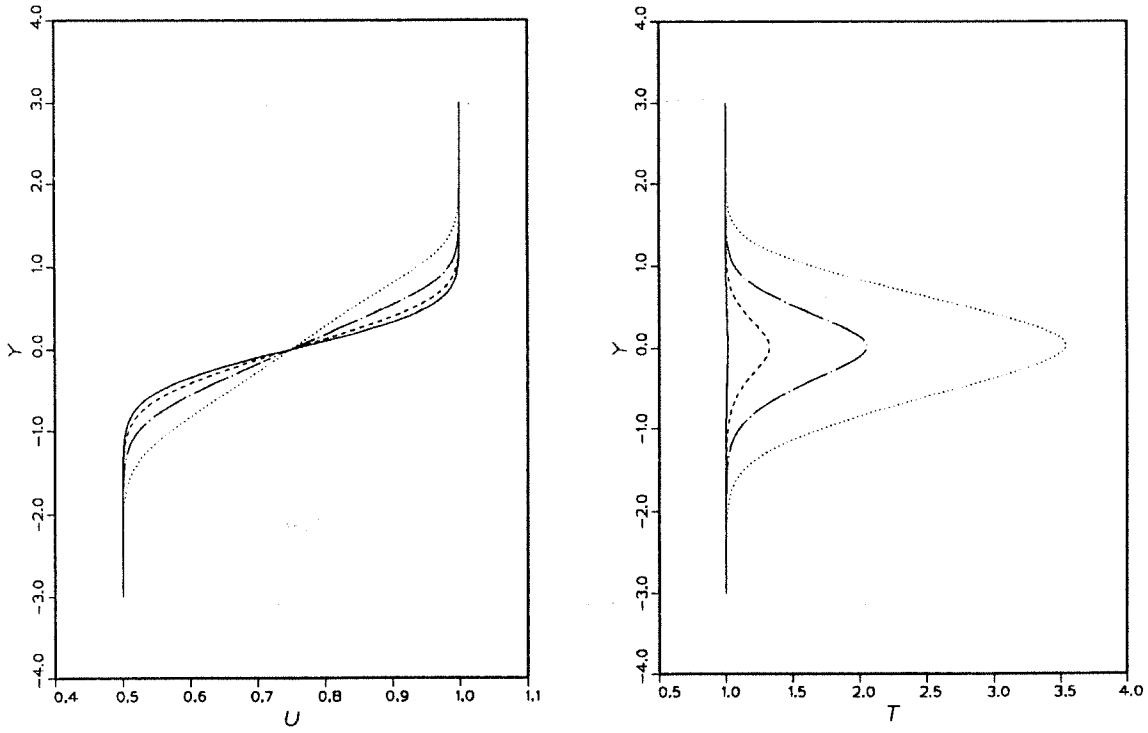

(a) (b)

FIGURE 2.6. Continued.

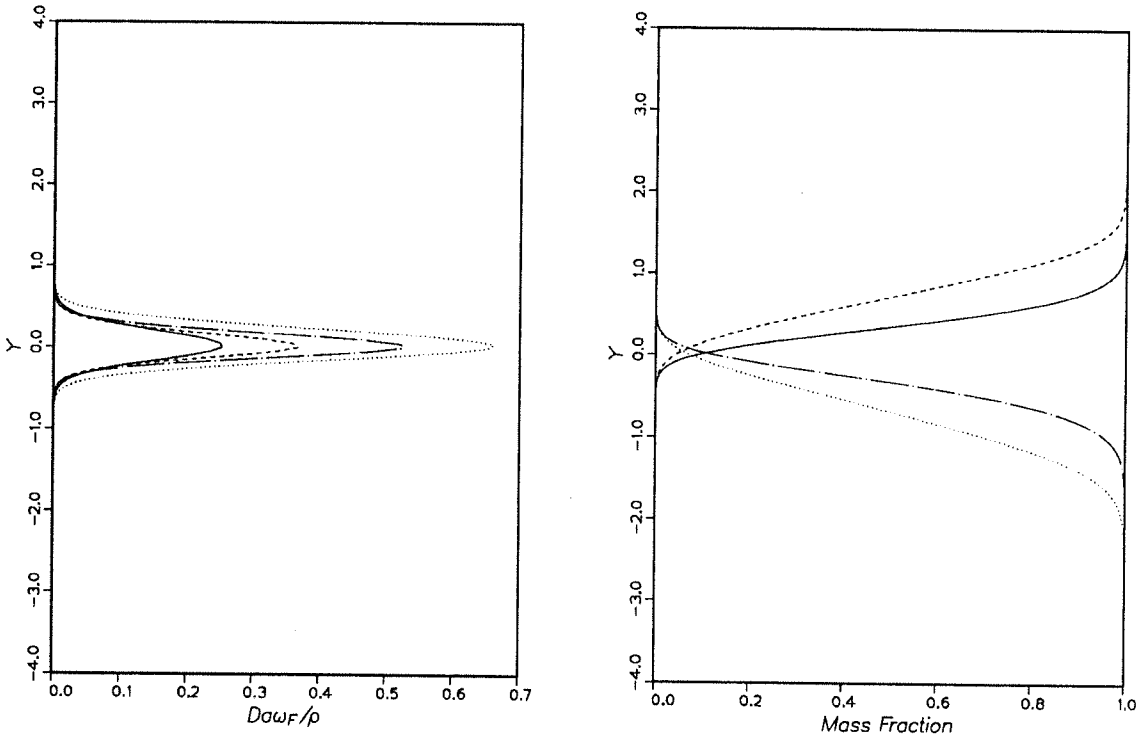

FIGURE 2.6. Effect of heat release on laminar flow structure. Da=10, x=7.5, M_1=1 (M_c=0.25). (a) velocity (b) temperature (c) reaction rate. ——— , T_{ad}=1; ---- , T_{ad}=2; —·— , T_{ad}=4; ····· , T_{ad}=8. (d) mass fraction. ——— , Y_F, T_{ad}=2; ---- , Y_F, T_{ad}=8; —·— , Y_O, T_{ad}=2; ····· , Y_O, T_{ad}=8.

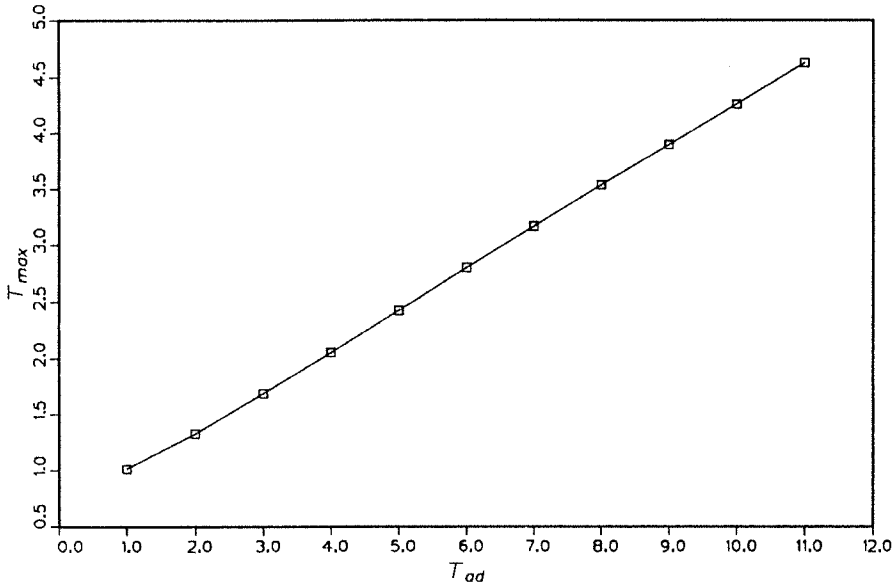

(a)

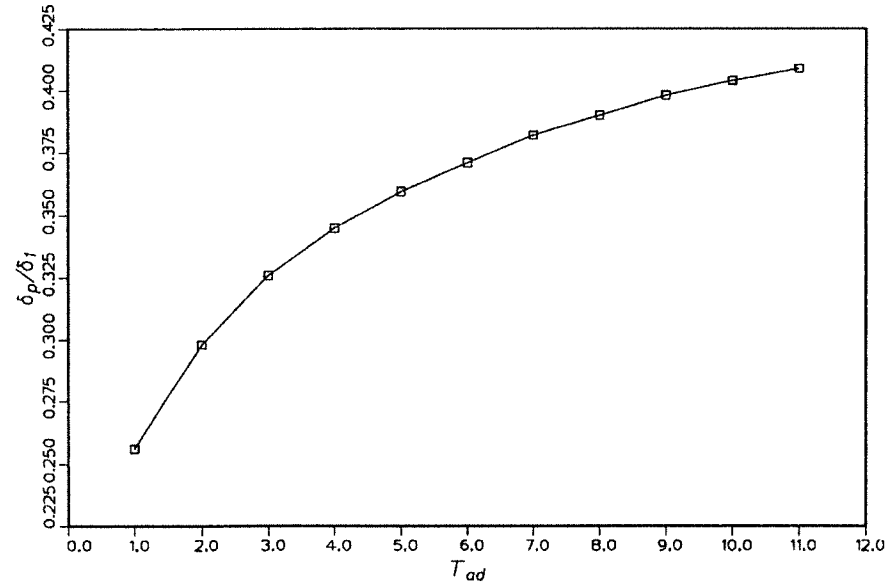

(b)

FIGURE 2.7. (a) Maximum temperature and (b) normalized product thickness vs. adiabatic flame temperature. Da=10, M_1=1 (M_c=0.25), x=7.5.

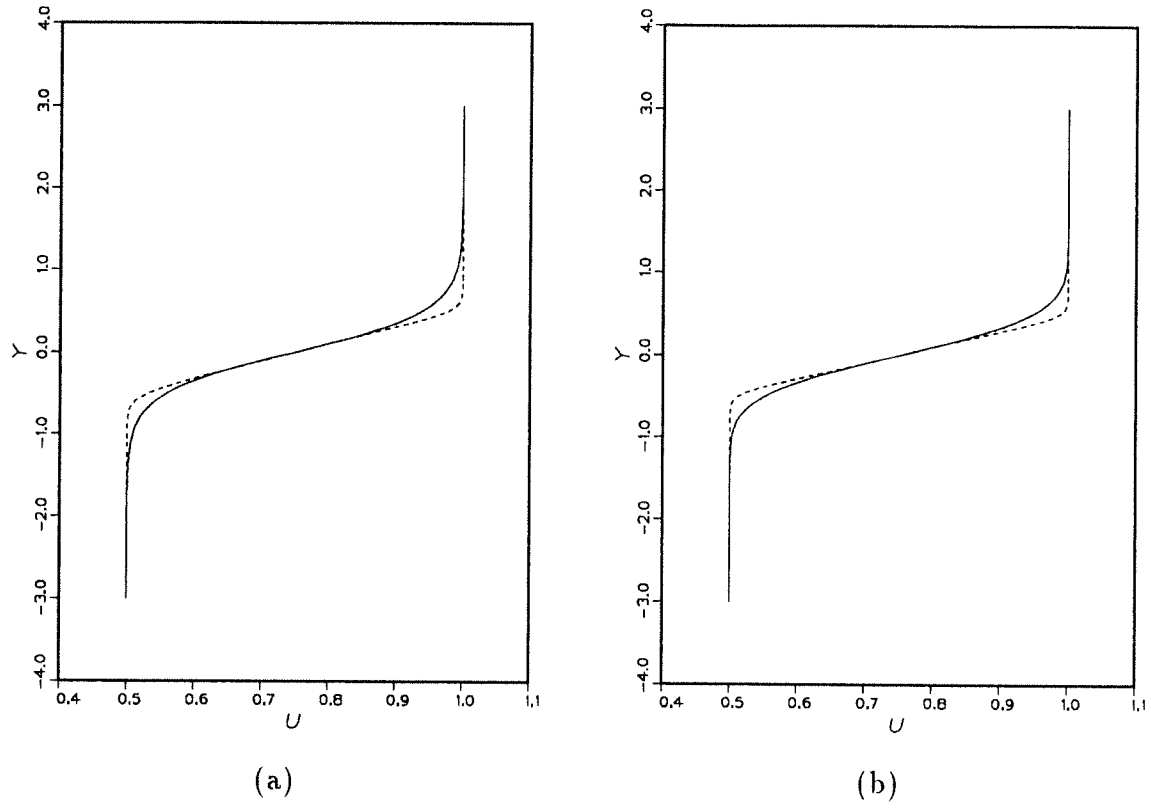

FIGURE 2.8. Comparison of laminar soutions and analytic functions. M_1=0, T_{ad}=8, Da=10. (a) spatial layer —— , hyperbolic-tangent; ---- , laminar (b) temporal layer —— , error; ---- , laminar.

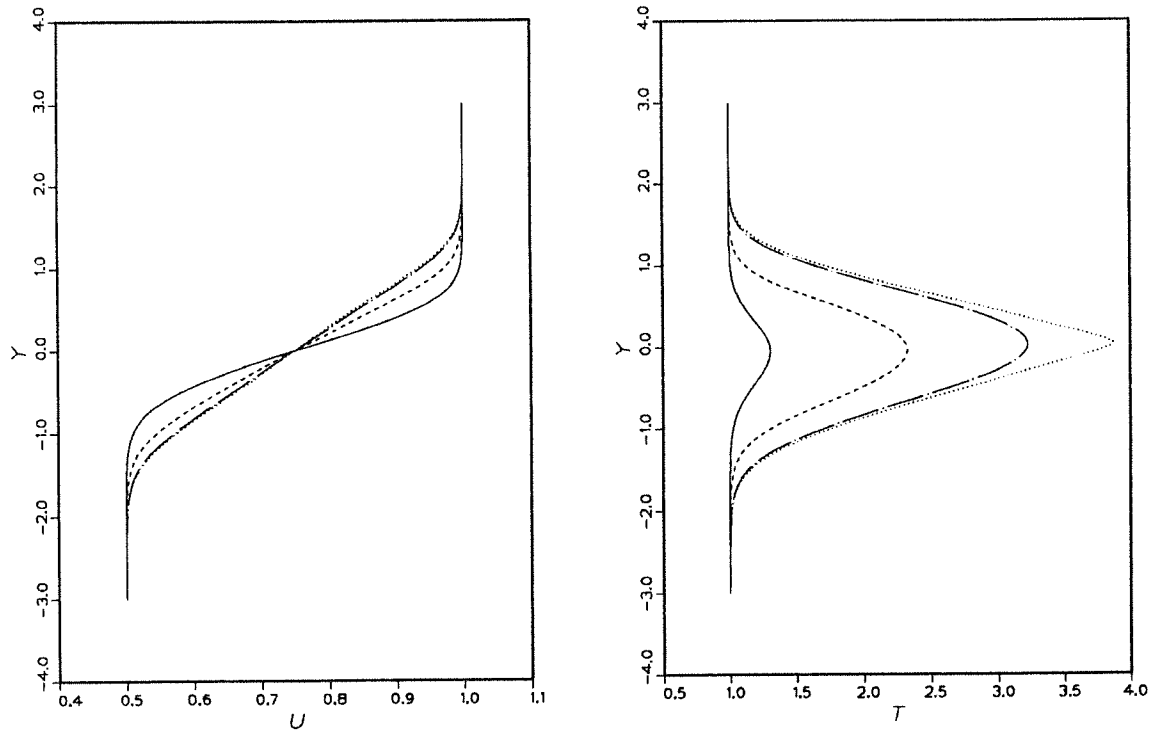

FIGURE 2.9. Continued.

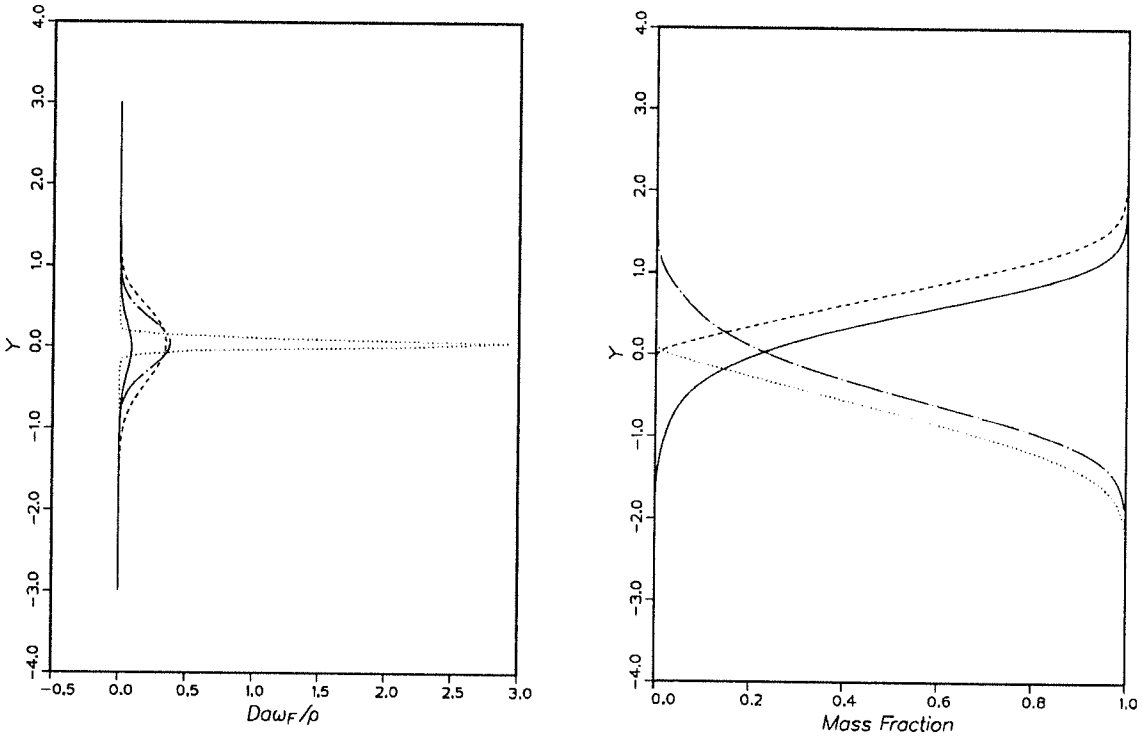

FIGURE 2.9. Effect of Damköhler number. M_1=0, T_{ad}=8, x=7.7. (a) velocity (b) temperature (c) reaction rate. —— , Da=0.2; ---- , Da=0.5; —·— , Da=2; ····· , Da=1000. (d) mass fraction. —— , Y_F, Da=0.5; ---- , Y_F, Da=1000; —·— , Y_O, Da=0.5; ····· , Y_O, Da=1000.

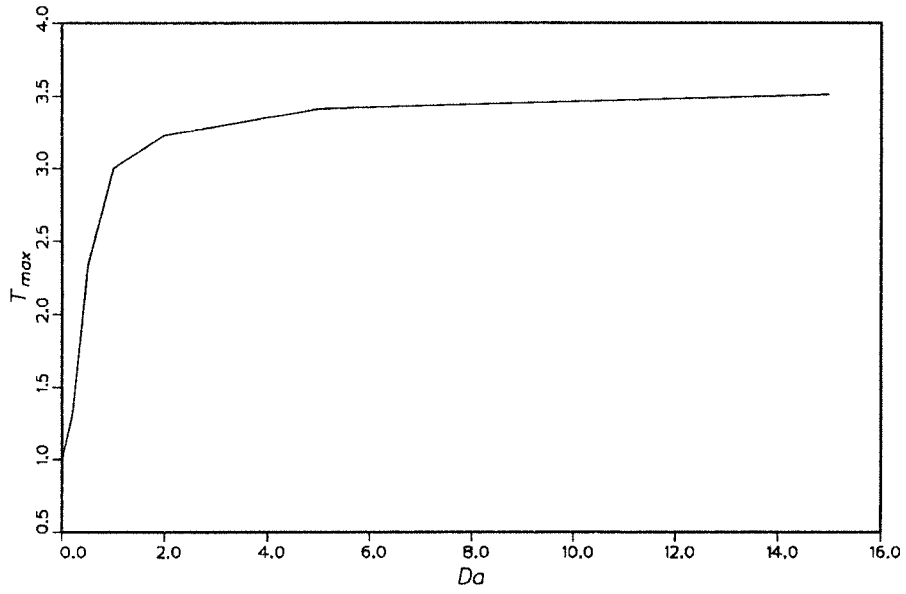

(a)

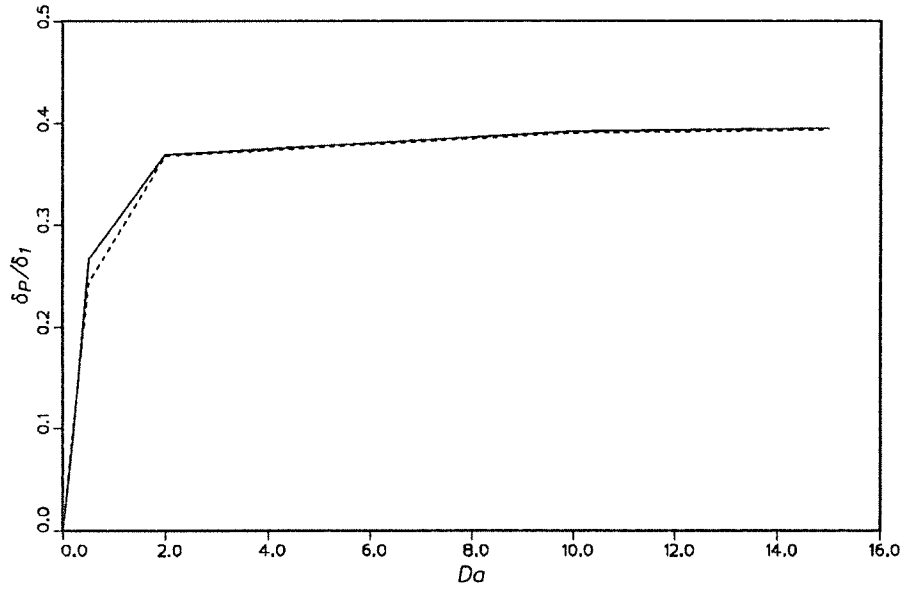

(b)

FIGURE 2.10. (a) Maximum temperature (Re=1000) and (b) normalized product thickness (——— , Re=500; ---- , Re=1000) vs. Da. T_{ad}=8, M_1=0, x=7.7.

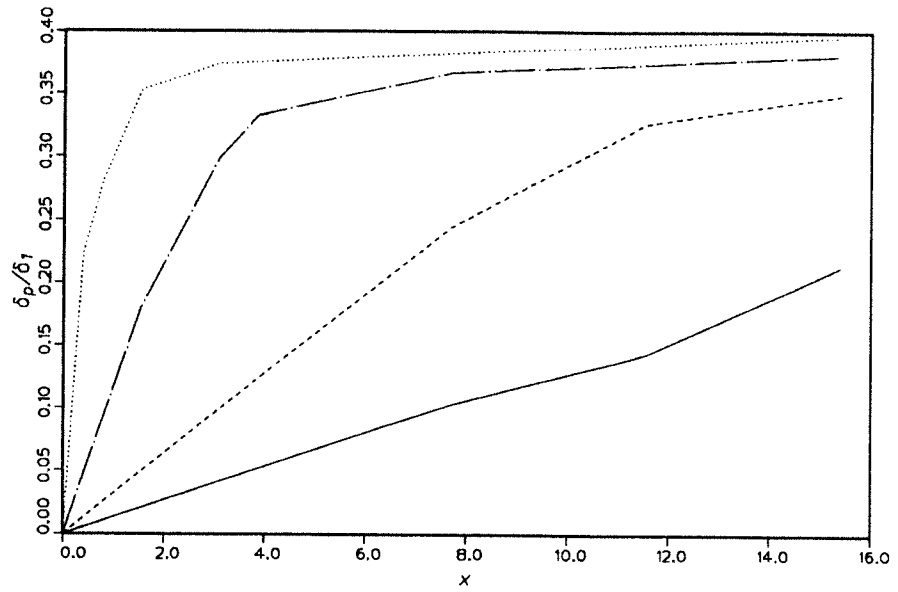

FIGURE 2.11. Normalized product thickness vs. x. M_1=0, T_{ad}=8. —— , Da=0.2; ---- , Da=0.5; —·— , Da=2; ····· , Da=10.

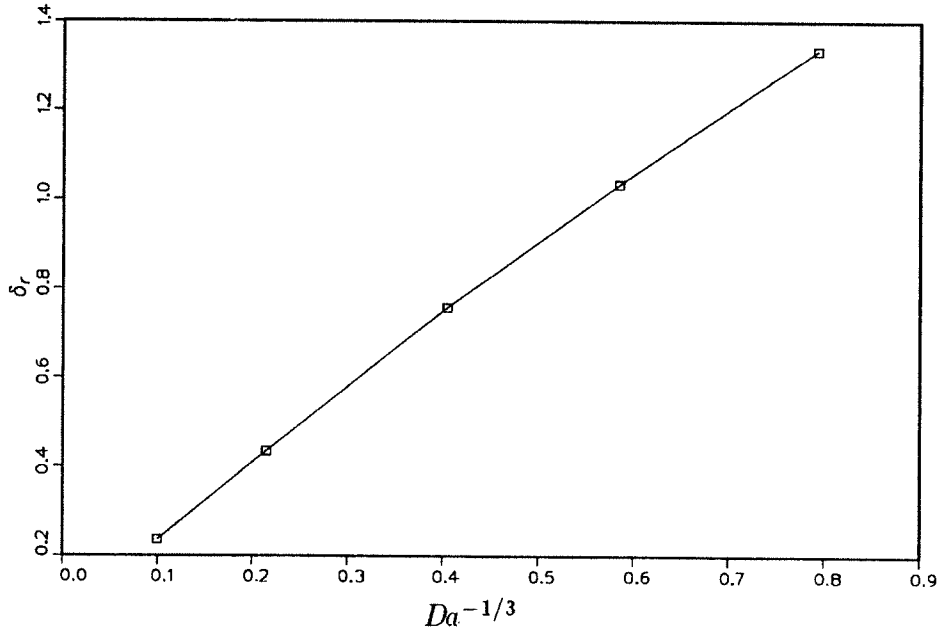

FIGURE 2.12. Reaction zone thickness vs. $Da^{-1/3}$. M_1=0, T_{ad}=8, x=7.7.

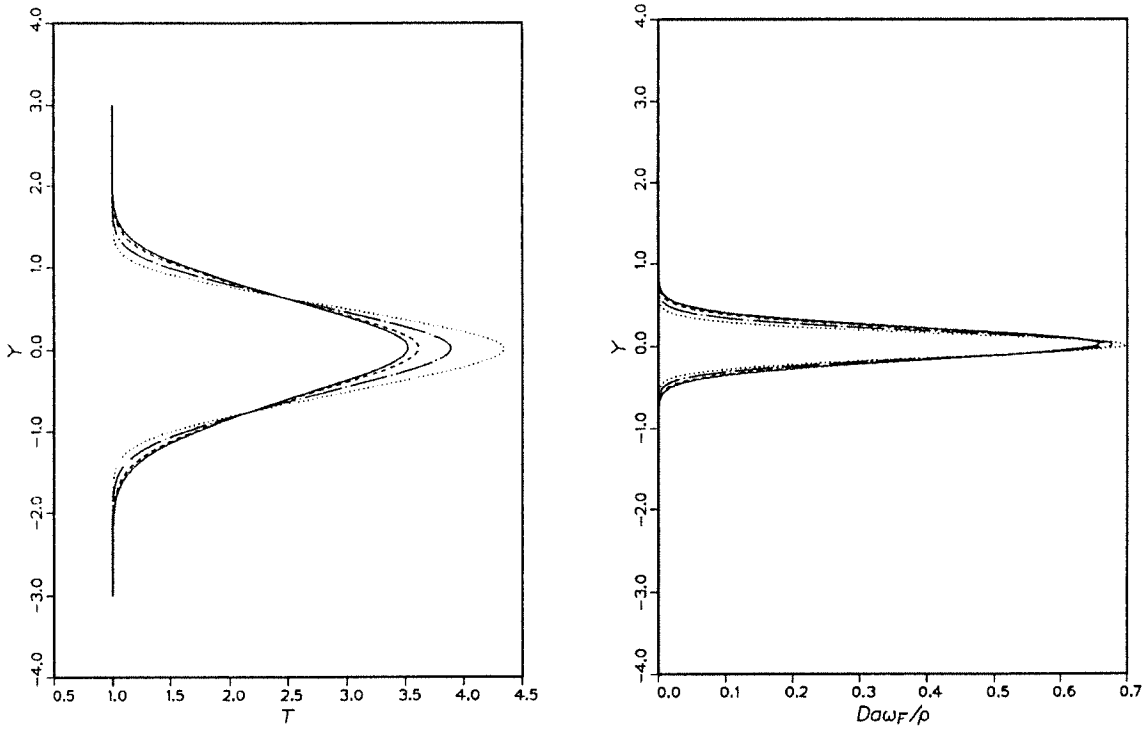

(a) (b)

FIGURE 2.13. Effect of Mach number. T_{ad}=8, Da=10. (a) temperature (b) reaction rate. ——— , M_1=0; ---- , M_1=2.5; —·— , M_1=5; ····· , M_1=7.5.

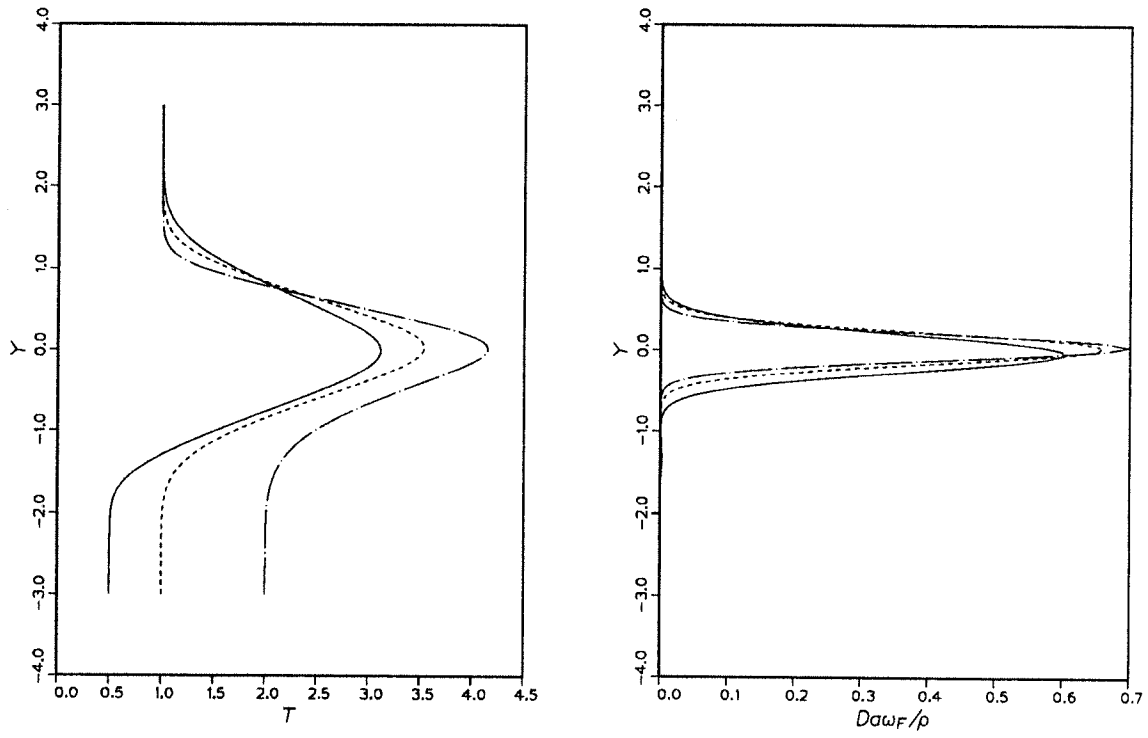

FIGURE 2.14. Effect of density ratio. T_{ad}=8, Da=10, M_1=1. (a) temperature (b) reaction rate. —— , ρ_2/ρ_1=2; ---- , ρ_2/ρ_1=1; —·— , ρ_2/ρ_1=0.5.

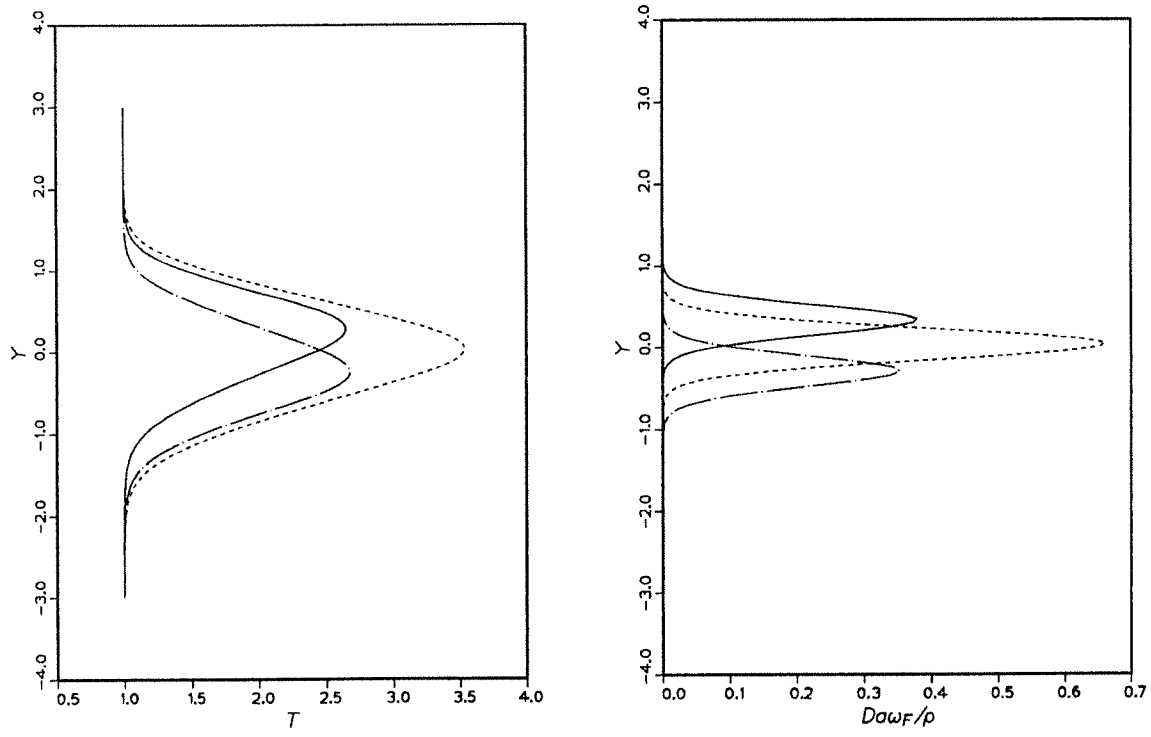

(a) (b)

FIGURE 2.15. Effect of equivalence ratio. T_{ad}=8, Da=10, M_1=1. (a) temperature (b) reaction rate. —— , ϕ=0.5; ---- , ϕ=1; —·— , ϕ=2.

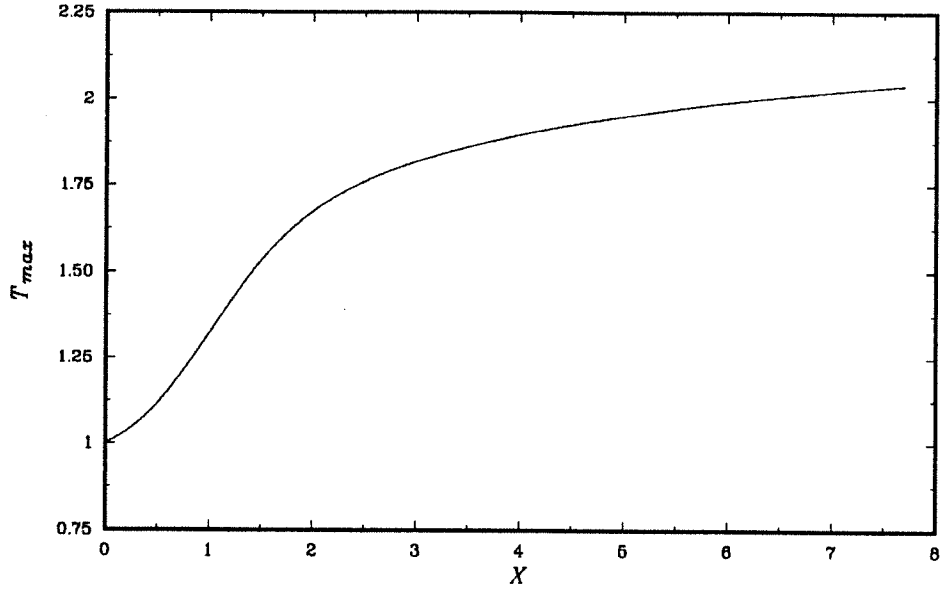

(a)

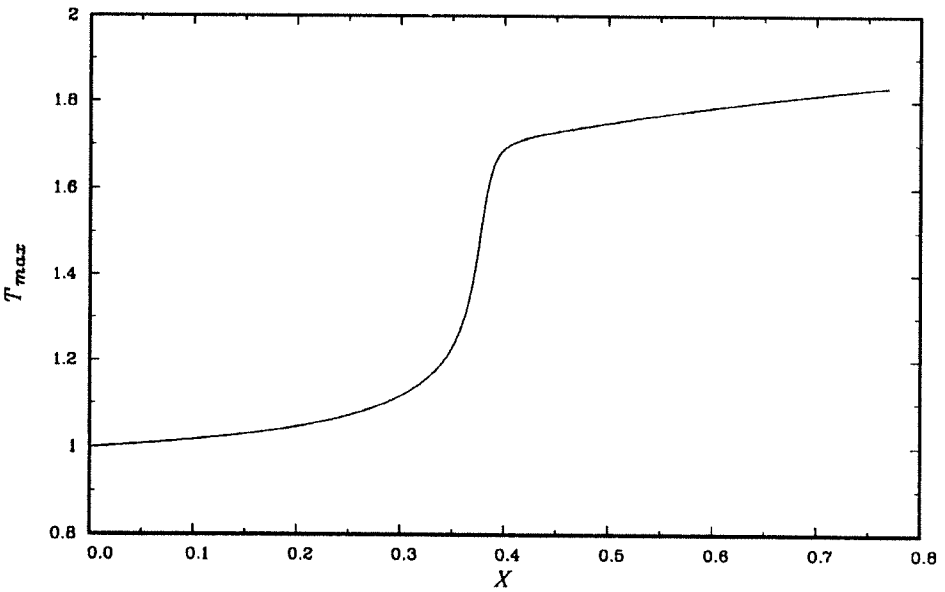

(b)

FIGURE 2.16. Maximum temperature vs. x. (a) β'=6 (b) β'=20. M_1=0, T_{ad}=4.

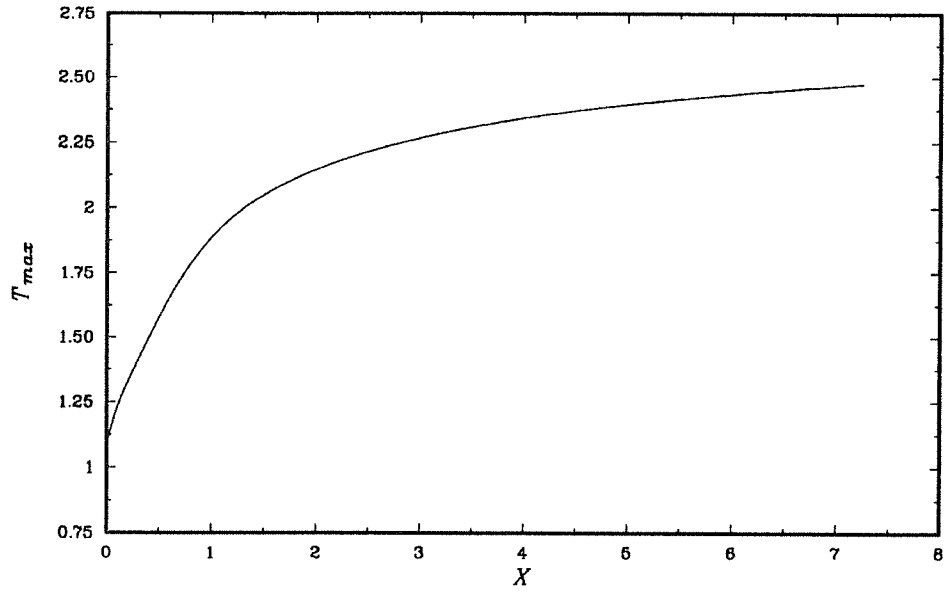

(a)

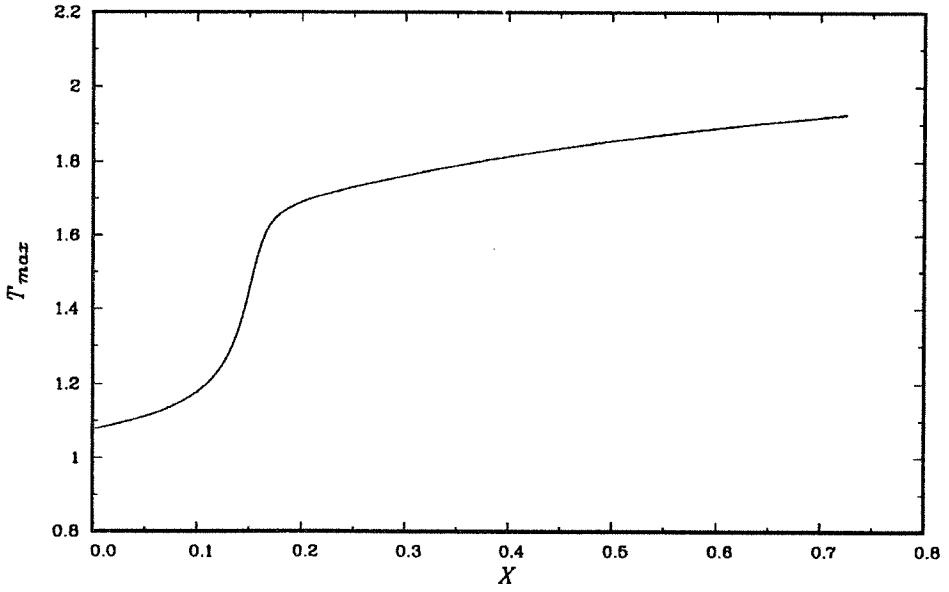

(b)

FIGURE 2.17. Maximum temperature vs. x. (a) β'=6 (b) β'=20. M_1=2.5, T_{ad}=4.

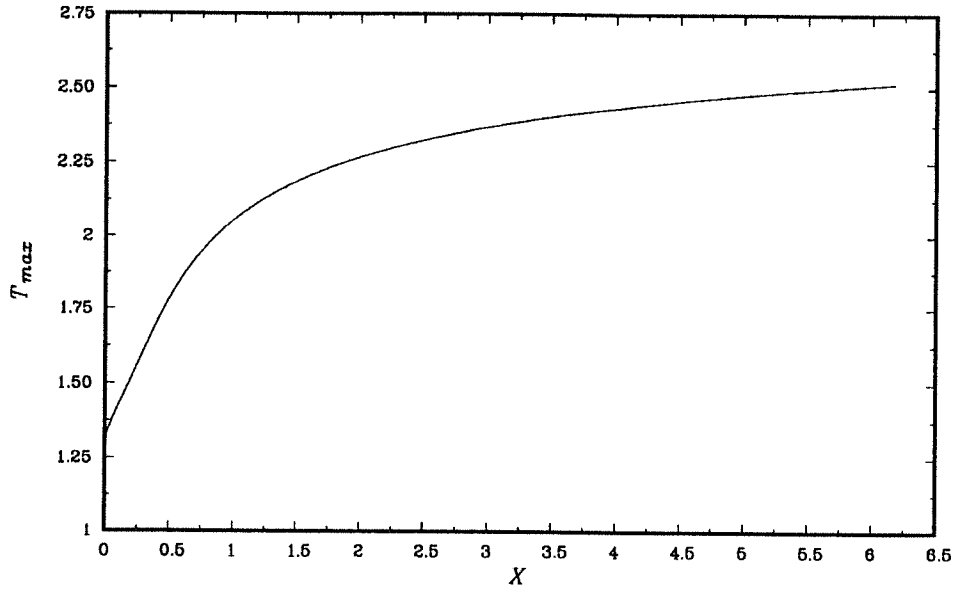

(a)

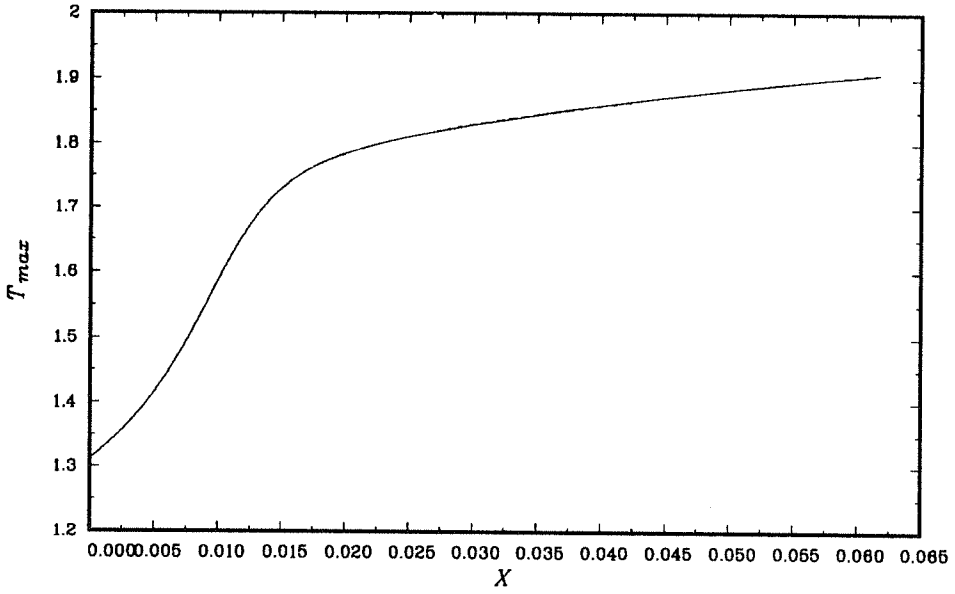

(b)

FIGURE 2.18. Maximum temperature vs. x. (a) β'=6 (b) β'=20. M_1=5, T_{ad}=4.

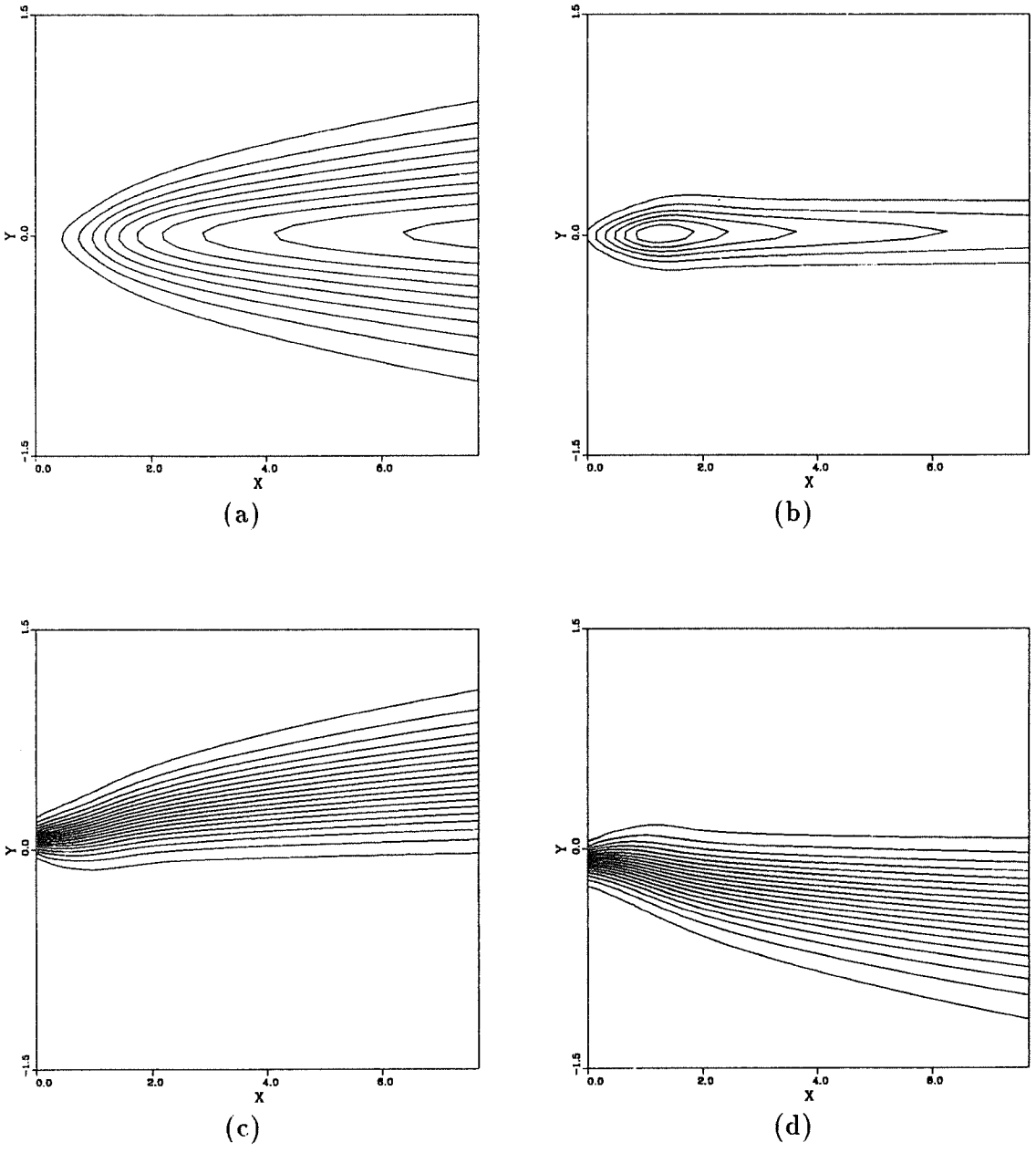

FIGURE 2.19. Contours of the (a) temperature (b) reaction rate (c) mass fraction of fuel (d) mass fraction of oxidizer. M_1=0, T_{ad}=4, β'=6.

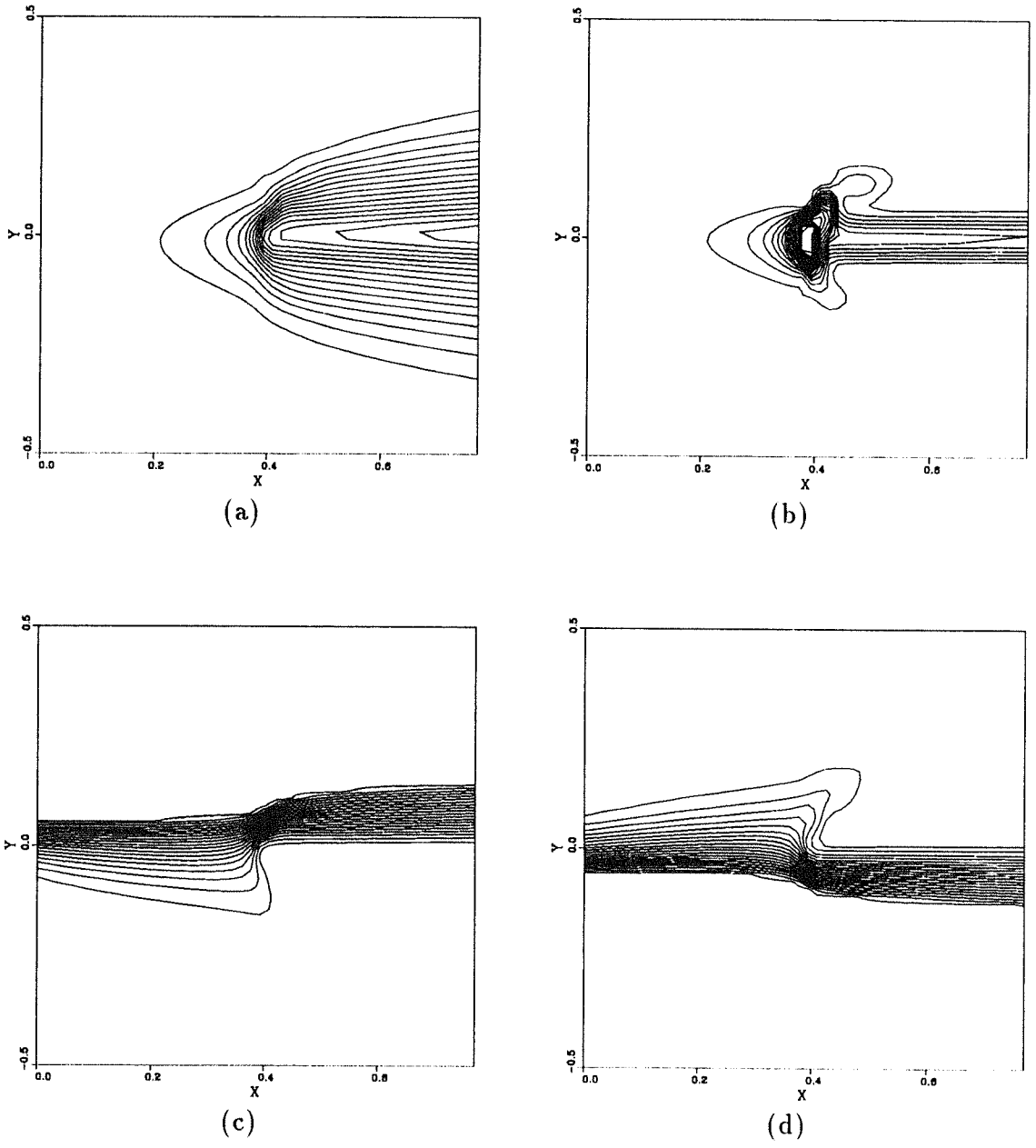

FIGURE 2.20. Contours of the (a) temperature (b) reaction rate (c) mass fraction of fuel (d) mass fraction of oxidizer. M_1=0, T_{ad}=4, β'=20.

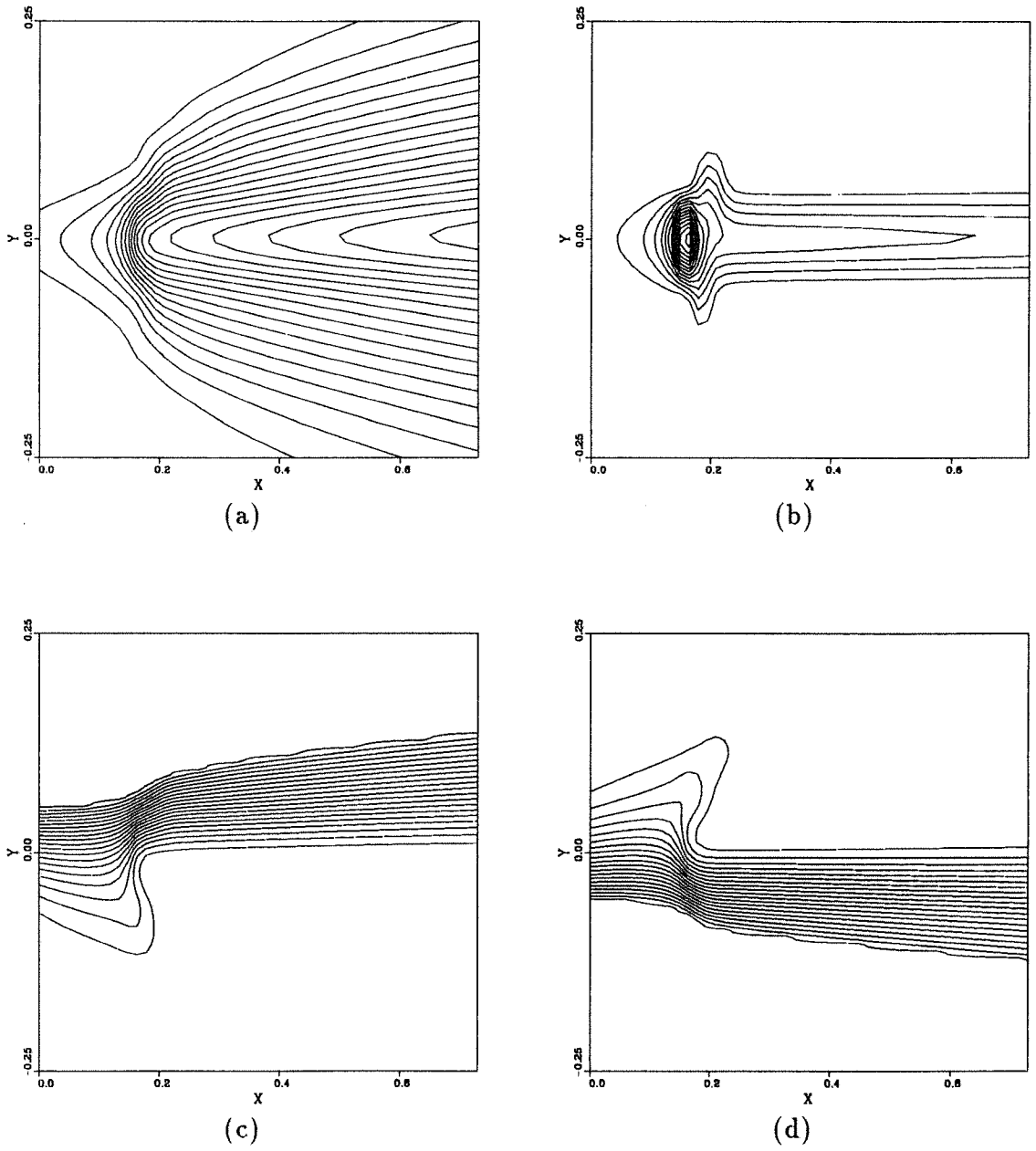

FIGURE 2.21. Contours of the (a) temperature (b) reaction rate (c) mass fraction of fuel (d) mass fraction of oxidizer. M_1=2.5, T_{ad}=4, β'=20.

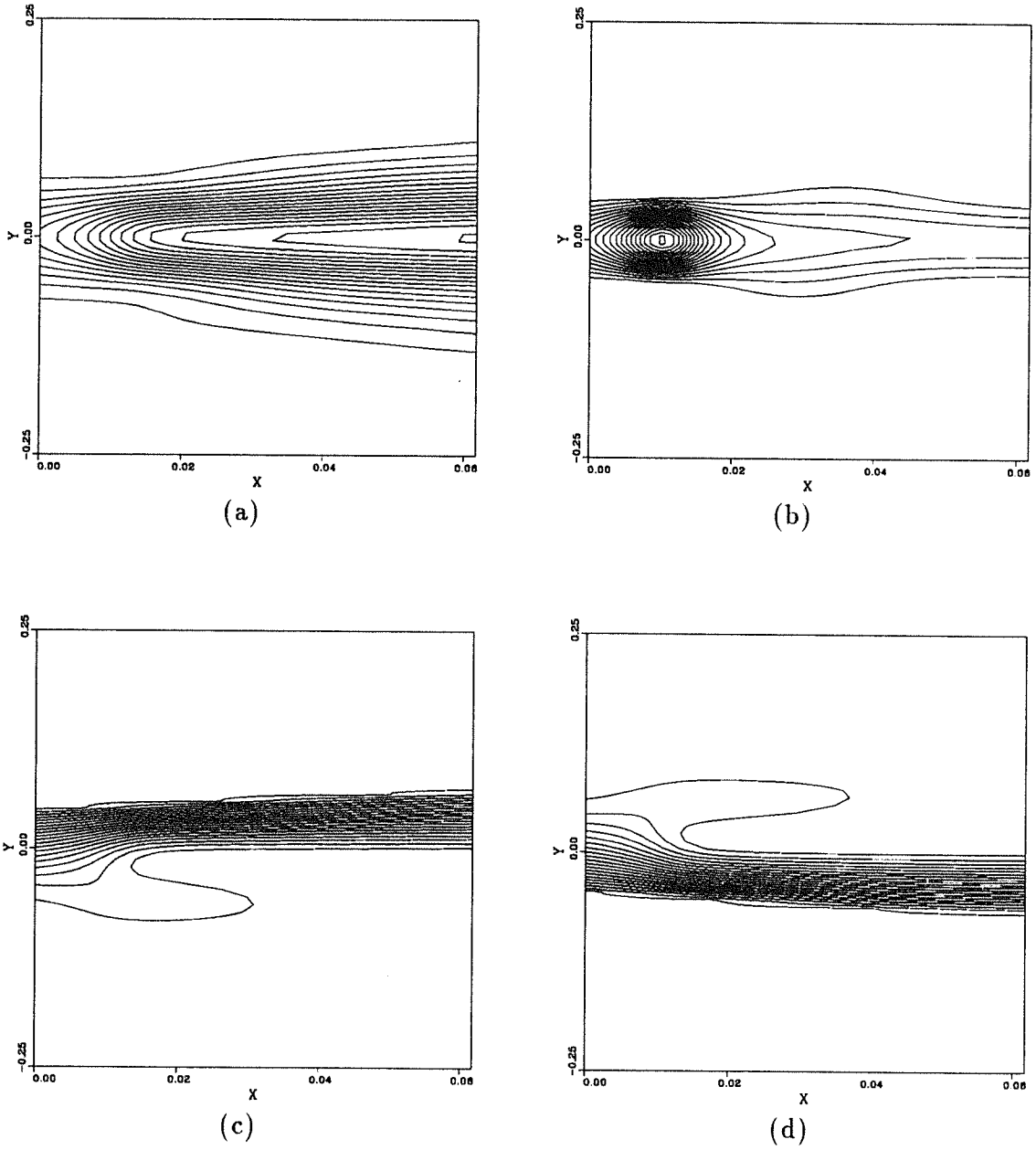

FIGURE 2.22. Contours of the (a) temperature (b) reaction rate (c) mass fraction of fuel (d) mass fraction of oxidizer. M_1=5, T_{ad}=4, β'=20.

Chapter 3

Inviscid Linear Stability: Formulation and Numerical Method

This chapter develops the equations governing the inviscid stability of a compressible reacting plane mixing layer. We assume that the laminar flow is parallel and that the disturbances are wave-like. Shooting and Newton/Raphson methods used to solve the resulting equations are described.

3.1 Linearized Disturbance Equations

In free shear flows, the viscosity acts to damp growing disturbances. Therefore, we shall solve the simpler inviscid stability problem in this study. We start from the Euler equations, which are obtained by dropping the diffusion terms from the Navier-Stokes equations. After applying the non-dimensionalization of Sec. 2.1.2, we can write the continuity, momentum, energy, species and state equations as follows:

$$\frac{\partial \rho}{\partial t} + u_i \frac{\partial \rho}{\partial x_i} + \rho \frac{\partial u_i}{\partial x_i} = 0 \tag{3.1}$$

$$\rho \left(\frac{\partial u_i}{\partial t} + u_j \frac{\partial u_i}{\partial x_j} \right) = -\frac{1}{\gamma M_1^2} \frac{\partial p}{\partial x_i} \tag{3.2}$$

$$\rho \left(\frac{\partial T}{\partial t} + \frac{\partial u_i T}{\partial x_i} \right) = -p(\gamma - 1) \frac{\partial u_i}{\partial x_i} + Da\, \omega_T \tag{3.3}$$

$$\rho \left(\frac{\partial y_i}{\partial t} + \rho u_j \frac{\partial y_i}{\partial x_j} \right) = Da\, \omega_i \tag{3.4}$$

$$p = \rho T \tag{3.5}$$

Here, γ is the specific heat ratio and M_1 is the Mach number of the upper stream.

To simplify the stability analysis, we assume that the laminar flow is parallel, i.e. that its variation is entirely in the direction normal to the flow. In order to perform stability calculations, the laminar velocity, density, temperature and species profiles need to be specified. The mean pressure is assumed constant and its non-dimensional

value is unity. All variables are taken to be sums of their laminar values and small perturbations of travelling wave form. Thus, all flow variables can be represented as

$$f(x,y,z,t) = \overline{f}(y) + f'(x,y,z,t) \tag{3.6}$$

where

$$f'(x,y,z,t) = \hat{f}(y)\, e^{i(\alpha x+\beta z-\omega t)} \tag{3.7}$$

and $\overline{f}(y)$ is the laminar profile of a quantity, $\hat{f}$ depends only on the y coordinate, and α and β are wavenumbers in the streamwise (x) and spanwise (z) directions respectively, and ω is the frequency. The relation between the wavenumbers and the propagation angle of disturbance relative to the x direction is

$$\tan\theta = \beta/\alpha_r \tag{3.8}$$

where α_r is the real part of α. Since the disturbances do not grow in z, the wavenumber β is real. The forms of α and ω depend on the problem. In temporal stability analysis α is real and ω may be complex while in spatial stability analysis ω is real and α is allowed to be complex. The amplification rate is ω_i or $-\alpha_i$ in the two cases, respectively. For neutral disturbances ω and α are real. The complex wave velocity c is ω/α.

Substituting Eqs. (3.6) and (3.7) into Eqs. (3.2) and (3.3) and neglecting products of perturbations, we obtain the following linearized equations:

$$i(\alpha\bar{u}-\omega)\hat{\rho} + \bar{\rho}'\hat{v} + \bar{\rho}[i(\alpha\hat{u}+\beta\hat{w}) + \hat{v}'] = 0 \tag{3.9}$$

$$i\bar{\rho}(\alpha\bar{u}-\omega)\hat{u} + \bar{\rho}\bar{u}'\hat{v} = \frac{-i\alpha\hat{p}}{\gamma M_1^2} \tag{3.10}$$

$$i\bar{\rho}(\alpha\bar{u}-\omega)\hat{v} = \frac{-\hat{p}'}{\gamma M_1^2} \tag{3.11}$$

$$i\bar{\rho}(\alpha\bar{u}-\omega)\hat{w} = \frac{-i\beta\hat{p}}{\gamma M_1^2} \tag{3.12}$$

where a prime indicates differentiation with respect to y. Eliminating $\hat{u}, \hat{v}$ and $\hat{w}$ from these equations, we obtain an equation involving only the pressure and density

$$\hat{p}'' - \frac{2\alpha\bar{u}'}{(\alpha\bar{u}-\omega)}\hat{p}' + \gamma M_1^2(\alpha\bar{u}-\omega)^2\hat{\rho} - (\alpha^2+\beta^2)\hat{p} = 0 \tag{3.13}$$

Eq. (3.13) becomes the Rayleigh equation (Rayleigh [1880]) if density is constant, i.e. when $\hat{\rho}$=0.

The linearized state equation obtained from Eq. (3.5) is

$$\hat{p} = \bar{\rho}\hat{T} + \bar{T}\hat{\rho} \tag{3.14}$$

and allows $\hat{\rho}$ to be expressed in terms of $\hat{T}$ and $\hat{p}$. To relate $\hat{T}$ to $\hat{p}$, we linearize the species and energy equations. After using Eq. (3.11), we have the following equation for the perturbed fuel concentration:

$$\hat{y}_F\left\{i\bar{\rho}(\alpha\bar{u}-\omega) + Da\,\bar{\rho}^2\bar{y}_O\,exp\left[-\beta'\left(\frac{1}{\bar{T}}-1\right)\right]\right\} =$$

$$\frac{\hat{p}'}{\gamma M_1^2}\left[\frac{-\bar{y}_F' i}{(\alpha\bar{u}-\omega)}\right] - 2\hat{p}Da\,\bar{\rho}^2\bar{y}_F\bar{y}_O\,exp\left[-\beta'\left(\frac{1}{\bar{T}}-1\right)\right] +$$

$$\hat{T}\left[-\frac{\bar{\rho}^2}{\bar{T}^2}\bar{y}_F\bar{y}_O\beta' + 2\frac{\bar{\rho}^2}{\bar{T}}\bar{y}_F\bar{y}_O\right]Da\,exp\left[-\beta'\left(\frac{1}{\bar{T}}-1\right)\right] -$$

$$\hat{y}_O Da\,\bar{\rho}^2\bar{y}_F\,exp\left[-\beta'\left(\frac{1}{\bar{T}}-1\right)\right] \tag{3.15}$$

Following the same procedure for y_O and T, we can write symbolically the resulting equations, including Eq. (3.15), as

$$A\hat{y}_F = B\frac{\hat{p}'}{\gamma M_1^2} - C\hat{y}_O + D\hat{T} - E\hat{p} \tag{3.16}$$

$$F\hat{y}_O = G\frac{\hat{p}'}{\gamma M_1^2} - H\hat{y}_F + I\hat{T} - J\hat{p} \tag{3.17}$$

$$K\hat{T} = L\frac{\hat{p}'}{\gamma M_1^2} + M\hat{y}_O + N\hat{y}_F + O\hat{p} \tag{3.18}$$

The coefficients denoted by capital letters are given in the Appendix. Eqs. (3.16), (3.17) and (3.18) may be written in matrix form:

$$\begin{bmatrix} A & C & -D \\ H & F & -I \\ N & M & -K \end{bmatrix} \begin{bmatrix} \hat{y}_F \\ \hat{y}_O \\ \hat{T} \end{bmatrix} = \frac{\hat{p}'}{\gamma M_1^2} \begin{bmatrix} B \\ G \\ -L \end{bmatrix} - \hat{p} \begin{bmatrix} E \\ J \\ O \end{bmatrix} \tag{3.19}$$

By eliminating the species mass fractions from these equations, we can relate $\hat{T}$ to $\hat{p}$:

$$\hat{T} = [RXN1]\frac{\hat{p}'}{\gamma M_1^2} - [RXN2]\,\hat{p} \tag{3.20}$$

The coefficients of this equation can be written as ratios of determinants whose elements are the coefficients in the above equations.

$$[RXN1] = \frac{\begin{vmatrix} A & C & B \\ H & F & G \\ N & M & -L \end{vmatrix}}{\begin{vmatrix} A & C & -D \\ H & F & -I \\ N & M & -K \end{vmatrix}}, \qquad [RXN2] = \frac{\begin{vmatrix} A & C & E \\ H & F & J \\ N & M & O \end{vmatrix}}{\begin{vmatrix} A & C & -D \\ H & F & -I \\ N & M & -K \end{vmatrix}} \tag{3.21}$$

These terms represent the effect of density variation due to chemical reaction and compressibility on the instability.

Using Eqs. (3.14) and (3.20) to relate $\hat{\rho}$ to $\hat{p}$, we get the disturbance equation for the pressure:

$$\hat{p}'' - \left\{ \frac{2\alpha\bar{u}'}{(\alpha\bar{u}-\omega)} + \frac{\bar{\rho}}{\bar{T}}(\alpha\bar{u}-\omega)^2[RXN1] \right\} \hat{p}' -$$

$$\left[(\alpha^2+\beta^2) - \gamma {M_1}^2 (\alpha\bar{u}-\omega)^2 \left\{ \frac{1}{\bar{T}} + \frac{\bar{\rho}}{\bar{T}}[RXN2] \right\} \right] \hat{p} = 0 \tag{3.22}$$

Note that this is a homogeneous second order ordinary differential equation.

Squire's transformation [1933] allows a three dimensional problem to be reduced to a two dimensional one. If we discard the chemical reaction during the instability, use Eq. (3.8), and let

$$\tilde{\alpha} = (\alpha^2+\beta^2)^{1/2},\ \tilde{p}/\alpha = \hat{p}/\tilde{\alpha},\ \tilde{\omega}/\tilde{\alpha} = \omega/\alpha,\ \tilde{M}_1/\alpha = M_1/\tilde{\alpha} \tag{3.23}$$

then Eq. (3.22) becomes

$$\tilde{p}'' - \left\{ \frac{2\tilde{\alpha}\bar{u}'}{(\tilde{\alpha}\bar{u} - \tilde{\omega})} + \frac{\bar{T}'}{\bar{T}} \right\} \tilde{p}' - \left[\tilde{\alpha}^2 - \frac{\tilde{M}_1^2}{\bar{T}} (\tilde{\alpha}\bar{u} - \tilde{\omega})^2 \right] \tilde{p} = 0 \tag{3.24}$$

Eq. (3.24) is exactly the two dimensional version of Eq. (3.22) if the effects of chemical reaction are neglected in the stability analysis. Thus, provided that chemical reaction is neglected, Squire's transformation reduces a three dimensional problem to an equivalent two dimensional problem.

3.2 Boundary Conditions and Nature of Disturbances

As Eq. (3.22) is second order, it requires two boundary conditions. These require the pressure perturbation to be bounded as $|y| \to \infty$. This can be made more precise by considering the asymptotic form of the solutions of Eq. (3.22). As $y \to \pm\infty$, $\bar{u}'$ and $[RXN1]$ become negligible and $[RXN2]$ becomes $-\bar{T}(\gamma - 1)/\gamma$. Eq. (3.22) then reduces to

$$\hat{p}'' - q^2 \hat{p} = 0 \tag{3.25}$$

where

$$q^2 = (\alpha^2 + \beta^2) - \frac{{M_1}^2}{\bar{T}} (\alpha\bar{u} - \omega)^2 \tag{3.26}$$

Note that q^2 can be positive, negative or complex. This will play an important role below. Far from the shear layer, the pressure must behave like

$$\hat{p} \to \exp(\pm qy) \qquad \text{as} \quad y \to \mp\infty \tag{3.27}$$

The asymptotic behavior of the disturbances can be inferred from this result. The nature of the disturbance can be described in terms of the relative Mach numbers, M_{ri} (i=1,2), which are defined as the Mach numbers of the disturbances in the direction of the wavevector (α, β) relative to the free-streams i (i=1 denotes the upper stream and i=2, the lower stream):

$$M_{r1} = \frac{\alpha(c^* - \bar{u}_1^*)}{(\alpha^2 + \beta^2)^{1/2}\, a_1^*}, \qquad M_{r2} = \frac{\alpha(c^* - \bar{u}_2^*)}{(\alpha^2 + \beta^2)^{1/2}\, a_2^*} \tag{3.28}$$

where the superscript $*$ denotes a dimensional quantity and c^* is the phase velocity of the disturbance. After applying the non-dimensionalization of Sec. 2.1.2 and using Eqs. (2.20), (2.21) and (3.23), $M_{r1,2}$ become

$$M_{r1} = \frac{\alpha M_1 (c-1)}{(\alpha^2+\beta^2)^{1/2}} = \tilde{M}_1 (c-1), \qquad M_{r2} = \frac{\alpha M_1 (c-\bar{u}_2)}{(\alpha^2+\beta^2)^{1/2}\,\bar{T}_2^{1/2}} = \frac{\tilde{M}_1 (c-\bar{u}_2)}{\bar{T}_2^{1/2}} \tag{3.29}$$

When the magnitude of a relative Mach number is less than unity, the instability wave is said to be subsonic with respect to that boundary; when it is greater than unity, it is said to be supersonic with respect to that boundary. At the zeros of q^2, the instability waves are sonic ($|M_r|$=1).

We define c_u as the phase speed of a disturbance that is sonic with respect to the upper stream and c_l as the corresponding speed with respect to the lower stream.

$$c_u = 1 - \frac{(\alpha^2+\beta^2)^{1/2}}{\alpha M_1} = 1 - \frac{1}{\tilde{M}_1}, \qquad c_l = \bar{u}_2 + \frac{(\alpha^2+\beta^2)^{1/2}\,\bar{T}_2^{1/2}}{\alpha M_1} = \bar{u}_2 + \frac{\bar{T}_2^{1/2}}{\tilde{M}_1} \tag{3.30}$$

We plot $c_{u,l}$ versus M_1 for $\bar{u}_2$=0.5, $\bar{T}_2$=1 and β=0 in Fig. 3.1. These curves divide the (c_r, M_1) plane into four regions. The regions correspond to disturbances which are subsonic with respect to both boundaries ($|M_{r1,2}| < 1$, region I), subsonic with respect to the upper stream and supersonic with respect to the lower stream ($|M_{r1}| < 1, |M_{r2}| > 1$, region II), subsonic with respect to the lower stream and supersonic with respect to the upper stream ($|M_{r1}| > 1, |M_{r2}| < 1$, region IV), and, finally, supersonic with respect to both boundaries ($|M_{r1,2}| > 1$, region III). The relative Mach number of the most unstable mode was called the convective Mach number by Mack [1975] and was also used by Zhuang *et al.* [1988]. The quantity q is real only for neutral subsonic disturbances; for neutral supersonic disturbances it is purely imaginary; in all other cases it is complex. When the disturbances are subsonic with respect to either free-stream, Eq. (3.27) must be satisfied so that the disturbances remain bounded at infinity. These modes are similar to the ones arising in incompressible stability theory. For supersonic disturbances, the instability waves are oscillatory and move along the constant phase lines

$$\alpha_r x + \beta_r z \pm q_i\, y - \omega t = 0 \tag{3.31}$$

Supersonic neutral disturbances may be classified as incoming (if $q_i > 0$) or outgoing (if $q_i < 0$) for the upper free-stream; the signs are reversed for the lower free-stream. Only outgoing waves are acceptable; incoming waves must be rejected. Setting the amplitudes of the incoming waves to zero provides the required boundary conditions.

3.3 Solution Procedure

An iterative method based on the shooting and Newton/Raphson methods is used to solve Eq. (3.22). It requires profiles of $\bar{u}$, $\bar{\rho}$, $\bar{T}$, $\bar{y}_F$, $\bar{y}_O$ and values of parameters M_1, Da, β', Q, γ, $W_i\nu_i$ as inputs. To begin, a guess at the eigenvalue is made. For a spatial analysis, ω is specified and α is guessed, whereas for temporal analysis, α is specified and ω guessed. Given the eigenvalue, $\hat{p}$ for large y is given by Eq. (3.25). The computation starts at some large value of y on each side; the starting value of y must be within the range of y for which laminar flow is tabulated but large enough for the solution to be essentially constant. Then we integrate Eq. (3.22) from both free-streams toward the centerline of the mixing layer. We used the subroutine ODE (Shampine & Gordon [1975]) for the integration with an error control parameter of 10^{-7}.

At the centerline, y=0, the values of $\hat{p}$ and $\hat{p}'$ computed by integration from the upper stream are compared with the values computed by integration from the lower stream. If we let $\hat{p}_1$ be the upper solution and $\hat{p}_2$ the lower solution at y=0, then we can write

$$\hat{p}_1 = C_1\hat{p}_{r1} + C_1\hat{p}_{i1}, \qquad \hat{p}_2 = C_2\hat{p}_{r2} + C_2\hat{p}_{i2} \tag{3.32}$$

where $C_{1,2}$ are arbitrary constants that depend on the starting values. The matching condition requires that

$$\hat{p}_1 = \hat{p}_2, \qquad \hat{p}_1' = \hat{p}_2' \tag{3.33}$$

If we define F as

$$F(\alpha) = \frac{(-\hat{p}_1\hat{p}_2' + \hat{p}_1'\hat{p}_2)}{C_1C_2} \tag{3.34}$$

then, Eq. (3.33) requires that $F(\alpha)$=0. If F=0, the process has converged; if not, a new eigenvalue is chosen by the Newton-Raphson method

$$\begin{pmatrix} \alpha_r \\ \alpha_i \end{pmatrix}_{n+1} = \begin{pmatrix} \alpha_r \\ \alpha_i \end{pmatrix}_n - \begin{bmatrix} \partial F_r/\partial \alpha_r & \partial F_r/\partial \alpha_i \\ \partial F_i/\partial \alpha_r & \partial F_i/\partial \alpha_i \end{bmatrix}_n^{-1} \begin{pmatrix} F_r \\ F_i \end{pmatrix}_n \tag{3.34}$$

and iteration continues until the eigenvalue increment is reduced to 10^{-6}. We used double precision arithmetic, which allowed computation of even weakly amplified unstable modes at high Mach numbers. Once we found the eigenvalues, we can calculate the eigenfunction $\hat{p}$ by integrating Eq. (3.22) from the centerline to the free-stream. The other components of the eigenfunctions are calculated from Eqs. (3.10), (3.11), (3.12), (3.14) and (3.19). The eigenfunctions are normalized so that maximum absolute value of $\hat{u}$ is 1. Eigenvalues and eigenfunctions can be calculated in this way for unstable, neutral and damped temporal, spatial and temporal/spatial cases.

3.4 Validation

To confirm the validity of our equations and numerical methods, we compared our results to published data including the incompressible case without chemical reaction (Michalke [1965]), and a reacting flow case with hyperbolic-tangent mean profiles (Trouvé and Candel [1988]). Figure 3.2 shows the temporal growth rates of the incompressible mixing layer with a hyperbolic-tangent velocity profile. The temperature is uniform. There is excellent agreement with Michalke's results. Numerical comparison is presented in Table 3.1. Figure 3.3 shows the spatial growth rates of the reacting mixing layer with hyperbolic-tangent mean velocity and temperature profiles, $U(y) = 1 + \tanh(y/2)$ and $T(y) = 1 + \lambda_t \tanh(y/2)$, where λ_t depends on the heat release. We checked the results for four different free-stream temperature ratios $\bar{T}_2$=0.5, 1, 2, 5 against the results by Trouvé and Candel. Again, excellent agreement is obtained.

3.5 Chapter Summary

In this chapter, we developed the governing equations for the inviscid stability of a compressible reacting plane mixing layer, assuming parallel laminar flow and wave-

α_r	ω_i (Michalke)	ω_i (current)
0.1	0.04184	0.04180
0.2	0.06975	0.06970
0.3	0.08654	0.08650
0.4	0.09410	0.09409
0.5	0.09376	0.09377
0.6	0.08650	0.08652
0.7	0.07305	0.07304
0.8	0.05388	0.05389
0.9	0.02942	0.02942

TABLE 3.1. Comparison of the temporal growth rates of the incompressible flow.

like disturbances. We described the numerical methods used to solve the resulting equations and validated the code by comparison with published results.

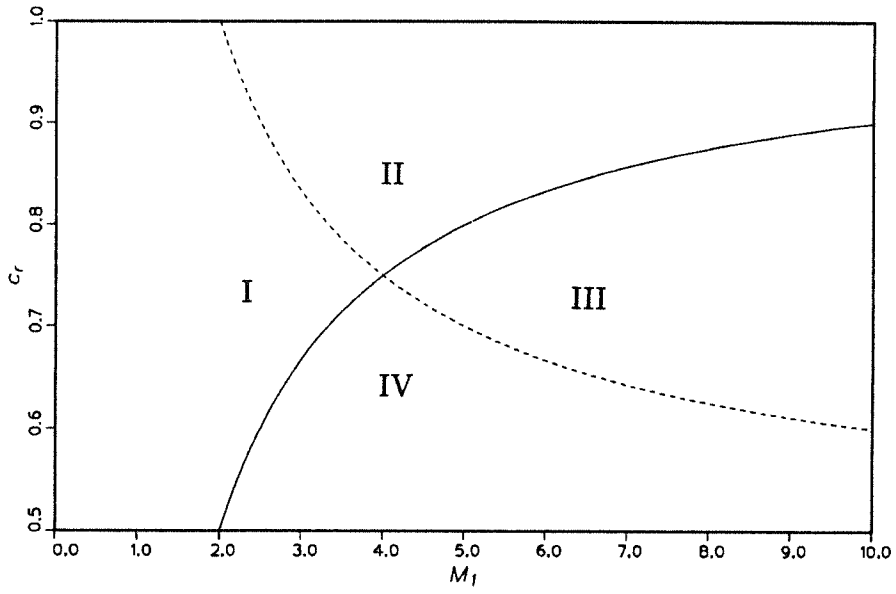

FIGURE 3.1. The sonic phase speeds of disturbances vs. Mach number. $\bar{u}_2$=0.5, $\bar{T}_2$=1, β=0. ——— , c_u; ---- , c_l.

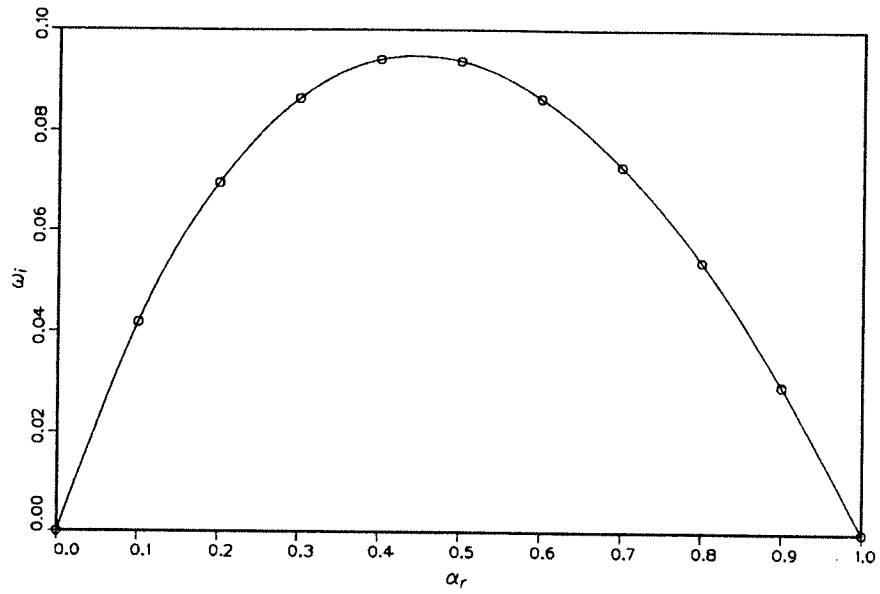

FIGURE 3.2. Temporal growth rates of incompressible case with hyperbolic-tangent velocity profile. ○ , Michalke [1965]; —— , current.

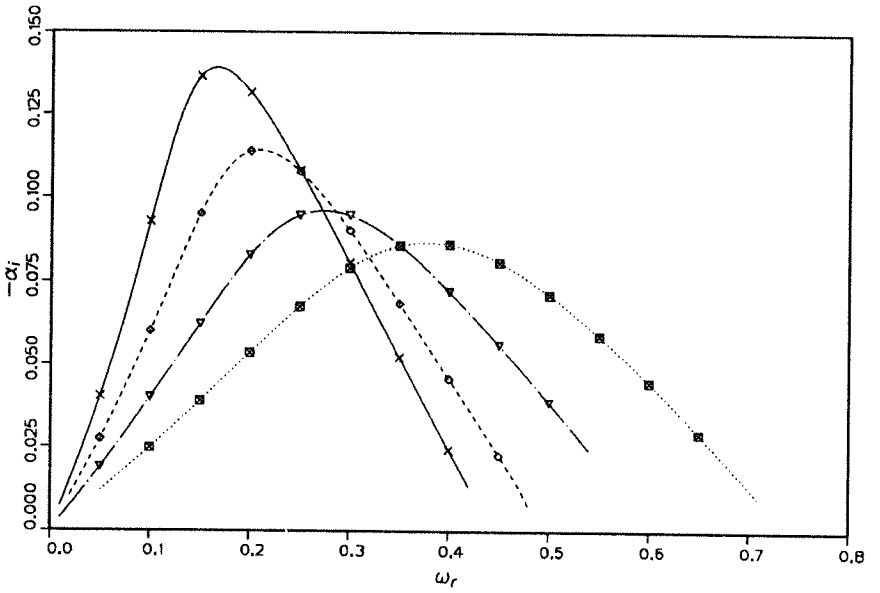

FIGURE 3.3. Spatial growth rates with variable free-stream temperature ratios (symbols, Trouvé & Candel [1988]; lines, current). —— , ×, $\bar{T}_2$=0.5; ---- , ◇ , $\bar{T}_2$=1; —·— , ▽ , $\bar{T}_2$=2; ····· , ☒ , $\bar{T}_2$=5.

Chapter 4

Instability of the Incompressible Reacting Free Shear Layer

This chapter presents the results of linear stability analyses of incompressible reacting mixing layers. The governing equations given in Chapter 3 valid for fully compressible flows become singular in the limit of zero Mach number (see Eq. (3.2)). However, for the incompressible plane mixing layer with variable density, we can derive a set of equations that apply in the limit of zero Mach number. This derivation is given in Sec. 4.1. A similar procedure was used by McMurtry *et al.* [1985] and Mahalingam *et al.* [1989]. We also derive a necessary condition for instability of the incompressible reacting plane mixing layer. We consider both temporally and spatially developing layers; the former are easier to understand while the latter are used for comparison with experiment. We find that new inflectional modes of instability may exist in the outer part of the mixing layer and that heat release stabilizes the flow.

4.1 Low Mach Number Approximation

We start from the exact governing equations of Sec. 3.1, assume the Mach number is low, and use a low Mach number expansion. Let $\epsilon = \gamma M_1^2$ and assume that $\epsilon \ll 1$; then all the dependent variables may be expanded as power series in ϵ:

$$f = f^{(0)} + \epsilon f^{(1)} + \epsilon^2 f^{(2)} \ldots \tag{4.1}$$

Substituting these series into Eqs. (3.1) through (3.5) and equating terms of zeroth order, we obtain the following equations:

$$\frac{\partial \rho^{(0)}}{\partial t} + \rho^{(0)} \frac{\partial u_i^{(0)}}{\partial x_i} + u_i^{(0)} \frac{\partial \rho^{(0)}}{\partial x_i} = 0 \tag{4.2}$$

$$\frac{\partial p^{(0)}}{\partial x_i} = 0 \tag{4.3}$$

$$\rho^{(0)}\left(\frac{\partial T^{(0)}}{\partial t}+u_i^{(0)}\frac{\partial T^{(0)}}{\partial x_i}\right)=-p^{(0)}(\gamma-1)\frac{\partial u_i^{(0)}}{\partial x_i}+Da\,\omega_T^{(0)} \tag{4.4}$$

$$\rho^{(0)}\left(\frac{\partial y_i^{(0)}}{\partial t}+u_j^{(0)}\frac{\partial y_i^{(0)}}{\partial x_j}\right)=Da\,\omega_i^{(0)} \tag{4.5}$$

$$p^{(0)}=\rho^{(0)}T^{(0)} \tag{4.6}$$

Note that, to zeroth order, the momentum equation (4.3) reduces to the statement that the spatial gradient of thermodynamic pressure is zero. To define the zeroth order velocity field, the first order momentum equation is required; it is

$$\rho^{(0)}\left(\frac{\partial u_i^{(0)}}{\partial t}+u_j^{(0)}\frac{\partial u_i^{(0)}}{\partial x_i}\right)=-\frac{\partial p^{(1)}}{\partial x_i} \tag{4.7}$$

where $p^{(1)}$ is the dynamic pressure associated with the fluid flow and, to this order, does not affect the thermodynamic properties. Eqs. (4.2)-(4.7) are the governing equations for the limit of vanishingly small Mach number. Note that only the zeroth order dependent variables are retained except for the pressure, for which both the zeroth and first order quantities are required. Also note that the expansion is a regular perturbation expansion. We will drop the superscripts except to distinguish $p^{(0)}$ and $p^{(1)}$.

For the purpose of performing linear analysis of the stability of laminar flows, we shall represent all flow variables in the form:

$$f(x,y,z,t)=\overline{f}(y)+\hat{f}(y)\,e^{i(\alpha x+\beta z-\omega t)} \tag{4.8}$$

where $\overline{f}(y)$ is the laminar profile of the quantity, $\hat{f}$ depends only on the normal or y coordinate, α and β are wavenumbers in the streamwise (x) and spanwise (z) directions respectively, and ω is the frequency and assume that $|\hat{f}| \ll |\bar{f}|$. Note that the spatial fluctuation of thermodynamic pressure, $\hat{p}^{(0)}$, is zero according to Eq. (4.3). Substituting Eq. (4.8) into Eqs. (4.2) and (4.7) and neglecting the products of perturbation quantities, we obtain an equation that contains only the pressure and density:

$$\hat{p}'' - \frac{2\alpha\bar{u}'}{(\alpha\bar{u}-\omega)}\hat{p}' + (\alpha\bar{u}-\omega)^2\hat{\rho} - (\alpha^2+\beta^2)\hat{p} = 0 \tag{4.9}$$

where $\hat{p}$ is the fluctuation of the dynamic pressure $p^{(1)}$. The linearized state equation obtained from Eq. (4.6) is

$$\bar{\rho}\hat{T} + \bar{T}\hat{\rho} = 0 \tag{4.10}$$

and allows $\hat{\rho}$ to be expressed in terms of $\hat{T}$. To relate $\hat{T}$ to $\hat{p}$, we linearize the species and energy equations. After they are linearized, Eqs. (4.4) and (4.5) can be written symbolically as

$$A\hat{y}_F = B\hat{p}' - C\hat{y}_O + D\hat{T} \tag{4.11}$$

$$F\hat{y}_O = G\hat{p}' - H\hat{y}_F + I\hat{T} \tag{4.12}$$

$$K\hat{T} = L\hat{p}' + M\hat{y}_O + N\hat{y}_F \tag{4.13}$$

The coefficients are the same as in Chapter 3 and given in the Appendix. Eqs. (4.11), (4.12) and (4.13) may also be written in matrix form:

$$\begin{bmatrix} A & C & -D \\ H & F & -I \\ N & M & -K \end{bmatrix} \begin{bmatrix} \hat{y}_F \\ \hat{y}_O \\ \hat{T} \end{bmatrix} = \hat{p}' \begin{bmatrix} B \\ G \\ -L \end{bmatrix} \tag{4.14}$$

By eliminating the species mass fractions from these equations, we can relate $\hat{T}$ to $\hat{p}$:

$$\hat{T} = [RXN1]\hat{p}' \tag{4.15}$$

where $[RXN1]$ is identical to the quantity defined in Eq. (3.21). Using Eqs. (4.10) and (4.15) to relate $\hat{\rho}$ to $\hat{p}$, we get the disturbance equation for the pressure:

$$\hat{p}'' - \left\{ \frac{2\alpha\bar{u}'}{(\alpha\bar{u}-\omega)} + \frac{\bar{\rho}}{\bar{T}}(\alpha\bar{u}-\omega)^2[RXN1] \right\} \hat{p}' - (\alpha^2+\beta^2)\hat{p} = 0 \tag{4.16}$$

Using the asymptotic form of the solutions of Eq. (4.16) in place of the boundary conditions, we solve Eq. (4.16) by a combination of the shooting and Newton-Raphson method. These methods were described in Chapter 3.

4.2 Inflection Points and Multiple Modes of Instability

According to Rayleigh's inflection-point theorem [1888], a necessary condition for instability of incompressible flows is that the laminar velocity profile have an inflection point; this condition requires that $\bar{u}''$ change sign at least once or, equivalently, that the vorticity, $\bar{u}'$, have a maximum in the flow domain. Derivation of this condition from physical arguments using vorticity concepts has been attempted by several authors (Lin [1955], Gill [1965]). A stronger form of the above condition was obtained by Fjørtoft [1955] who proved that a necessary condition for instability is that $\bar{u}''(\bar{u}-\bar{u}_s) < 0$ somewhere in the field, where y_s is a point at which $\bar{u}''=0$ and $\bar{u}_s=\bar{u}(y_s)$. In this section, we generalize these theorems to incompressible flows with density variation.

If we ignore chemical reaction by setting $Da=0$ to simplify the problem, Eq. (4.16) can be rewritten in terms of the normal fluctuating velocity $\hat{v}$ (Eq. (3.11)). For temporally evolving flow, we have:

$$\left(\frac{\hat{v}'}{\bar{\rho}}\right)' - \left\{\frac{(\bar{\rho}\bar{u}')'}{\bar{\rho}^2(\bar{u}-c)} + \frac{(\alpha^2+\beta^2)}{\bar{\rho}}\right\}\hat{v} = 0 \tag{4.17}$$

where c is the complex wave velocity, ω/α. On multiplying this equation by the complex conjugate of v, v^*, integrating from $-\infty$ to ∞, and integrating the first term by parts, we obtain

$$\int_{-\infty}^{\infty}\left\{\frac{|D\hat{v}|^2+(\alpha^2+\beta^2)|\hat{v}|^2}{\bar{\rho}} + \frac{(\bar{u}-c_r)(\bar{\rho}\bar{u}')'|\hat{v}|^2}{\bar{\rho}^2|\bar{u}-c|^2}\right\}dy +$$

$$ic_i\int_{-\infty}^{\infty}\frac{(\bar{\rho}\bar{u}')'|\hat{v}|^2}{\bar{\rho}^2|\bar{u}-c|^2}\,dy = 0 \tag{4.18}$$

where D is the differential operator, d/dy, and c_r and c_i are the real and imaginary parts of the wave velocity. The imaginary part of Eq. (4.18) is

$$c_i\int_{-\infty}^{\infty}\frac{(\bar{\rho}\bar{u}')'|\hat{v}|^2}{\bar{\rho}^2|\bar{u}-c|^2}\,dy = 0 \tag{4.19}$$

and can be satisfied only if $(\bar{\rho}\bar{u}')'$ changes sign at least once in the open domain $(-\infty, \infty)$; this is a necessary condition for instability. Note that this condition requires that the angular momentum $(\rho u')$, not the vorticity (u'), to have a maximum in the flow domain. A stronger form of this condition can be obtained by considering the real part of Eq. (4.18)

$$\int_{-\infty}^{\infty} \frac{(\bar{u} - c_r)(\bar{\rho}\bar{u}')'|\hat{v}|^2}{\bar{\rho}^2|\bar{u} - c|^2}\, dy = -\int_{-\infty}^{\infty} \frac{|D\hat{v}|^2 + (\alpha^2 + \beta^2)|\hat{v}|^2}{\bar{\rho}}\, dy \tag{4.20}$$

Supposing that $c_i > 0$, multiplying Eq. (4.19) by $(c_r - \bar{u}_s)/c_i$ and adding it to Eq. (4.20), we have

$$\int_{-\infty}^{\infty} \frac{(\bar{u} - \bar{u}_s)(\bar{\rho}\bar{u}')'|\hat{v}|^2}{\bar{\rho}^2|\bar{u} - c|^2}\, dy = -\int_{-\infty}^{\infty} \frac{|D\hat{v}|^2 + (\alpha^2 + \beta^2)|\hat{v}|^2}{\bar{\rho}}\, dy \tag{4.21}$$

Thus, a necessary condition for instability is $(\bar{\rho}\bar{u}')'(\bar{u} - \bar{u}_s) < 0$ somewhere in the domain $-\infty < y < \infty$.

The laminar profiles were searched for points that satisfy conditions (4.19) and (4.21). Fig. 4.1 shows that the cold flow has just one inflection point while the reacting flow with significant heat release ($T_{ad} \geq 3$) has three. Fig. 4.2 shows a test of the strong necessary condition for instability. All three inflection points satisfy the strong necessary condition. The reacting mixing layer should therefore be unstable to three distinct modes.

Fig. 4.3 shows the temporal amplification rate and phase velocity as functions of the wavenumber for a variable property flow with $T_{ad} = 8$. Because the symmetry of the temporal case dictates that two of the modes be reflections of each other and have the same amplification rate, only two amplification rates appear. The first is the mode arising from the central inflection point where both the mean vorticity and the angular momentum are maxima; its phase velocity is the laminar velocity at the central inflection point, namely, the average of the two free stream velocities, the same as in the cold flow. The second amplification rate pertains to the two modes due to the outer inflection points. Since the mean angular momentum, not the vorticity, is maximum at the outer inflection points, the outer modes are not connected with the mean vorticity. For large heat release, the outer modes are more amplified than the center mode and should dominate the flow. Note that their maximum amplification rates occur at wavenumbers ten times as large as those of the center mode; thus the

outer modes have much shorter wavelengths. The outer modes are also very sensitive to the temperature variation of the properties which is very large in reacting flows (see Sec. 4.3.1). The phase velocities of the two outer modes are different as shown in Fig. 4.3b. One travels at lower speed than the center mode while the other travels at a higher speed; both asymptote to the laminar velocity at the corresponding inflection point as the wavenumber increases.

4.3 Results

4.3.1 *Effect of Heat Release and Variable Properties*

This section studies the effect of heat release and variable properties on the maximum growth rate of unstable modes of the spatially developing layer; computed laminar profiles including variable property effects were used as inputs for these calculations. Fig. 4.4 shows the effect of heat release on the maximum growth rates of unstable modes; the maximum is with respect to wavenumber. In the spatial case, the growth rates of the two outer modes are unequal due to the asymmetry of the laminar profiles. Because the slow modes are slightly more amplified than the fast modes, we show only the center and slow modes. As the heat release increases, the maximum amplification rate of the center mode decreases rapidly. The maximum amplification rate in the cold (no heat release) flow is 0.128, but with the variable properties included and T_{ad}=8, it is only 0.01, or 8% that of the cold flow. On the other hand, the amplification rates of the outer modes change very little as the heat release increases. Consequently, at high heat release, the outer modes are actually more amplified than the center mode. When T_{ad}=8, the slow mode has almost three times the amplification rate of the center mode. Thus, reacting flows with high heat release should be unstable to the outer modes for moderate equivalence ratio ϕ.

In Sec. 2.3, we showed that the variation of the properties influences the mean flow profiles of the reacting shear layer significantly. Fig. 4.5 shows that this variation results in a large difference in the stability characteristics, when T_{ad}=8. The constant property center mode has twice the growth rate of the corresponding variable property mode; this is due to the smoothing of the central portion of the profile by the increased viscosity reducing the severity of the central inflection point. However, the growth rates of the outer modes are increased by the effects of the property variation. In the

constant property case, the center and outer modes have comparable amplification rates; in the variable property case, the outer modes dominate the center mode.

4.3.2 *Effect of Damköhler Number*

In Sec. 2.3.2, we studied the effect of Damköhler number, Da, on the laminar flow structure. In this subsection, the effect of Damköhler number on the stability of the spatially developing layer is considered. Fig. 4.6 shows the maximum growth rate of the unstable modes versus Damköhler number at T_{ad}=8. The Damköhler numbers used in the laminar flow and stability calculations are identical. The growth rates decrease considerably until $Da \simeq 1$ after which they rapidly approach the asymptotic value for high Da. In the high Damköhler number range the flame sheet model applies; these results show that the flame sheet model is valid down to Damköhler numbers as small as 1 (cf. Mungal & Frieler [1988]). Comparing Fig. 4.6 and Fig. 4.4, we see that the effect of Damköhler number is different from that of heat release. Increasing heat release stabilizes the low-speed shear layer; increasing Damköhler number stabilizes at low Damköhler numbers but has little effect (it slightly destabilizes) at high Damköhler numbers.

In order to study the importance of chemical reaction during the instability, we used various Damköhler numbers in a series of stability calculations with the same laminar profile (this is not possible in the laboratory). Fig. 4.7a shows amplification rates for five different Damköhler numbers with a fixed laminar profile based on the relatively low Damköhler number of 0.2, at which the layer can be said to be reaction limited. In this case, the Damköhler number changes the stability characteristics considerably, i.e. the direct effect of chemical reaction on the disturbances is not small. Therefore, in low Damköhler number flows ($Da < 1$), it is important to use consistent Damköhler numbers in stability calculations. When we used various Damköhler numbers in stability calculations based on a laminar profile produced by the relatively high Damköhler number, 10, at which the layer is diffusion limited, however, we found almost no difference in amplification rates; Fig. 4.7b shows these results. Thus, in high Damköhler number flows ($Da \geq 1$), inclusion of chemical reaction rate terms in the inviscid stability analysis is not important. However, the heat release associated with chemical reaction has a large effect on laminar profiles and thereby influences the stability characteristics of the flow.

4.3.3 *Absolute and Convective Instability*

In stability studies, one has to choose between temporal and spatial instability. In temporal stability calculations it is assumed that the disturbances evolve in time from some given initial spatial distribution. In free shear flows, instabilities are often controlled by forcing the flow at a given frequency. The experimental results seem to follow the predictions of spatial theory, in which the frequency is real and the wavenumber is complex. Absolute and convective instabilities of a spatially developing layer are distinguished by the temporal growth rate for the mode which dominates the response at the source location; the growth rate is positive in the absolute and negative in the convective case. In physical terms, in an absolute instability a local small amplitude transient grows exponentially in time, while in a convective instability, the transient is convected away and leaves the local flow ultimately undisturbed.

Since previous researchers (Jackson & Grosch [1990]) reported that sufficient heat release can make a mixing layer absolutely unstable without backflow, we studied whether the instabilities are absolute or convective. Huerre and Monkewitz [1985] showed that a flow is convectively unstable if the modes which have zero group velocity are temporally damped, i.e. if the imaginary parts of the complex frequencies are negative and that it is absolutely unstable if they are positive. We used this criterion to determine the nature of the instability of the reacting mixing layer. First, we found the complex frequency ω_o which makes the group velocity $d\omega/d\alpha$ zero. The imaginary part of this frequency, ω_{oi}, is the absolute growth rate which determines the nature of the instability. Fig. 4.8 shows the imaginary part of ω_o as a function of the adiabatic flame temperature T_{ad}. All ω_{oi}'s are negative and, therefore, the reacting mixing layers considered here are convectively unstable.

4.3.4 *Three-Dimensionality*

Squire's theorem states that the lowest Reynolds number for transition occurs when the disturbances are two-dimensional, so two-dimensional modes dominate the viscous instability of incompressible flows. The reduction of a three-dimensional problem to a two-dimensional one lowers the order of the system of equations, reduces the number of integrations to find the eigenvalue (see Eqs. (3.23), and (3.24)), and reduces this size of the parameter space that must be investigated. Once the eigenvalue is known, calculation of the eigenfunction requires as many integrations as there

are components of the velocity. In inviscid problems (infinite Reynolds number), the transformation is of some help, but the advantages of Squire's theorem may not be obtained.

In compressible flows, the most amplified modes are three-dimensional (Mack [1984]; Sandham & Reynolds [1989]). We tried to determine whether the most amplified modes are two- or three-dimensional in the incompressible low-speed reacting mixing layer. Fig. 4.9 shows the amplification rates as a function of the obliqueness angle at T_{ad}=8. It shows that the disturbances become more stable as the obliquity increases. Therefore, two-dimensional modes are more amplified than three-dimensional ones and three-dimensionality is not important in this case.

4.3.5 *Analytical Laminar Profiles*

This section investigates the validity of using analytical flow profiles such as hyperbolic-tangent and error function profiles. To accomplish this, we compare results obtained from these profiles with ones based on the boundary-layer solutions. We normalized the length scales of the mean velocity profiles using their respective vorticity thicknesses, and used normalized density and temperature profiles obtained from the laminar solutions at T_{ad}=8.

The analytical profiles also have three modes of instabilities. Fig. 4.10 shows the amplification rates vs wavenumber. Fig. 4.10a gives the results for temporal layers using the error function and computed profile. For the center mode the differences are small but, for the outer mode, the growth rate obtained from the laminar solution is about twice that obtained with the error function. This is not surprising, since the principal differences in the profiles are found in the outer parts of the layers. Fig. 4.10b compares the hyperbolic-tangent function results with the laminar solution for the spatial layer. Again, there is little difference for the center mode, but, for the outer mode, the hyperbolic-tangent function has a much lower growth rate than the laminar solution. From these results, we find that the use of accurate laminar profiles is essential. This is consistent with the work of Monkewitz and Huerre [1982].

4.3.6 *Effect of Density Ratio*

Because the incoming fuel and oxidizer streams usually have different temperatures and densities in real combustion systems, we considered the effects of free-stream

density ratio on the stability of spatially developing layers. We assume that the fast stream is the fuel and the slow stream, the oxidizer. Fig. 4.11 shows the amplification rates and the phase speeds at T_{ad}=1 and Da=10 for density ratios $\bar{\rho}_2$=0.5, 1, 2. As density ratio decreases, the maximum amplification rate decreases but a wider range of wavenumber becomes unstable. Putting the heavier gas in the low-speed stream makes the flow more unstable, which agrees with the experimental result of Brown & Roshko [1974]. Fig. 4.11b shows that the speeds at which the unstable modes travel are close to the free-stream velocity of the heavier gas.

Fig. 4.12 shows the amplification rates and phase speeds at T_{ad}=8 and Da=10 for which there are unstable outer modes. The growth rates of the outer modes are very sensitive to free-stream density ratio. Putting the heavier gas in the low-speed stream makes the slow modes more unstable and the fast modes less unstable. Fig. 4.12a shows the growth rates of the slow modes. The maximum growth rates for $\bar{\rho}_2$=2 and $\bar{\rho}_2$=1 are almost equal but for $\bar{\rho}_2$=0.5 the growth rate is only two thirds of the value at $\bar{\rho}_2$=1. The corresponding phase speeds given in Fig. 4.12b show that the unstable modes move more slowly at high density ratios. Fig. 4.12c-d shows the growth rates and phase speeds of fast modes; they become more unstable with decreasing density ratio. Comparing the amplification rates between Fig. 4.12a and Fig. 4.12c, we see that slow modes at $\bar{\rho}_2$=2 are more amplified than fast modes at $\bar{\rho}_2$=0.5. From the study of the effect of density ratio on the stability, we found that instability is increased in the stream with higher density and that putting heavier gas in the slower stream makes the low-speed mixing layer more unstable.

4.3.7 *Effect of Equivalence Ratio*

In Sec. 2.3.3, we defined the equivalence ratio by

$$\phi = \frac{(Y_F/Y_O)_{real}}{(Y_F/Y_O)_{ideal}} \tag{4.22}$$

where Y_F and Y_O represent the mass fractions of the fuel and oxidizer in the free streams. If $\phi > 1$, the mixture is fuel rich, if $\phi < 1$ it is fuel lean, and if ϕ=1, it is stoichiometric. Here, we study the effect of the equivalence ratio on the stability of reacting mixing layers; three equivalence ratios, ϕ=0.5, 1, 2 are used at T_{ad}=8 and Da=10. At this adiabatic flame temperature, unstable outer modes exist. Figs. 4.13a

shows the maximum amplification rates at $\bar{T}_2$=1 ($\bar{\rho}_2$=1). The increase of temperature in the slower part of the mixing layer with increasing ϕ causes the maximum growth rates of the slow modes to decrease. Because any deviation from stoichiometric conditions reduces the total heat release, the slow modes at ϕ=0.5 have higher growth rates than the ones with ϕ=1. Maximum growth rates of fast modes increase with ϕ because the temperature rise is reduced in the fast part of the mixing layer. Comparison of the amplification rates of the slow and fast modes shows that the slow modes of the fuel-lean case are the most amplified ones for a given adiabatic flame temperature. Fig. 4.13b-c show the maximum growth rates at density ratios, $\bar{\rho}_2$=2, 0.5. They show the behavior qualtitively similar to the case in Fig. 4.13a ($\bar{\rho}_2$=1). As ϕ increases, slow modes become less unstable and fast modes more unstable. As was seen in the previous section, the instability connected with the higher density stream is more unstable. Comparing the maximum amplification rates in Fig. 4.13, we see that putting heavier gas in the slower stream in the fuel-lean case gives the most unstable low-speed mixing layer.

4.3.8 *Eigenfunctions*

This section presents the most unstable eigenfunctions of two-dimensional temporal instability to illustrate the effects of heat release on the linear eigenfunctions. The eigenfunctions are normalized so that the maximum absolute value of $\hat{u}$ is unity. These eigenfunctions can provide information about the large scale motions which result from linear instability and can be used as inputs to direct numerical simulations.

Figs. 4.14-15 show linear eigenfunctions of the most unstable center modes—Kelvin-Helmholtz modes—of the non-reacting (T_{ad}=1) and reacting (T_{ad}=4) flows. The vorticity structure of the cold flow shown in Fig. 4.14a is identical to Michalke's [1965]. The magnitude of vorticity has two maxima. Fig. 4.15 shows that heat release changes the structure of the center mode. The magnitude of vorticity now has four maxima; the two near the center of the layer are smaller than the others. The pressure component of the eigenfunctions has the behavior similar to that in the cold flow. The parts of the eigenfunctions corresponding to $\hat{\rho}, \hat{T}, \hat{y}_F$ and $\hat{y}_O$, which have no meaning in the cold flow, arise due to chemical reaction.

Figs. 4.16-17 show linear eigenfunctions corresponding to the most unstable outer modes—slow and fast modes—at T_{ad}=8. The main difference between the outer and center modes is that the former are concentrated in the outer part of the mixing

layer. Note that the density and temperature perturbations are an order of magnitude greater in the outer modes than in the center mode at T_{ad}=4. Because the slow mode is active principally in the slow part of the mixing layer, the fuel perturbation is relatively smaller.

From the eigenfunctions and the mean flow, an approximation to a typical flow variable, f, can be calculated.

$$f = \bar{f} + a\Re[\hat{f}e^{i\alpha x}] \tag{4.23}$$

where $\Re$ denotes the real part of a fluctuating variable. The amplitude of the disturbance, a, is arbitrary but was chosen as 0.1. Contour plots of the flow variables based on this approximation will be given.

Fig. 4.18 shows vorticity and pressure contours for the cold flow; the y axis has been stretched to better illustrate the structure. The vorticity structure is identical to Michalke's [1965]. The two elementary clockwise vortices formed by the instability will subsequently rotate around each other and merge to form a single vortex that can be identified as a large-scale coherent structure. The pressure contours show that high pressure (solid line) occurs in the braid (the region between the vortices) and low pressure (dashed line) is found near the cores of the vortices. Fig. 4.19 shows the contours for the reacting flow at T_{ad}=4. We consider the center mode because it is the most unstable mode at this adiabatic flame temperature. The vorticity structure is quite different from the cold flow structure. There are four clockwise vorticity maxima, compared to only two in the cold flow; the wavelength is twice as long as in the cold flow. Note the existence of the counterclockwise vorticity (solid line), which may affect the pairing of the clockwise vortices in the non-linear development. The pressure contours are little different from the those in the cold flow. High pressure again corresponds to the braid and low pressure to the core of the merged vortex.

Sandham & Reynolds [1989] used the compressible vorticity equations to explain the reduced growth rate in compressible mixing layers. Along these lines, we write the equations for ω_z and ω_z/ρ for two-dimensional variable density flow:

$$\omega_z = \frac{\partial u}{\partial x} - \frac{\partial v}{\partial x} \tag{4.24}$$

$$\frac{D\omega_z}{Dt} = -\omega_z\left(\frac{\partial u}{\partial x} + \frac{\partial v}{\partial y}\right) + \frac{1}{\rho^2}\left(\frac{\partial p}{\partial x}\frac{\partial \rho}{\partial y} - \frac{\partial p}{\partial y}\frac{\partial \rho}{\partial x}\right) \tag{4.25}$$

$$\frac{D(\omega_z/\rho)}{Dt} = \frac{1}{\rho^3}\left(\frac{\partial p}{\partial x}\frac{\partial \rho}{\partial y} - \frac{\partial p}{\partial y}\frac{\partial \rho}{\partial x}\right) \tag{4.26}$$

The contours of ω_z/ρ are not very different from those of ω_z. The terms on the right hand side of Eq. (4.25) are called the dilatational and baroclinic terms; they are plotted in Figs. 4.19e-f. In the region where the elementary vortices develop, the dilatational term has both negative and positive regions whereas the baroclinic term is negative and has a quadrupole structure. Because the baroclinic term is about four times larger than the dilatation term, the right hand side of Eq. (4.20) is negative and tends to inhibit the growth of the two-dimensional instability in low-speed reacting mixing layers. Figs. 4.19g-h show the contours of the fuel and oxidizer mass fractions respectively. The disturbance is largest in the region where the elementary vortex will develop.

When the heat release is large, the outer modes are more unstable than the center mode. Figs. 4.20-21 show the temporal perturbations produced by the slow and fast modes at T_{ad}=8 and a=0.025. The wavelengths of these modes are half the cold flow wavelength. The two outer modes have the same growth rates but different phase velocities. Because the action of the slow mode is concentrated in the lower part of the mixing layer, it disturbs this region more than the high speed region. Figs. 4.20a-b show that the extrema of ω_z and ω_z/ρ lie well below the center of the layer. The pressure and density contours (Figs. 4.20c-d) show that the extrema of these quantities are also located in the lower part of the layer. The dilatational term in Eq. (4.20) is most negative near the vorticity extrema but the baroclinic term has both signs (Figs. 4.20e-f). Because the latter is much larger than the former and has both signs, its effect on the growth of the vorticity is not clear. Figs. 4.20g-h shows the mass fractions of the reactants. Because the fuel occupies the upper part of the layer and the oxidizer the lower part, the slow mode principally affects the oxidizer. The fuel is hardly perturbed and the slow mode is unlikely to increase mixing between the reactants very much. The contours of the fast mode are obtained by reflection (Fig. 4.21).

Because the two outer modes have the same growth rates in the temporal case, the most likely mode of instability is a combination of the two outer modes. Thus, we look at the combined effects of the eigenfunctions of the two outer modes:

$$f = \bar{f} + a\Re[(\hat{f}_s + \hat{f}_f)e^{i\alpha x}] \tag{4.27}$$

Here, the subscripts s and f denote the slow and fast modes respectively. Fig. 4.22 shows the contours of various quantities provided by the combined modes. The vorticity structure is quite different from what is found in the cold flow. The baroclinic term dominates the dilatational term in Eq. (4.20) at the vorticity extrema. We cannot use the vorticity equation to predict the growth of the mixing layer because the baroclinic term has both signs near the vorticity maxima. Figs. 4.22g-h show that the interface between the fuel and oxidizer is less disturbed by the outer modes than the center mode (T_{ad}=4) and mixing between the reactants may be relatively weak.

4.3.9 *Streaklines*

A streakline is a line connecting the current positions of the fluid particles that have passed through the same point. Smoke or dye injectors allow one to visualize streaklines experimentally. In this subsection, we calculate streaklines from the linear stability eigenfunctions. The velocity components of the disturbed shear layer, u and v, have the form

$$u = \bar{u}(y) + a\Re[\hat{u}(y)e^{i(\alpha x - \omega t)}], \qquad v = a\Re[\hat{v}(y)e^{i(\alpha x - \omega t)}] \tag{4.28}$$

The position of a particle at time t, $(x(t), y(t))$, can be calculated from

$$\frac{dx}{dt} = u(x(t), y(t), t), \qquad \frac{dy}{dt} = v(x(t), y(t), t) \tag{4.29}$$

We calculate a pathline with the initial conditions

$$x(t_0) = x_0, \qquad y(t_0) = y_0 \tag{4.30}$$

Michalke [1965] calculated streakline patterns for the hyperbolic-tangent velocity profile.

In our calculation, we chose a=0.0005 and t=0 and considered the most unstable modes for spatially developing layers. Fig. 4.23a shows the streaklines for the cold flow (T_{ad}=1). There is a clear tendency to roll up. The flow patterns show that

the center mode develops into the large-scale instability found in experiment. Figs. 4.23b-c show the streaklines for the outer modes of the reacting flow (T_{ad}=8). In the case shown in Fig. 4.23b, only the lower part of the mixing layer is disturbed and shows a tendency to roll up, whereas the upper part remains undisturbed. The reverse is true in Fig. 4.23c. Fig. 4.23d shows the streaklines of the shear layer disturbed by the combined outer modes. Because the slow mode is more unstable than the fast mode, the lower part is more disturbed than the upper part. The flow patterns show that the outer modes in a reacting mixing layer do not cause the flow to roll up in the same way as the center mode of an incompressible non-reacting mixing layer and that large-scale coherent struectures may not exist. Therefore, mixing between the fuel and oxidizer will not be strong. Pairing between the elementary vortices may also be inhibited because the phase speeds of the subharmonic unstable modes differ from the phase speeds of the fundamental modes (Fig. 4.3b).

4.3.10 *Comparison with Experimental Results*

Heat release might be expected to increase the growth rate of the thickness of a mixing layer due to displacement effects caused by dilatation. However, the experiments of Wallace [1981] suggested a slight decrease in the growth rate of reacting mixing layers with increasing heat release. More recently, Hermanson & Dimotakis [1989] conducted experiments with hydrogen and fluorine at $\bar{u}_2$=0.4 and $\bar{T}_2$=1. Fig. 4.24 compares their experimental data with our computed normalized maximum growth rates. The growth rates are normalized by their values at zero heat release and $\Delta\bar{T}_{max}$ is the maximum temperature rise over the ambient temperature. The maximum amplification rate $|\alpha_i|_{max}$ is linearly related to the growth rate of the shear layer $d\delta/dx$ (Morkovin [1988]; Sandham & Reynolds [1989]). Fig. 4.24 shows a good qualitative agreement between the linear stability results and the experimental growth rates; the growth rate decreases with increasing heat release. Because of using maximum growth rates instead of the combination of unstable modes, linear stability theory predicts too large a decrease.

Winant & Browand [1974] and Brown & Roshko [1974] identified large spanwise vortices as the principal features of two-dimensional mixing layers in the non-linear region preceding the establishment of fully turbulent flow conditions. The observed initial vortex spacings very nearly correspond to the wavelength of the most amplified mode of instability. We compare the normalized mean vortex spacings measured by

Hermanson and Dimotakis [1989] with the wavelengths of the most unstable modes. The wavelengths have been normalized by the wavelengths at zero heat release. To represent the effect of heat release, we used a normalized mean density reduction defined by Hermanson & Dimotakis [1989]

$$\Delta\bar{\rho}/\bar{\rho}_1 = 1 - \bar{\rho}/\bar{\rho}_1 = 1 - \int_{\eta_2}^{\eta_1} \frac{\bar{T}_1}{\bar{T}_1 + \Delta\bar{T}} d\eta \tag{4.31}$$

where $\bar{\rho}$ is the integrated mean density in the layer, $\eta_{1,2}$ are the 1% points of the mean temperature profile on the high- and low-speed sides, and $\Delta\bar{T}$ is the temperature rise at each point across the layer. Fig. 4.25 shows that the wavelengths of the outer modes, which are more unstable than the center modes at high heat release, agree well with the experimental mean vortex spacings. The wavelength of the center mode increases with increasing heat release. Ganji & Sawyer [1980] and Hermanson & Dimotakis [1989] also pointed out that identification of large-scale structures was sometimes difficult as heat release increased. This difficulty may be due to the domination by the outer modes at high heat release.

4.4 Chapter Summary

In this chapter, we considered the inviscid stability of incompressible reacting mixing layers. We found that the growth rates are very sensitive to the mean profiles. Boundary-layer equation solutions obtained with variable transport properties are more realistic representations of an actual flow than analytically prescribed functions and provide a better basis for stability analysis. For the reacting plane mixing layer with variable density, a necessary condition for instability has been derived. New inflectional modes of instability were found in the outer parts of the mixing layer. Heat release stabilizes the flow and, in particular, greatly reduces the growth rate of the center mode. The growth rates of the outer modes, which do not exist in a cold flow, are relatively insensitive to heat release. For the large heat releases typical of combusting flows, the outer mode is more amplified than the center mode; its wavelength is shorter than that of the center mode. Even at high heat release, two-dimensional waves are more amplified than three dimensional ones. From the eigenfunctions of the linear theory, information about the vortex structure of the flow that develops from the instability can be obtained. Both the outer and the center modes have four vorticity maxima per wavelength. The streakline patterns suggest

that the outer modes in reacting mixing layers do not cause the flow to roll up in the same way as the center mode of an incompressible non-reacting mixing layer. Mixing between the fuel and oxidizer is therefore expected to be lower in reacting flows.

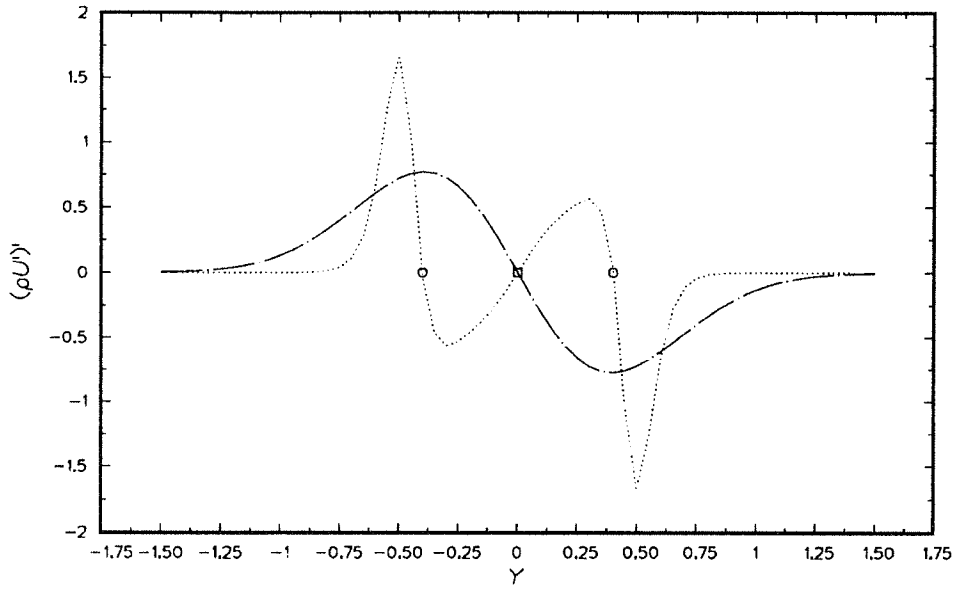

FIGURE 4.1. The function appearing in the necesary condition for temporal instability. M_1=0, $\bar{T}_2$=1, β=0, Da=10. —·— , T_{ad}=1; ——— , T_{ad}=8; ▫ , ○ , inflection points.

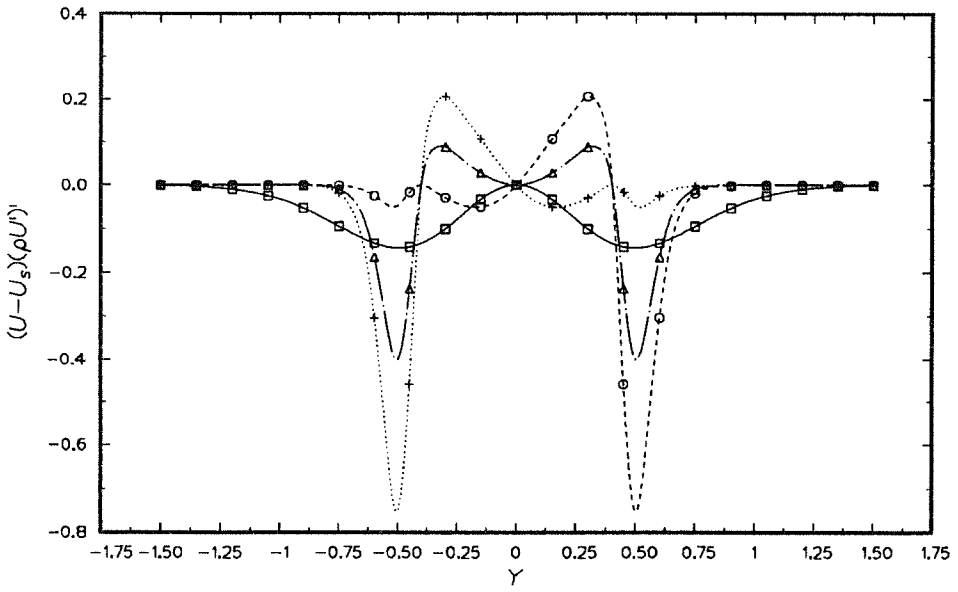

FIGURE 4.2. The function appearing in the strong necesary condition for temporal instability. M_1=0, $\bar{T}_2$=1, β=0, Da=10. ▫ , T_{ad}=1, $\bar{u}_s$=0.75; ○ , T_{ad}=8, $\bar{u}_s$=0.64; △ , T_{ad}=8, $\bar{u}_s$=0.75; +, T_{ad}=8, $\bar{u}_s$=0.96.

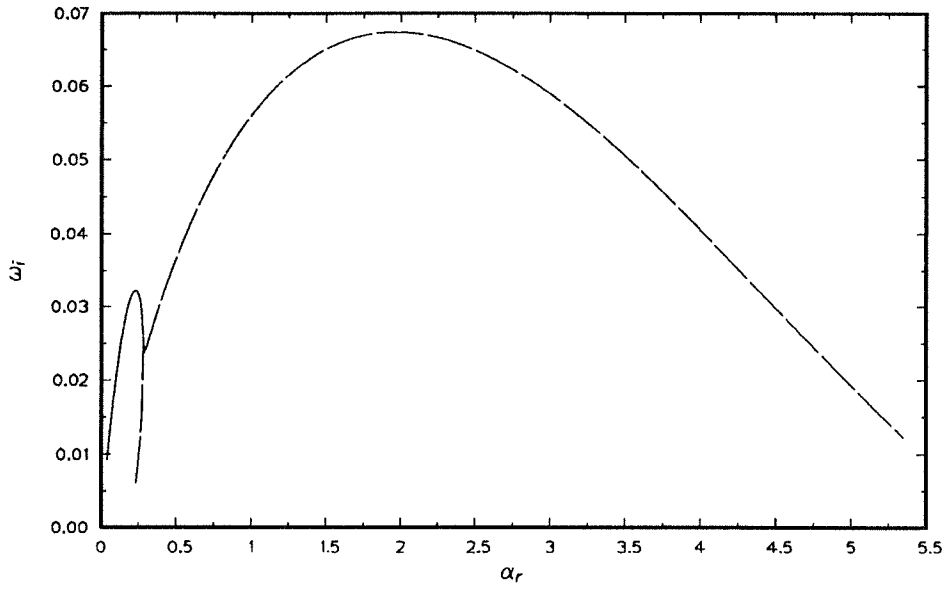

(a)

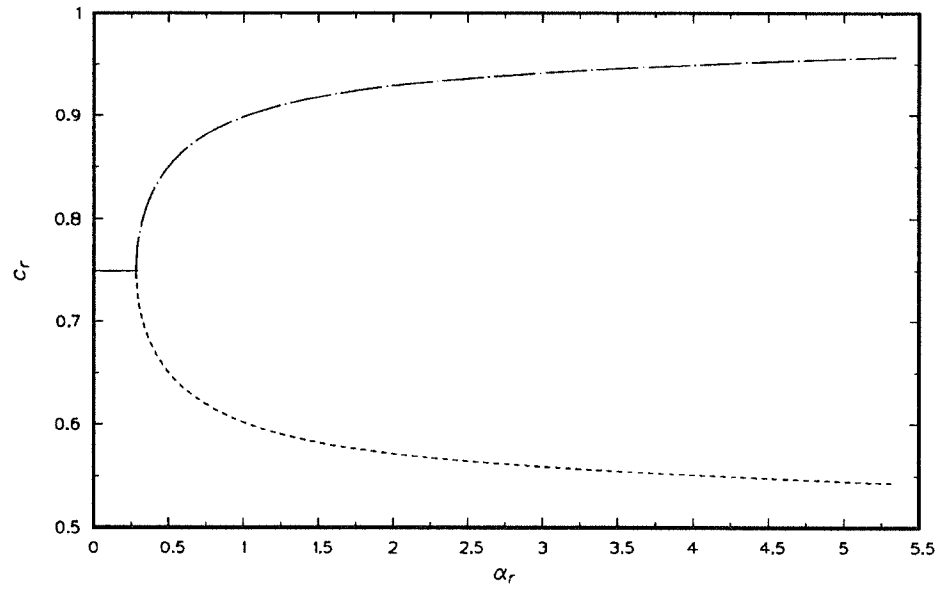

(b)

FIGURE 4.3. The multiple instability modes in the temporal flow. (a) growth rate (b) phase velocity. M_1=0, $\bar{T}_2$=1, T_{ad}=8, β=0, Da=10. —— , center mode; ---- , slow mode; —-— , fast mode. Note that the two outer modes have identical growth rates.

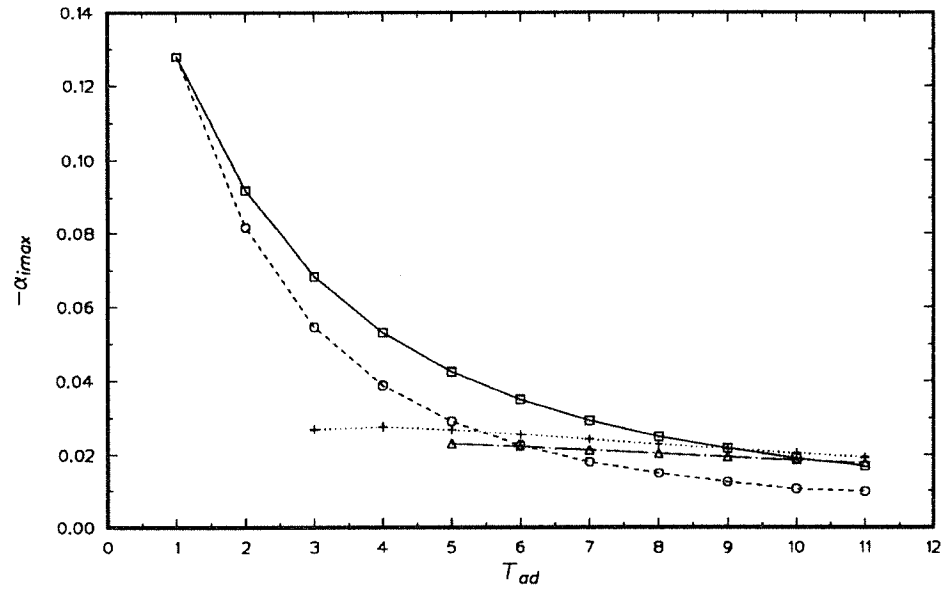

FIGURE 4.4. Effect of heat release on the amplification rate (spatial instability). M_1=0, $\bar{T}_2$=1, β=0, Da=10. □ , center mode, constant property; ○ , center mode, variable property; △ , slow mode, constant property; +, slow mode, variable property.

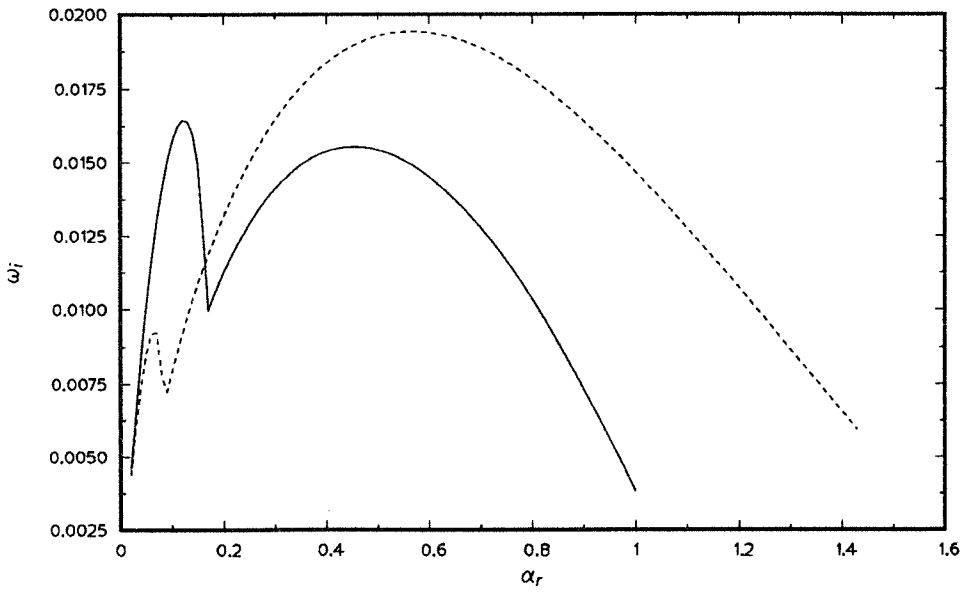

FIGURE 4.5. Effect of variation of properties on the growth rate (temporal instability). M_1=0, $\bar{T}_2$=1, T_{ad}=8, β=0, Da=10. —— , constant property; ---- , variable property.

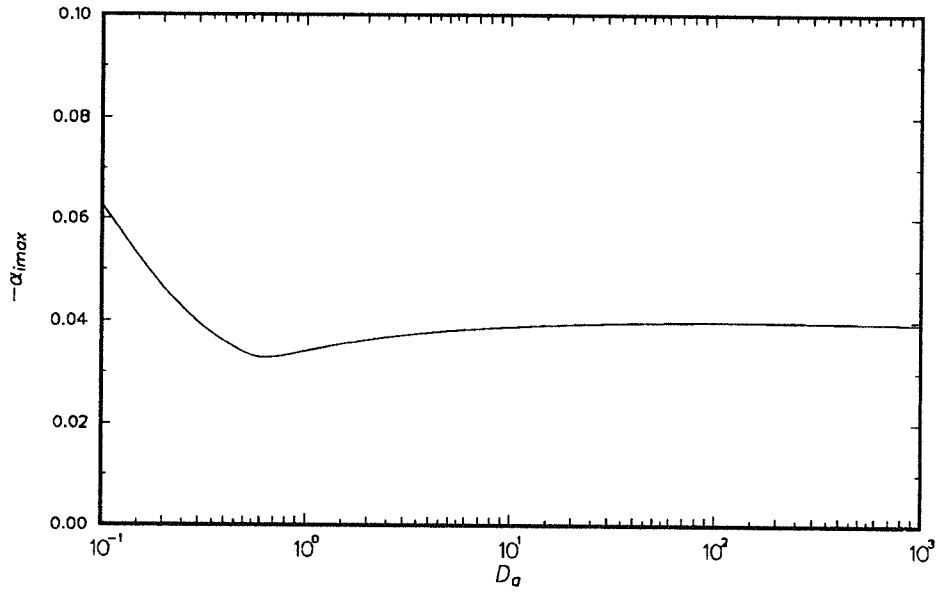

FIGURE 4.6. Maximum growth rate versus Damköhler number. M_1=0, $\bar{T}_2$=1, T_{ad}=8, β=0.

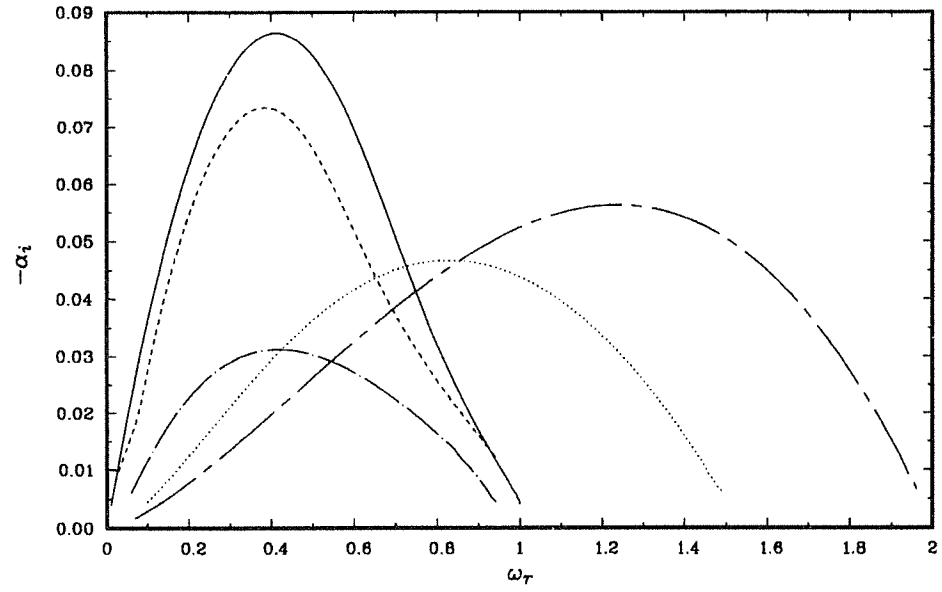

(a)

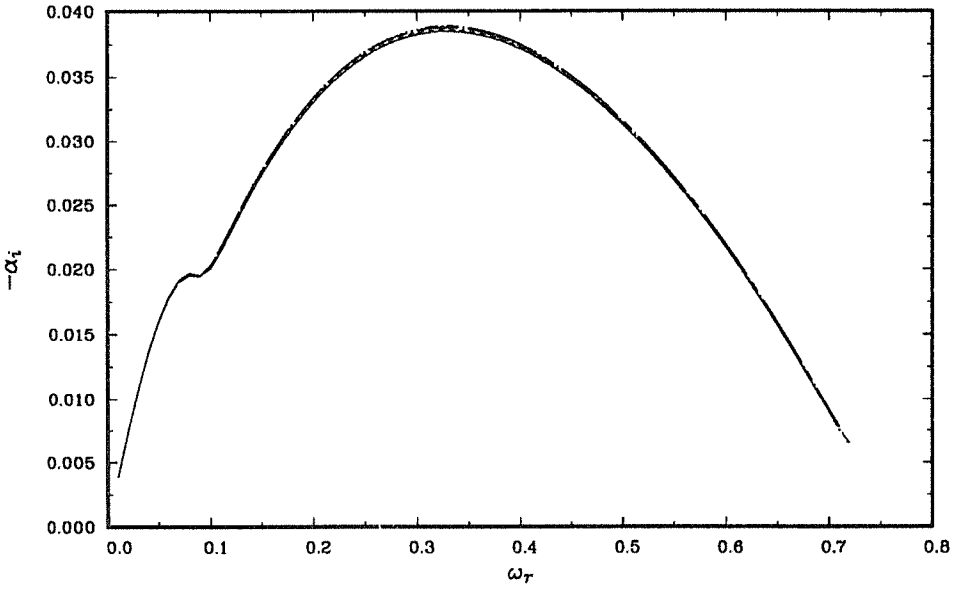

(b)

FIGURE 4.7. Growth rates with different Damköhler numbers in stability calculation. (a) Da=0.2 (b) Da=10 in laminar flow. M_1=0, $\bar{T}_2$=1, T_{ad}=8, β=0. —— , Da=0.0; ---- , Da=0.005; —·— , Da=0.02; ····· , Da=0.2; —·· , Da=10.

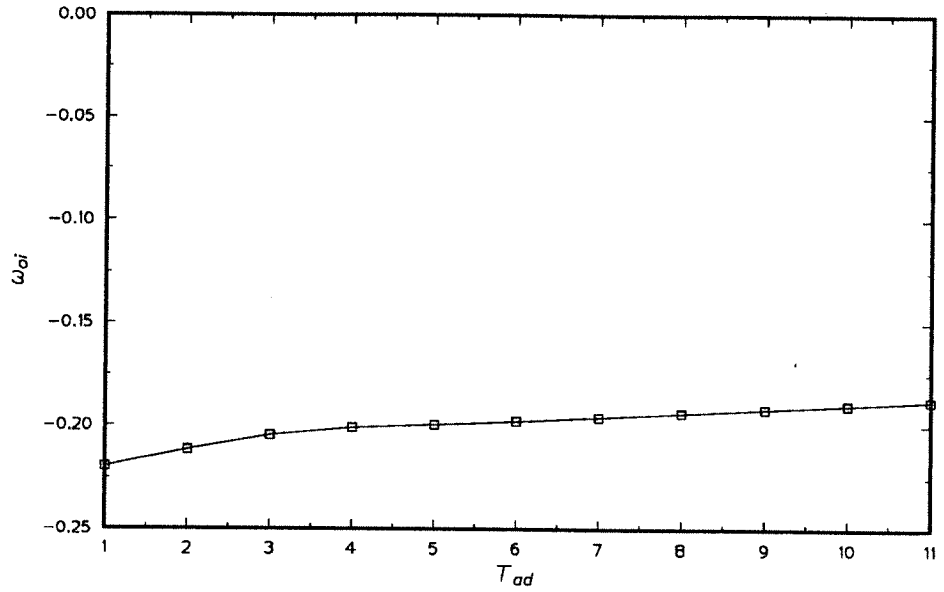

FIGURE 4.8. Variation of ω_{oi} with adiabatic flame temperature (spatial instability). M_1=0, $\bar{T}_2$=1, β=0, Da=10.

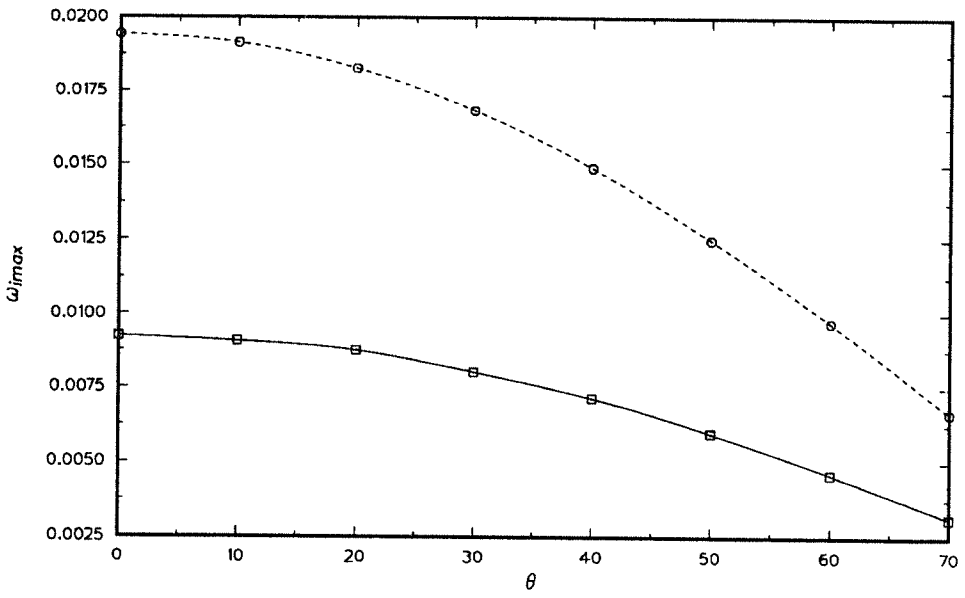

FIGURE 4.9. Growth rates versus obliqueness angle (temporal instability). M_1=0, T_{ad}=8, $\bar{T}_2$=1, Da=10. □ , center mode; ○ , outer mode.

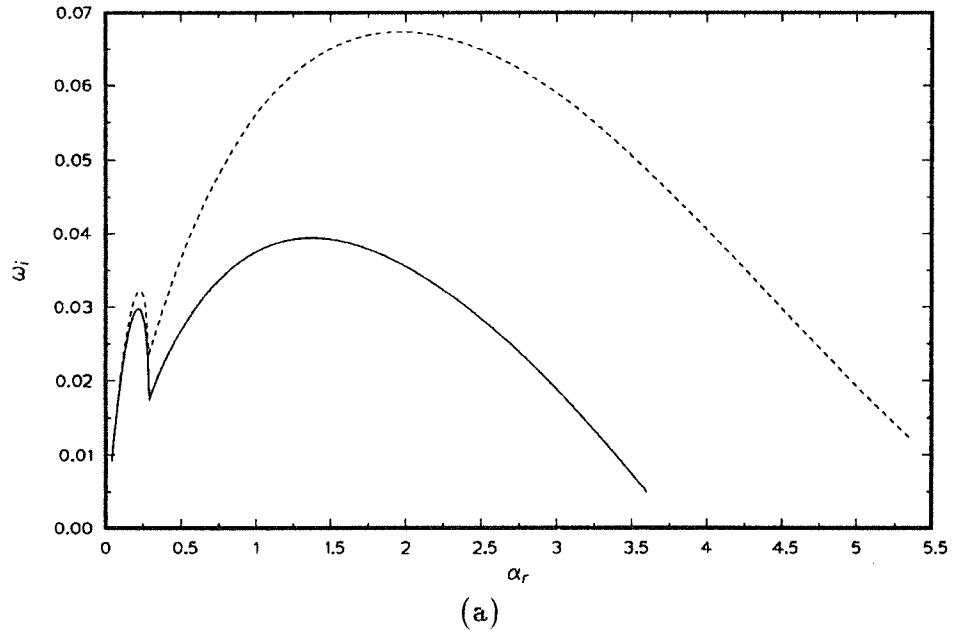

(a)

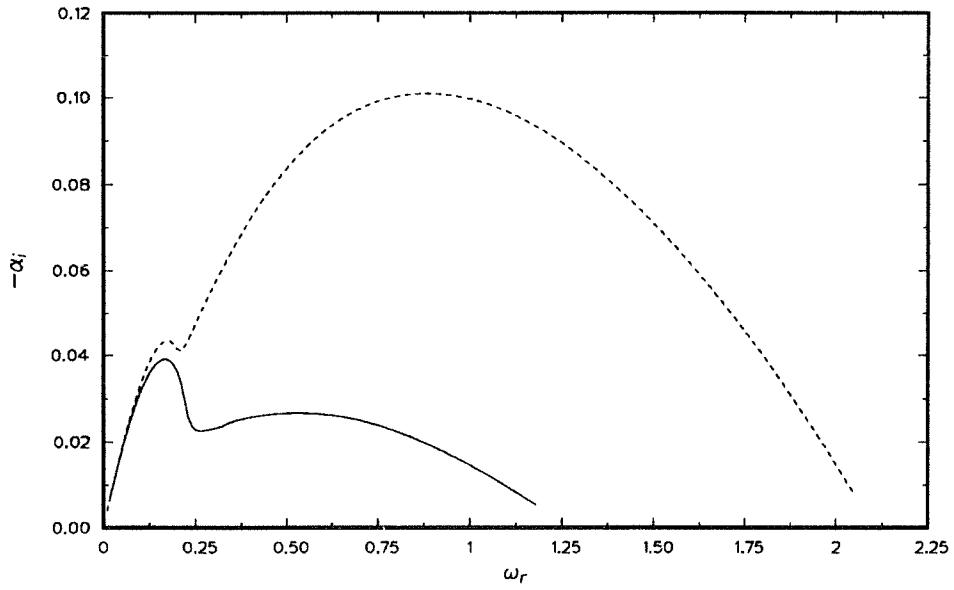

(b)

FIGURE 4.10. Effect of velocity profiles on linear growth rates. (a) temporal instability. ——, error function; ----, laminar solution. (b) spatial instability. ——, hyperbolic-tangent function; ----, laminar solution. M_1=0, $\bar{T}_2$=1, T_{ad}=8, β=0, Da=10.

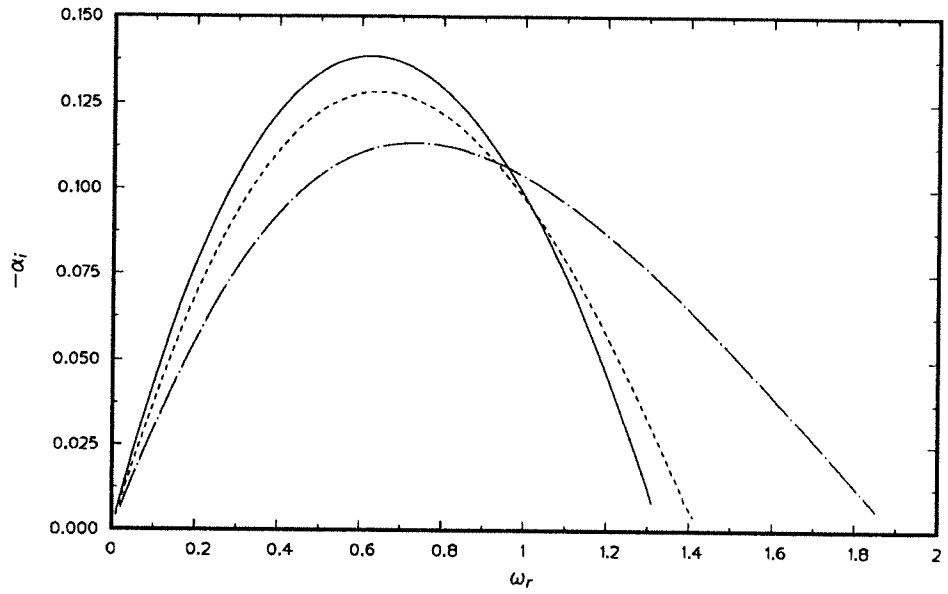

(a)

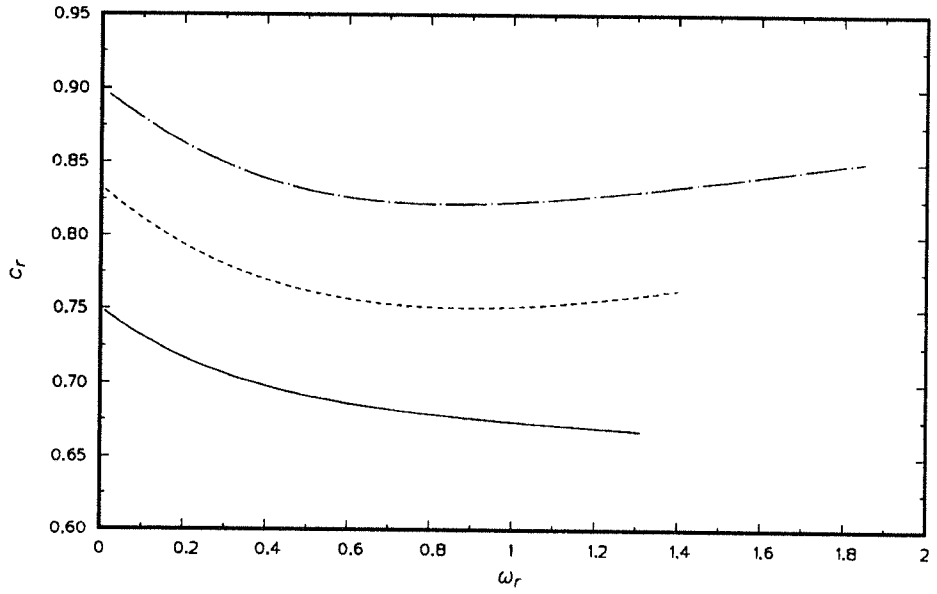

(b)

FIGURE 4.11. Effect of density ratios in the cold flow (spatial instability). (a) amplification rates (b) phase speeds. M_1=0, $\bar{T}_2$=1, T_{ad}=1, β=0, Da=10. ——— , $\bar{\rho}_2$=2; - - - - , $\bar{\rho}_2$=1; —·— , $\bar{\rho}_2$=0.5.

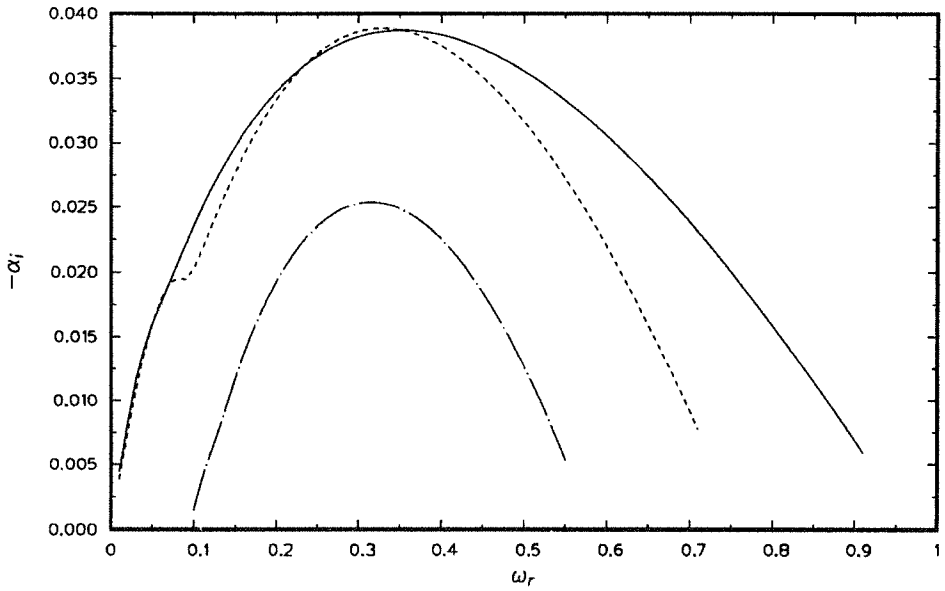

(a)

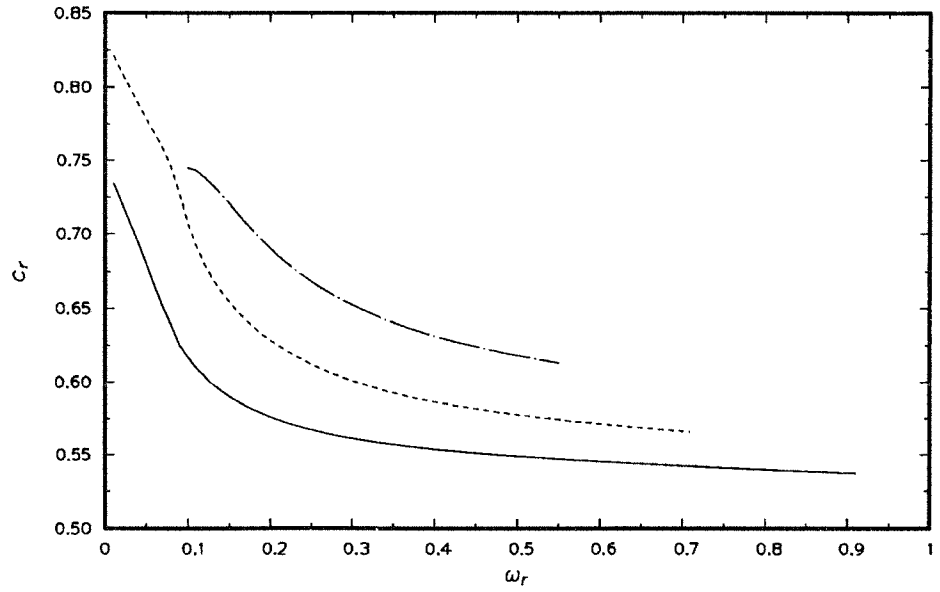

(b)

FIGURE 4.12. Continued.

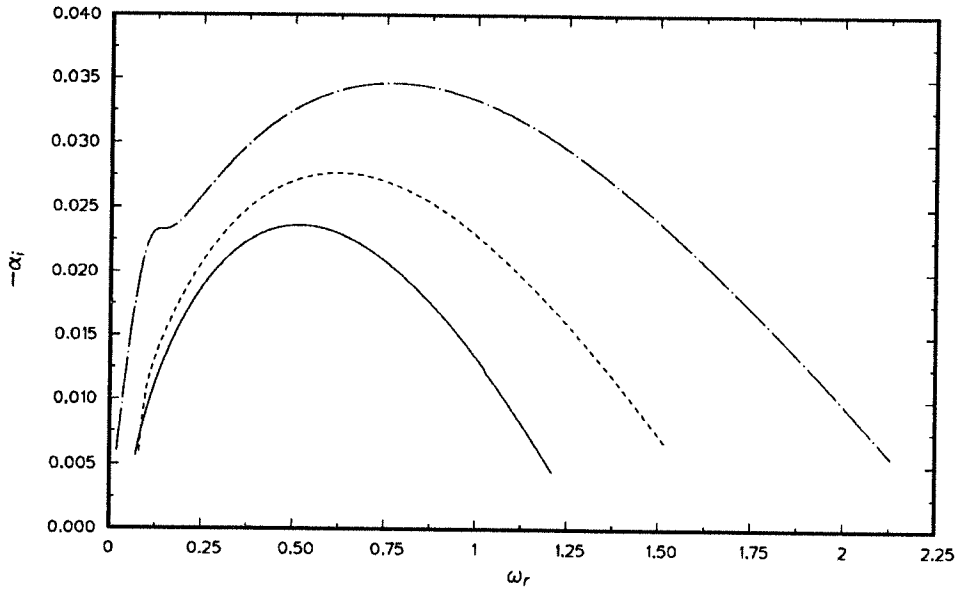

(c)

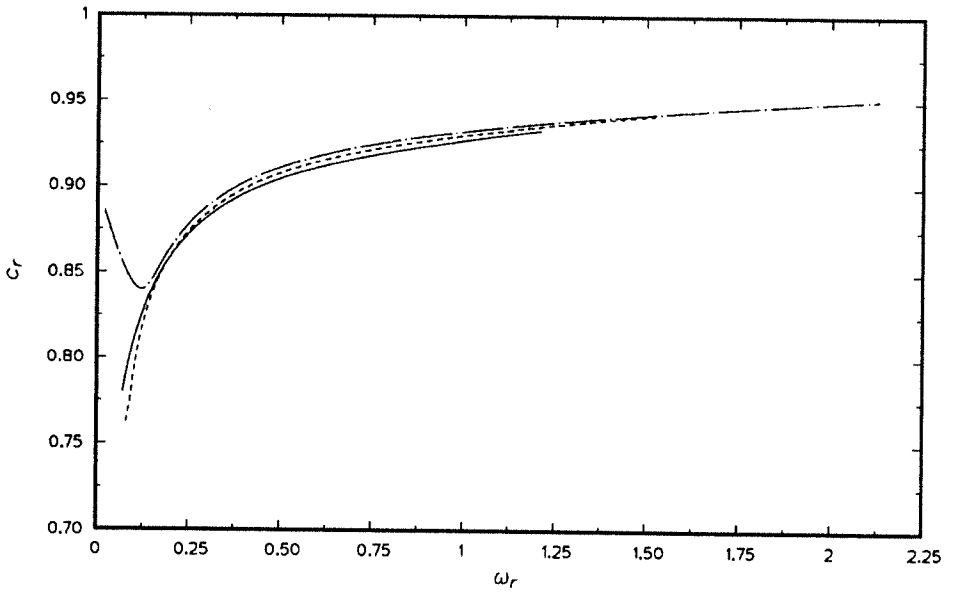

(d)

FIGURE 4.12. Effect of density ratios in the reacting flow (spatial instability). (a) amplification rates (slow modes) (b) phase speeds (slow modes) (c) amplification rates (fast modes) (d) phase speeds (fast modes). M_1=0, T_{ad}=8, β=0, Da=10. ——— , $\bar{\rho}_2$=2; ---- , $\bar{\rho}_2$=1; —·— , $\bar{\rho}_2$=0.5.

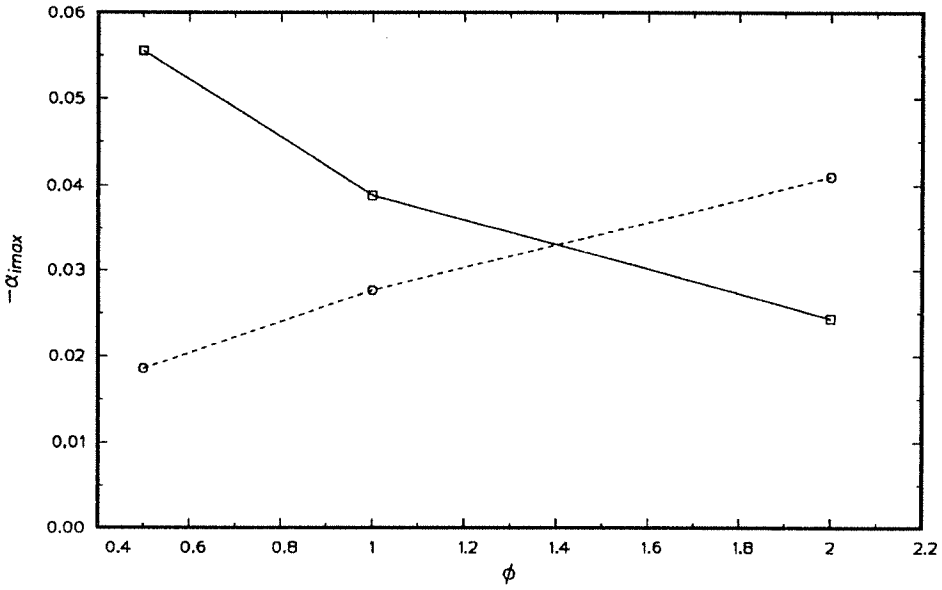

(a)

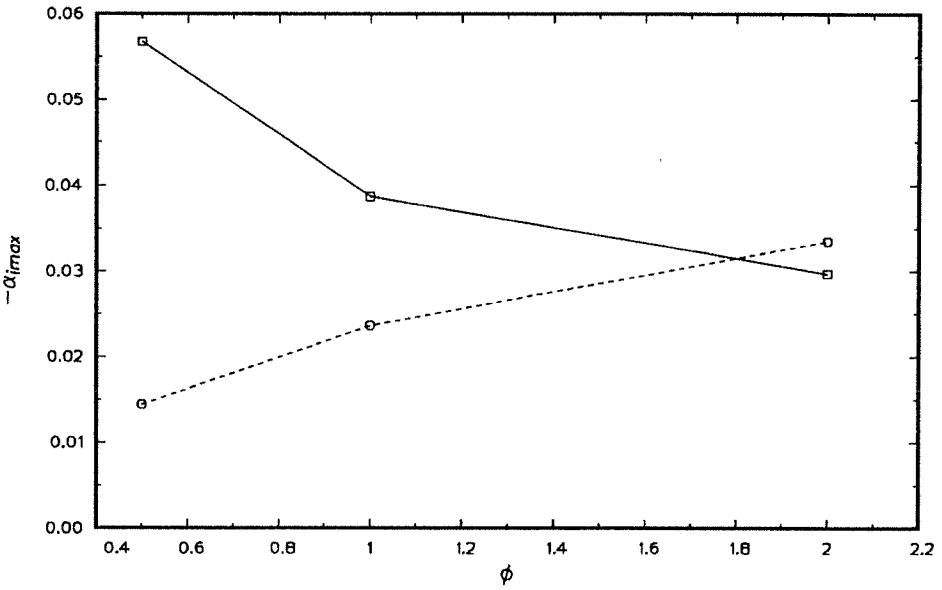

(b)

FIGURE 4.13. Continued.

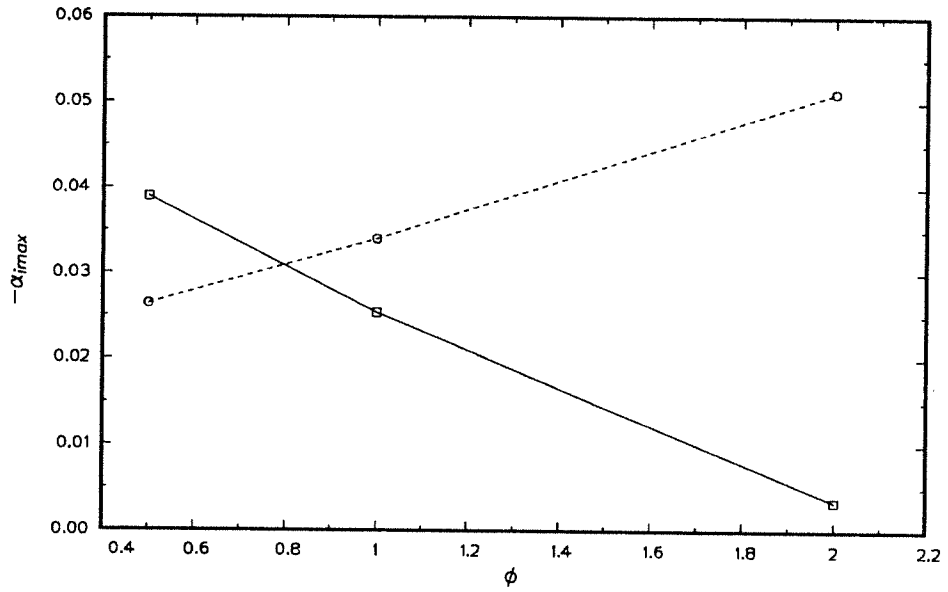

(c)

FIGURE 4.13. Effect of equivalence ratios on the maximum amplification rates in reacting flows (spatial instability). (a) $\bar{\rho}_2$=1 ($\bar{T}_2$=1) (b) $\bar{\rho}_2$=2 ($\bar{T}_2$=0.5) (c) $\bar{\rho}_2$=0.5 ($\bar{T}_2$=2). M_1=0, T_{ad}=8, β=0, Da=10. ▫ , slow mode; ○ , fast mode.

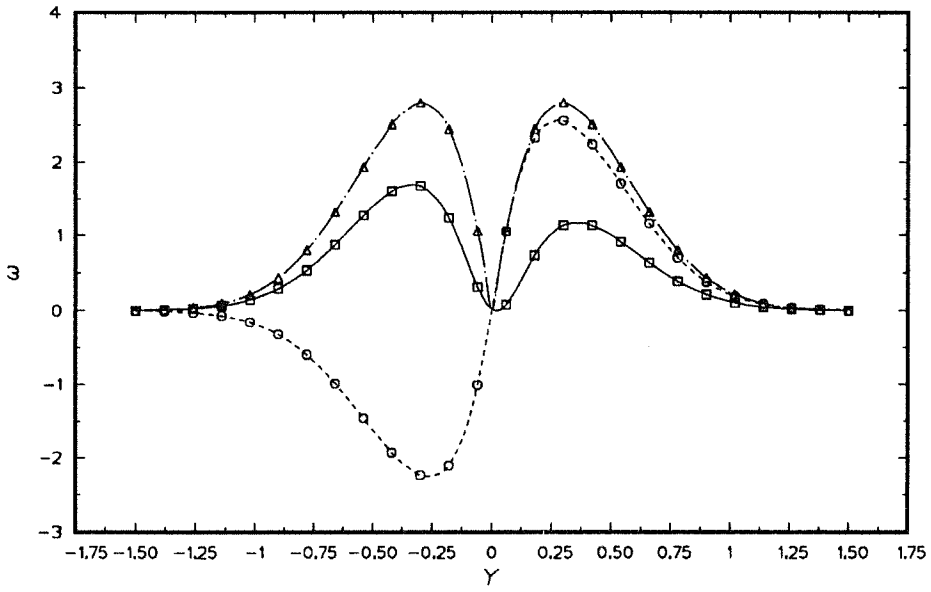

(a)

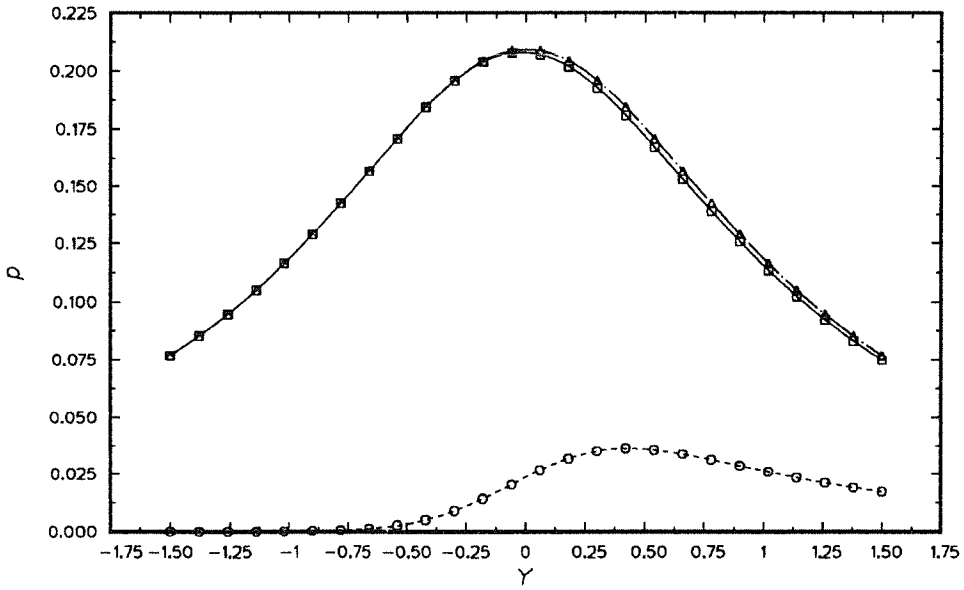

(b)

FIGURE 4.14. Linear eigenfunctions of the cold flow. (a) $\hat{\omega}_z$ (b) $\hat{p}$. M_1=0, $\bar{T}_2$=1, T_{ad}=1, β=0, Da=10. □ , real; ○ , imaginary; △ , absolute.

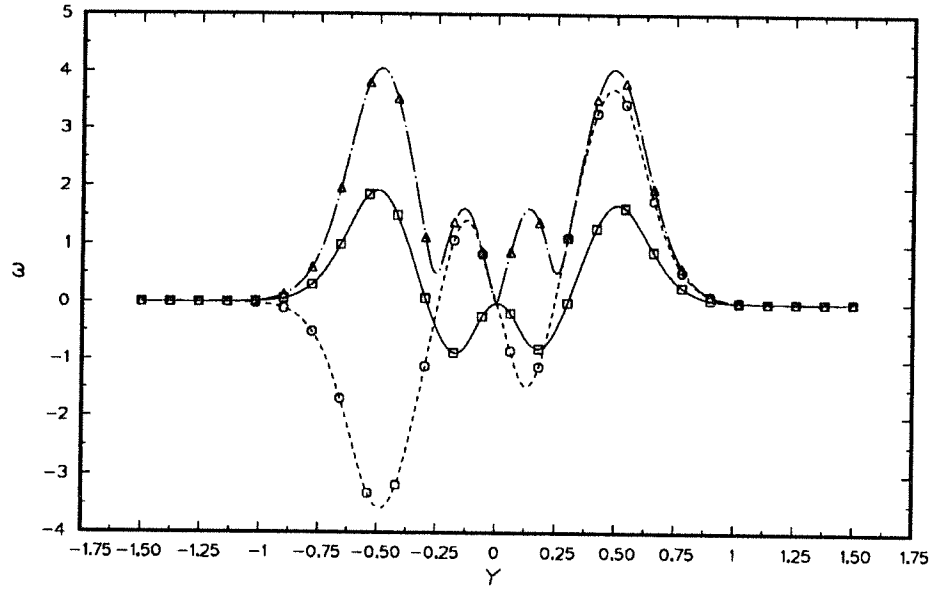

(a)

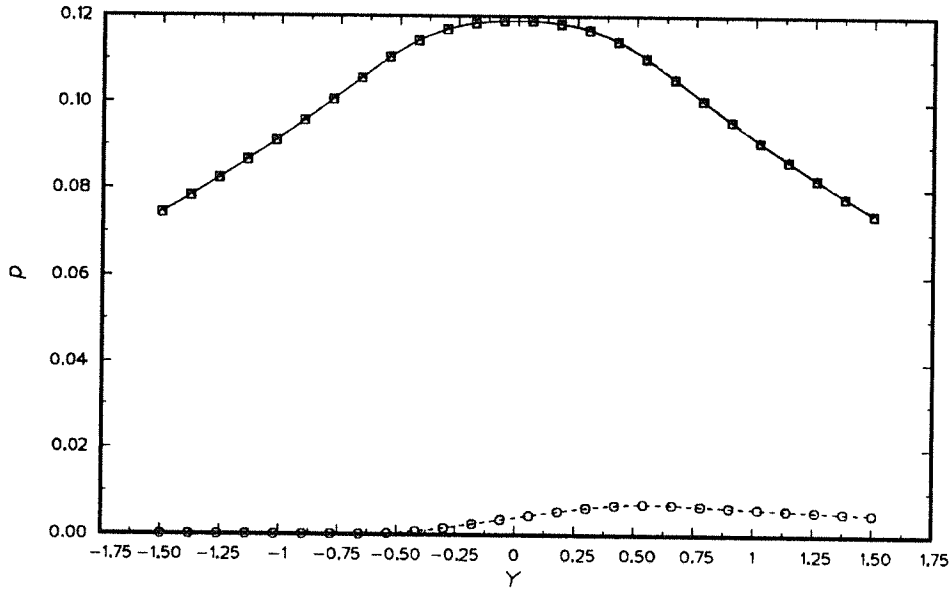

(b)

FIGURE 4.15. Continued.

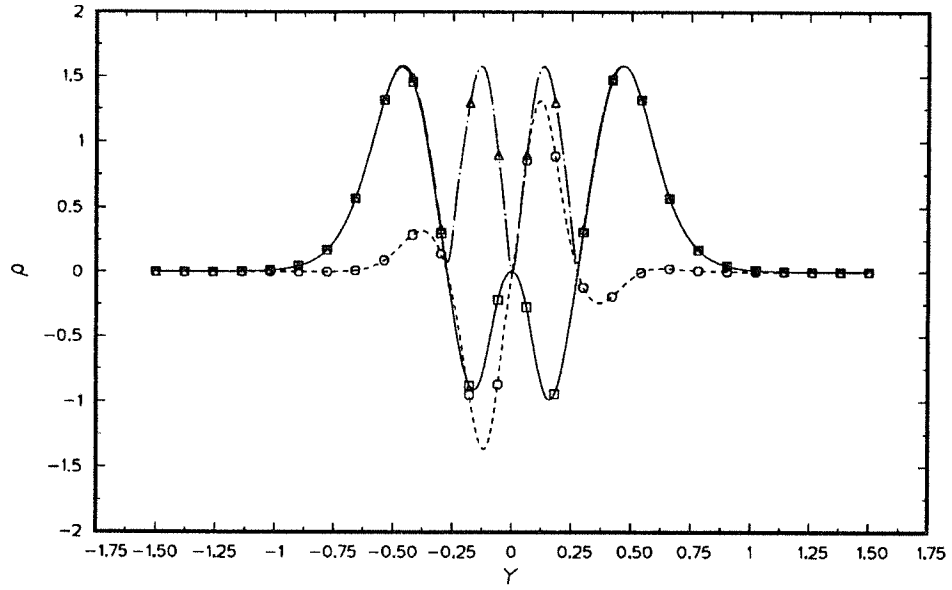

(c)

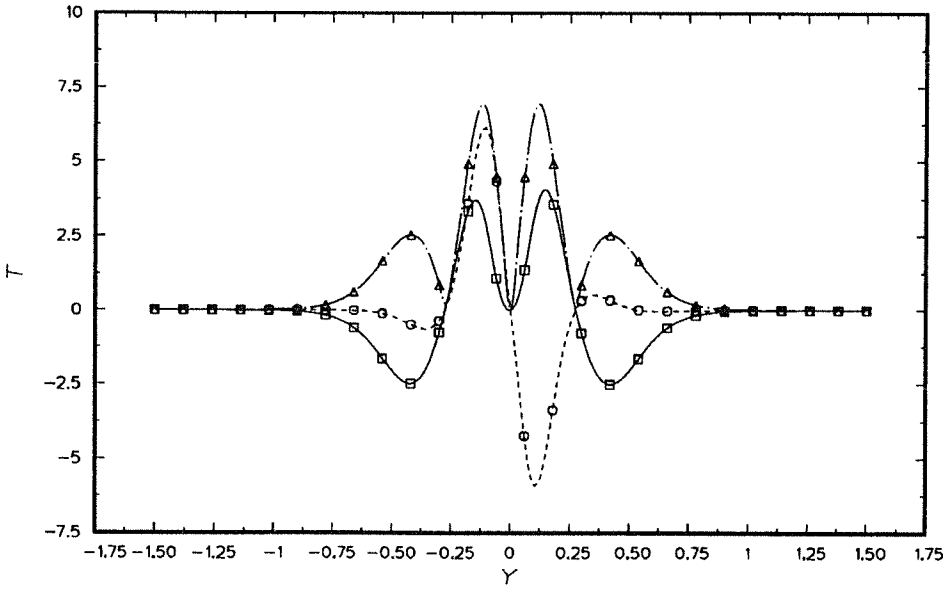

(d)

FIGURE 4.15. Continued.

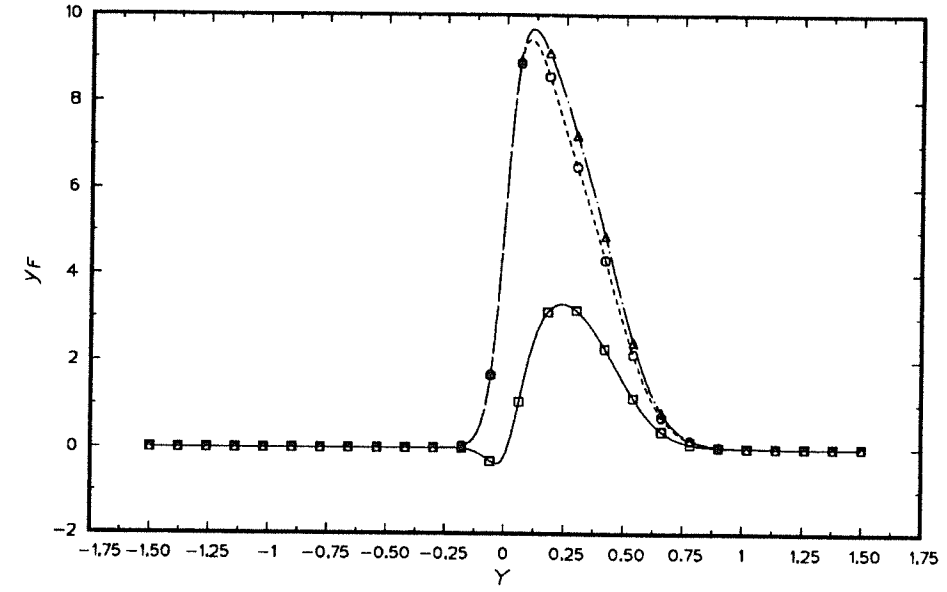

(e)

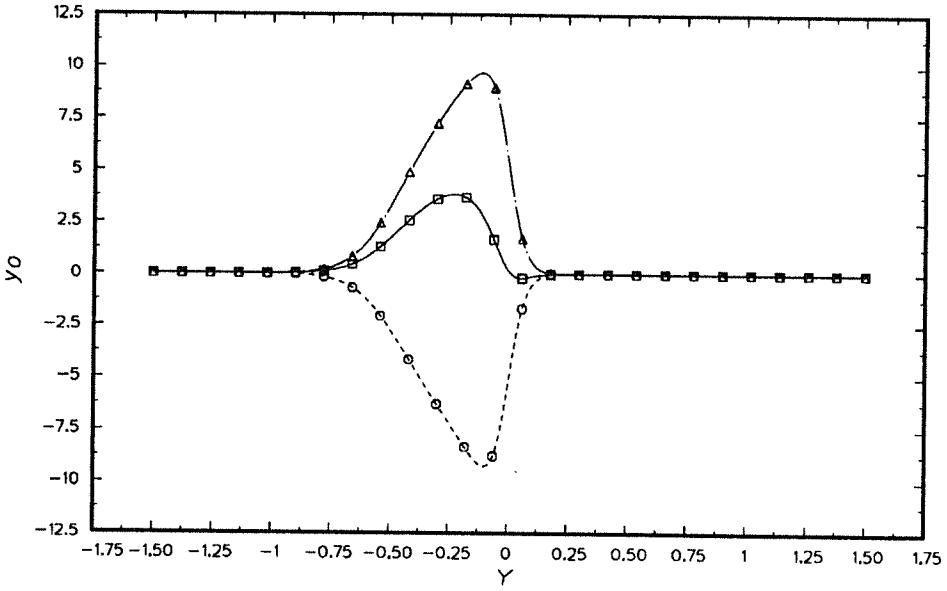

(f)

FIGURE 4.15. Linear eigenfunctions of the reacting flow (center mode) (a) $\hat{\omega}_z$ (b) $\hat{p}$ (c) $\hat{\rho}$ (d) $\hat{T}$ (e) $\hat{y}_F$ (f) $\hat{y}_O$. M_1=0, $\bar{T}_2$=1, T_{ad}=4, β=0, Da=10. ▫ , real; ○ , imaginary; △ , absolute.

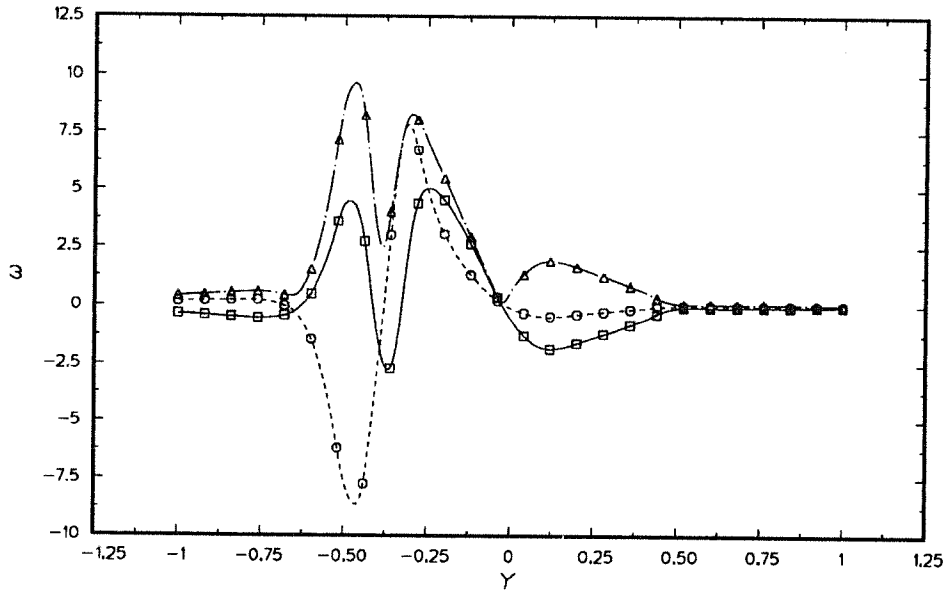

(a)

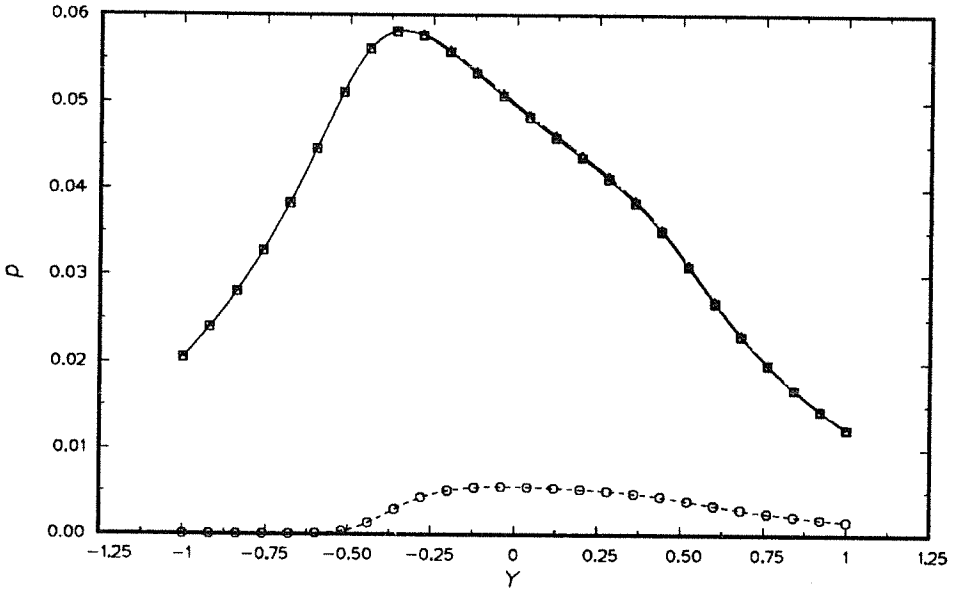

(b)

FIGURE 4.16. Continued.

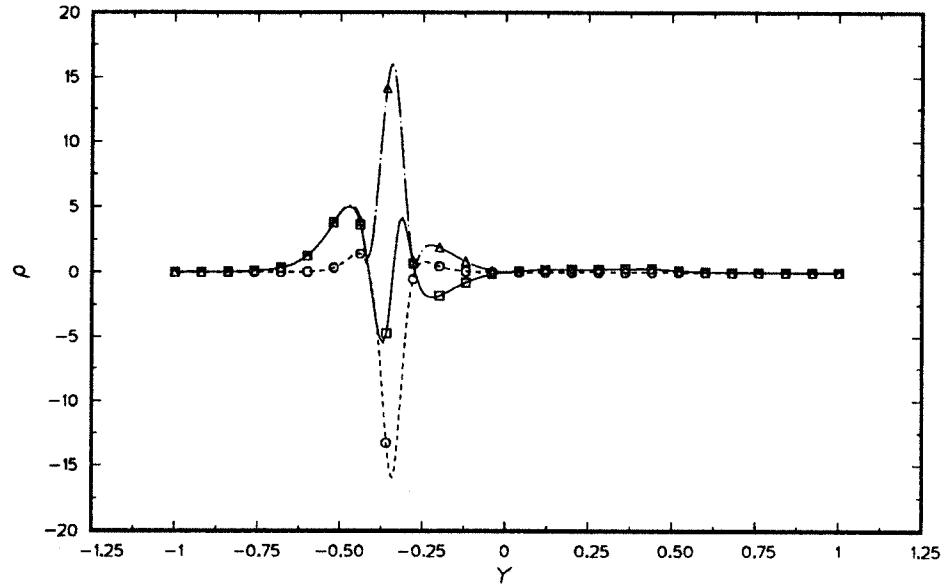

(c)

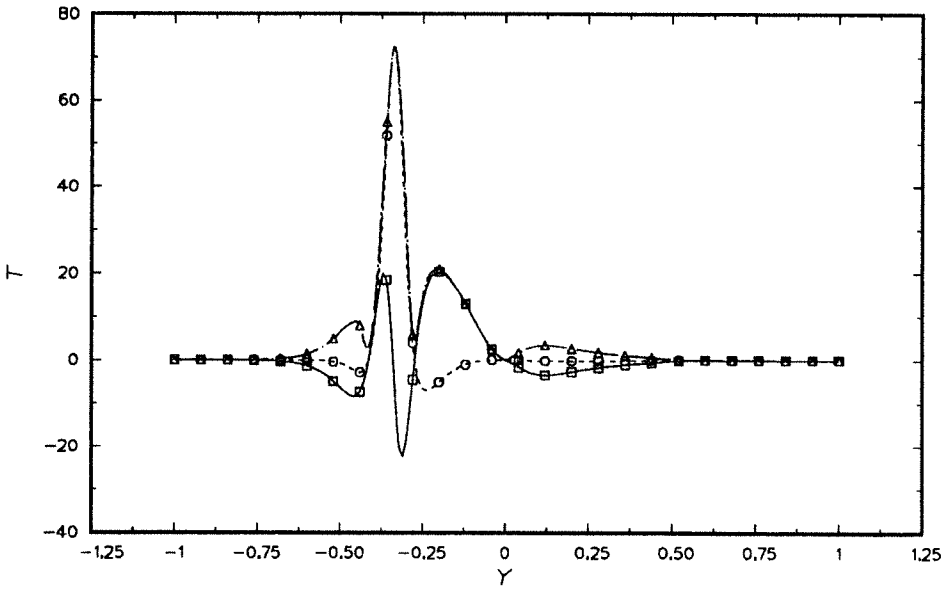

(d)

FIGURE 4.16. Continued.

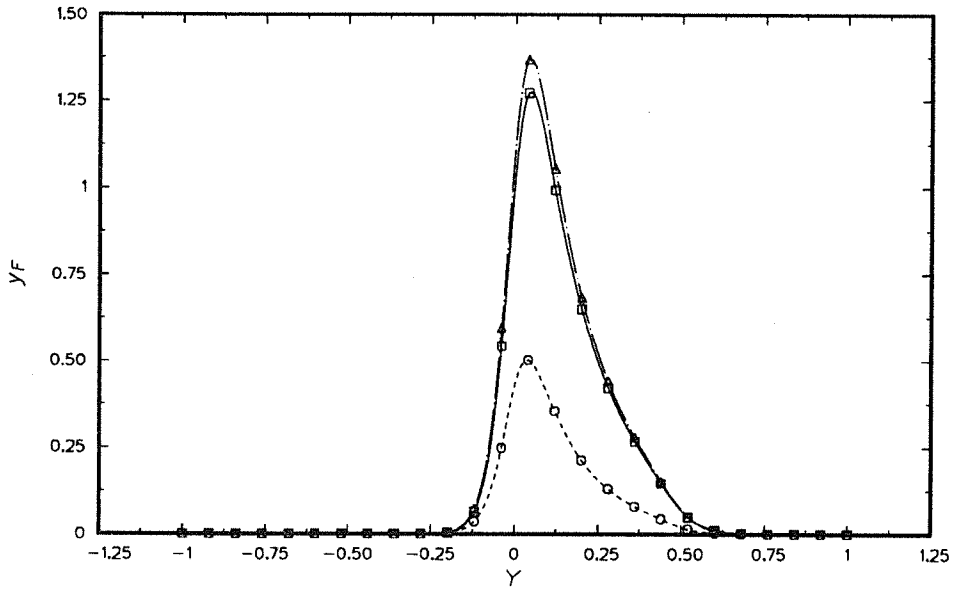

(e)

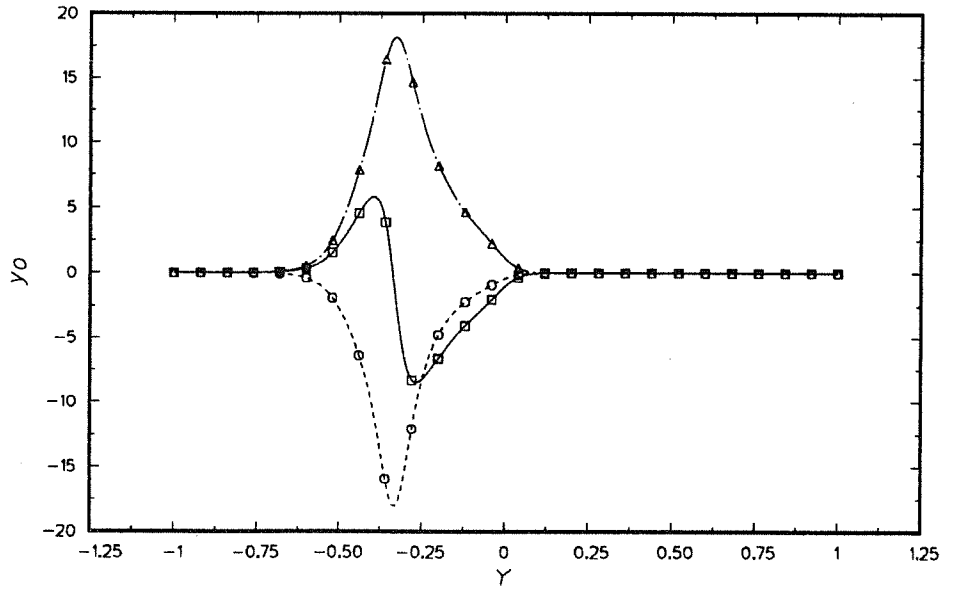

(f)

FIGURE 4.16. Linear eigenfunctions of the reacting flow (slow mode) (a) $\hat{\omega}_z$ (b) $\hat{p}$ (c) $\hat{\rho}$ (d) $\hat{T}$ (e) $\hat{y}_F$ (f) $\hat{y}_O$. M_1=0, $\bar{T}_2$=1, T_{ad}=8, β=0, Da=10. ▫ , real; ○ , imaginary; △ , absolute.

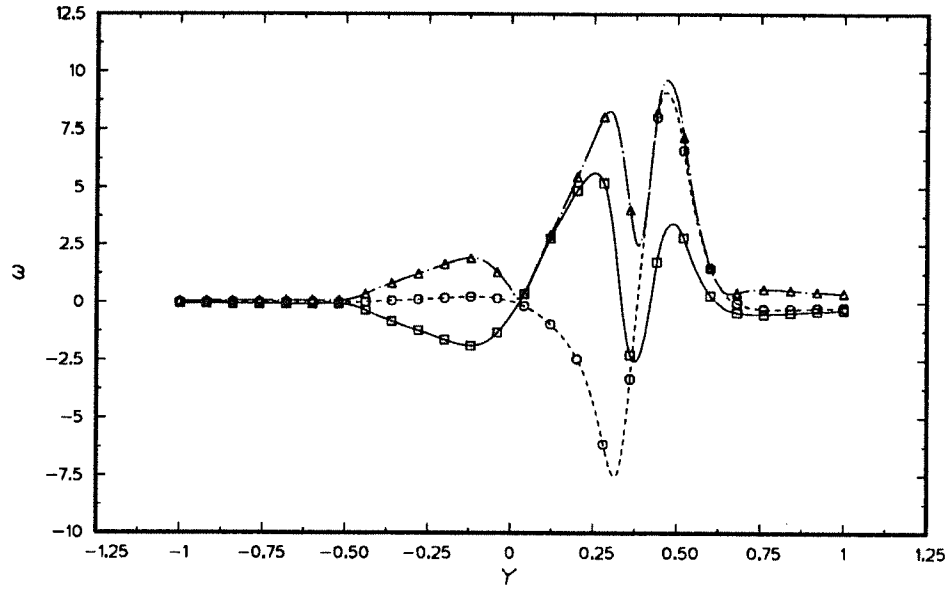

(a)

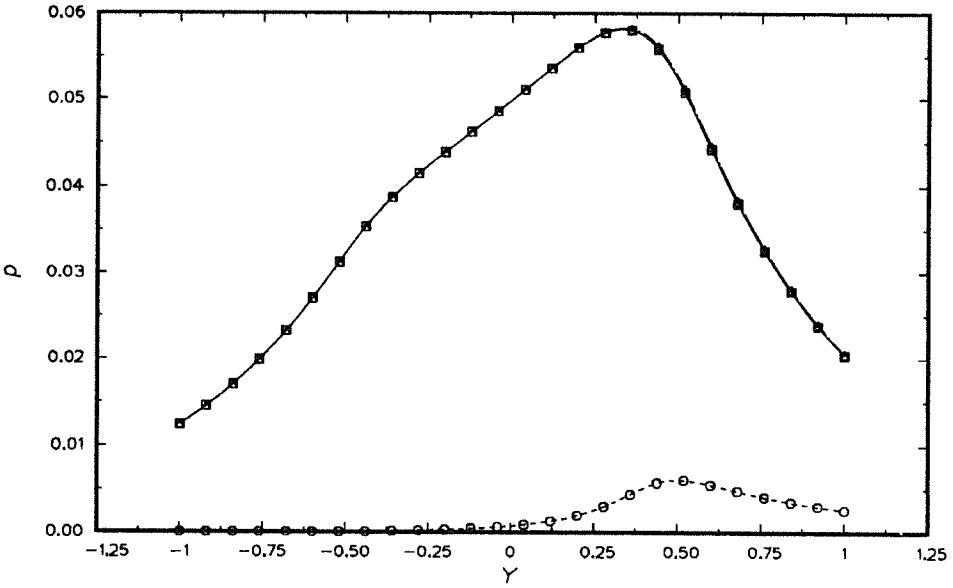

(b)

FIGURE 4.17. Continued.

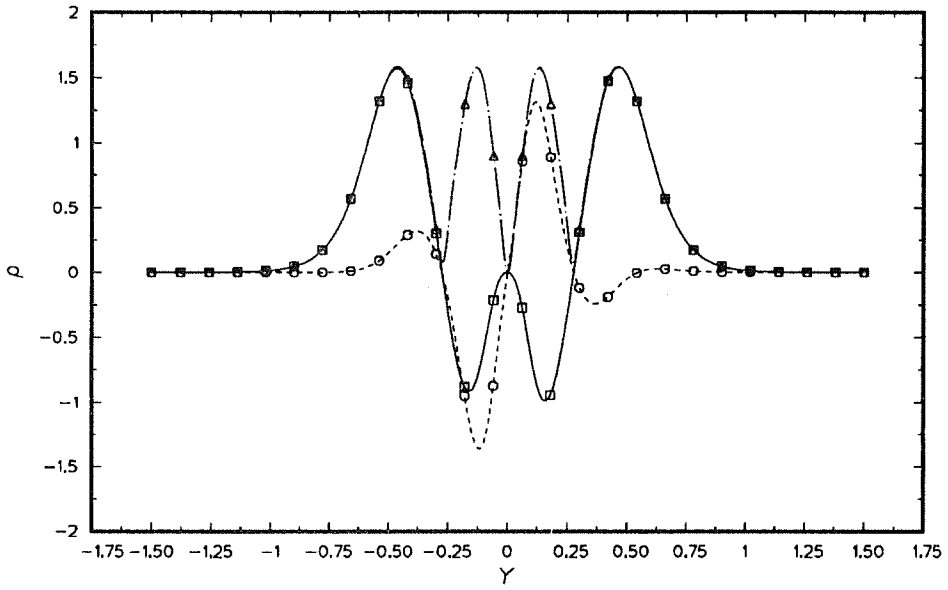

(c)

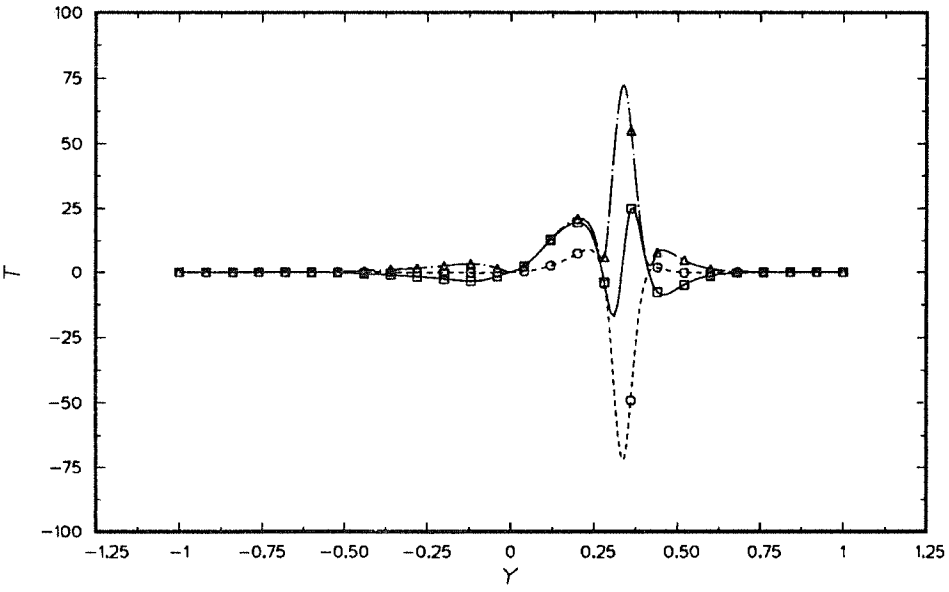

(d)

FIGURE 4.17. Continued.

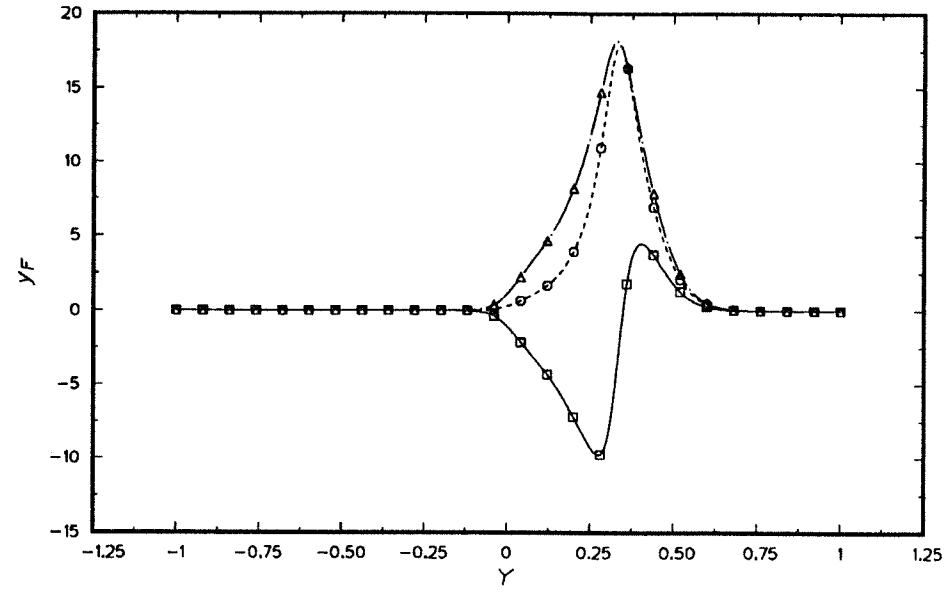

(e)

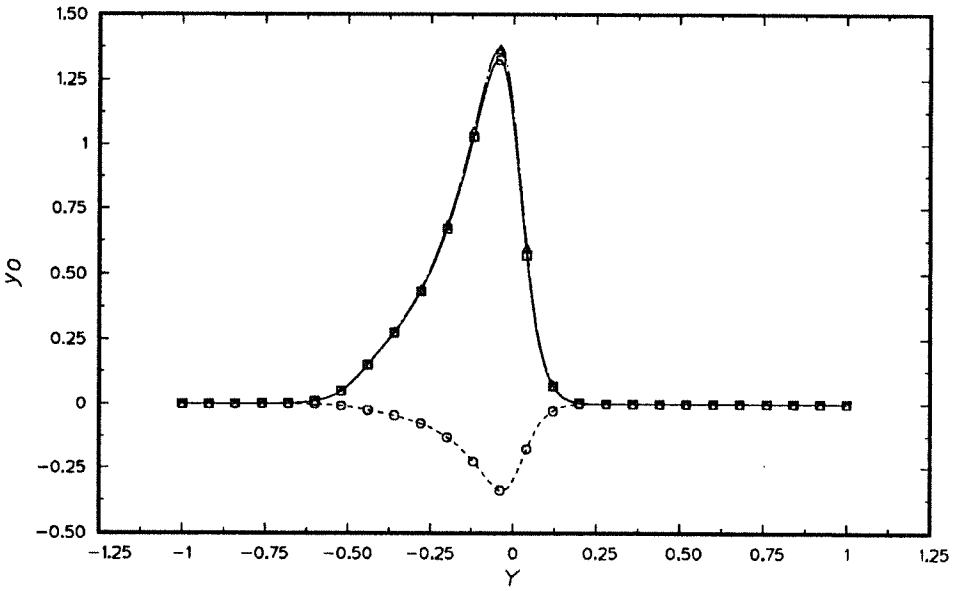

(f)

FIGURE 4.17. Linear eigenfunctions of the reacting flow (fast mode) (a) $\hat{\omega}_z$ (b) $\hat{p}$ (c) $\hat{\rho}$ (d) $\hat{T}$ (e) $\hat{y}_F$ (f) $\hat{y}_O$. M_1=0, $\bar{T}_2$=1, T_{ad}=8, β=0, Da=10. ▫ , real; ○ , imaginary; △ , absolute.

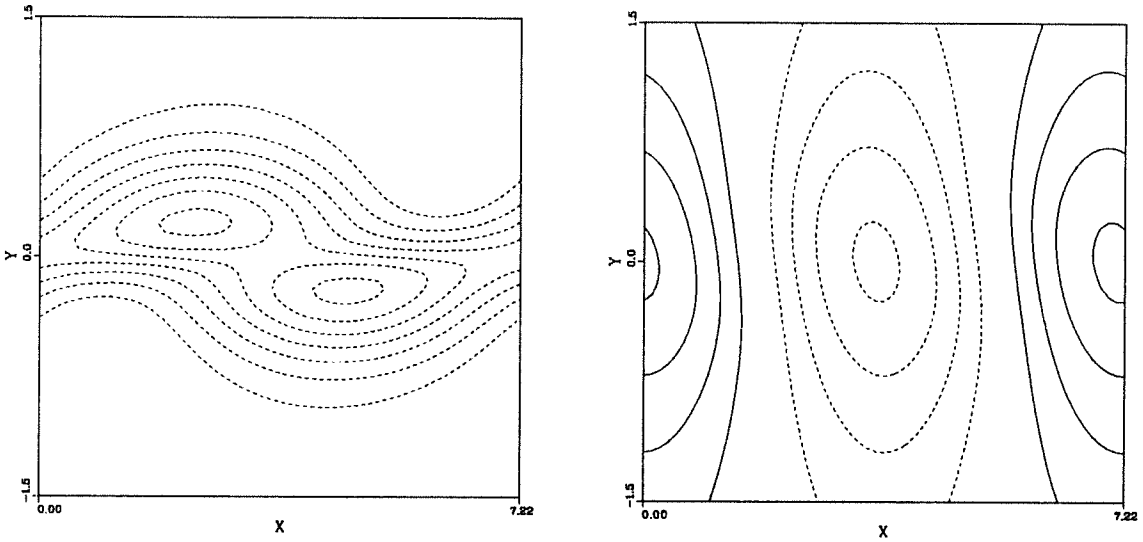

(a) max=2.52x10^{-2}, min=-0.366 (b) max=1.021, min=0.979

FIGURE 4.18. Contour plots from linear eigenfunctions of the cold flow. (a) ω_z (b) pressure. M_1=0, $\bar{T}_2$=1, T_{ad}=1, β=0, Da=10.

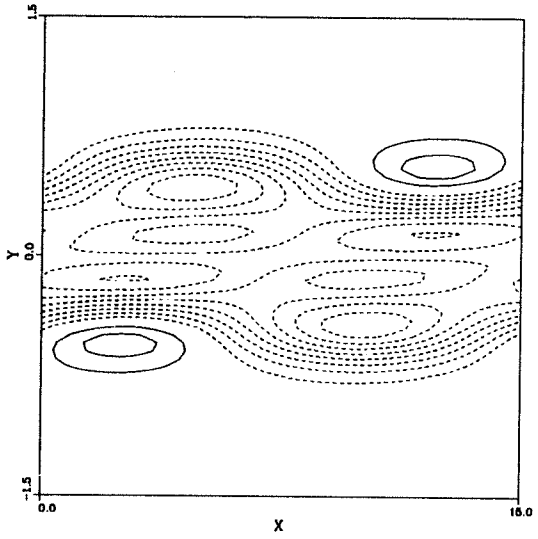

(a) max=0.102, min=-0.349

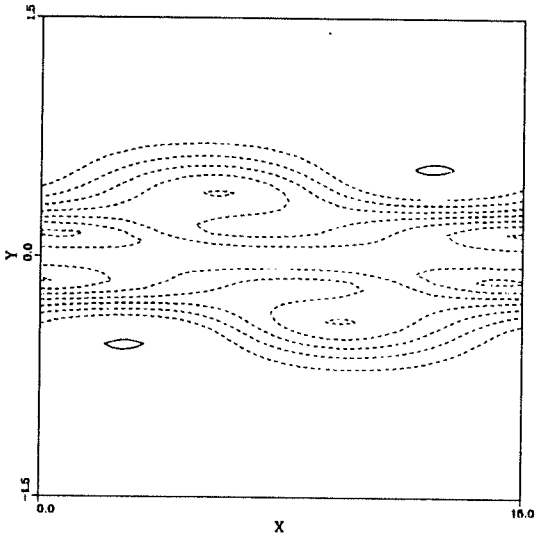

(b) max=0.107, min=-0.718

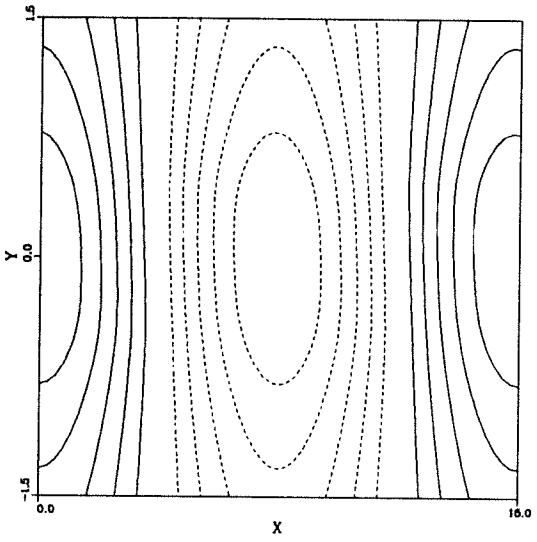

(c) max=1.019, min=0.981

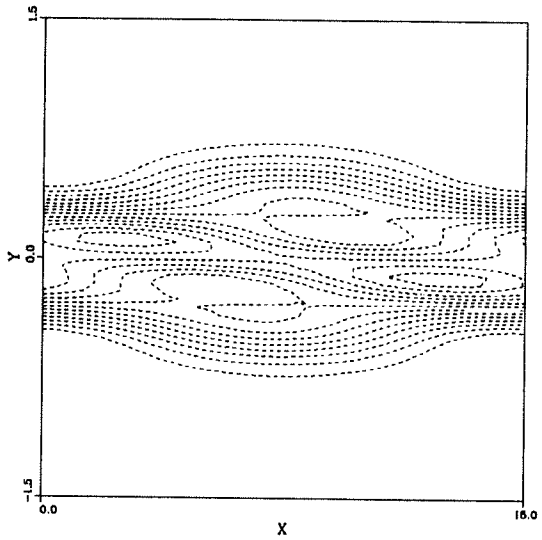

(d) max=1.029, min=0.321

FIGURE 4.19. Continued.

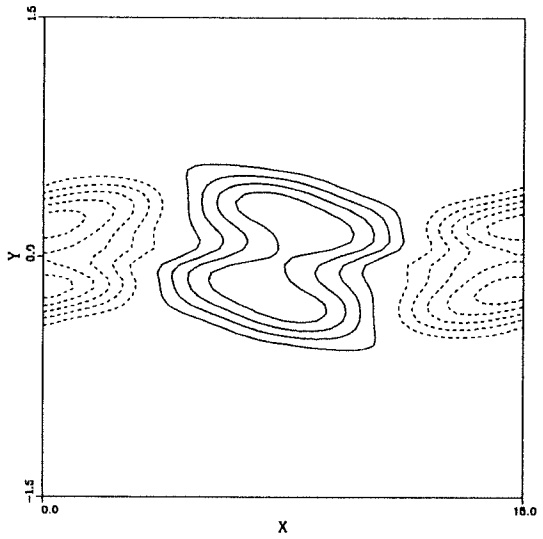

(e) max=4.83x10^{-3}, min=-5.83x10$De-3$

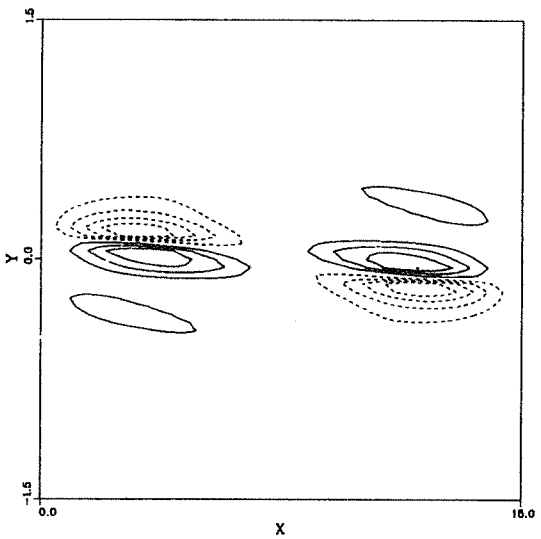

(f) max=2.x10^{-2}, min=-2.41x10^{-2}

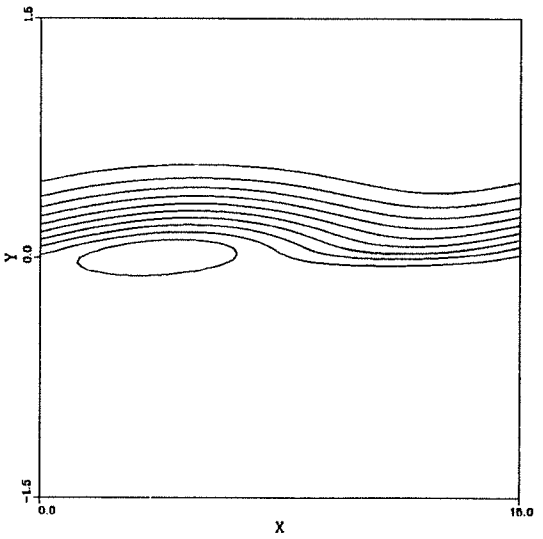

(g) max=1.0, min=0.0

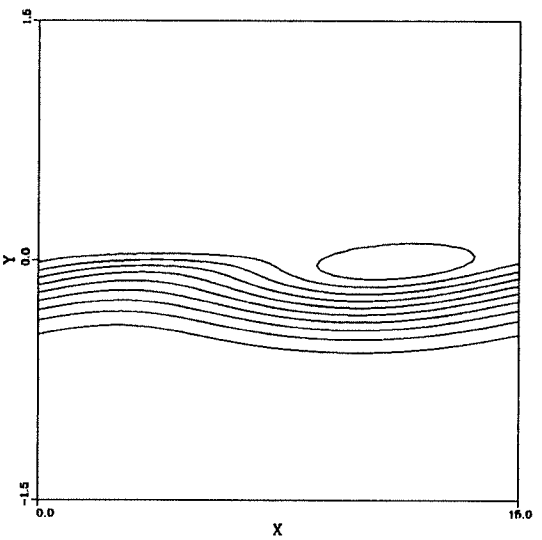

(h) max=1.0, min=0.0

FIGURE 4.19. Contour plots from linear eigenfunctions of the reacting flow (center mode). (a) ω_z (b) ω_z/ρ (c) pressure (d) density (e) dilatation term (f) baroclinic term (g) fuel (h) oxidizer. M_1=0, $\bar{T}_2$=1, T_{ad}=4, β=0, Da=10.

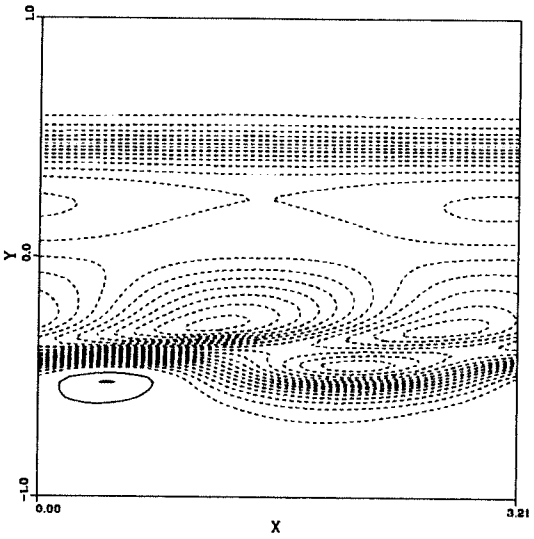

(a) max=0.004, min=-0.388

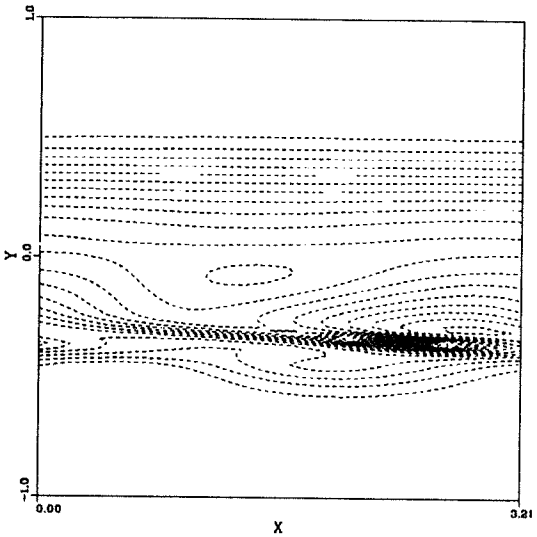

(b) max=0.004, min=-2.45

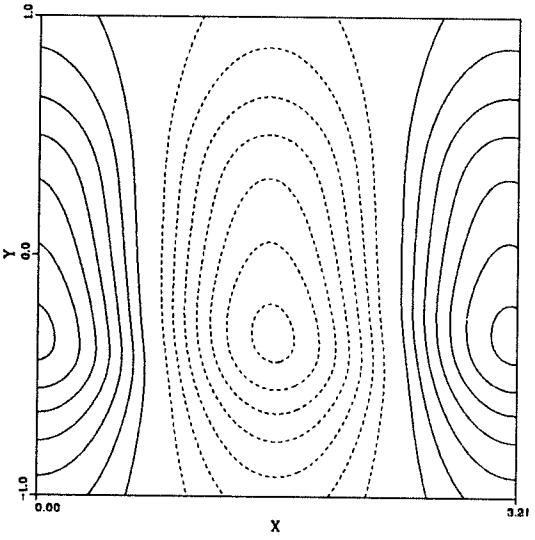

(c) max=1.002, min=0.998

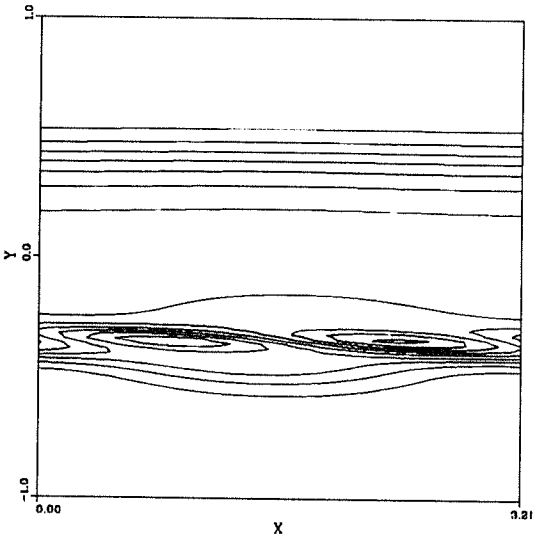

(d) max=1.0, min=0.07

FIGURE 4.20. Continued.

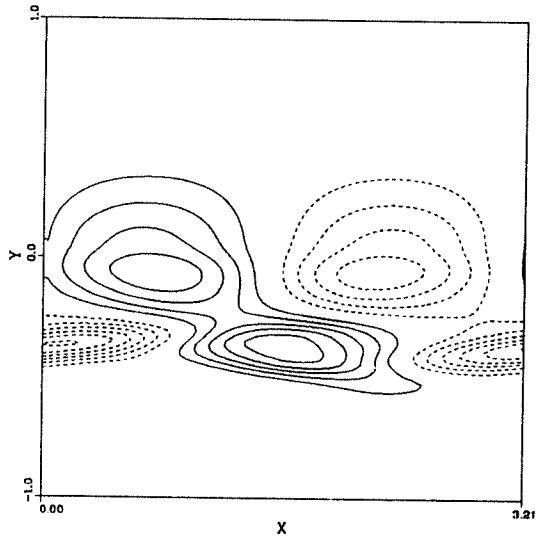

(e) max=5.65x10^{-3}, min=-6.19x10^{-3}

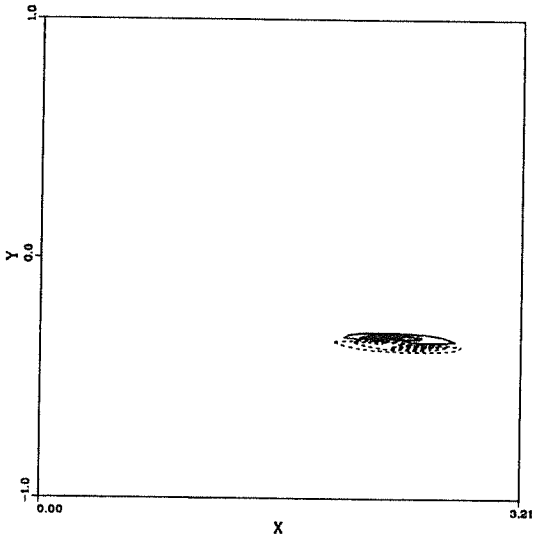

(f) max=0.332, min=-0.379

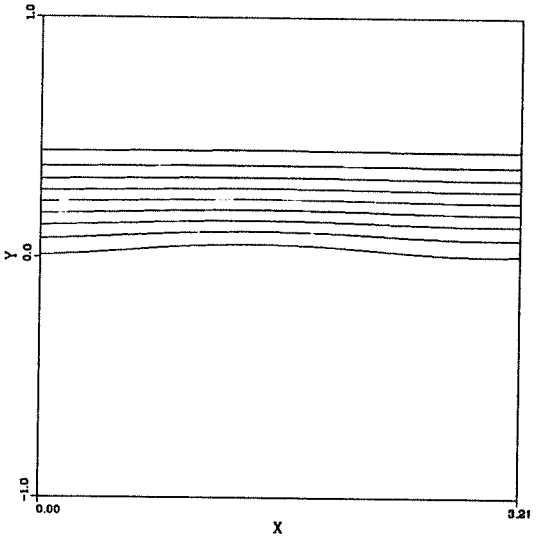

(g) max=1.0, min=0.0

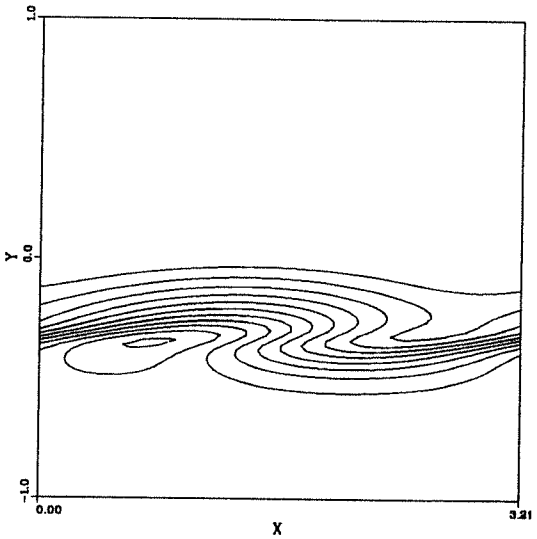

(h) max=1.0, min=0.0

FIGURE 4.20. Contour plots from linear eigenfunctions of the reacting flow (slow mode). M_1=0, $\bar{T}_2$=1, T_{ad}=8, β=0, Da=10. (a) ω_z (b) ω_z/ρ (c) pressure (d) density (e) dilatation term (f) baroclinic term (g) fuel (h) oxidizer.

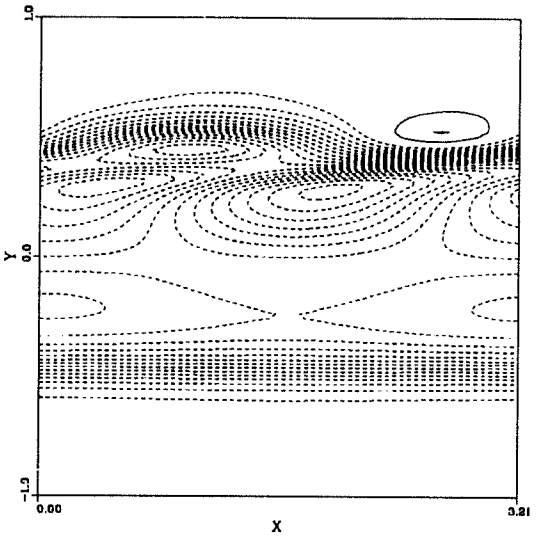

(a) max=0.004, min=-0.388

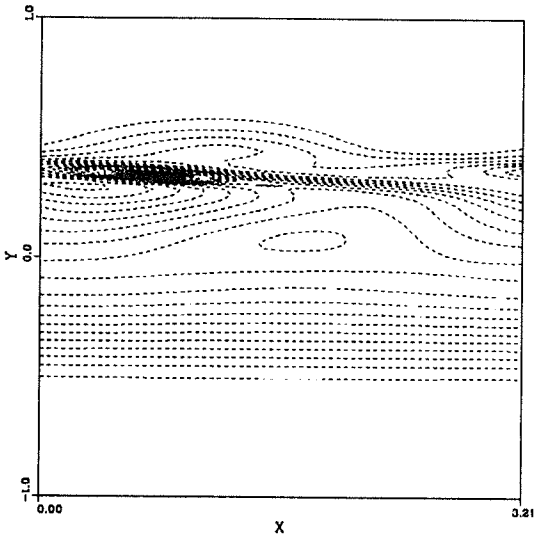

(b) max=0.004, min=-2.45

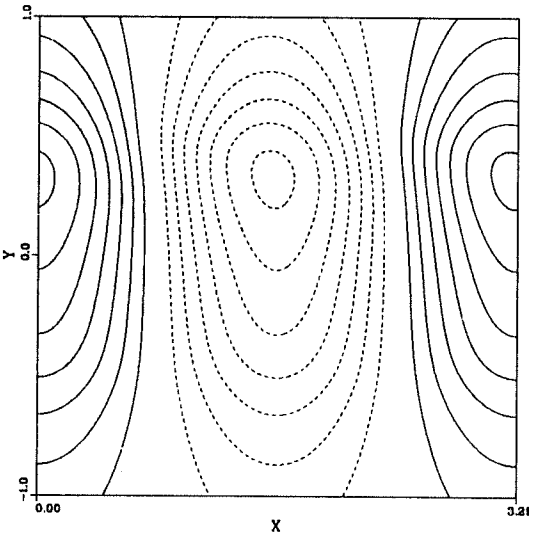

(c) max=1.002, min=0.998

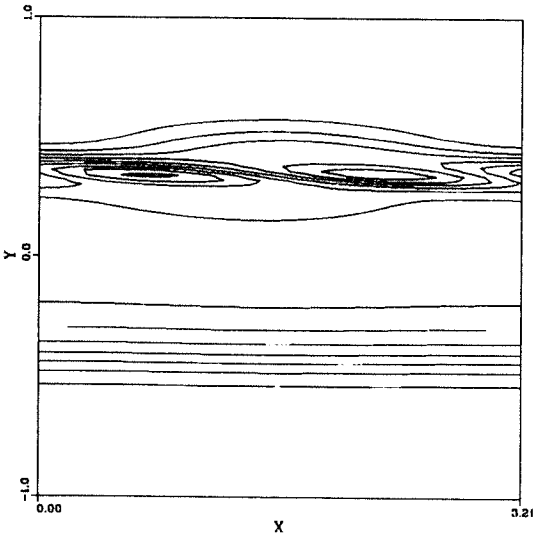

(d) max=1.0, min=0.07

FIGURE 4.21. Continued.

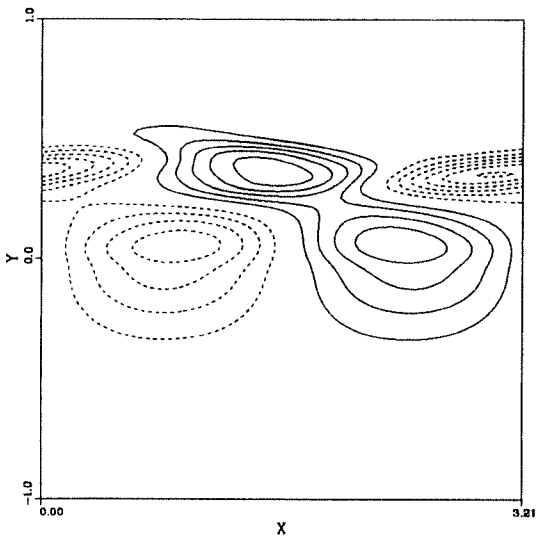

(e) max=5.65x10^{-3}, min=-6.19x10^{-3}

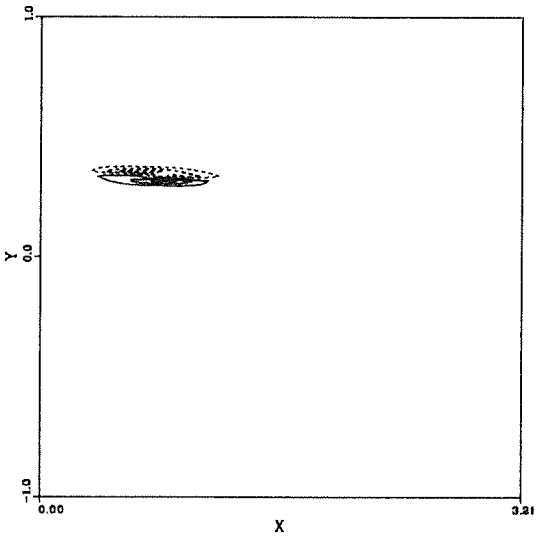

(f) max=0.332, min=-0.379

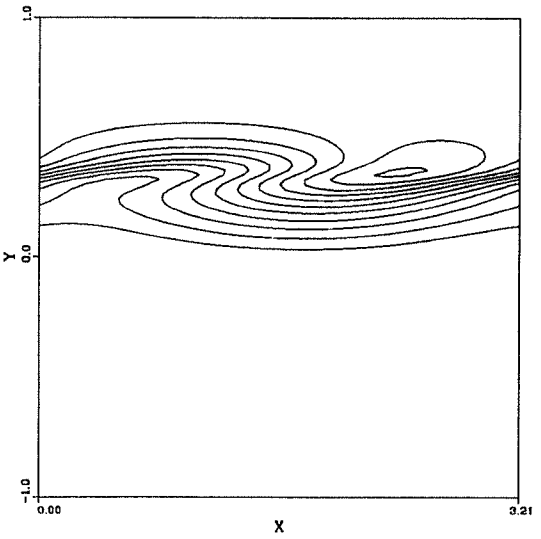

(g) max=1.0, min=0.0

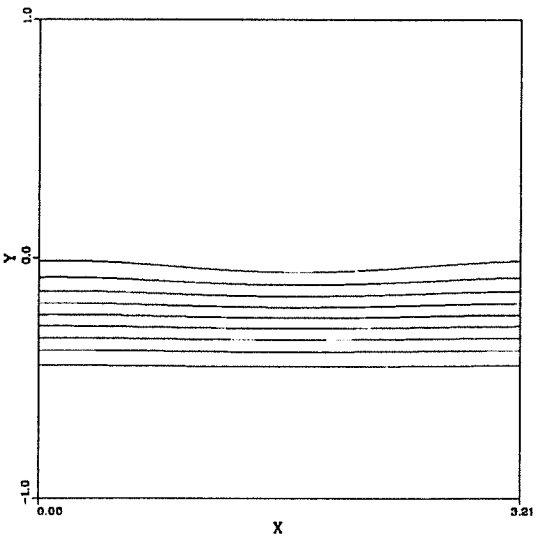

(h) max=1.0, min=0.0

FIGURE 4.21. Contour plots from linear eigenfunctions of the reacting flow (fast mode). M_1=0, $\bar{T}_2$=1, T_{ad}=8, β=0, Da=10. (a) ω_z (b) ω_z/ρ (c) pressure (d) density (e) dilatation term (f) baroclinic term (g) fuel (h) oxidizer.

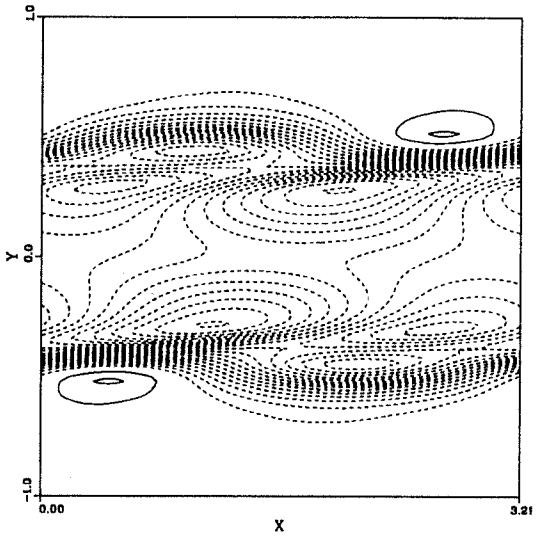

(a) max=0.004, min=-0.38

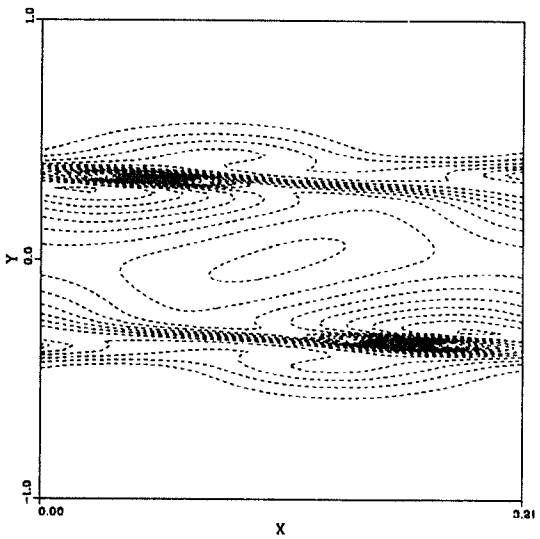

(b) max=0.005, min=-2.43

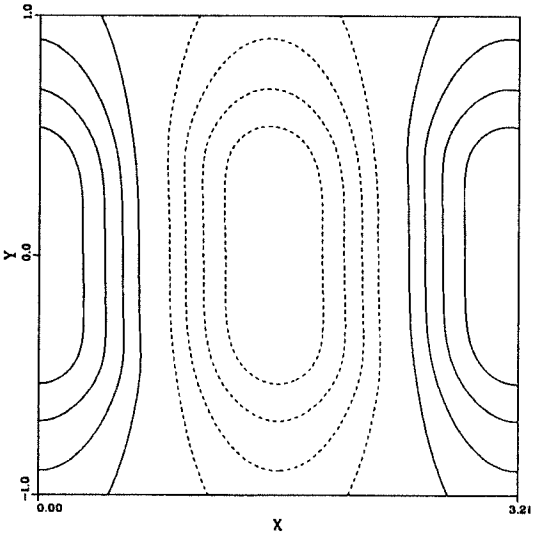

(c) max=1.003, min=0.997

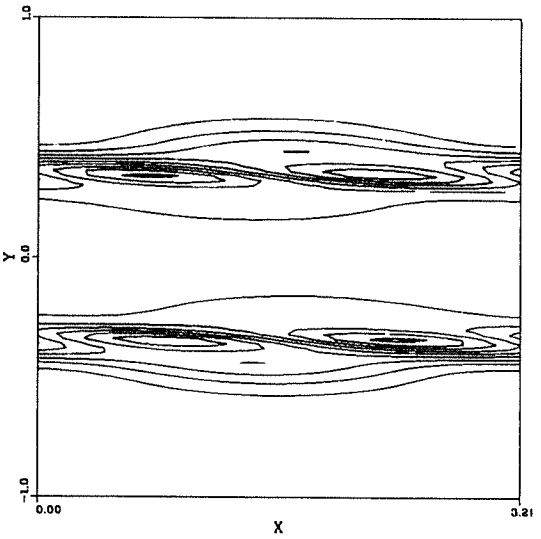

(d) max=1.0, min=0.07

FIGURE 4.22. Continued.

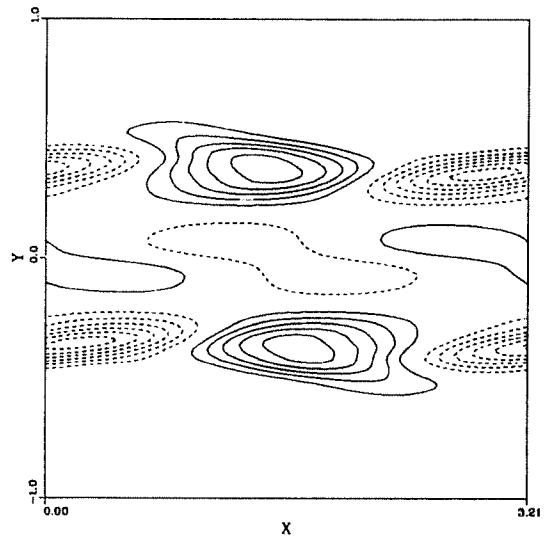

(e) max=5.48x10^{-3}, min=-6.54x10^{-3}

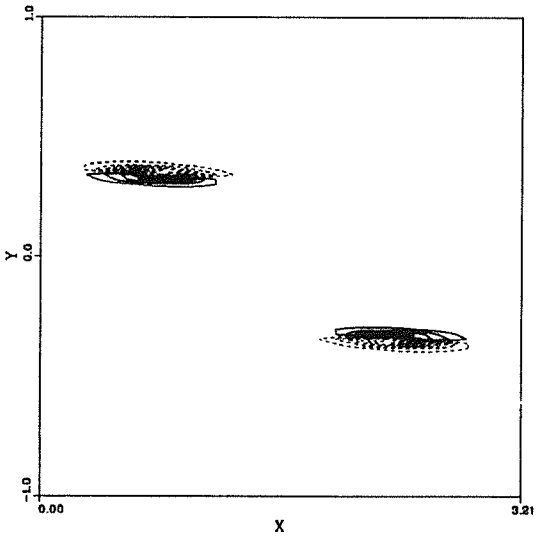

(f) max=0.567, min=-0.625

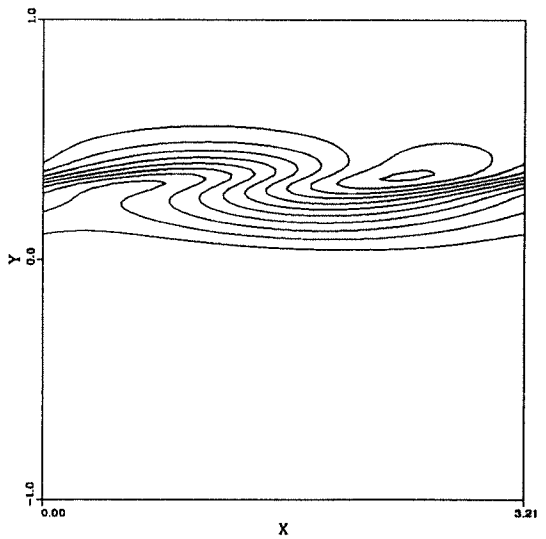

(g) max=1.0, min=0.0

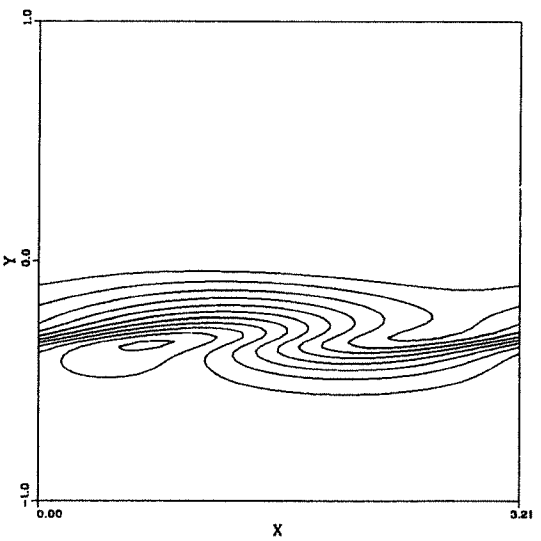

(h) max=1.0, min=0.0

FIGURE 4.22. Contour plots from linear eigenfunctions of the reacting flow (combined mode). M_1=0, $\bar{T}_2$=1, T_{ad}=8, β=0, Da=10. (a) ω_z (b) ω_z/ρ (c) pressure (d) density (e) dilatation term (f) baroclinic term (g) fuel (h) oxidizer.

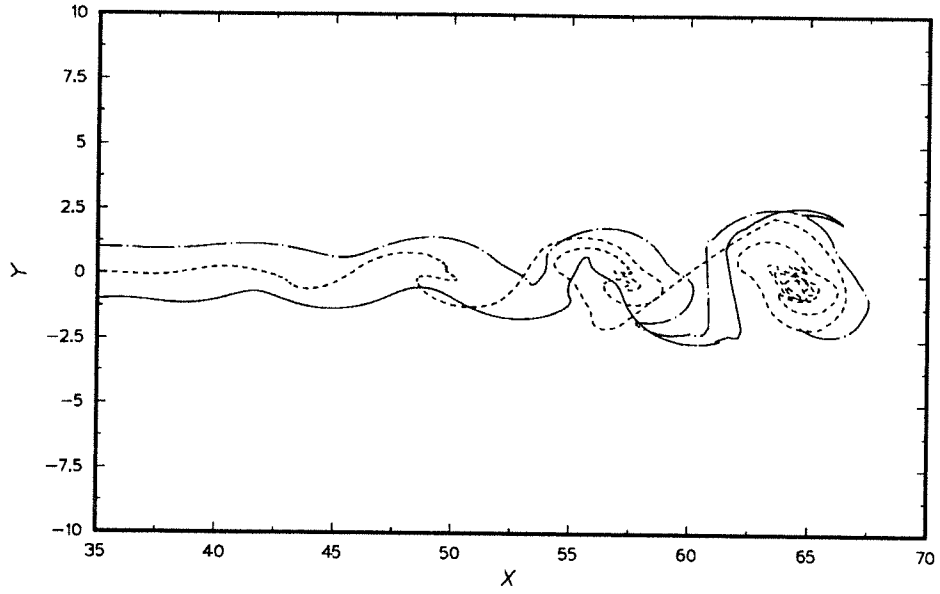

(a)

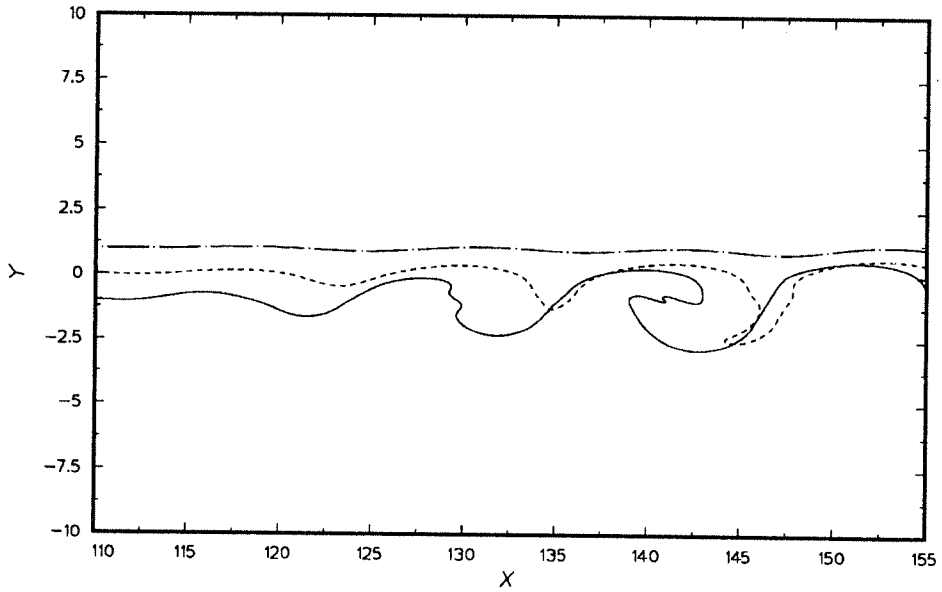

(b)

FIGURE 4.23. Continued.

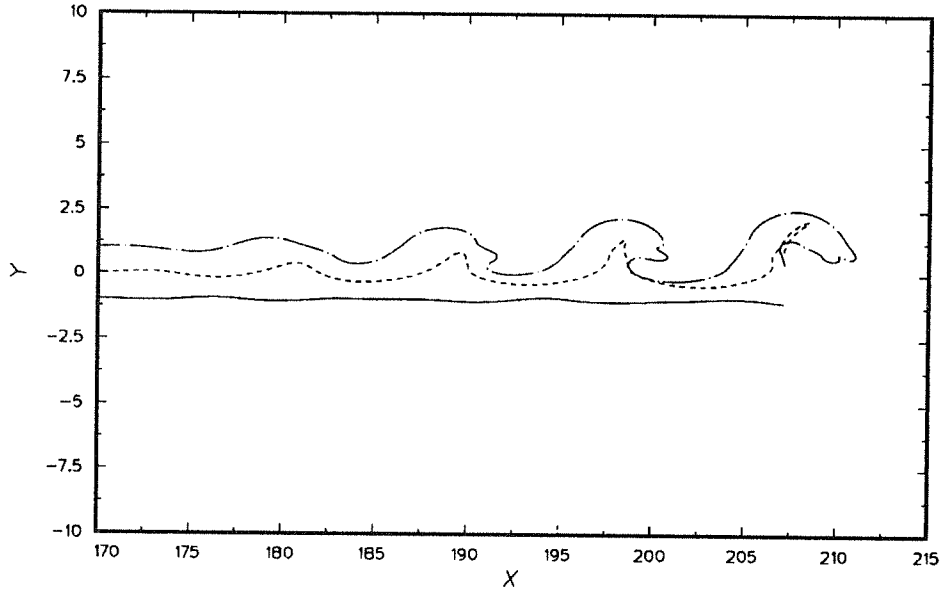

(c)

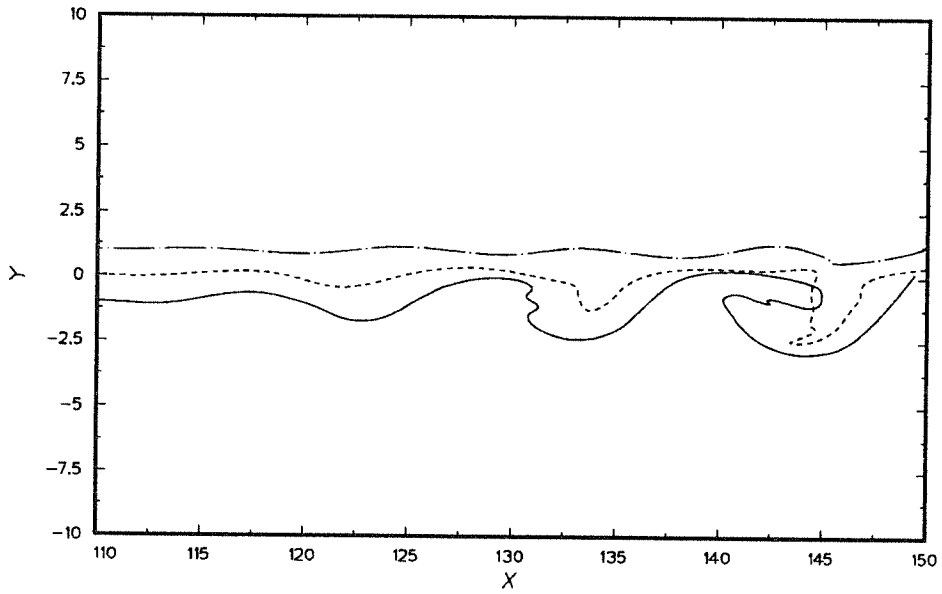

(d)

FIGURE 4.23. Streaklines for the spatially developing layers. (a) center mode (T_{ad}=1) (b) slow mode (T_{ad}=8) (c) fast mode (T_{ad}=8) (d) combined modes (T_{ad}=8). M_1=0, $\bar{T}_2$=1, β=0.

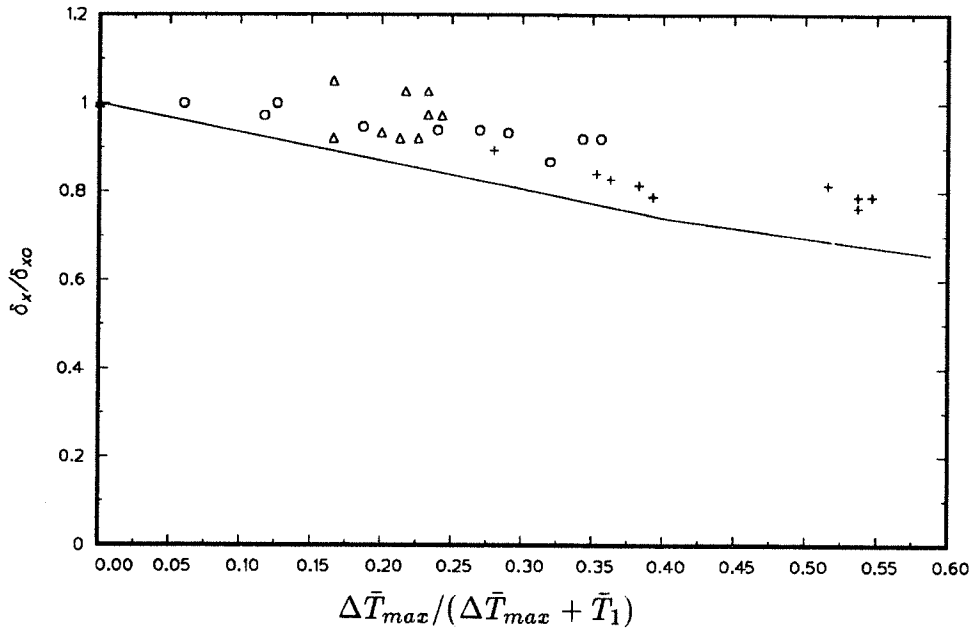

FIGURE 4.24. Normalized growth rate versus heat release. M_1=0, $\bar{T}_2$=1, $\bar{u}_2$=0.4. ——— , current; ○ , Wallace [1981]; △ , Mungal (unpublished data); +, Hermanson & Dimotakis [1989].

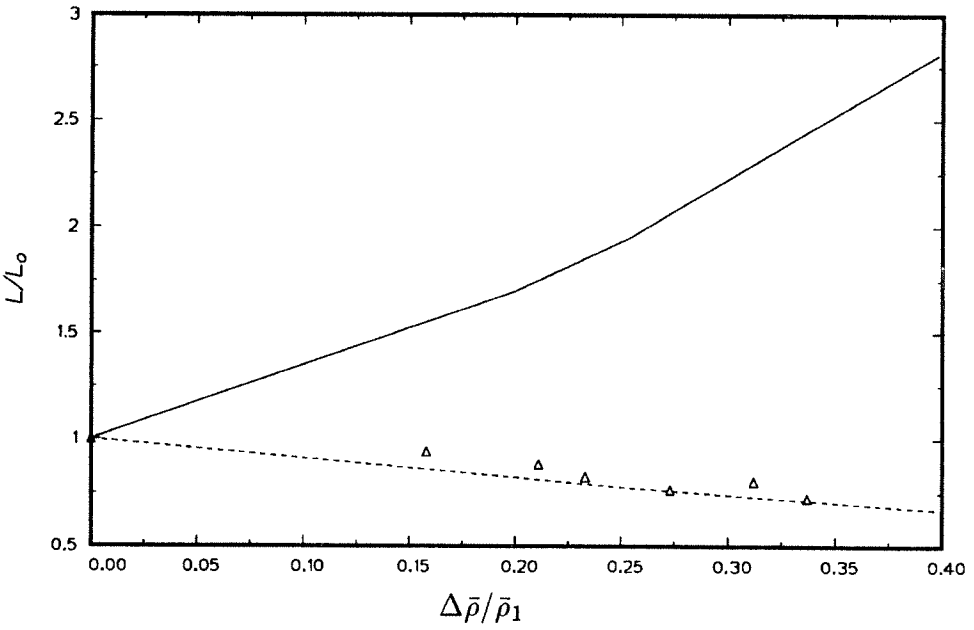

FIGURE 4.25. Normalized mean vortex spacing versus heat release. M_1=0, $\bar{T}_2$=1. ——— , current (center mode); - - - - , current (outer mode); △ , Hermanson & Dimotakis [1989].

Chapter 5

Instability of the Compressible Reacting Free Shear Layer

This chapter investigates the inviscid linear stability of a compressible reacting mixing layer with special emphasis on the effects of heat release and compressibility. Since Chapter 4 showed the importance of using computed laminar profiles rather than assumed analytical ones, we used laminar solutions of the compressible boundary-layer equations from Chapter 2 as base flows. We consider spatially developing layers; temporally developing layers are not different qualitatively. Because the compressibility does not change the criterion for the absolute/convective instability (Hu *et al.* [1991]), the spatial layers considered here are convectively unstable (cf. Sec. 4.3.2). We use non-dimensional adiabatic flame temperature, T_{ad}, to express the amount of heat release from combustion. For a given T_{ad}, the actual temperature rise in high Mach number flows may be higher than in low Mach number flows due to viscous dissipation. How best to express the temperature rise from combustion and viscous dissipation in a single parameter is still an open question.

5.1 Possibility of Non-Inflectional Supersonic Modes

In compressible flows, the necessary and sufficient condition for the existence of a neutral subsonic wave is $(\bar{u}'/\bar{T})'=0$ (Lees & Lin [1946]). The location of the zero is called the generalized inflection point. The proof of sufficiency given by Lees & Lin requires the relative Mach number—the Mach number of the disturbance relative to the free stream (see Sec. 3.2)—to be subsonic at the generalized inflection point. In Chapter 4, we derived a similar criterion for low Mach number reacting flows and found that non-reacting incompressible mixing layers have a single inflection point, whereas reacting mixing layers with sufficient heat release have three.

The existence of multiple unstable modes at supersonic relative Mach numbers was first discovered in the extensive numerical work of Mack [1965]. At about the same time, Gill [1965] found multiple solutions in his study of "top hat" jets and wakes. The modes that they found do not require a generalized inflection point. The reason for these multiple modes can be understood by examining the two-dimensional inviscid

stability equation for the pressure disturbance, Eq. (3.25). Using the definition of the relative Mach number, M_r (Eq. (3.29)), Eq. (3.25) can be written

$$\hat{p}'' - \alpha^2(1 - M_r^2)\hat{p} = 0 \tag{5.1}$$

Using Eq. (3.7), we may rewrite Eq. (5.1) as a partial differential equation

$$\frac{\partial^2 p'}{\partial y^2} + (1 - M_r^2)\frac{\partial^2 p'}{\partial x^2} = 0 \tag{5.2}$$

where p' is the pressure disturbance. When $M_r^2 < 1$, Eq. (5.2) is elliptic, and the unique solution is connected with the generalized inflection point (Lees & Lin [1946]). However, when $M_r^2 > 1$, Eq. (5.2) becomes hyperbolic, and many solutions can satisfy the boundary conditions at $y=\pm\infty$. Mack [1975] found similar behavior in compressible boundary layers.

Like non-reacting compressible boundary layers (Mack [1975]), non-reacting mixing layers have one generalized inflection point even at high Mach numbers. Fig. 5.1 shows that the non-reacting mixing layer at M_1=5 (M_2=2.5) has one generalized inflection point whereas the reacting mixing layer (T_{ad}=4) at the same Mach number has three such points as do the low Mach number flows in Chapter 4. In this case, M_c, the convective Mach number defined by Papamoschou & Roshko [1988], is 1.25. The convective Mach number will be discussed further below. Even though the non-reacting mixing layer has just one generalized inflection point, multiple unstable modes may exist when a region of flow is supersonic relative to the disturbance phase velocity. In other words, supersonic unstable modes can exist in the absence of a generalized inflection point.

5.2 Effect of Mach Number and Heat Release

Fig. 5.2 shows the amplification rates and phase speeds as functions of frequency for M_1=5 (M_c=1.25). The non-reacting mixing layer (T_{ad}=1) has two unstable modes even though it has but one generalized inflection point. One is supersonic relative to the lower free stream and the other is supersonic relative to the upper free stream. We call the former the fast mode and the latter the slow mode in accord with their phase speeds. Each has nearly the same growth rate but the fast mode is more broad-band. Neither resembles the vorticity modes of boundary layers and low-speed

reacting mixing layers, which require generalized inflection points to be unstable, and are of course, subsonic.

The reacting mixing layer (T_{ad}=4) also has two supersonic unstable modes, even though it has three generalized inflection points in Fig. 5.1. They are outer modes and their asymptotic phase speeds shown in Fig. 5.2b are very close to the laminar velocities at the outer generalized inflection points in Fig. 5.1, even though the mean velocities at the generalized inflection points are supersonic relative to one of the free-stream velocities. This suggests that the instability modes in reacting flows may be continuations of the inflectional modes of low Mach number flows. The outer modes have twice the growth rate of the corresponding modes of the non-reacting flow; the fast mode is slightly less amplified and more broad-band than the slow mode. Fig. 5.2b shows that the phase velocity of the fast mode approaches an asymptotic value close to the upper free stream speed as the frequency increases; the slow mode phase speed asymptotes to the speed of the lower free stream. Increasing the adiabatic flame temperature raises the speed of the fast mode and reduces the speed of the slow mode, as in low-speed reacting mixing layers.

In order to study the effect of Mach number on the type of disturbances produced, we give the phase speeds of the most unstable modes, c_r, as functions of Mach number in Fig. 5.3 for both non-reacting (T_{ad}=1) and reacting (T_{ad}=4) flows. The solid curve is the phase speed of a disturbance that is sonic with respect to the upper stream, c_u, and the dashed curve is the corresponding speed with respect to the lower stream, c_l. When the relative Mach number is subsonic ($|M_{r1,2}| < 1$, region I), the non-reacting flow has only center modes—Kelvin-Helmholtz modes—that travel at the average speed of two streams. As the Mach number increases, the center modes become supersonic with respect to both streams ($|M_{r1,2}| > 1$, region III); they also become less unstable and, for the high enough Mach number, they become stable. At supersonic relative Mach numbers, unstable modes that are independent of the generalized inflection points arise as shown in Fig. 5.2. For the non-reacting flow, Fig. 5.3a shows that the fast mode is subsonic with respect to the upper stream and supersonic with respect to the lower stream ($|M_{r1}| < 1, |M_{r2}| > 1$, region II) and the slow mode is supersonic with respect to the upper stream and subsonic with respect to the lower stream ($|M_{r1}| > 1, |M_{r2}| < 1$, region IV). The phase speeds of the outer modes approach the free stream velocities as the Mach number increases. For the reacting flow with T_{ad}=4, Fig. 5.3b shows that three inflectional unstable

modes exist at low Mach numbers. As the Mach number increases, the phase speeds of the outer modes become supersonic. The center mode also becomes supersonic at high Mach numbers. The outer modes at high Mach numbers are continuations of the inflectional modes of low Mach number flows. However, the generalized inflection point—the mean angular momentum maximum—is less important at supersonic flows than at subsonic flows because the former is not a necessary condition for instability.

Now we study the effect of the Mach number on the maximum growth rates of two-dimensional modes. Fig. 5.4 gives results for T_{ad}=1 and 4. First consider the unheated flow (T_{ad}=1). As has been demonstrated by Gropengiesser [1970] and others, the growth rate of the center mode decreases dramatically as the Mach number increases. In the high supersonic regime, the growth rate is miniscule compared to its incompressible value. At supersonic speeds, a second set of modes (outer modes) become unstable. The growth rates of these modes are relatively insensitive to the Mach number and, for a sufficiently high Mach number, are much larger than the growth rate of the center mode. However, they are small compared to the growth rate of the center mode at low speeds. The outer modes should be the predominant instabilities at supersonic Mach numbers.

Next, consider the reacting flow (T_{ad}=4). As shown in Chapter 4, the low density created by reaction in the center of the shear layer reduces the growth rate of the center mode. Fig. 5.4b shows that the growth rate of this mode is further reduced as the Mach number increases and is always smaller than the growth rate of the corresponding cold flow mode. As shown in Chapter 4, when T_{ad} is large enough, outer modes arise in the reacting flow even at low Mach numbers. For the case shown here (T_{ad}=4), the outer modes are slightly less unstable than the center mode at M_1=0; this situation reverses at higher heat release. At low Mach numbers the slow mode is more unstable than the fast mode; the difference becomes very small at high Mach numbers. The growth rate of these outer modes falls off much more slowly than that of the center mode with increasing Mach number and, for the heat release used here, they dominate for $M_1 > 2.5$. At $M_1 > 4$, the center mode is stable.

Fig. 5.5a shows the maximum growth rates of unstable modes as functions of adiabatic flame temperature for a high-speed flow (M_1=5) as well as a lower-speed flow (M_1=1); the maximum is with respect to frequency of the perturbation. At M_1=1, as the heat release increases, the maximum amplification rate of the center mode decreases rapidly; its value in the cold flow is 0.118, while for T_{ad}=8 it is 0.018,

or 15% of the cold flow value. The amplification rates of the outer modes change very little as heat release increases and the slow mode remains more unstable than the fast mode. Consequently, at high heat release, the outer modes have larger amplification rates than the center mode and the slow mode should dominate. For T_{ad}=8, the outer modes have almost twice the amplification rate of the center mode. Flows with high heat release should be unstable to the slow mode, but heat release stabilizes the flow at M_1=1 (M_c=0.25).

At M_1=5 (M_c=1.25), only the supersonic outer modes are unstable. As heat release increases, their maximum growth rates increase. The maximum growth rate of the slow mode of the non-reacting flow is 0.0095, while for T_{ad}=8 it is 0.027, or about three times as large. The fast mode is less unstable than the slow mode, but at T_{ad}=8 it has twice the growth rate of the most unstable mode in the non-reacting flow. In contrast to the low-speed case, heat release destabilizes the supersonic flow. The corresponding phase velocities in Fig. 5.5b show that the speeds of the outer modes approach asymptotic values as the heat release increases, and become less sensitive to the heat release when the latter is large.

5.3 Effect of Variable Properties and Damköhler number

In Secs. 2.3 and 4.3, we showed that the variation of properties through the reacting shear layer influences the mean flow profiles significantly and changes the stability characteristics of the flow. In this section, we study the effect of property variation on the maximum growth rate of high-speed reacting mixing layers. Fig. 5.6 shows the effect of variable properties on the stability characteristics when T_{ad}=8 and M_1=1 (M_c=0.25). The variable property center mode growth rate is two-thirds of its value in the constant property case; however, the maximum growth rate of the outer mode is almost 30% higher. The constant property profile gives center and outer modes with comparable amplification rates, but with the variable property profile, the outer modes dominate.

In the low-speed flow, the variation in the Damköhler number changes the stability at low Damköhler numbers ($Da \leq 1$) but has little effect at high Damköhler numbers ($Da > 1$). Now consider the high-speed flow. Fig. 5.7 shows the maximum growth rate of the unstable modes as a function of Damköhler number at M_1=5 and T_{ad}=4. Because Sec. 4.3 showed that the importance of using the same Damköhler

number in the laminar flow and stability calculations, the Damköhler numbers used in the laminar flow and stability calculation are equal. The growth rates decrease considerably until $Da \simeq 0.5$, after which they rapidly approach the asymptotic high Da value. Increasing Damköhler number stabilizes the flow at low Damköhler numbers but has little effect (it slightly destabilizes) at high Damköhler numbers; this behavior is similar to the low-speed case. These results show that the flame sheet model is valid at high Damköhler numbers ($Da \geq 0.5$) but finite rate chemistry needs to be considered at low Damköhler numbers ($Da < 0.5$).

5.4 Three-Dimensionality

Sandham & Reynolds [1989] reported that the most unstable mode in compressible flows becomes three-dimensional when $M_c > 0.6$. In this section, we study the effect of heat release (T_{ad}=4) on the obliquity of the most amplified mode in high-speed flows (M_1=3, 5).

Fig. 5.8 shows the maximum amplification rates of subsonic disturbances for various angles of propagation at M_1=3 (M_c=0.75). Only the slow mode growth rates are given for readability; the fast mode growth rates are almost same. In a non-reacting mixing layer, the most unstable mode is an oblique center mode (θ=40°) that has growth rate 11% higher than the corresponding two-dimensional mode. Sandham & Reynolds [1989] found that, for the most amplified disturbance,

$$M_c \cos\theta \approx 0.6 \tag{5.3}$$

This relation predicts the most unstable mode to be at 37° for M_c=0.75; our result is in good agreement with this value. In a reacting mixing layer at T_{ad}=4, the outer modes dominate in the two-dimensional case. As the angle increases, the outer modes become stable but the center mode becomes more unstable and its maximum growth rate occurs at θ=50°. However, the growth rate of the most unstable oblique center mode is smaller than those of the two-dimensional outer modes by 20%. Thus the most unstable mode with heat release is two-dimensional. Eq. (5.3) is apparently not applicable in a reacting mixing layer.

Now, we consider a supersonic disturbance at M_1=5 (M_c=1.25). Fig. 5.9 shows the maximum growth rates and phase speeds for both non-reacting (T_{ad}=1) and reacting (T_{ad}=4) flows. In a non-reacting mixing layer, for angles less than about 37°,

the outer modes are dominant and the maximum growth rates change little with angle. They are supersonic unstable modes that have no connection with the generalized inflection points. However, when the angle is greater than 37°, the outer modes disappear and the center mode begins to dominate. The reason for the transition from outer mode dominance to center mode dominance can be understood by examining the relative Mach number, M_r (Eq. (3.29)). For waves propagating at angle θ relative to the x direction, Eqs. (3.29) and (3.30) become

$$M_{r1} = M_1(c-1)\cos\theta, \qquad M_{r2} = \frac{M_1(c-\bar{u}_2)\cos\theta}{\bar{T}_2^{1/2}} \tag{5.4}$$

$$c_u = 1 - \frac{1}{M_1\cos\theta}, \qquad c_l = \bar{u}_2 + \frac{\bar{T}_2^{1/2}}{M_1\cos\theta} \tag{5.5}$$

where c is the phase velocity, ω/α. $c_{u,l}$ are the phase speeds of disturbances that are sonic with respect to the upper and lower streams, respectively ($|M_{r1,2}|$=1). $c_{u,l}$ are plotted in Fig. 5.9b for M_1=5. Because the relative Mach numbers are functions of the propagation angle, there is a possibility of transition from supersonic (regions II, III and IV) to subsonic (region I) disturbances as the angle increases. c_u=c_l defines the smallest transition angle and, for M_1=5, it is about 37°. The center modes in Fig. 5.9b above 37° are subsonic relative to both free streams and may cause the flow to roll up as in incompressible flows. For M_c=1.25 (M_1=5), Eq. (5.3) suggests that the angle of the most unstable mode is 62°, which is very close to the angle of maximum instability of the center mode (65°). The relative Mach number for the most unstable center mode is 0.53 and is subsonic. Note that the maximum growth rate of oblique center modes is much greater than the growth rate of two-dimensional outer modes. Therefore, the most unstable mode is oblique and subsonic for non-reacting flow at M_1=5.

At T_{ad}=4, even though the relative Mach number becomes subsonic with increasing obliquity, the center mode is stabilized by the heat release and only the outer modes are amplified. The latter are inflectional modes whose maximum amplification rates decrease as the obliquity increases. Therefore, heat release makes the dominant mode two-dimensional even in the high Mach number regime. The three-dimensional modes which dominate in the non-reacting case are stable.

Fig. 5.10 shows the variation of the two- and three-dimensional maximum growth rates for the non-reacting flow as functions of the upper stream Mach number M_1.

Two-dimensional growth rates are found by setting θ=0° and three-dimensional ones are obtained by varying θ and finding a maximum. The angle of the most unstable mode is found to increase as the Mach number increases (see Eq. (5.3)). The results show that three-dimensional modes are more amplified than two-dimensional ones for $M_1 > 2.4$ ($M_c > 0.6$), which is consistent with Sandham & Reynolds' results [1989]. All the most unstable oblique modes are subsonic relative to both free streams. Even though the growth rates of the oblique waves are higher than the corresponding two-dimensional ones, they decrease as Mach number increases.

5.5 Effect of Equivalence Ratio

In Sec. 4.3.7, we showed that for low-speed flows with fuel on the fast side, the fuel-lean case (ϕ=0.5) is most unstable for a given adiabatic flame temperature. In this section, we study the effect of equivalence ratio on the stability of high-speed reacting flows; three equivalence ratios, ϕ=0.5, 1, 2 are used at T_{ad}=4 and Da=10. As in previous chapters, we assume that the fast stream is the fuel and the slow stream, the oxidizer. Fig. 5.11 shows the maximum growth rates as a function of the Mach number for various equivalence ratios. The effect of equivalence ratio is large at low Mach numbers. Because any deviation from stoichiometric conditions reduces the total heat release, the stoichoimetric case (ϕ=1) has the lower growth rate than the others (ϕ=0.5, 2). The fuel-lean case (ϕ=0.5) is the most unstable one up to M_1=3.5. At high Mach numbers, the growth rate for the stoichiometric case is larger than the others because heat release now destabilizes the flow (see Sec. 5.2). However, the change in growth rates at high Mach numbers is smaller than at low Mach numbers.

5.6 Eigenfunctions and Streaklines

Figs. 5.12-13 present two-dimensional linear eigenfunctions of the most unstable modes of non-reacting (T_{ad}=1) and reacting (T_{ad}=4) flows at M_1=5 (M_c=1.25). The eigenfunctions are normalized so that the maximum absolute value of $\hat{u}$ is unity. Only the slow supersonic mode is shown; the fast supersonic mode can be obtained by reflection.

The behavior of the pressure and density components of the eigenfunctions on the high-speed side of the non-reacting supersonic slow mode (Figs. 5.12b-c), show

the nature of a supersonic mode. Note that the y axis has been stretched for $\hat{p}$ and $\hat{\rho}$ to better illustrate the damped oscillation. On the low-speed side, the perturbations decay exponentially as $y \rightarrow -\infty$; this is typical subsonic mode behavior. The reacting flow supersonic slow mode shown in Figs. 5.13b-c has similar behavior. However, the density and temperature components of the eigenfunctions are an order of magnitude larger than those in the non-reacting flow. Note that the eigenfunctions of the high-speed reacting flow slow mode (Fig. 5.13) behave similarly to those of the corresponding low-speed mode (Fig. 4.16). Because the slow mode is active principally in the slow part of the mixing layer, it perturbs the fuel distribution much less than the oxidizer distribution; the reverse is true for the fast mode.

From the eigenfunctions and the mean flow, we can construct contours of the flow variables (see Sec. 4.6.8). Fig. 5.14 shows the contours of the flow variables produced by the supersonic slow mode for the non-reacting (T_{ad}=1) flow at M_1=5 (M_c=1.25). Although the supersonic slow mode of the non-reacting flow is not connected with a generalized inflection point (angular momentum maximum), the former induces a single clockwise vortex on the slow side of the layer (Fig. 5.14a). The contours of ω_z/ρ are not very different from the contours of ω_z. The pressure contours in Fig. 5.14c show clearly the radiative nature of the supersonic mode. On the lower side of the layer, which is subsonic relative to the disturbance, the pressure distribution is similar to what is found in incompressible flows. However, the upper side, which is supersonic relative to the disturbance, shows compression (solid lines) and expansion (dashed lines) waves propagating to infinity. The radiation of wave energy to infinity is probably a major cause of the decreased growth rate. To predict the change in vorticity structure, we use the vorticity equations (4.24)-(4.26) for two-dimensional variable density flows. The equations derived in Sec. 4.3.8 are valid in compressible flows. Figs. 5.14e-f show the dilatational and baroclinic terms of Eq. (4.30). In the region near the vortex, both the dilatational and baroclinic terms are negative (dashed contours), and act to reduce the growth of the two-dimensional instability.

Fig. 5.15 gives contours produced by the supersonic slow mode for the reacting flow (T_{ad}=4) at M_1=5 (M_c=1.25). The supersonic slow mode behaves similarly to the supersonic slow mode in the non-reacting flow, although the latter is not connected with an inflection point. Figs. 5.15a-b show that the extrema of ω_z and ω_z/ρ lie well below the center of the layer. The pressure contours in Fig. 5.15c exhibit the radiation of compression (solid lines) and expansion (dashed lines) waves on the upper

side. The dilatational and baroclinic terms in Figs. 5.15e-f are both negative and tend to inhibit the growth of the two-dimensional instability. Figs. 5.15g-h shows the mass fractions of the reactants. The contours are very similar to those caused by the reacting low-speed slow mode (Figs. 4.20g-h). The slow mode principally affects the oxidizer because the oxidizer occupies the lower part of the layer and the fuel the upper part. The fuel distribution is hardly perturbed and the supersonic slow mode does not increase mixing between the reactants very much. Two-dimensional simulations of the compressible reacting mixing layer (Planché & Reynolds [1991]) showed that the above structure is dominant not only in the linear regime but also in the non-linearly developed regime.

In Sec. 5.4, we showed that the most unstable mode in a M_1=5 (M_c=1.25) non-reacting flow, is a center mode with oblique angle θ=65° and that it is subsonic relative to both free streams. To check the subsonic nature of the oblique center mode, we plot linear eigenfunctions and contours of pressure produced by this mode in Fig. 5.16. Fig. 5.16a shows the exponential decay of the perturbed pressure as y goes to $\pm\infty$; similar behavior was found in the incompressible flow (Fig. 4.14b). The pressure contours are similar to the ones in subsonic flows in Fig. 4.18b and show no pressure wave propagation toward the boundaries. This flow is similar to a subsonic flow in many ways.

In Sec. 4.3.9, we calculated the streaklines for the most unstable two-dimensional modes and suggested that the reacting outer modes would not increase mixing between the reactants. We followed the same procedure and obtained streaklines for the high Mach number flow. Figs. 5.17-18 show the streaklines at M_1=5 (M_c=1.25) for the cold flow (T_{ad}=1) and the reacting flow (T_{ad}=4), respectively, and Fig. 5.19 shows the flow patterns produced by the combined outer modes. As in low-speed reacting flows, the slow mode mainly disturbs the lower part of the mixing layer, whereas the upper part remains undisturbed. The reverse is true for the fast mode. The flow patterns show that the mixing layer with supersonic disturbances will not roll up in the same way in an incompressible cold flow, which is consistent with two-dimensional simulations by Planché & Reynolds [1991]. In particular, mixing of the fuel and oxidizer will be reduced.

5.7 Convective Mach Number

This section considers the possible use of the convective Mach number as a mean of characterizing compressible flows. We first review the definitions of the convective Mach numbers and then check their usefulness for non-reacting and reacting mixing layers.

5.7.1 *Definitions*

The large number of parameters needed to describe them, including free stream Mach number, temperature ratio, velocity ratio and chemical reaction rate, make the stability characteristics of compressible flows very complicated. Use of the convective Mach number has been suggested as a way of collapsing the growth-rate data onto one curve. Since Bogdanoff [1983] first proposed this concept, several definitions have been given. The best known definition of M_c is based on the velocity of a reference frame convecting with large structures of the mixing layer (Bogdanoff [1983]; Papamoschou & Roshko [1988]). In that reference frame, the convective Mach numbers of the free streams are

$$M_{c1} = \frac{U_1^* - U_c^*}{c_1^*}, \qquad M_{c2} = \frac{U_c^* - U_2^*}{c_2^*} \tag{5.6}$$

where U_c^* is the convective velocity of the large structure, U_1^* and U_2^* are the free stream velocities, and c_1^* and c_2^* the sound speeds in the free streams. In incompressible flows, in a frame moving at U_c^*, there is a stable stagnation point in the braid region. If we assume the existence of a similar point in the compressible flow, that the dynamic pressures on the two sides of the stagnation point are equal and that the process is isentropic, one can compute U_c^* (Papamoschou & Roshko [1988]). For gases with equal specific heat ratio, U_c^* and M_c are

$$U_c^* = \frac{U_1^* c_2^* + U_2^* c_1^*}{c_1^* + c_2^*}, \qquad M_c = M_{c1} = M_{c2} = \frac{U_1^* - U_2^*}{c_1^* + c_2^*} = \frac{M_1(1 - \bar{u}_2)}{1 + \sqrt{\bar{T}_2}} \tag{5.7}$$

For equal free stream static pressures, U_c^* reduces to the incompressible expression. Papamoschou and Roshko suggested that the growth rate of a compressible shear layer normalized by the growth rate of an incompressible shear layer might be a function

solely of the convective Mach number for a wide range of velocity and temperature ratios. They showed that the normalized growth rate of turbulent free shear layers decreases with increasing convective Mach number. Recently, Ragab & Wu [1988] studied the influence of the velocity ratio on stability characteristics of a compressible shear layer found that the convective Mach number does correlate compressibility effects on the growth rate.

A second definition takes the convective velocity to be the phase velocity of the most unstable mode according to linear stability theory. This was proposed by Mack [1975] for compressible boundary layers and later used by Zhuang *et al.* [1988, 1990] for compressible shear layers. The convective Mach number for the two free streams can be written as

$$\hat{M}_{c1} = \frac{U_1^* - c_r^*}{c_1^*} = M_1(1 - c_r), \qquad \hat{M}_{c2} = \frac{c_r^* - U_2^*}{c_2^*} = \frac{M_1(c_r - \bar{u}_2)}{\sqrt{\bar{T}_2}} \tag{5.8}$$

where c_r^* is the phase velocity of the most unstable mode. The convective Mach numbers of Eqs. (5.8) and (5.9) are identical when the dominant mode is the center mode and $\bar{T}_2$=1, because the large structures then move with the phase speed of the center mode which is also the average speed of the two free stream velocities. When the outer modes dominate due to heat release or compressibility, the isentropic convective velocity remains the center mode phase velocity but the convective velocity based on the most unstable mode becomes the phase velocity of the outer modes, and, therefore, convective Mach numbers of Eqs. (5.7) and (5.8) become different. We should note that the convective Mach number of Eq. (5.8) is identical to the relative Mach number (Eq. (3.29)), the Mach number of the disturbance relative to the free-streams. Zhuang *et al.* [1988], who used the convective Mach number based on the most unstable mode, compared their results with those of Ragab & Wu [1988] who used the insentropic convective Mach number. Even though the difference in supersonic convective Mach numbers is not small, the comparison showed a good agreement in the normalized growth rates because they change little at supersonic convective Mach numbers.

Fig. 5.20 compares the convective Mach numbers based on Eqs. (5.7) and (5.8) at $\bar{T}_2$=1 for non-reacting (T_{ad}=1) and reacting (T_{ad}=4) flows. In Eq. (5.8), the phase velocities of the most unstable modes obtained from linear stability analysis based on laminar flows computed from compressible boundary-layer equations are

used. Because Eq. (5.7) does not consider the effect of heat release, the isentropic convective Mach numbers of non-reacting and reacting flows are the same. However, the convective Mach numbers of Eq. (5.8) for non-reacting and reacting flows are different because the phase speeds of the most unstable modes are different.

For the non-reacting flow, the two dominant outer modes have almost the same growth rates but different phase velocities when $M_{c1}, \hat{M}_{c1} > 1$ (see Fig. 5.2). Thus, $\hat{M}_c$ of Eq. (5.8) become different from M_c of Eq. (5.7) at supersonic convective Mach numbers. For the convective Mach numbers based on Eq. (5.8), we should note that if one convective Mach number ($\hat{M}_{c1}$) is supersonic, the other ($\hat{M}_{c2}$) is subsonic and *vice versa*, which agrees with the recent measurements of convective Mach numbers by Papamoschou [1989]. These results contradicts the isentropic model which requires the two convective Mach numbers to be equal (see Eq. (5.7)). His experiments revealed that in highly compressible flows, the convective velocity, U_c^* approaches U_1^* or U_2^*. Therefore, Papamoschou [1989] and Dimotakis [1989] suggested that shocks may exist on only one side of shear layer and that the associated asymmetric losses in total pressure may be responsible for the asymmetries of the observed convective velocity, U_c^*. Although two-dimensional simulations of compressible mixing layers (Lele [1989], Sandham & Reynolds [1989]) showed the development of weak shock waves situated near the large-scale two-dimensional vortices, three-dimensional simulations (Sandham & Reynolds [1991]) found no shock waves at Mach numbers at which shock waves formed in two-dimensional simulations; this is consistent with experimental observations that have not detected shock waves (Hall *et al.* [1991]).

In reacting flows, the outer modes dominate the center modes even at low Mach numbers due to density variation. The convective Mach number of Eq. (5.8) then becomes different from the isentropic convective Mach number even at subsonic convective Mach numbers. Note that the convective Mach numbers of Eq. (5.8) are different for reacting flows than non-reacting flows at the same velocity and temperature ratios, which causes doubt on the validity of using the convective Mach number concept for reacting flows.

Planché & Reynolds [1991] introduced the flame convective Mach number to include the effects of chemical reaction. They assumed that all the chemical reaction occurs at a flame sheet and an isentropic process occurs between the free streams and the flame sheet. Following the arguments of Papamoschou & Roshko [1988], they

derived a fast flame convective Mach number, M_{f1}, and a slow flame convective Mach number, M_{f2}:

$$M_{f1} = \frac{\bar{u}_1 - \bar{u}_f}{\bar{u}_1 - \bar{u}_2}\left(\frac{\sqrt{T_1} + \sqrt{T_2}}{\sqrt{T_1} + \sqrt{T_f}}\right) M_c, \qquad M_{f2} = \frac{\bar{u}_f - \bar{u}_2}{\bar{u}_1 - \bar{u}_2}\left(\frac{\sqrt{T_1} + \sqrt{T_2}}{\sqrt{T_f} + \sqrt{T_2}}\right) M_c \quad (5.9)$$

where $\bar{u}_f$ and $\bar{T}_f$ are the velocity and temperature at the flame sheet and M_c is the convective Mach number defined by Papamoschou & Roshko. M_{f1} and M_{f2} are usually different and they suggested that compressibility effects can be significantly different for the two outer modes. However, since their flame convective Mach number is based on the existence of three distinct mean angular momentum maxima, the validity is questionable at supersonic convective Mach numbers where only one maximum exists but outer modes exist.

5.7.2 *Universal Dependence of the Growth Rate*

This section investigates whether the normalized growth rates of compressible mixing layers can be made universal by use of convective Mach number. Fig. 5.21 shows the normalized maximum growth rates of non-reacting compressible mixing layers for various temperature ratios as functions of the isentropic convective Mach number (Eq. (5.7) and the convective Mach number based on the most unstable mode (Eq. (5.8)). The growth rates have been normalized by incompressible growth rates at the same velocity and temperature ratios to isolate the effect of compressibility:

$$R(M) = \frac{-\alpha_{imax}(M, \bar{u}_2, \bar{T}_2)}{-\alpha_{imax}(0, \bar{u}_2, \bar{T}_2)} \quad (5.10)$$

where M is either M_c or $\hat{M}_c$. The results validate use of the isentropic convective Mach number as a compressibility parameter. The normalized maximum amplification rates decrease significantly with increasing M_c ($\hat{M}_c$) in the region $M_c < 1$ ($\hat{M}_c < 1$); in this regime, the convective Mach numbers are nearly identical. For $M_c > 1$ ($\hat{M}_c > 1$), there is some scatter in the data. However, since the normalized growth rates change little with convective Mach number for $M_c > 1$ ($\hat{M}_c > 1$), although the difference between M_c and $\hat{M}_c$ is not small, one can correlate with one or the other. Thus,

either M_c or $\hat{M}_c$ can be used as an overall measure of shear layer compressibility for non-reacting flows.

The maximum amplification rate $|\alpha_i|_{max}$ is linearly related to the growth rate of the shear layer thickness $d\delta/dx$ (Morkovin [1988]; Sandham & Reynolds [1989]). We plot the normalized two- and three-dimensional growth rates from the current study versus the isentropic convective Mach number, M_c, in Fig. 5.22, along with experimental data. It shows that present results agree well with the experimental trend that growth rates decrease with increasing convective Mach number but the large spread in the experimental data prevents a definitive comparison. As expected, the three-dimensional growth rates from the current study show better agreement with the experimental data at high Mach numbers than two-dimensional ones. Note that three-dimensional growth rates of instabilities decrease as the Mach number increases but the experimental data by Papamoschou & Roshko [1988] approach an asymptotic value.

In order to see whether convective Mach number can correlate shear layer compressibility in reacting mixing layers, we normalized maximum growth rates for various temperature ratios and adiabatic flame temperatures by incompressible growth rates at the same velocity and temperature ratios and adiabatic flame temperatures to isolate the effect of compressibility:

$$R(M) = \frac{-\alpha_{imax}(M, \bar{u}_2, \bar{T}_2, T_{ad})}{-\alpha_{imax}(0, \bar{u}_2, \bar{T}_2, T_{ad})} \tag{5.11}$$

where M is M_c, $\hat{M}_c$ or M_f. Fig. 5.23 shows the normalized growth rates versus the three convective Mach numbers. The results show that the growth rates do not collapse with either isentropic convective Mach number or the one based on the most unstable mode. Although the flame convective Mach number (Fig. 5.23c) correlates the data better than the others, the discrepancy is as large as 30%. Therefore, the flame convective Mach number appears not to be a universal parameter for expressing compressibility effects in reacting mixing layers with finite rate chemistry because the combustion process must be non-isentropic.

5.8 Chapter Summary

In this chapter, we considered the inviscid stability of compressible reacting mixing layers. The calculations are based on laminar flow profiles generated by solving the compressible boundary-layer equations with finite rate chemistry. We found that supersonic unstable modes may exist in the absence of a generalized inflection point, provided that a region of laminar flow is supersonic relative to the disturbance phase velocity. The growth rate decreases with increasing Mach number. At supersonic Mach numbers, the outer modes dominate. Heat release stabilizes low-speed flows but destabilizes high-speed flows. However, all growth rates are small compared to the incompressible cold flow value. For non-reacting supersonic flows at $M_c > 0.6$, the most unstable modes are oblique center modes that are subsonic relative to both free streams. For reacting flows with $T_{ad} > 3$, the most unstable modes are two-dimensional outer modes even at high Mach numbers. The radiative nature of supersonic disturbances is demonstrated by the pressure contours; the radiation of energy is one reason for the decreased growth rates. Supersonic disturbances do not mix the reactants very well because they are largely confined to one side of the flow. For reacting flows, the growth rates normalized by the corresponding incompressible growth rates are not functions of the convective Mach number alone, so the latter cannot be used as an overall measure of shear layer compressibility. However, the flame convective Mach number appears to give the best collapse.

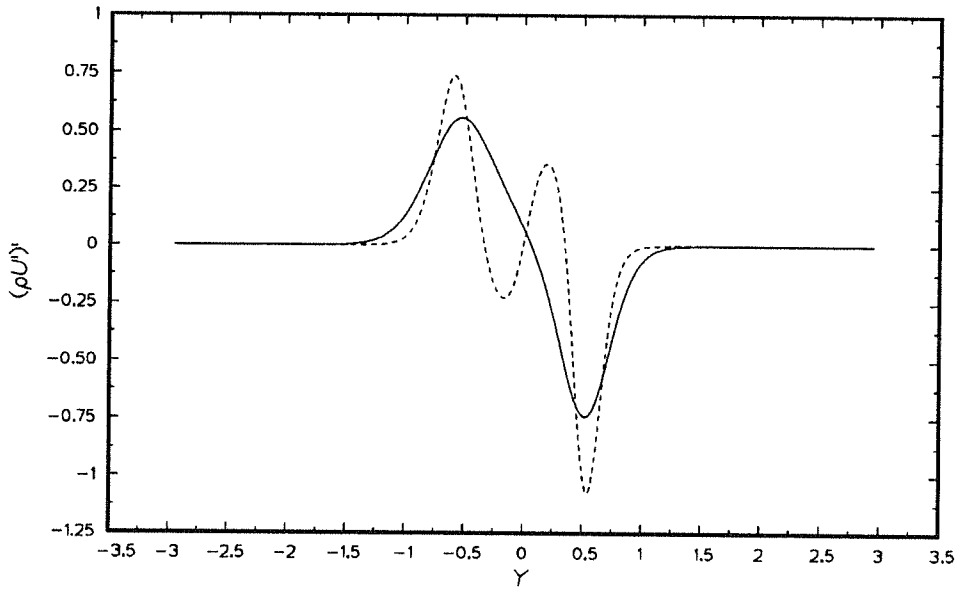

FIGURE 5.1. $(\bar{\rho}\bar{u}')'$ in the laminar flow. M_1=5, $\bar{T}_2$=1. —— , T_{ad}=1; ---- , T_{ad}=4.

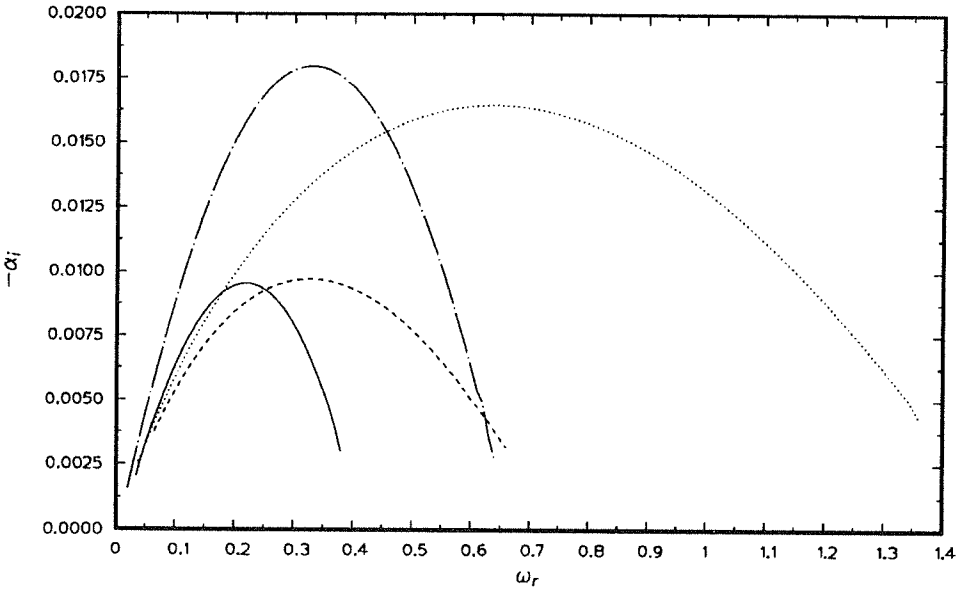

(a)

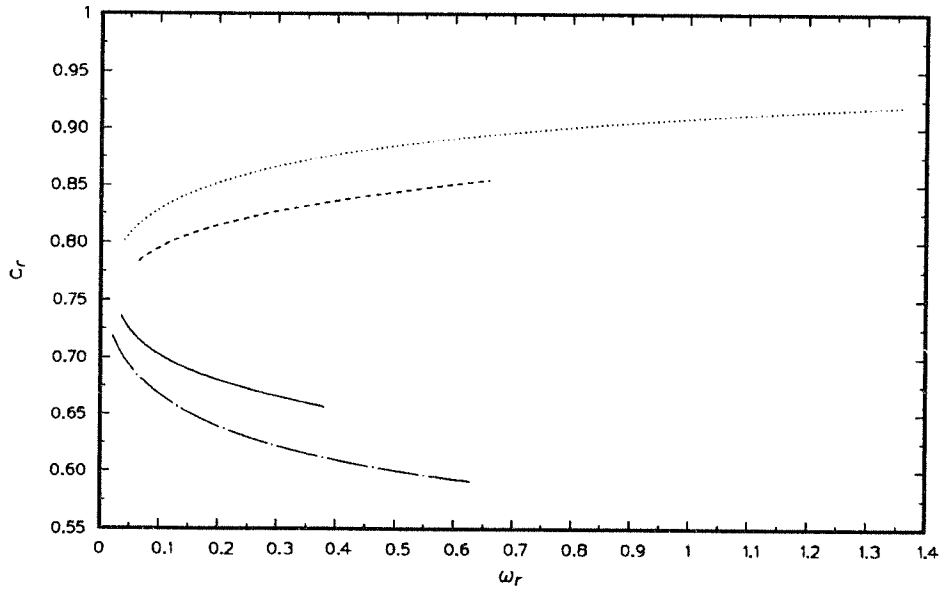

(b)

FIGURE 5.2. The multiple instability modes in the compressible flow. (a) growth rate (b) phase velocity. M_1=5, $\bar{T}_2$=1, β=0. —— , slow mode (T_{ad}=1); ---- , fast mode (T_{ad}=1); —·— , slow mode (T_{ad}=4); ····· , fast mode (T_{ad}=4).

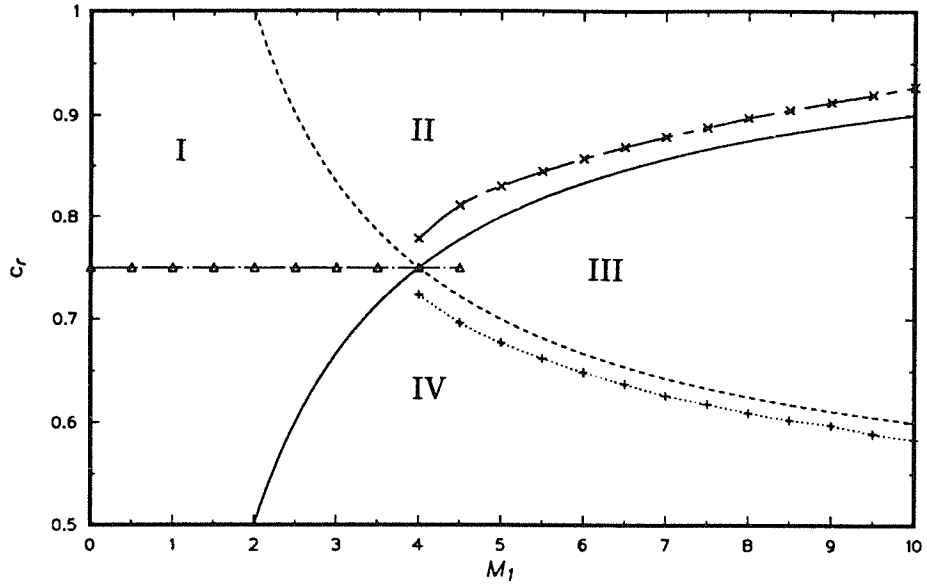

(a)

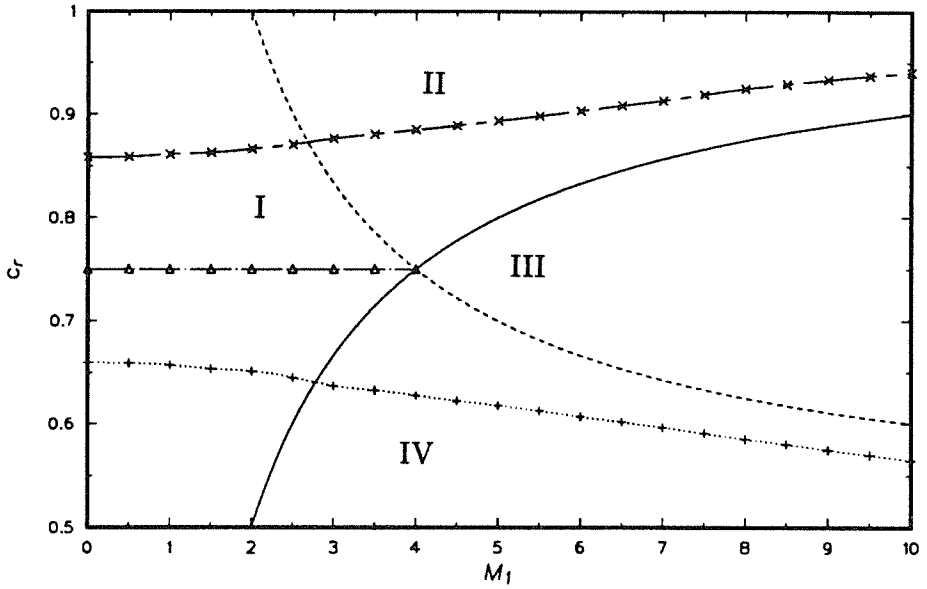

(b)

FIGURE 5.3. Phase speeds of the most unstable modes versus Mach number. (a) non-reacting flow (T_{ad}=1) (b) reacting flow (T_{ad}=4). $\bar{T}_2$=1, β=0. —— , c_u; ---- , c_l; $\triangle$, center mode; +, slow mode; $\times$, fast mode.

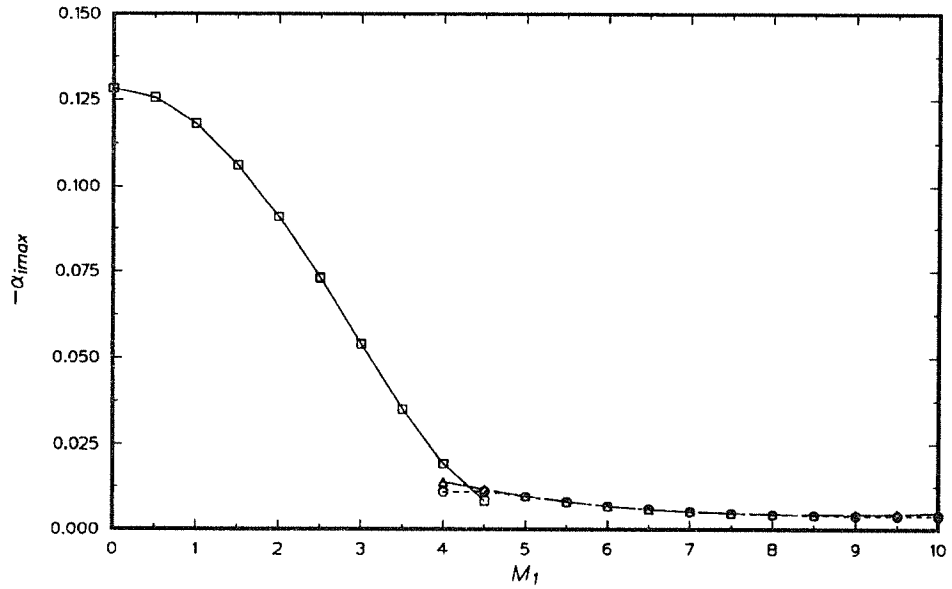

(a)

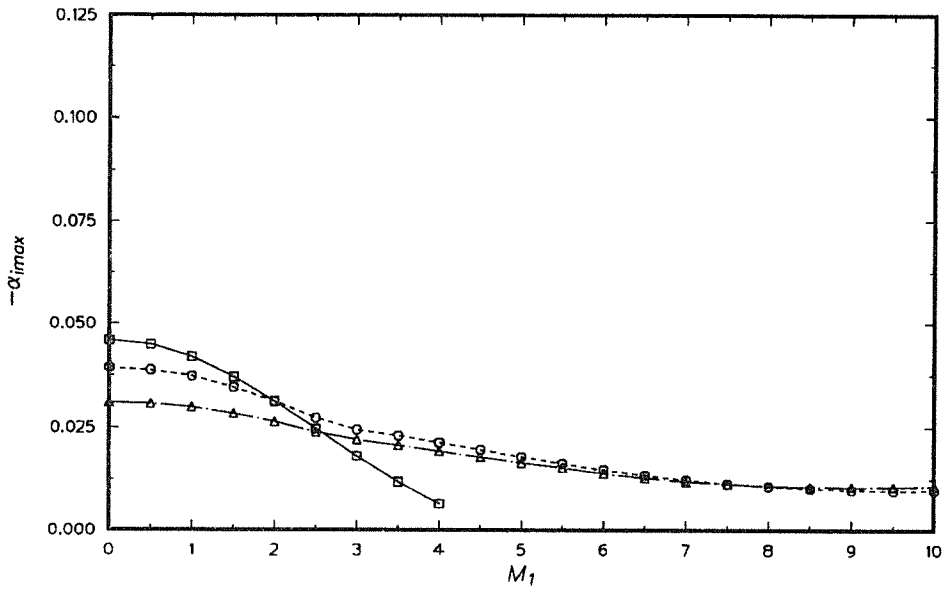

(b)

FIGURE 5.4. Maximum growth rates versus Mach number. (a) non-reacting flow (T_{ad}=1) (b) reacting flow (T_{ad}=4). $\bar{T}_2$=1, β=0. ▫ , center mode; ○ , slow mode; △ , fast mode.

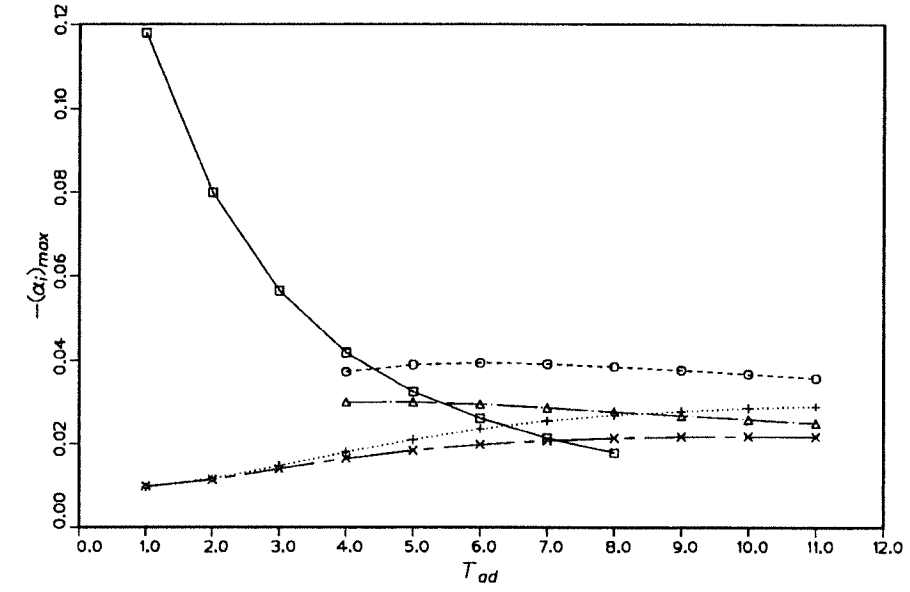

(a)

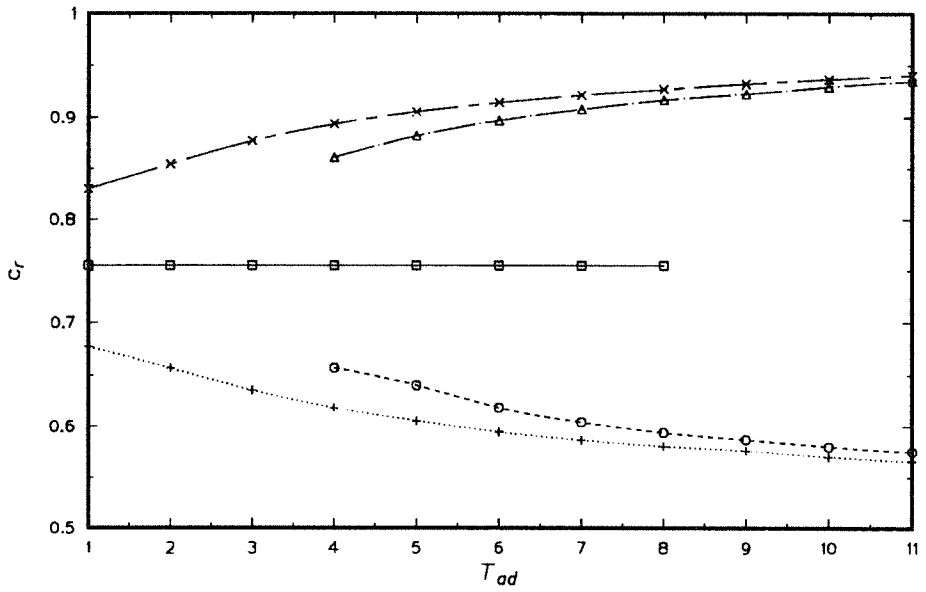

(b)

FIGURE 5.5. (a) Maximum growth rate and (b) corresponding phase velocity versus adiabatic flame temperature. $\bar{T}_2$=1, β=0. ▫ , M_1=1 (center mode); ○ , M_1=1 (slow mode); △ , M_1=1 (fast mode); +, M_1=5 (slow mode); ×, M_1=5(fast mode).

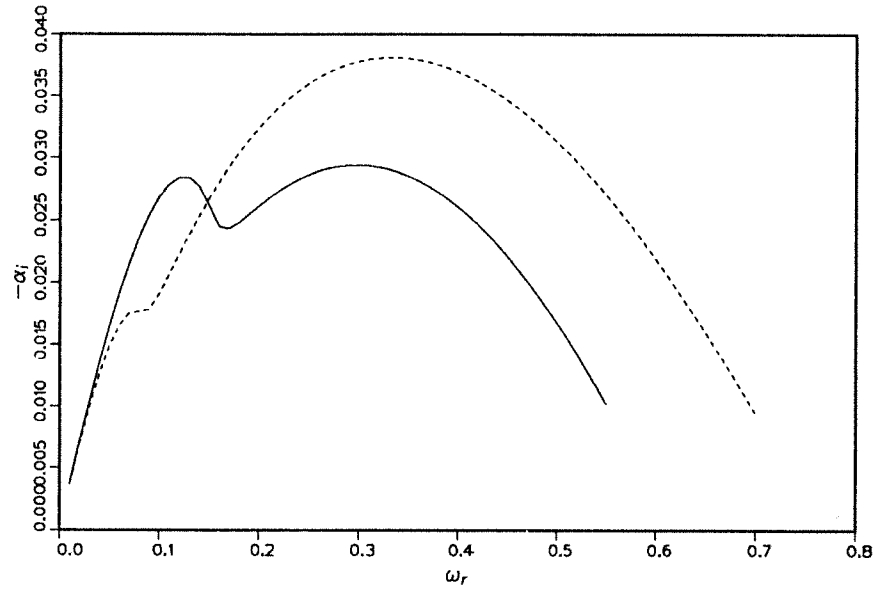

FIGURE 5.6. Effect of variation of properties on the growth rate. T_{ad}=8, M_1=1, $\bar{T}_2$=1, β=0. ——— , constant property; ---- , variable property.

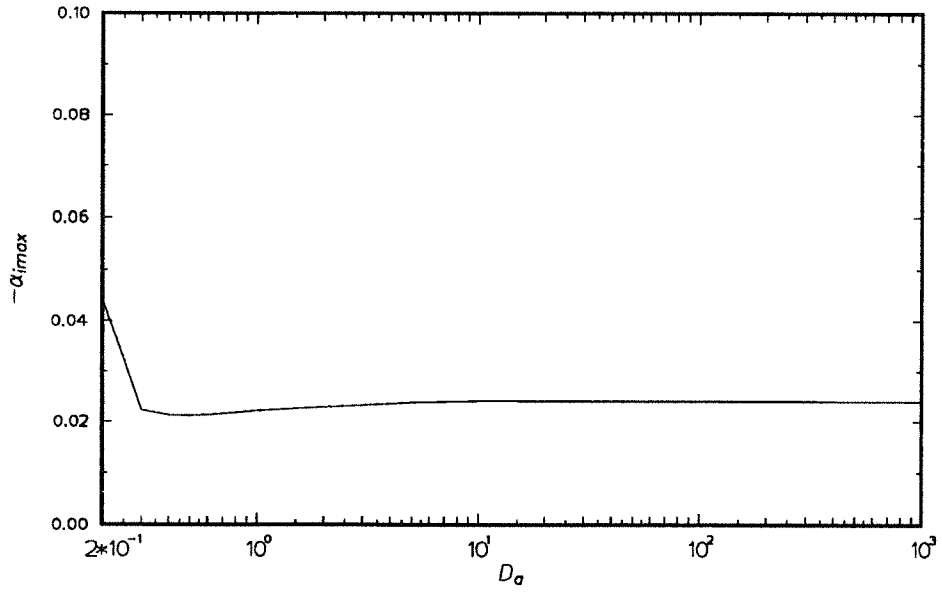

FIGURE 5.7. Maximum growth rate versus Damköhler number. M_1=5, $\bar{T}_2$=1, T_{ad}=4, β=0.

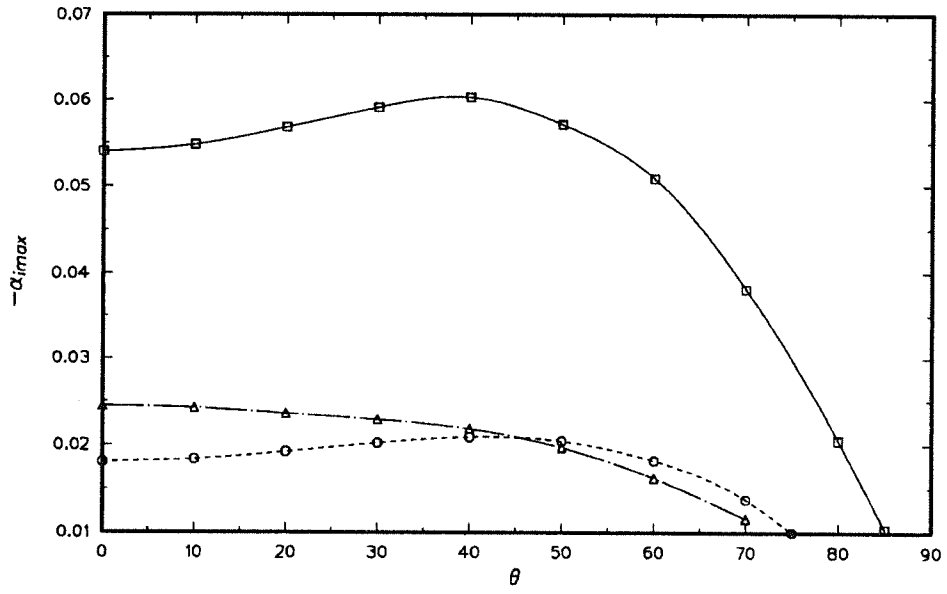

FIGURE 5.8. Maximum growth rate versus obliqueness angle at M_1=3 (M_c=0.75) and $\bar{T}_2$=1. □ , T_{ad}=1 (center mode); ○ , T_{ad}=4 (center mode); △ , T_{ad}=4 (slow mode).

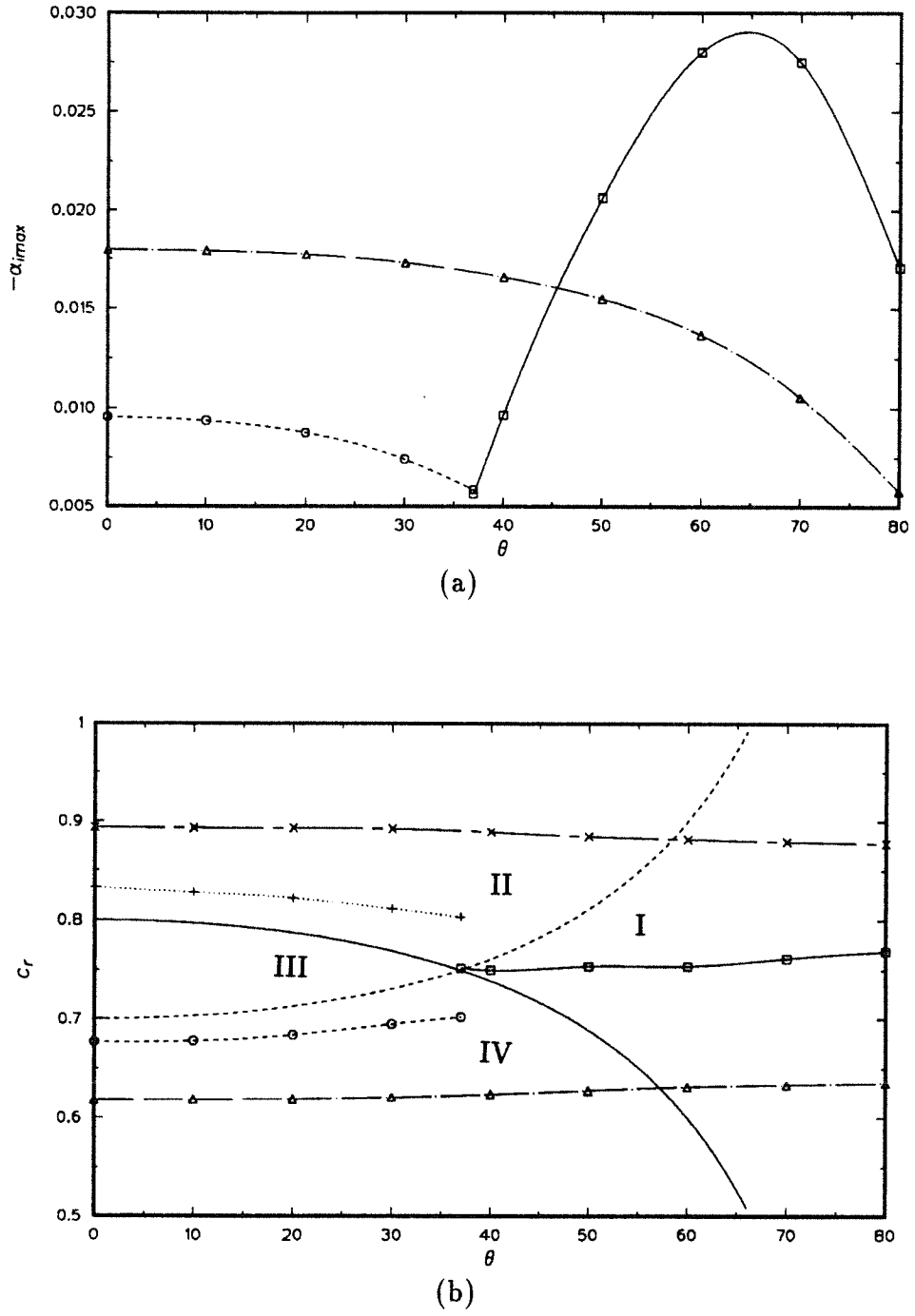

FIGURE 5.9. (a) Maximum growth rate versus oblique angle and (b) corresponding phase velocity. M_1=5 (M_c=1.25), $\bar{T}_2$=1. —— , c_u; ---- , c_l. ▫ , T_{ad}=1 (center mode); ○ , T_{ad}=1 (slow mode); +, T_{ad}=1 (fast mode); △ , T_{ad}=4 (slow mode); ×, T_{ad}=4 (fast mode).

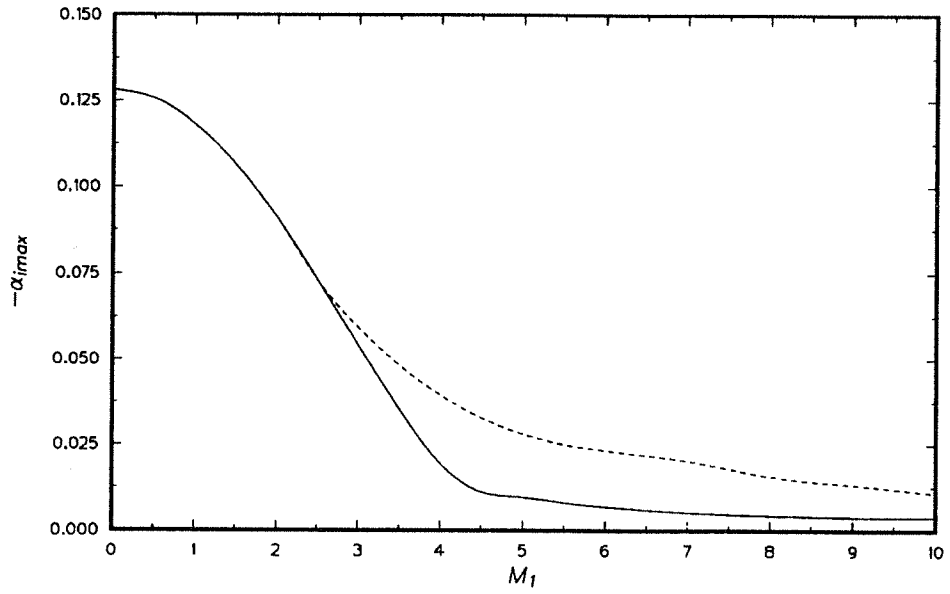

FIGURE 5.10. Two- and three-dimensional maximum growth rate versus Mach number for non-reacting flows. T_{ad}=1, $\bar{T}_2$=1. —— , two-dimensional; ---- , three-dimensional.

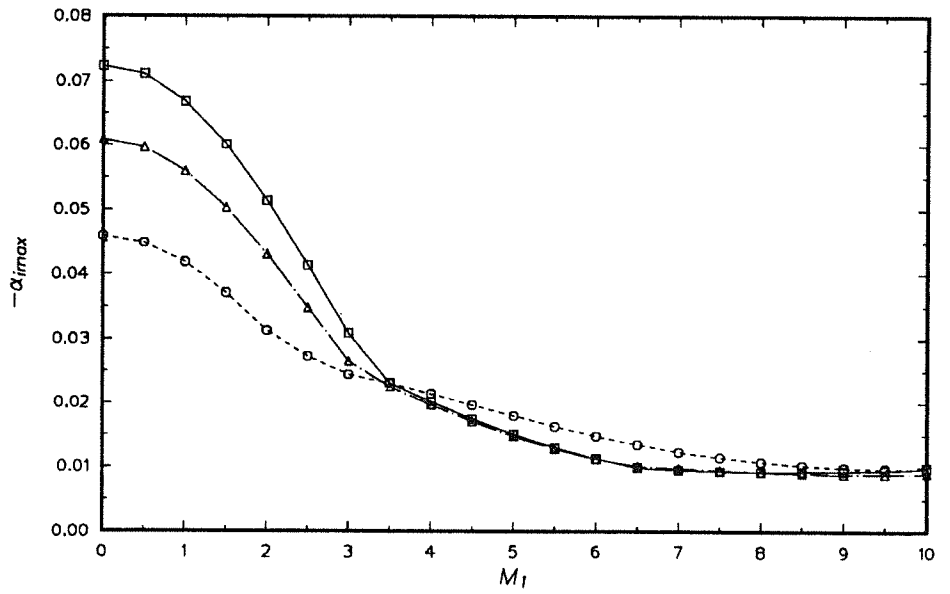

FIGURE 5.11. Effect of equivalence ratio on maximum growth rate. T_{ad}=4, $\bar{T}_2$=1, β=1. □ , ϕ=0.5; ○ , ϕ_2=1; △ , ϕ=2.

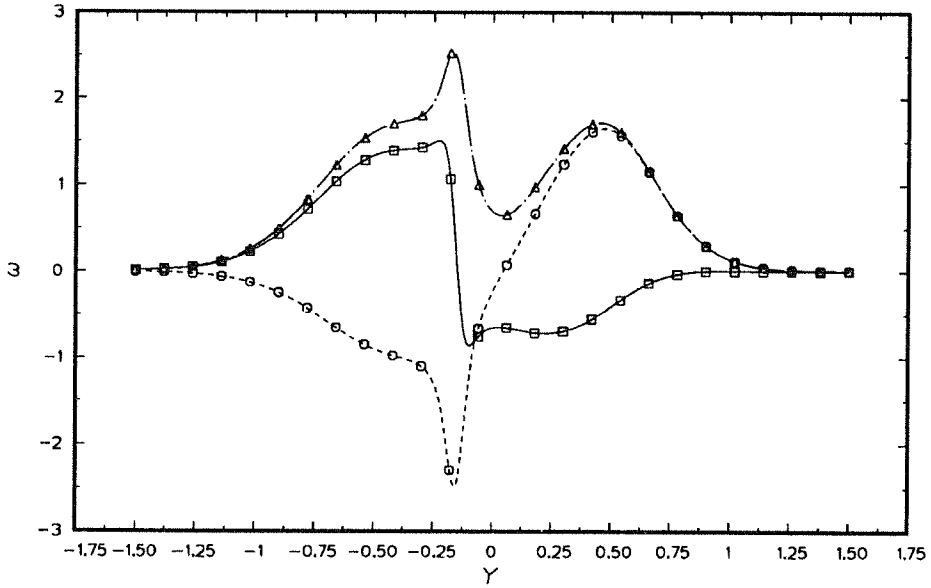

(a)

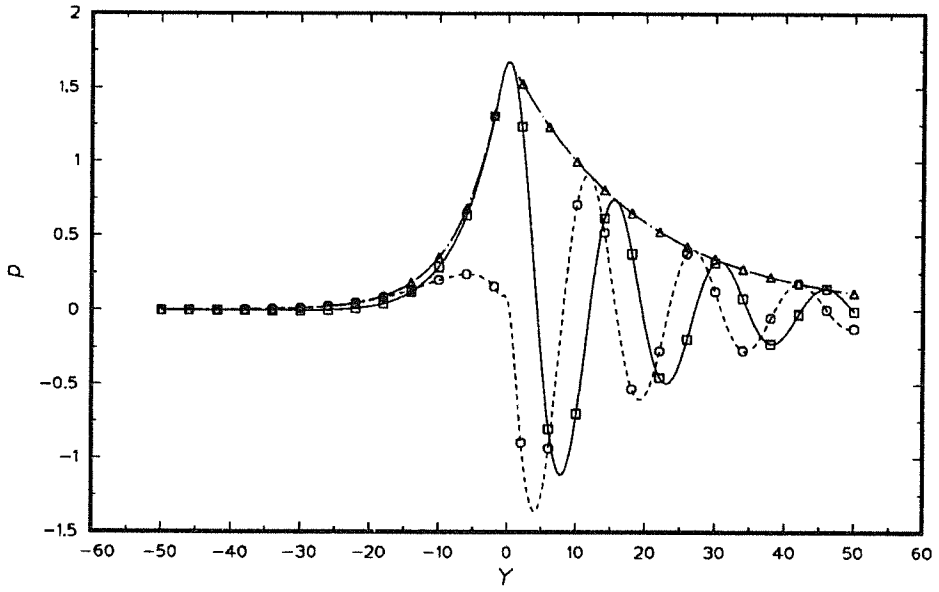

(b)

FIGURE 5.12. Continued.

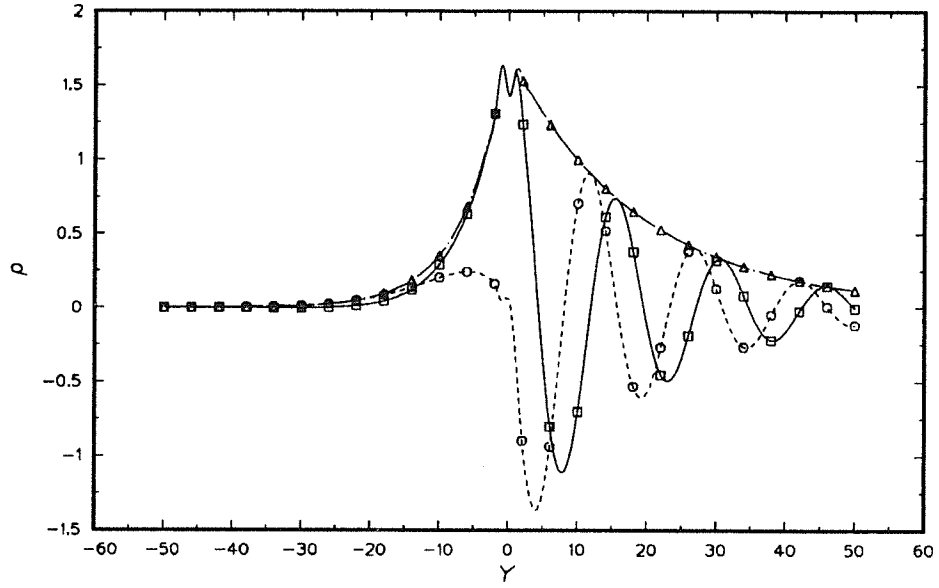

(c)

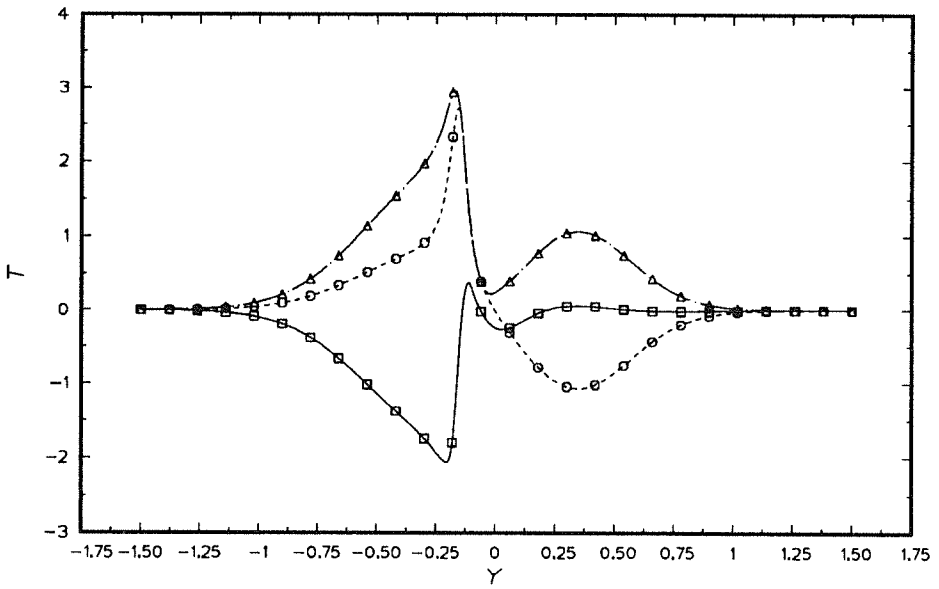

(d)

FIGURE 5.12. Linear eigenfunctions of the non-reacting flow (slow mode) (a) $\hat{\omega}_z$ (b) $\hat{p}$ (c) $\hat{\rho}$ (d) $\hat{T}$. M_1=5 (M_c=1.25), $\bar{T}_2$=1, T_{ad}=1, β=0. ▫ , real; ○ , imaginary; △ , absolute.

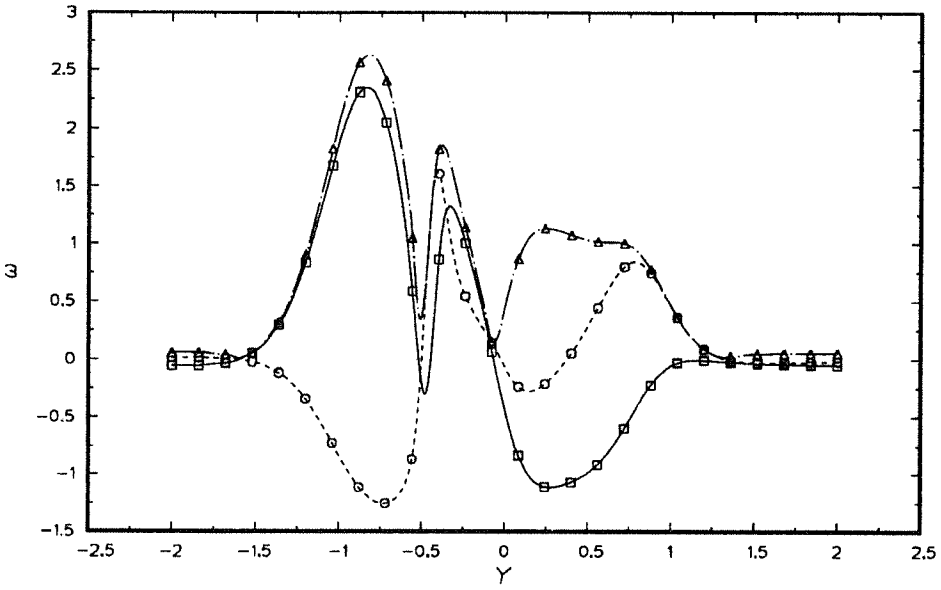

(a)

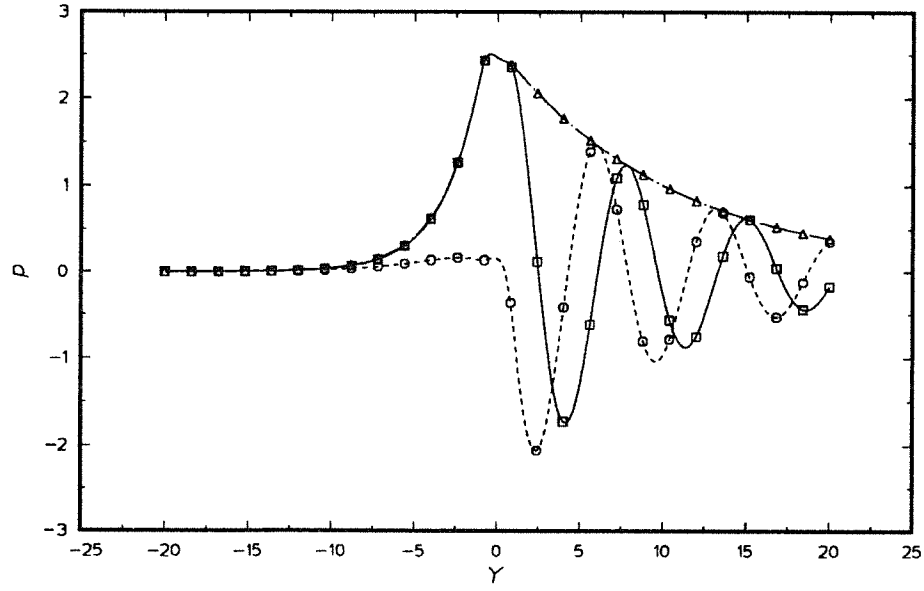

(b)

FIGURE 5.13. Continued.

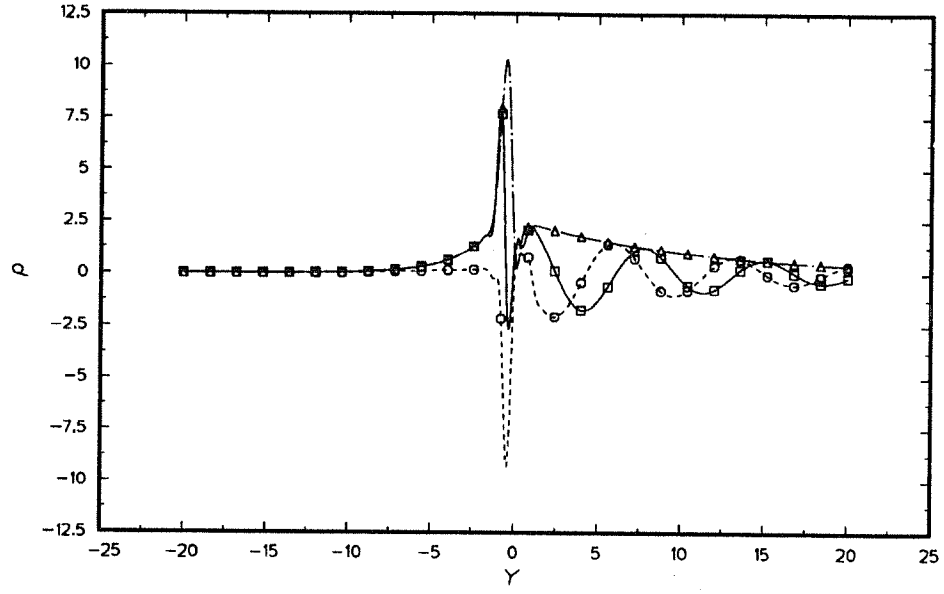

(c)

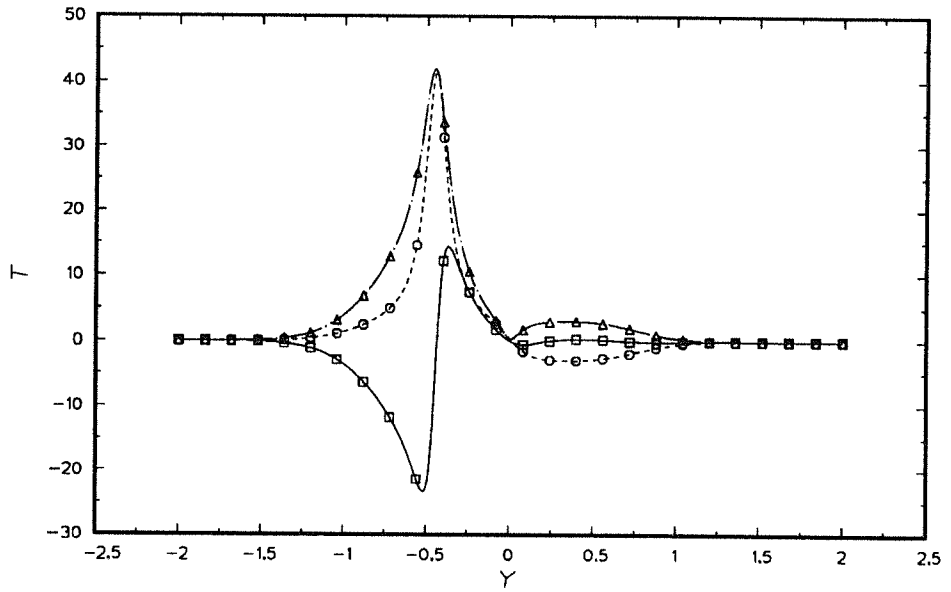

(d)

FIGURE 5.13. Continued.

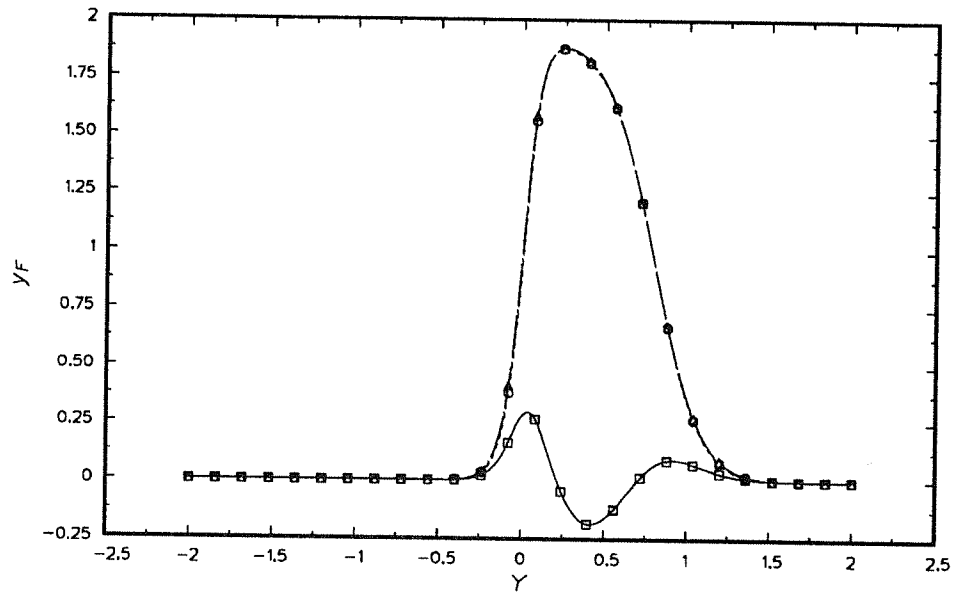

(e)

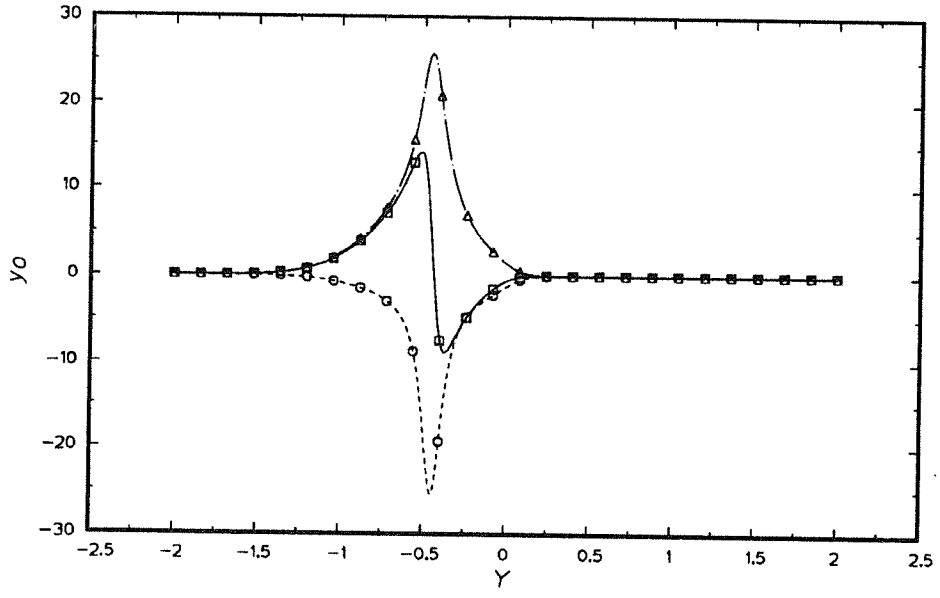

(f)

FIGURE 5.13. Linear eigenfunctions of the reacting flow (slow mode) (a) $\hat{\omega}_z$ (b) $\hat{p}$ (c) $\hat{\rho}$ (d) $\hat{T}$ (e) $\hat{y}_F$ (f) $\hat{y}_O$. M_1=5 (M_c=1.25), $\bar{T}_2$=1, T_{ad}=4, β=0, Da=10. □ , real; ○ , imaginary; △ , absolute.

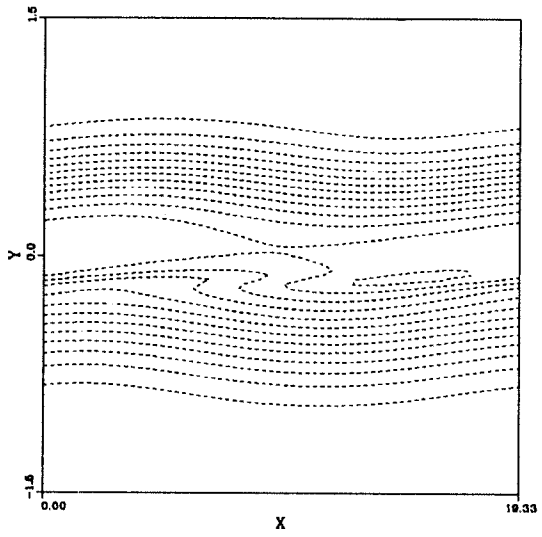

(a) max=8.56x10^{-4}, min=-0.266

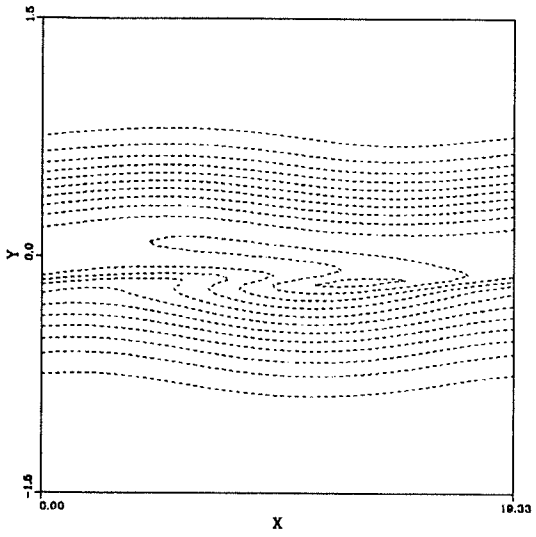

(b) max=8.58x10^{-4}, min=-0.367

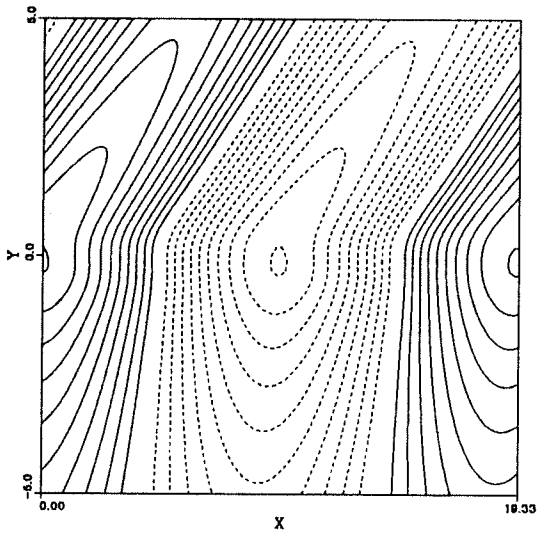

(c) max=1.05, min=0.95

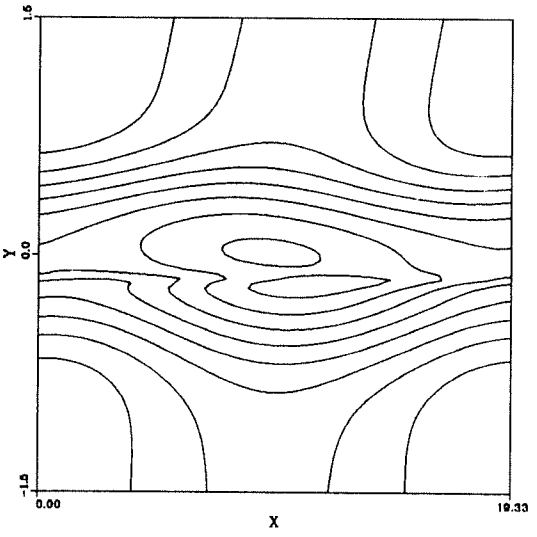

(d) max=1.05, min=0.702

FIGURE 5.14. Continued.

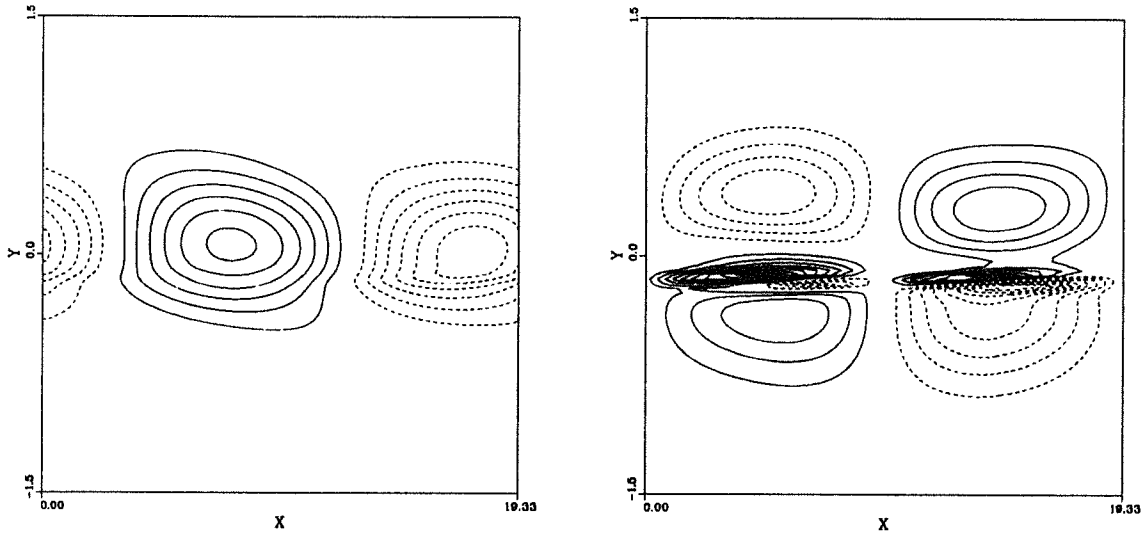

(e) max=1.27x10^{-3}, min=-1.35x10^{-3} (f) max=9.56x10^{-3}, min=-8.87x10^{-3}

FIGURE 5.14. Contour plots from linear eigenfunctions of the non-reacting flow (slow mode). (a) ω_z (b) ω_z/ρ (c) pressure (d) density (e) dilatation term (f) baroclinic term. M_1=5 (M_c=1.25), $\bar{T}_2$=1, T_{ad}=1, β=0.

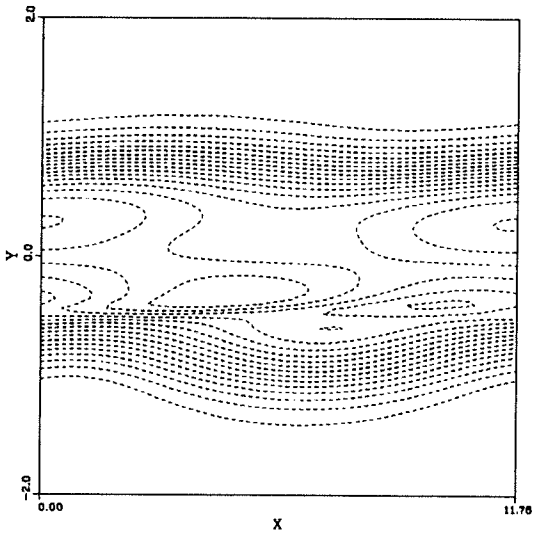

(a) max=$2.55\text{x}10^{-4}$, min=-0.171

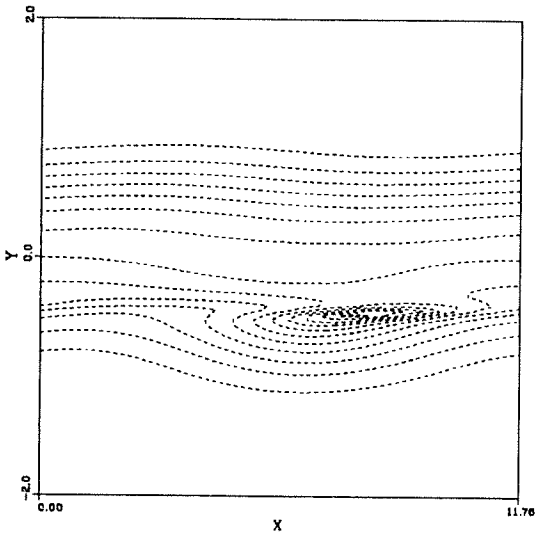

(b) max=$2.43\text{x}10^{-4}$, min=-0.564

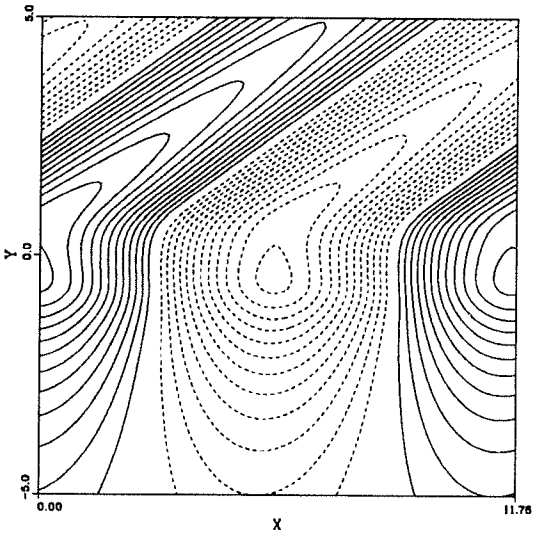

(c) max=1.062, min=0.938

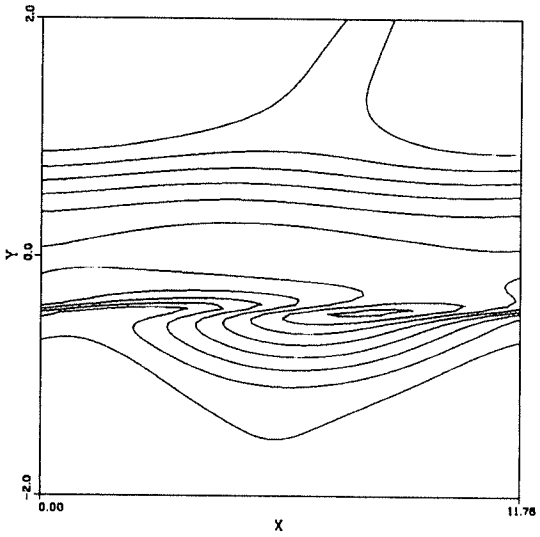

(d) max=1.055, min=0.228

FIGURE 5.15. Continued.

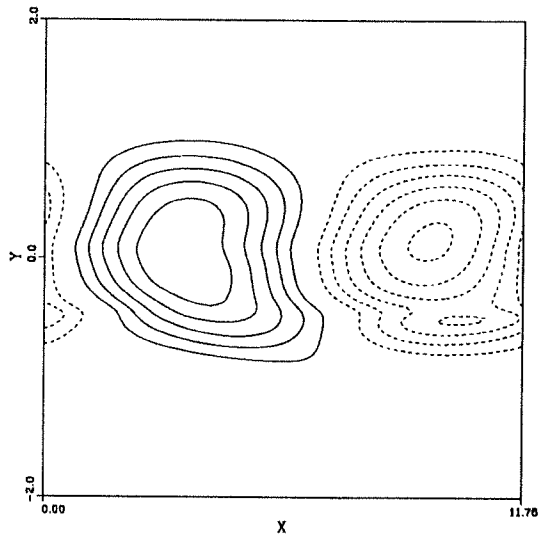

(e) max=$1.2\text{x}10^{-3}$, min=$-1.25\text{x}10^{-3}$

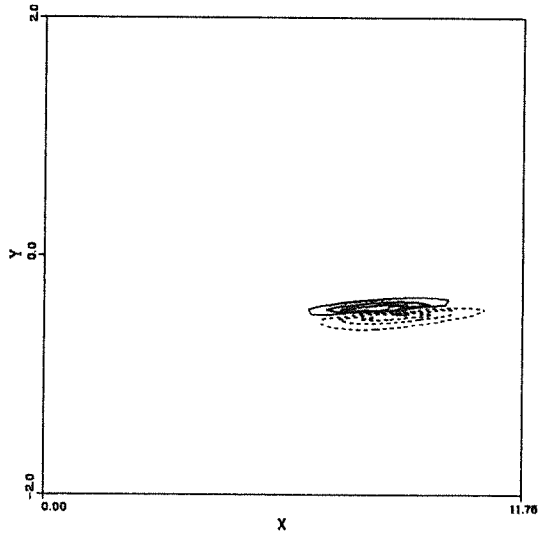

(f) max=0.403, min=-0.414

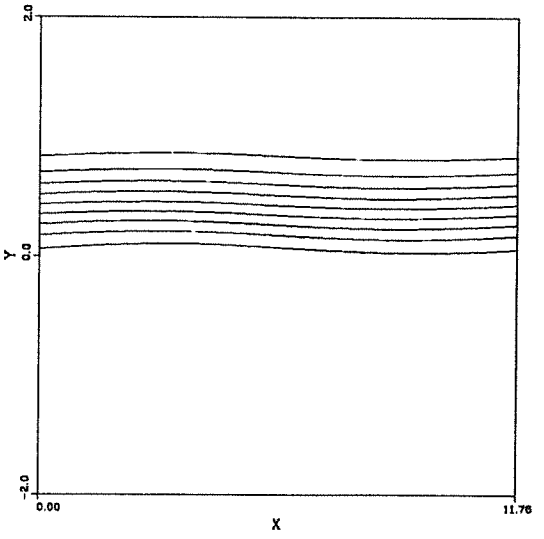

(g) max=1.0, min=0.0

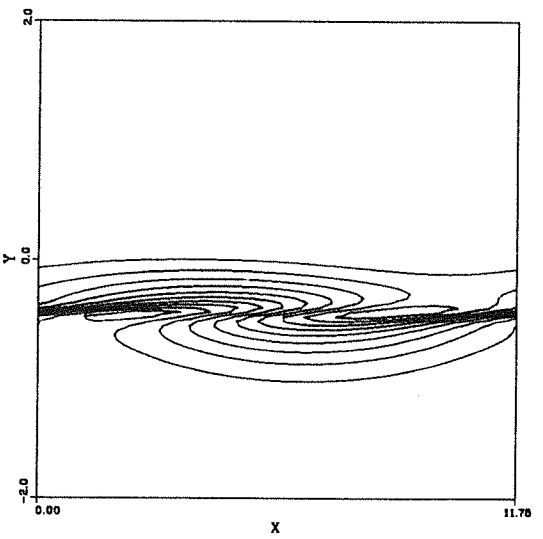

(h) max=1.0, min=0.0

FIGURE 5.15. Contour plots from linear eigenfunctions of the reacting flow (slow mode). (a) ω_z (b) ω_z/ρ (c) pressure (d) density (e) dilatation term (f) baroclinic term (g) fuel (h) oxidizer. M_1=5 (M_c=1.25), $\bar{T}_2$=1, T_{ad}=4, β=0, Da=10.

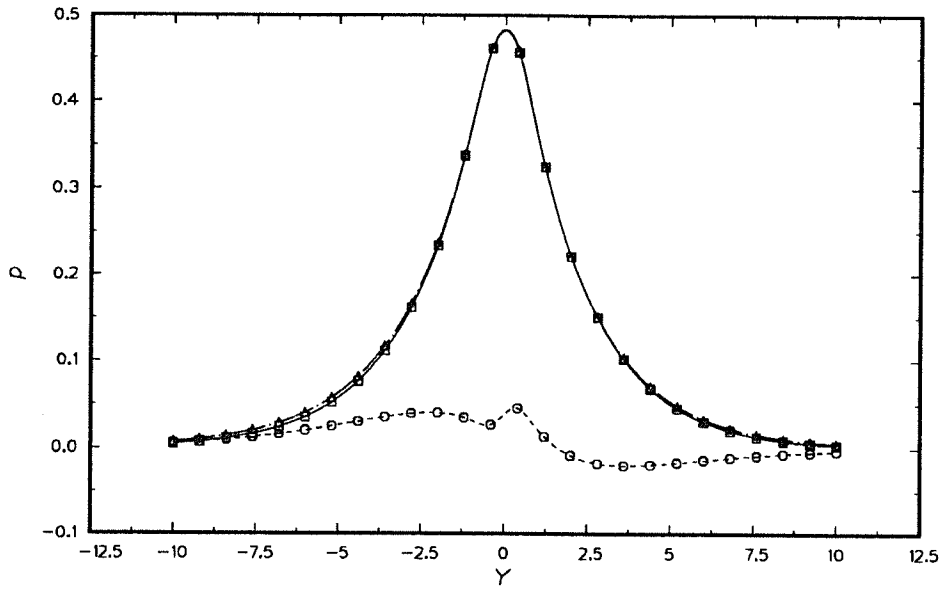

(a)

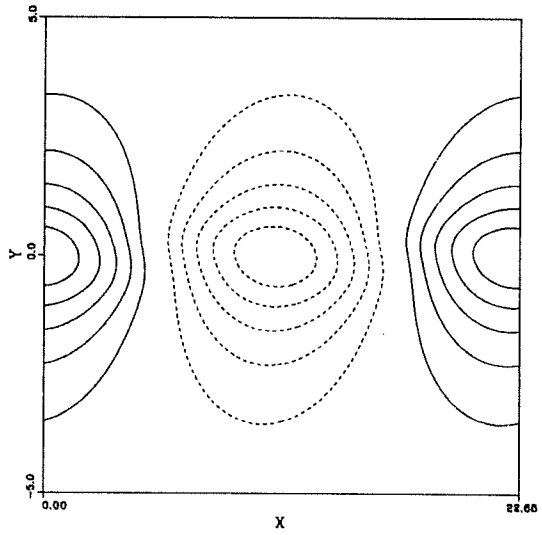

(b) max=1.018, min=0.982

FIGURE 5.16. Pressure (a) eigenfunction and (b) contours of the most unstable oblique center mode (θ=65°). M_1=5 (M_c=1.25), $\bar{T}_2$=1, T_{ad}=1. □ , real; ○ , imaginary; △ , absolute.

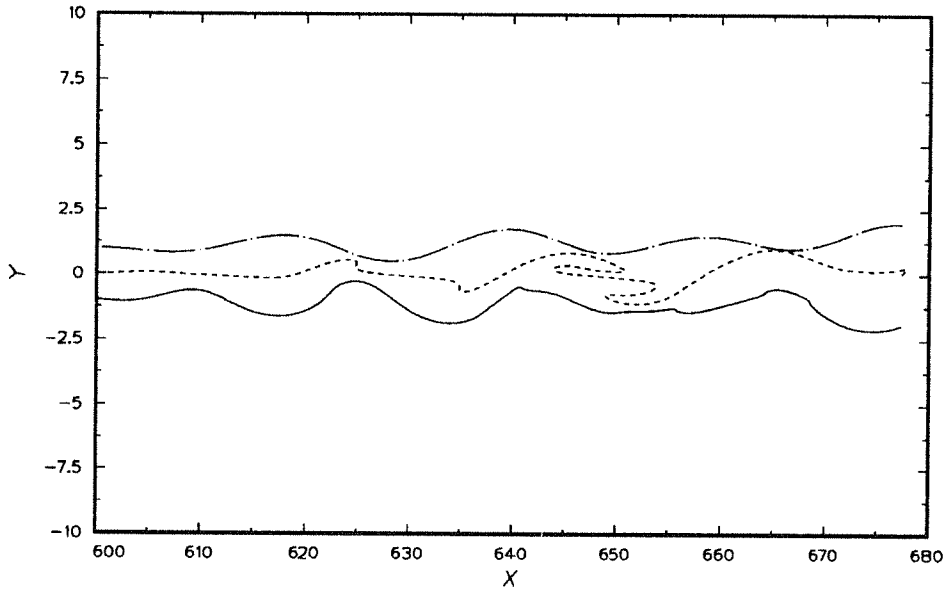

(a)

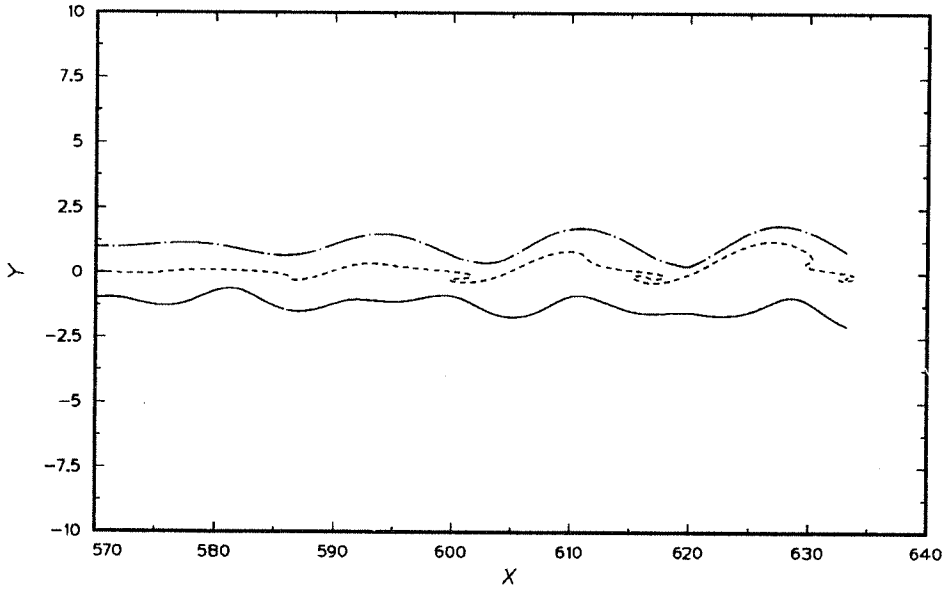

(b)

FIGURE 5.17. Streaklines for the spatially developing layers at T_{ad}=1. (a) slow (b) fast mode. M_1=5 (M_c=1.25), $\bar{T}_2$=1, β=0.

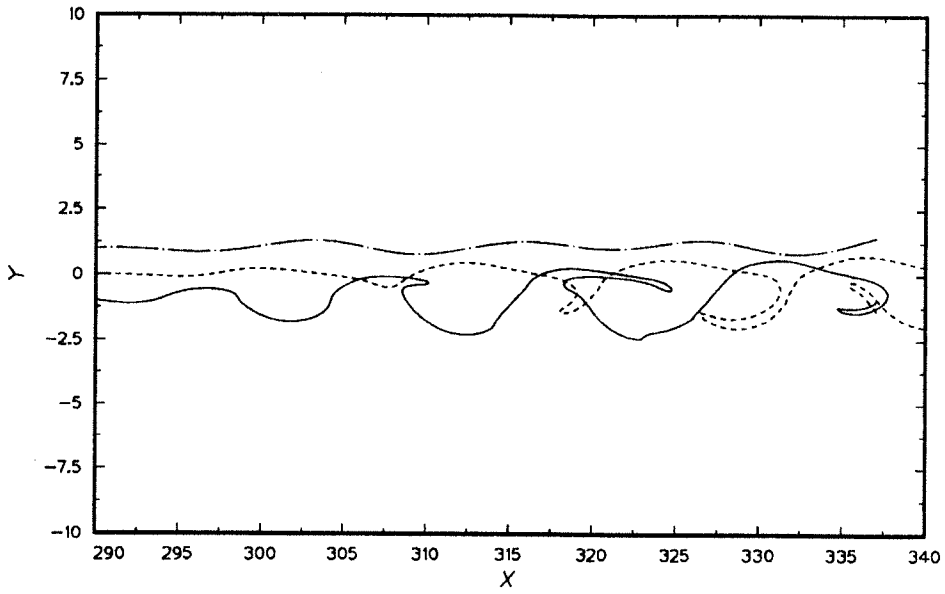

(a)

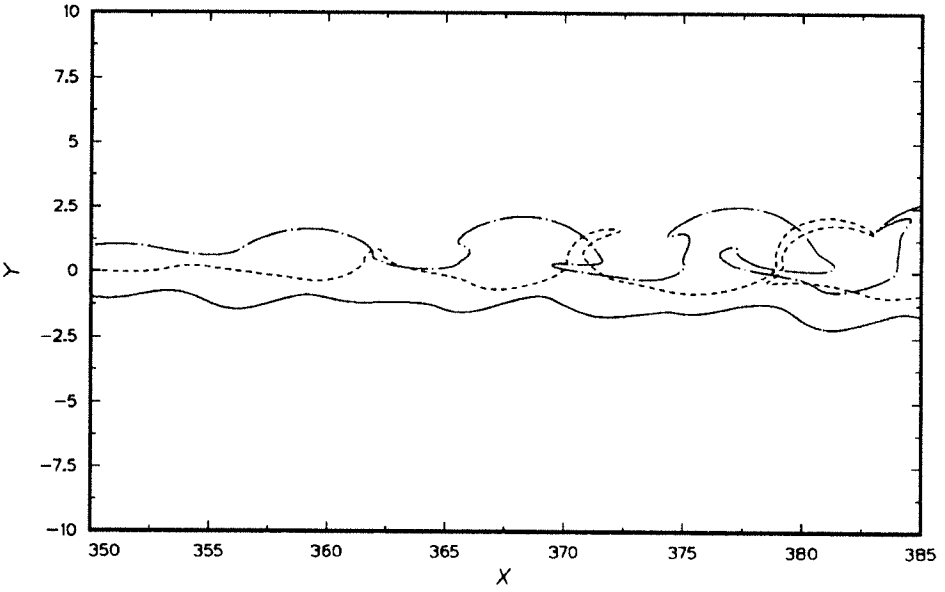

(b)

FIGURE 5.18. Streaklines for the spatially developing layers at T_{ad}=4. (a) slow (b) fast mode. M_1=5 (M_c=1.25), $\bar{T}_2$=1, β=0.

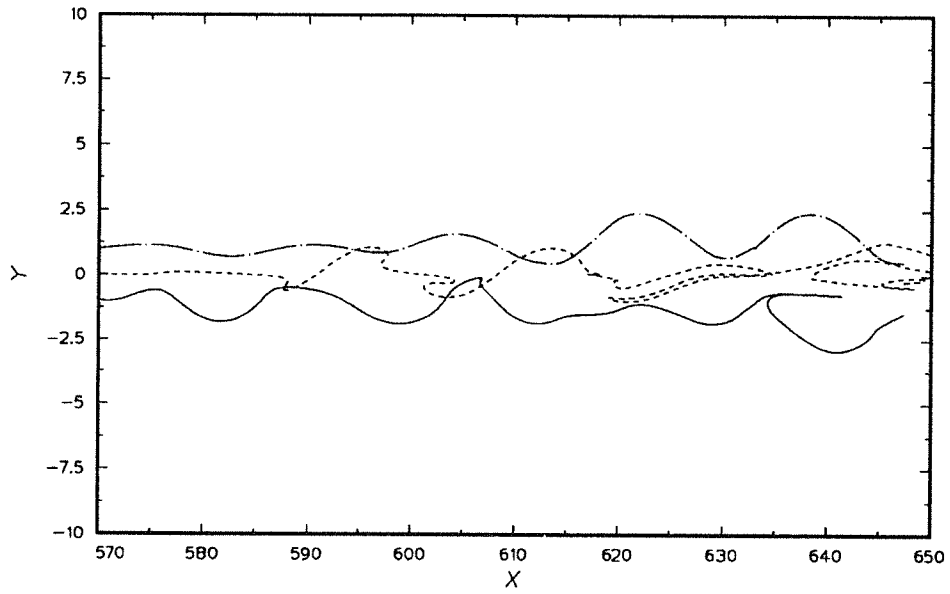

(a)

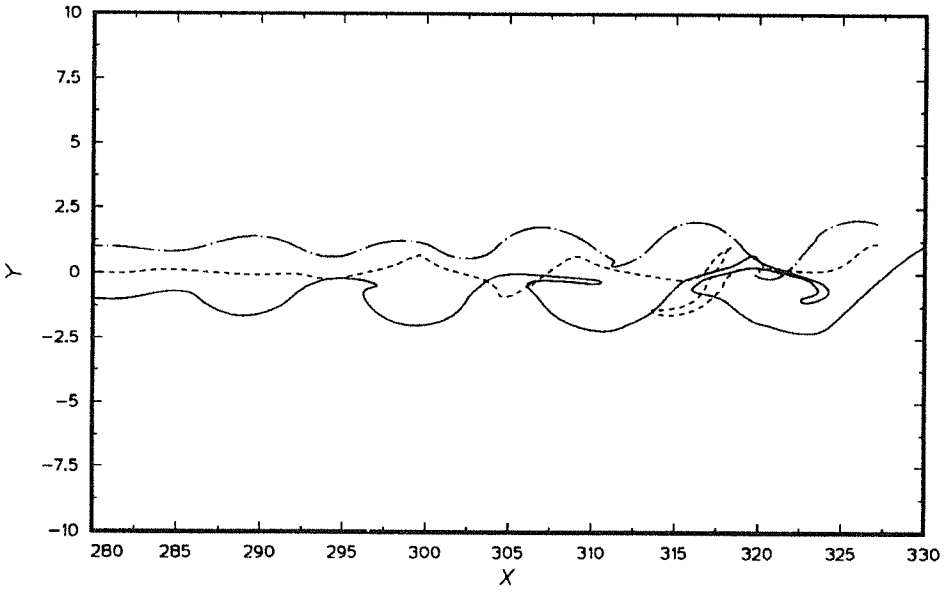

(b)

FIGURE 5.19. Streaklines for the spatially developing layers with combined modes. (a) T_{ad}=1 (b) T_{ad}=4. M_1=5 (M_c=1.25), $\bar{T}_2$=1, β=0.

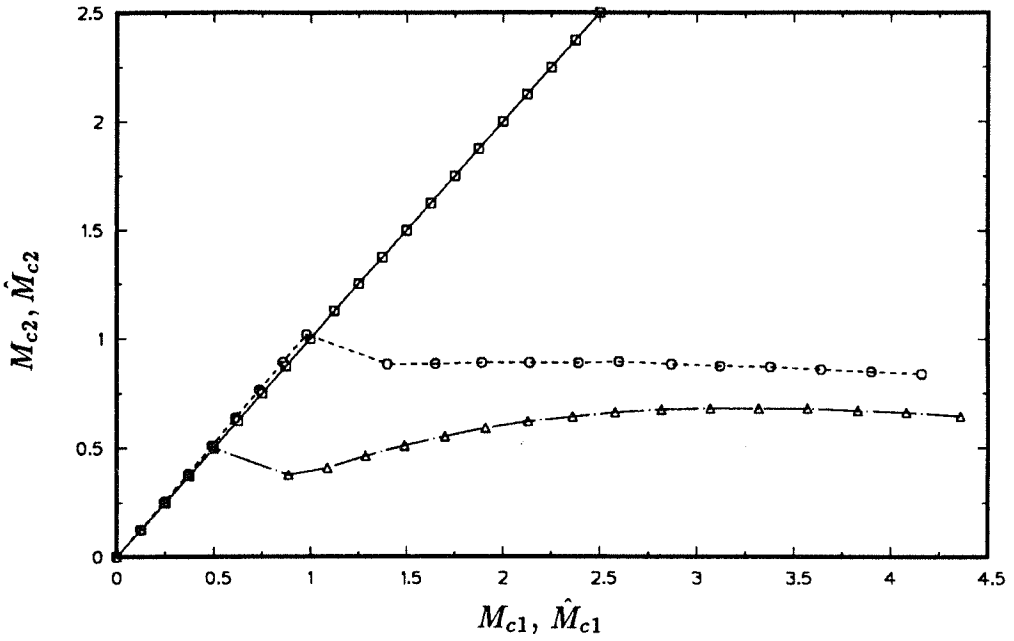

FIGURE 5.20. Comparison of convective Mach numbers. $\bar{u}_2$=0.5, $\bar{T}_2$=1, β=0. ▫ , isentropic, Eq. (5.7), T_{ad}=1 and 4; ○ , based on the most unstable mode, Eq. (5.8), T_{ad}=1; △ , based on the most unstable mode, Eq. (5.8), T_{ad}=4.

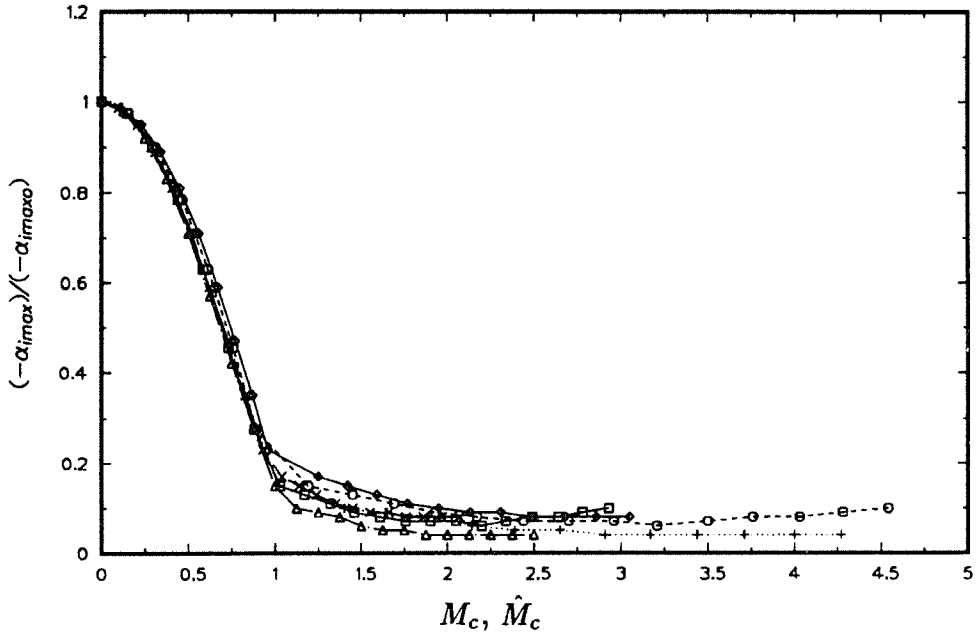

FIGURE 5.21. Maximum growth rates normalized by corresponding incompressible growth rates for non-reacting flows. T_{ad}=1, $\bar{u}_2$=0.5, β=0. ▫ , $\bar{T}_2$=0.5, Eq. (5.7); ○ , $\bar{T}_2$=0.5, Eq. (5.8); △ , $\bar{T}_2$=1, Eq. (5.7); +, $\bar{T}_2$=1, Eq. (5.8); ×, $\bar{T}_2$=2, Eq. (5.7); ◇ , $\bar{T}_2$=2, Eq. (5.8).

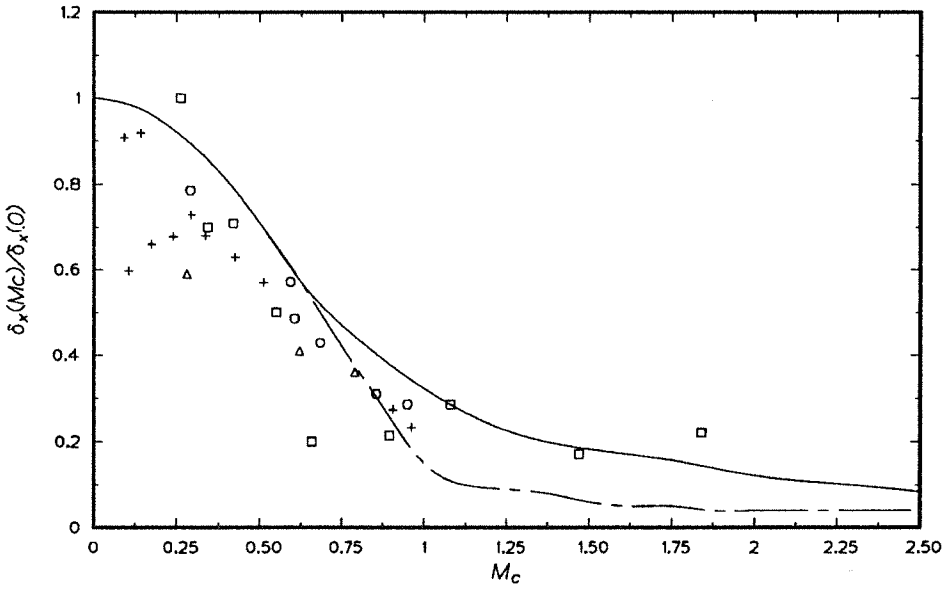

FIGURE 5.22. Comparison of normalized growth rates between theory and experiment. □ , Papamoschou & Roshko [1988]; ○ , Chinzei *et al.* [1986]; △ , Clemens & Mungal [1990]; +, Hall *et al.* [1991]; — — , current, two-dimensional; —— , current, three-dimensional.

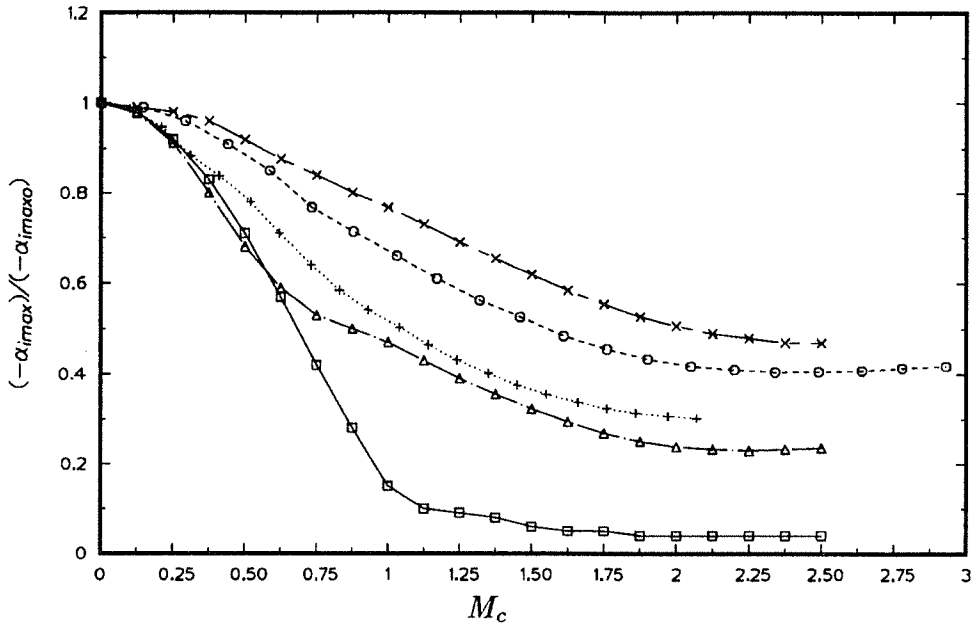

(a)

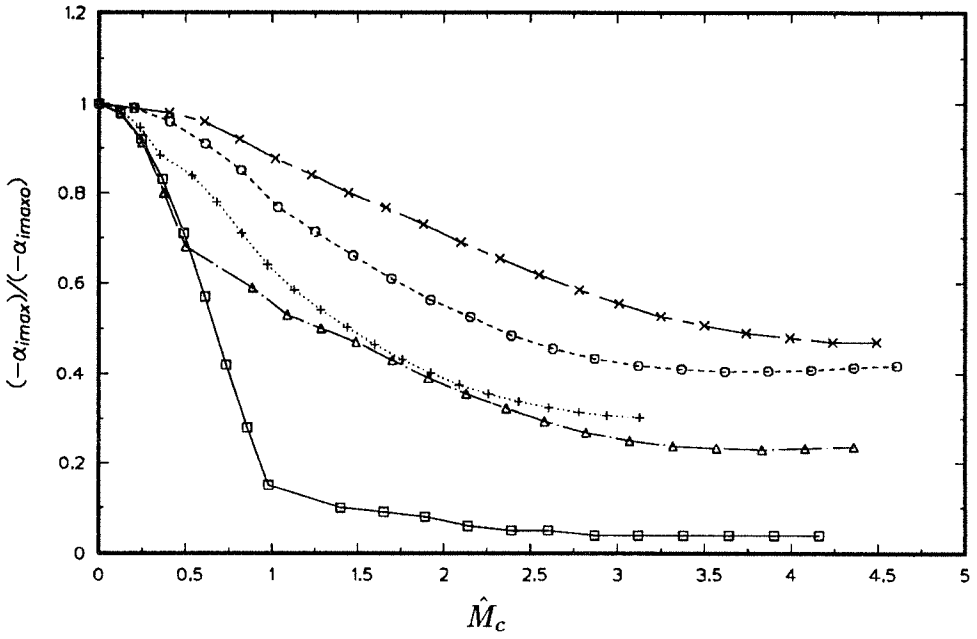

(b)

FIGURE 5.23. Continued

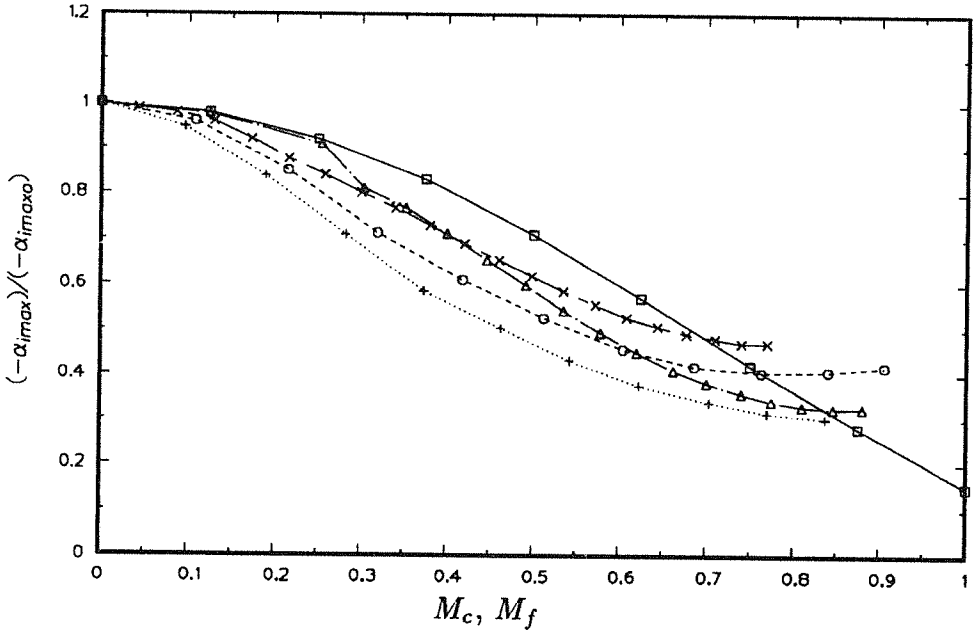

(c)

FIGURE 5.23. Maximum growth rates normalized by corresponding incompressible growth rates versus convective Mach number for reacting flows. (a) M_c (b) $\hat{M}_c$ (c) M_c, M_f. $\bar{u}_2$=0.5, β=0. ▫ , $\bar{T}_2$=1, T_{ad}=1; ○ , $\bar{T}_2$=0.5, T_{ad}=4; △ , $\bar{T}_2$=1, T_{ad}=4; +, $\bar{T}_2$=2, T_{ad}=4; ×, $\bar{T}_2$=1, T_{ad}=8.

Chapter 6

Instability of the Confined Compressible Reacting Shear Layer

Until now, we have considered only unconfined shear layers. However, the supersonic mixing layers in ramjet combustors and most experiments are confined by solid walls. Two distinct types of instabilities may occur in confined shear layers. One is the Kelvin-Helmholtz instability found in subsonic shear layers; the other is the acoustic instability. In low speed flows, the effects of walls on the Kelvin-Helmholtz instability are relatively weak so long as they are separated by many shear layer thicknesses. However, in high speed flows, some of the energy of the acoustic waves that would ordinarily radiate to infinity is reflected by the walls. This reflection can alter the stability characteristics of the flow significantly. Although we do not know which type of instability is responsible for transition of the supersonic shear layer, the acoustic instability is the most likely candidate.

To include the effect of chemical reaction, we shall consider a reacting mixing layer in a channel. Laminar flows obtained in Chapter 2 are used as the basis for the stability study because the confining walls hardly change the profiles of the laminar flows (Fig. 6.1). All flow variables are nondimensionalized as in previous chapters.

The boundary conditions for the disturbance equations are modified to account for confined walls. We shall consider the effects of all the parameters considered in previous chapters including heat release, Mach number, frequency, wavenumber, thickness of shear layer as well as distance between walls and direction of propagation of the disturbance waves. Results with and without walls will be compared.

6.1 Formulation

As in the preceding chapters, we consider a spatially developing plane mixing layer in which the fuel and oxidizer are initially unmixed. The flow is confined to a rectangular channel of height $2H$ and breadth B. We assume locally parallel mean flow and small wavelike disturbances propagating in the x direction.

At the walls, we could apply no-slip boundary conditions. However, the focus of this study is on the shear layer and the boundary layers are not important so long as

they are much thinner than the shear layer and channel width. Hence we allow fluid slip at the walls but no penetration. Furthermore, heat loss and chemical reaction at the walls are excluded. Boundary conditions for the disturbances at the sidewalls ($z=\pm B/2$) are therefore

$$\frac{\partial u'}{\partial z} = \frac{\partial v'}{\partial z} = w' = \frac{\partial \rho'}{\partial z} = \frac{\partial T'}{\partial z} = \frac{\partial p'}{\partial z} = \frac{\partial y_F'}{\partial z} = \frac{\partial y_O'}{\partial z} = 0 \tag{6.1}$$

Solutions for the disturbances which satisfy the above boundary conditions are assumed to have the form:

$$\begin{bmatrix} u' \\ v' \\ w' \\ \rho' \\ T' \\ p' \\ y_F' \\ y_O' \end{bmatrix} = \begin{bmatrix} \hat{u}(y)\cos(2m\pi z/B) \\ \hat{v}(y)\cos(2m\pi z/B) \\ \hat{w}(y)\sin(2m\pi z/B) \\ \hat{\rho}(y)\cos(2m\pi z/B) \\ \hat{T}(y)\cos(2m\pi z/B) \\ \hat{p}(y)\cos(2m\pi z/B) \\ \hat{y}_F(y)\cos(2m\pi z/B) \\ \hat{y}_O(y)\cos(2m\pi z/B) \end{bmatrix} e^{i(\alpha x - \omega t)} \qquad (m = 0, 1, 2, ...) \tag{6.2}$$

Substituting Eq. (6.2) into the linearized governing equations, we derive a second order ordinary differential equation for the pressure (see Sec. 3.1)

$$\hat{p}'' - \left\{ \frac{2\alpha\bar{u}'}{(\alpha\bar{u}-\omega)} + \frac{\bar{\rho}}{\bar{T}}(\alpha\bar{u}-\omega)^2[RXN1] \right\} \hat{p}' -$$

$$\left[\left\{ \alpha^2 + \left(\frac{2m\pi}{B}\right)^2 \right\} - \gamma {M_1}^2 (\alpha\bar{u}-\omega)^2 \left\{ \frac{1}{\bar{T}} + \frac{\bar{\rho}}{\bar{T}}[RXN2] \right\} \right] \hat{p} = 0 \tag{6.3}$$

This equation is the same as Eq. (3.21) except that $2m\pi/B$ replaces the transverse wavenumber β. The boundary conditions at the top and bottom walls become

$$\hat{p}'(H) = \hat{p}'(-H) = 0 \tag{6.4}$$

With these boundary conditions, Eq. (6.3) is solved by a combination of shooting and Newton-Raphson methods (see Sec. 3.3).

6.2 Results

6.2.1 *Effect of Walls*

First, the effect of walls on the instability is examined. We begin by looking at the two-dimensional waves (m=0) in the non-reacting flow (T_{ad}=1) with H=5. Because all length scales are nondimensionalized by initial vorticity thickness, H=5 means that wall separation is five times the vorticity thickness, which is small enough to permit interaction between the wall and unstable acoustic modes. Fig. 6.2 shows the amplification rates and phase speeds as functions of frequency at Mach numbers M_1=0, 2, 3. It shows that when the Mach number of the disturbance relative to either free-stream is subsonic ($|M_r| < 1$), there is only one unstable mode and its phase velocity is about the average of two free stream velocities; we can identify this as a Kelvin-Helmholtz mode. The amplification rate of this mode decreases as the Mach number increases, just as in unconfined shear flows. The effect of walls on these modes is weak.

Flows with supersonic relative Mach number ($|M_r| > 1$) yield many supersonic unstable modes; these are similar to the supersonic modes found by Mack [1989] in boundary layers. They arise from reflection of acoustic waves by the walls and do not exist in the absence of walls. Fig. 6.3 shows the growth rates of these unstable modes and their phase velocities at M_1=6 and M_2=3. There are further unstable modes at higher frequencies; their amplification rates are lower. The unstable modes can be classified into the three families found in unconfined flows: center, slow and fast modes. The phase velocities of the fast modes decrease as the frequency increases, while those of slow modes increase with frequency. They appear to approach the average of the two free-stream velocities. This behavior contrasts with what was found in unconfined flows, for which the phase velocities approach the free-stream velocities. Each mode is unstable only over a relatively narrow frequency band. For this set of parameters, the most unstable mode is a center mode but it is only slightly more unstable than one of the outer modes.

For the reacting flow with T_{ad}=4 and H=5, the two-dimensional amplification rates and phase velocities at subsonic relative Mach numbers are shown in Fig. 6.4. Fig. 6.4a shows the amplification rates of center and slow modes and Fig. 6.4b shows the amplification rates of fast modes at Mach numbers M_1=0, 2, 3. Fig. 6.4c shows the corresponding phase velocities. The amplification rates of all modes decrease

as the Mach number increases. The fast modes have smaller amplification rates than their slow counterparts. When the relative Mach number is supersonic, three families of modes are unstable. Fig. 6.5 shows the growth rates of these unstable modes and the corresponding phase velocities for M_1=6 and M_2=3. Other unstable modes with lower amplification rates and higher frequencies are not shown. The fast and slow modes have comparable amplification rates, while the center mode is less unstable. Unlike the situation in non-reacting flows, neither phase velocity approaches the average speed. Rather, the phase velocities of the outer modes appear to be almost independent of frequency.

Because the walls change the characteristics of supersonic unstable modes from those found in unconfined flows, the distance between the walls is an important parameter. For two-dimensional modes, m=0, the growth rates are independent of the aspect ratio of the duct, i.e. the breadth has no effect on the stability. We calculated the properties of spatially growing waves at various values of H for fixed upper stream Mach number M_1 and fixed mean velocity and temperature profiles. The instability behavior of the subsonic shear layer hardly varies with the distance between the walls. However, the instability characteristics of supersonic shear layers change considerably as height increases. Fig. 6.6 shows the maximum amplification rates as functions of H at M_1=6 (M_2=3). The smallest H considered is 1. For non-reacting flows, the most unstable modes are center modes when the walls are closely spaced ($H \leq 10$). However, as the distance between the walls increases ($H > 10$), slow modes become more unstable as in the unconfined flow cases. For reacting flows (T_{ad}=4 and 8), the most unstable modes are always slow modes. The maximum growth rates of both the non-reacting and reacting shear layers reach their maximum values and decrease as the distance between the walls decreases. The maximum growth rates occur about at H=2 for the non-reacting flow and about at H=5 for the reacting flows. As expected, reflection of acoustic waves by moderately closely spaced walls prevents radiation of energy and makes the flow more unstable. The effect is much larger in the non-reacting case for which the maximum growth rate at H=5 is about twice as large as that at H=20. For T_{ad}=4, the maximum growth rate at H=5 is about 1.4 times larger than that at H=20. When H is relatively small ($H < 4$), the non-reacting flow is more unstable than the reacting flows; the reverse is true for large H ($H > 4$). Although the much closely spaced walls tend to make

the flow less unstable than the moderately spaced walls, the real combustor will have a considerably large height and the effect will be small.

6.2.2 *Three-Dimensional Modes*

In partially confined-channel flows, which have no sidewalls, the disturbances are of the form (3.7) and the equation for the pressure disturbance is Eq. (3.21). The only difference between partially-confined flows and rectangular channel flows is the boundary condition at the side walls, Eq. (6.1). We studied the growth rate of three-dimensional modes in both types of flows. Because heat release favors two-dimensional instability, we considered only the non-reacting case (T_{ad}=1); because walls have little effect on the low-speed flow, only high-speed flows (M_1=6, M_2=3) were studied. Fig. 6.7 shows the maximum amplification rates for various angles of propagation at H=5 and 20 for the case without sidewalls. Only the slow mode growth rates are given for readability; the fast mode growth rates are almost the same. When the distance between the walls is large (H=20), the outer modes are dominant for angles less than about 45°, and the maximum growth rates change only slightly with angle. When the angle is greater than 45°, the outer modes disappear and the center mode begins to dominate, as in the unconfined flow. For angles greater than 45°, the center modes are subsonic relative to both free streams. The angle of maximum instability of the center mode is 67°, which is very close to the prediction (66°) of Eq. (5.3). The relative Mach number of the most unstable center mode is 0.59 and is subsonic. Note that the maximum growth rate of oblique center modes is much greater than the growth rate of two-dimensional outer modes. Therefore, the most unstable mode is oblique and subsonic at M_1=6.

For closely spaced walls (H=5), the center mode is slightly more unstable than the outer modes at θ=0°. As the angle increases, the center modes become less unstable. At large angles ($\theta > 55°$), the center modes reappear and dominate; they are subsonic relative to both free streams. The most unstable center mode occurs at θ=70° and the corresponding relative Mach number is 0.51; the amplification rate is slightly higher (about 8%) than that of the two-dimensional mode. The outer modes become more stable with increasing angle as in the unconfined flows. Thus the behavior of partially confined flows is similar to that of unconfined flows, but the close spacing of the walls weakens the three-dimensionality.

A rectangular channel might display three-dimensional instabilities due to reflections from the sidewalls. Because the transverse-boundary conditions (Eq. (6.1)) allow only integer values of the transverse wavenumber m, the three-dimensional modes in a rectangular channel are different from travelling modes in the transverse direction. We investigated the three-dimensional instability modes for both non-reacting (T_{ad}=1) and reacting (T_{ad}=4) rectangular-channel flows. Because a smaller distance between the walls makes the flow more unstable and the results with a larger distance agree well with unconfined flow cases, we chose 10 as the wall height. The breadth of the channel B was 10 in this study. We studied two different Mach numbers, M_1=2 and 6 (M_2=1 and 3); the first is considered a low-speed flow and the second, a high-speed flow.

Fig. 6.8a shows the amplification rates for the non-reacting cases. We consider only the center mode for non-reacting flows (T_{ad}=1) and the slow mode for reacting flows (T_{ad}=4) because they are the most unstable modes of the respective flows; m=0 corresponds to two-dimensional modes and m=1 to three-dimensional modes. We found only damped modes for $m > 1$. In the low-speed flow (M_1=2), the three-dimensional mode (m=1) has lower amplification rates than the two-dimensional mode (m=0); this is similar to what we found for unconfined flows. In high-speed flow (M_1=6), the three-dimensional mode (m=1) has lower amplification rates. This result shows that three-dimensional modes have lower amplification rates than two-dimensional modes in high-speed non-reacting flows unlike unconfined or partially confined flows. Thus side walls favor two-dimensionality. However, it will be difficult to identify the large structures as two- or three-dimensional in experiments because the dominant unstable modes have comparable growth rates but various phase speeds, which is consistent with the present observation (Papamoschou [1989]; Clemens & Mungal [1990]; Hall *et al.* [1991]). Fig. 6.8b shows the results for the reacting cases. The most amplified modes are still two-dimensional (m=0), which is similar to the situation in unconfined reacting shear layers. As a consequence, we consider only two-dimensional modes below.

6.2.3 *Effect of Mach Number, Heat Release and Damköhler Number*

This section studies the effect of the Mach number and heat release on the maximum growth rates of instabilities in confined shear layers. The wall height is fixed at 10. Fig. 6.9 gives the maximum amplification rate versus the upper-stream Mach

number and indicates that the maximum growth rate of the most unstable two-dimensional mode decreases with Mach number in both non-reacting (T_{ad}=1) and reacting (T_{ad}=4) flows. They appear to approach asymptotic values for $M_1 > 4$ ($M_c > 1$).

In the non-reacting case, there is little difference between the unconfined and the confined flows when the isentropic convective Mach number is subsonic ($M_1 < 4$). When the isentropic convective Mach number is supersonic ($M_1 > 4$), reflection of acoustic waves by the walls makes the confined flow more unstable than the unconfined flow. At M_1=8, the maximum growth rate of the confined flow is about four times that of the unconfined flow. However, it is small (about 16%) compared to the growth rate of the cold flow at M_1=0. The reacting flow shows a similar qualitative trend. Heat release seems to reduce the compressibility effect even more in confined flows; the ratio of the maximum amplification at M_1=8 to that at M_1=0 is about two, which is half of the ratio in the non-reacting flow.

Fig. 6.10 shows the normalized growth rates of non-reacting flows versus the isentropic convective Mach number, M_c, along with experimental data and the normalized two- and three-dimensional growth rates of unconfined flows in Chapter 5. The growth rates are normalized by incompressible growth rates at the same velocity and temperature ratio (see Eq. (5.10)). The results for confined flows agree with the experimental trend better than the two-dimensional results for unconfined flows at supersonic convective Mach numbers. Even though the three-dimensional growth rates of unconfined flows are comparable to the present results of confined flows, the latter agree better with Papamoschou & Roshko's growth rates [1988] that approach an asymptotic value for supersonic convective Mach number flows.

Fig. 6.11 shows the effect of heat release on the maximum amplification rate of unstable modes for low-speed (M_1=1) and high-speed (M_1=6) flows. In the low-speed flow, the walls make little difference. Heat release stabilizes the low-speed flow; the maximum amplification rate for T_{ad}=8 is about 15% of the cold flow value. At M_1=6, the confined flows are more unstable than the unconfined flows. The change of the maximum growth rate with Mach number is large in cold flow (T_{ad}=1); it becomes smaller as the heat release increases. The effect of the walls on the growth rate becomes negligible at large heat release. At high Mach numbers, the amplification rates change little with T_{ad}, which is consistent with the behavior of the supersonic-ramjet combustor (Drummond [1991], private communication).

Fig. 6.12 shows the effect of the Damköhler number in the high-speed flow (M_1=6). Unlike the case for unconfined flows, the Damköhler number does not affect the amplification rates much.

6.2.4 *Eigenfunctions and Streaklines*

Figs. 6.13-15 present two-dimensional linear eigenfunctions of the most unstable modes of non-reacting (T_{ad}=1) and reacting (T_{ad}=4) flows at M_1=6 (M_2=3). The eigenfunctions are normalized so that the maximum absolute value of $\hat{u}$ is unity. We chose H=5 in order to include the effect of confinement. We considered only the center and slow modes; the fast mode can be obtained by reflection of the slow mode.

For the non-reacting supersonic center mode in Fig. 6.13, the behavior of the pressure and density components of the eigenfunctions show the radiative behavior of a supersonic mode at both boundaries. The pressure and density fluctuations of the supersonic slow modes for both non-reacting (Fig. 6.14) and reacting (Fig. 6.15) flows display radiative behavior in the the high-speed side, showing the supersonic nature relative to the high-speed side. Note that the density and temperature perturbations of the reacting flow in Fig. 6.15c-d are an order of magnitude greater than those of the non-reacting flow, which is similar to what was found in unconfined flows. Because the slow mode lies principally in the slow part of the mixing layer, the oxidizer perturbation is relatively larger than that of the fuel; the reverse is true for the fast mode.

From the eigenfunctions corresponding to the most unstable modes and the mean flow, we can obtain contours of the flow variables. Fig. 6.16 shows the contours of various quantities produced by the supersonic center mode for the non-reacting (T_{ad}=1) flow at M_1=6 (M_2=3). The contours of ω_z and ω_z/ρ are qualitatively different from those for the corresponding low-speed mode. The two elementary clockwise vortices of the low-speed cold flow have been replaced by a single vortex in the center of the layer. The pressure and density contours in Figs. 6.16c-d show clearly the radiative nature of the supersonic center mode. Unlike the outer modes that radiate only to one free stream, the center modes are supersonic relative to both streams and the associated compression (solid line) and expansion waves (dashed line) propagate toward both boundaries. The patterns of compression/expansion waves in Fig. 6.16c suggest that the waves are reflected by the walls. The reflections carry energy back

to the shear layer, producing feedback that makes confined shear layers more unstable than free shear layers. Mack reported a similar observation for boundary layers [1984].

From the pressure contours we measured the Mach angle μ and estimated the convective Mach number $\hat{M}_c$ of the most unstable mode from

$$\hat{M}_c = \frac{1}{\sin\mu} \tag{6.5}$$

Measurement of the Mach angle from Fig. 6.16c gives μ=40°, from which we estimate the convective Mach number to be approximately 1.55. The convective Mach number of the most unstable mode from Eq. (5.8) is 1.49; this agreement is considered very good. Figs. 6.16e-f show the dilatational and baroclinic terms of the vorticity equation (Eq. (4.30)). The baroclinic term is larger than the dilatational term by two orders of magnitude and is thus much more important. The baroclinic term has both positive and negative regions near the vortex, so its effect on the growth of the two-dimensional vorticity is not clear.

Figs. 6.17-18 show contours for non-reacting and reacting supersonic slow modes at M_1=6 (M_2=3). The patterns are similar to those for the corresponding unconfined flows given in Figs. 5.14-15 except for the pressure contours. The latter again show reflections of compression/expansion waves propagating at Mach angle μ=27° for the non-reacting flow and μ=26° for the reacting flow. The convective Mach numbers according to Eq. (6.5) are 2.20 for the non-reacting flow and 2.28 for the reacting flow, while the convective Mach numbers based on the corresponding most unstable modes are 2.22 and 2.33 respectively; the agreement is again very good. The contours of the reactant concentrations in Figs. 6.18g-h show that the slow mode principally affects the oxidizer because the oxidizer occupies the lower part of the layer. The fuel distribution is hardly perturbed, so the supersonic slow mode will not yield much mixing between the reactants in confined reacting flows.

In Sec. 4.3.9 and 5.6, we calculated streaklines based on linear stability eigenfunctions for the most unstable two-dimensional modes. They suggested that the outer modes disturb only one side of the layer and do not increase mixing between the reactants. Similar streaklines for confined flows at high Mach numbers M_1=6 (M_2=3) are given in Fig. 6.19 for both cold (T_{ad}=1) and reacting (T_{ad}=4) flows. Only the center and slow modes are shown; the fast mode can be obtained by reflection of the

slow mode. In contrast to the behavior of the low-speed cold flow, the streaklines of the non-reacting center mode at high Mach number confined shear flows do not indicate roll-up, which suggests that the coherent structures might not be produced and that mixing between the fuel and oxidizer will not be active. As in unconfined flows, the slow mode primarily disturbs the lower part of the mixing layer, leaving the upper part mostly undisturbed. The reverse is true for the fast mode. Thus the outer modes in confined supersonic mixing layers do not cause roll-up, and mixing between the fuel and oxidizer will not be strong.

6.3 Chapter Summary

In this chapter, we investigated the effect of walls on the stability of reacting mixing layers, using laminar solutions of the compressible boundary-layer equations from Chapter 2 as base flows. We found that the effects of the walls on subsonic disturbances are relatively small but that reflection of supersonic disturbances by the walls makes the confined mixing layer more unstable than the unconfined free shear layer. Decreasing the distance between the walls makes the flow more unstable. The most unstable supersonic disturbances are three-dimensional in partially confined flows but two-dimensional in rectangular channel flows. Heat release and Mach number hardly change the maximum growth rates of supersonic disturbances. The supersonic center mode radiates to both boundaries, whereas the outer modes propagate only to the boundary relative to which they are supersonic. Pressure contours show the compression/expansion waves that propagate at the Mach angle. Finally, the reactants are not strongly mixed by supersonic instabilities which mainly disturb one side of the layer.

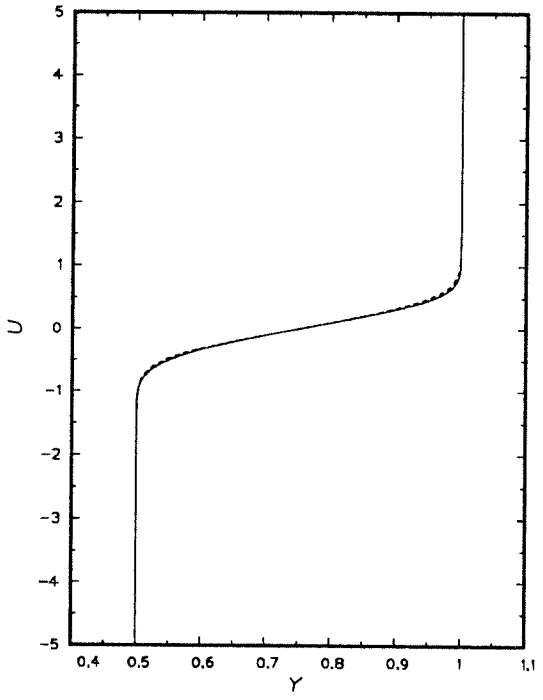

(a)

FIGURE 6.1. Streamwise velocity. T_{ad}=1, M_1=6 (M_2=3), $\bar{T}_2$=1, H=5. ——— , without walls (boundary-layer equations); ---- , with walls (full Navier-Stokes equations).

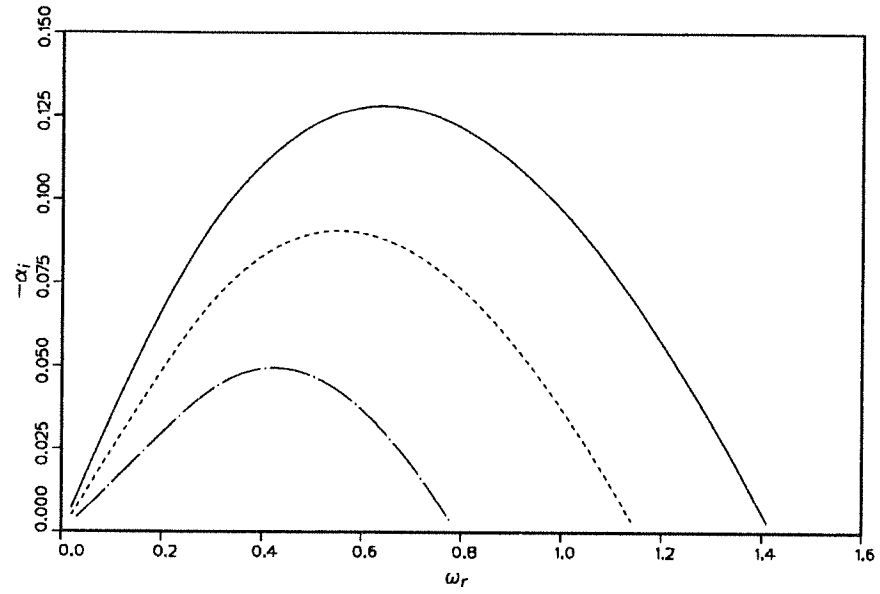

(a)

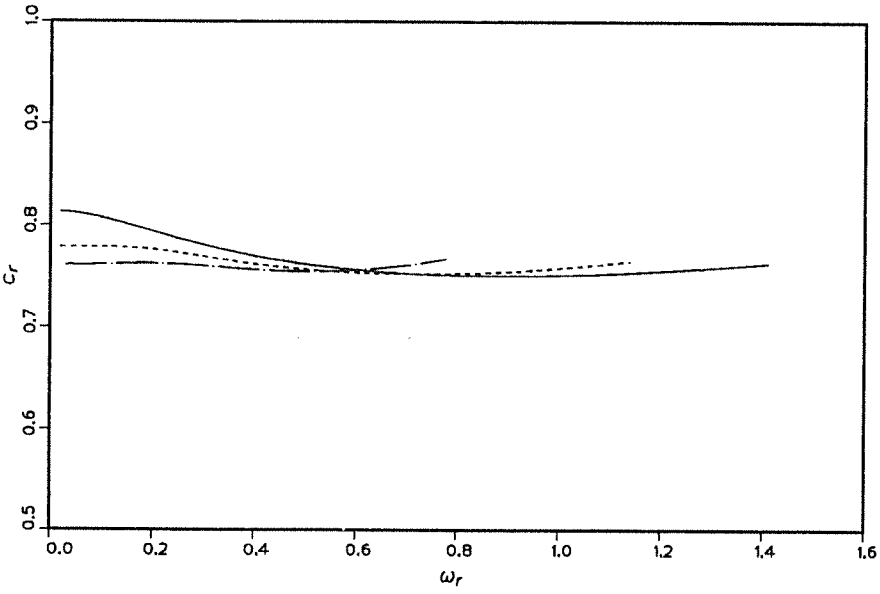

(b)

FIGURE 6.2. (a) Amplification rates and (b) phase velocities in subsonic relative Mach number. T_{ad}=1, m=0, H=5, $\bar{T}_2$=1. —— , M_1=0; ---- , M_1=2; —·— , M_1=3.

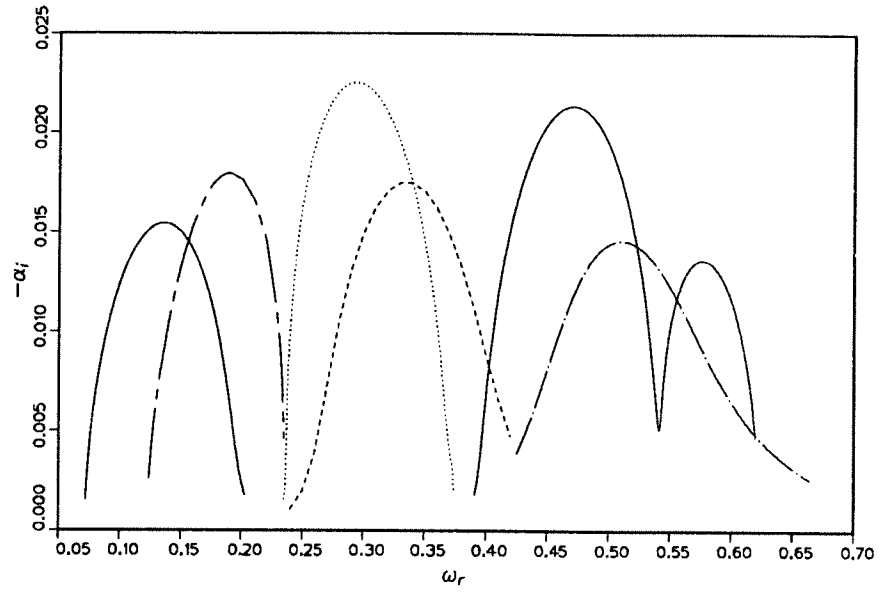

(a)

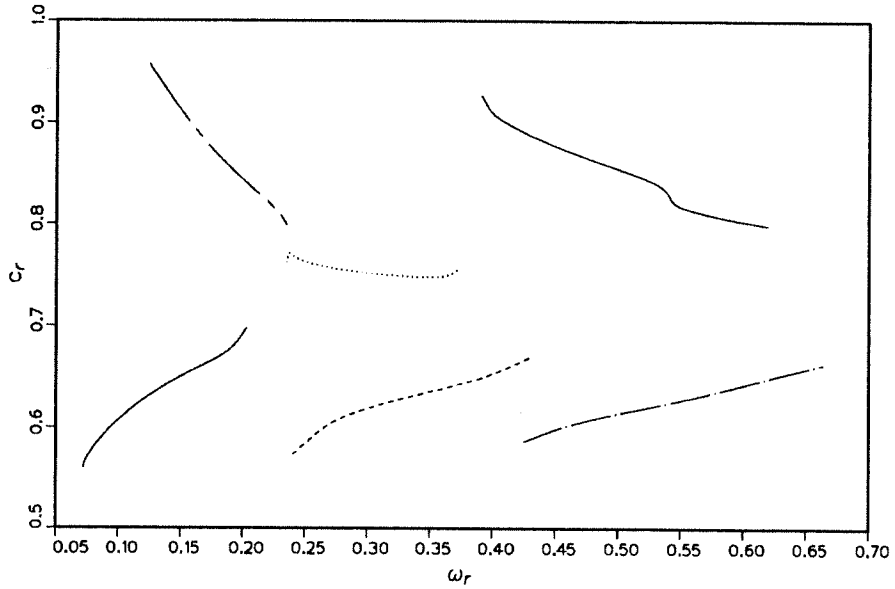

(b)

FIGURE 6.3. (a) Amplification rates and (b) phase velocities in supersonic relative Mach number. T_{ad}=1, M_1=6, M_2=3, m=0, H=5, $\bar{T}_2$=1.

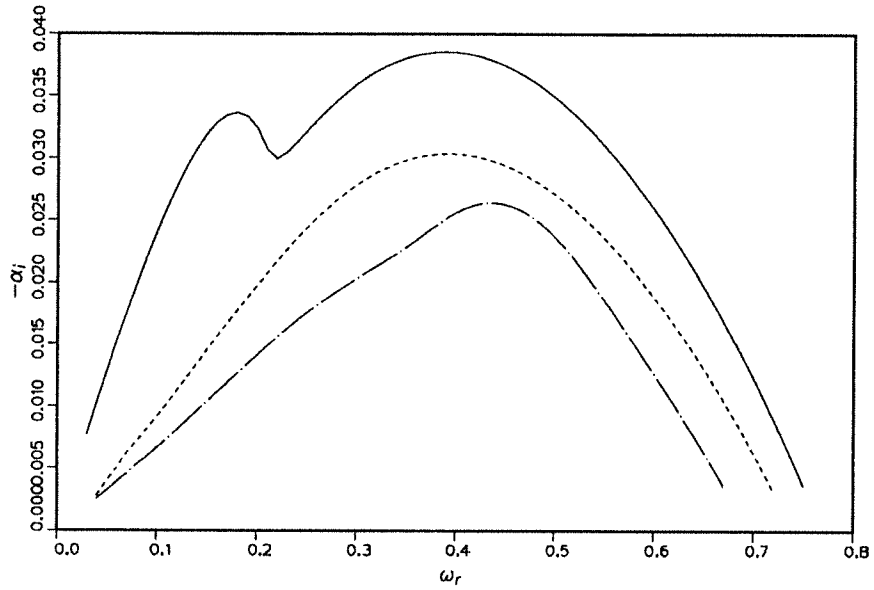

(a)

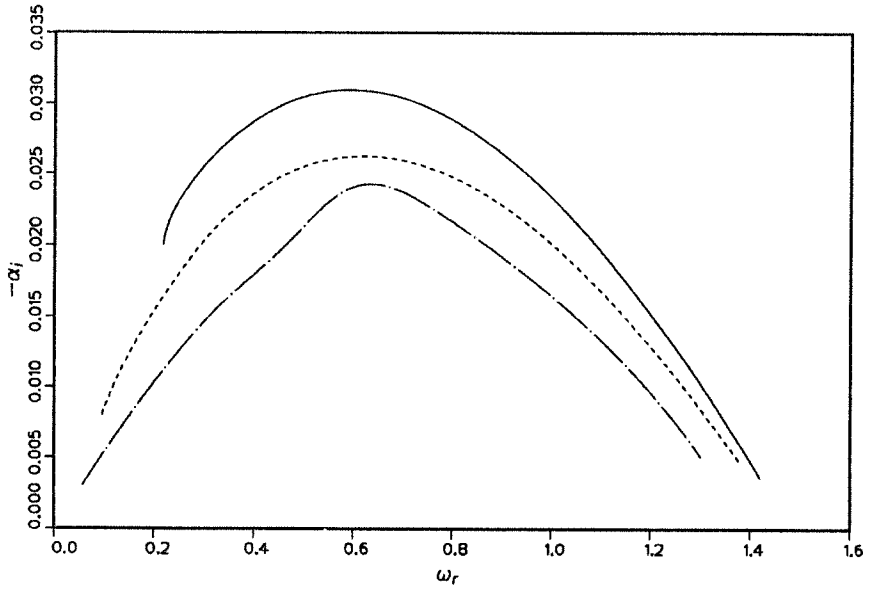

(b)

FIGURE 6.4. Continued.

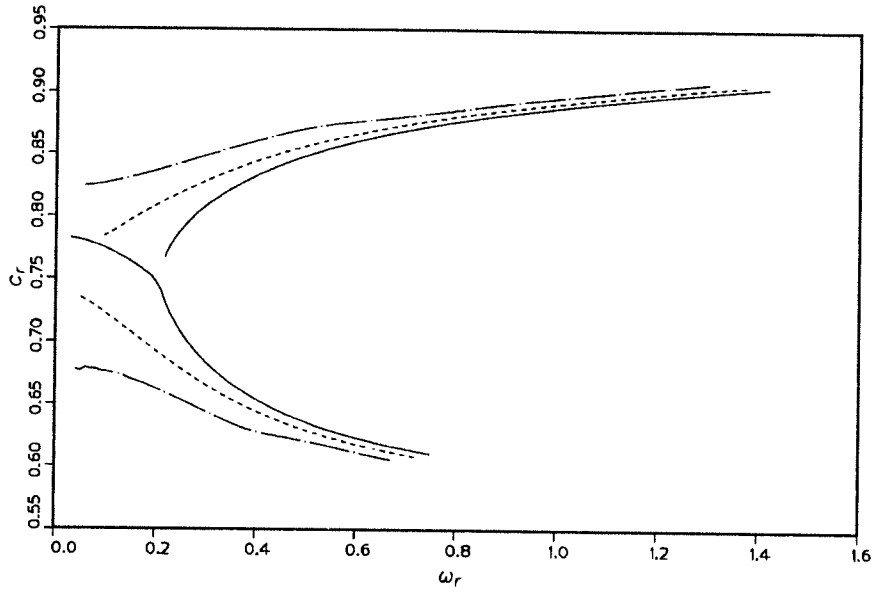

(c)

FIGURE 6.4. (a) Amplification rates of center and slow modes (b) amplification rates of fast modes and (c) corresponding phase velocities in subsonic relative Mach number. T_{ad}=4, m=0, H=5, $\bar{T}_2$=1. —— , M_1=0; ---- , M_1=2; —·— , M_1=3.

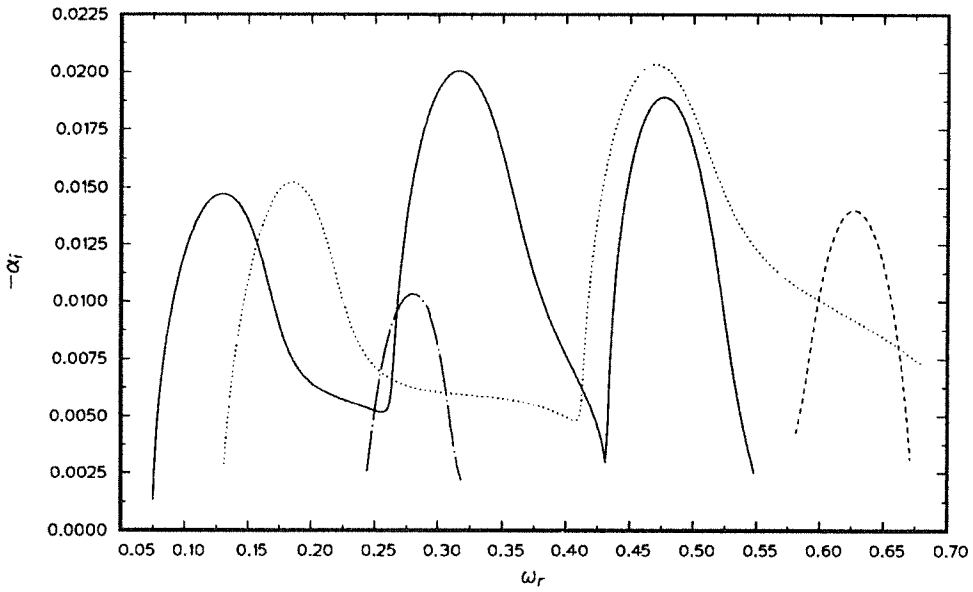

(a)

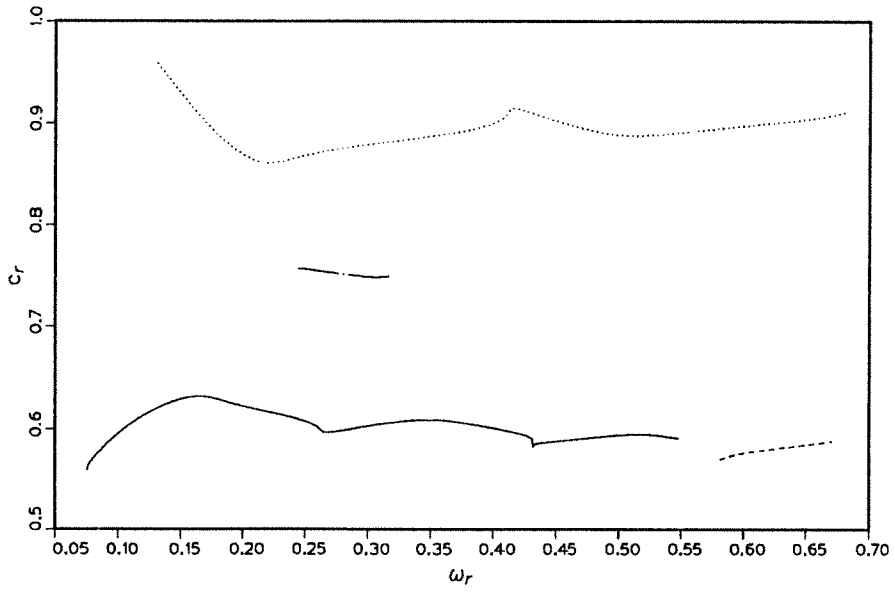

(b)

FIGURE 6.5. (a) Amplification rates and (b) phase velocities in supersonic relative Mach number. T_{ad}=4, M_1=6, M_2=3, m=0, H=5, $\bar{T}_2$=1.

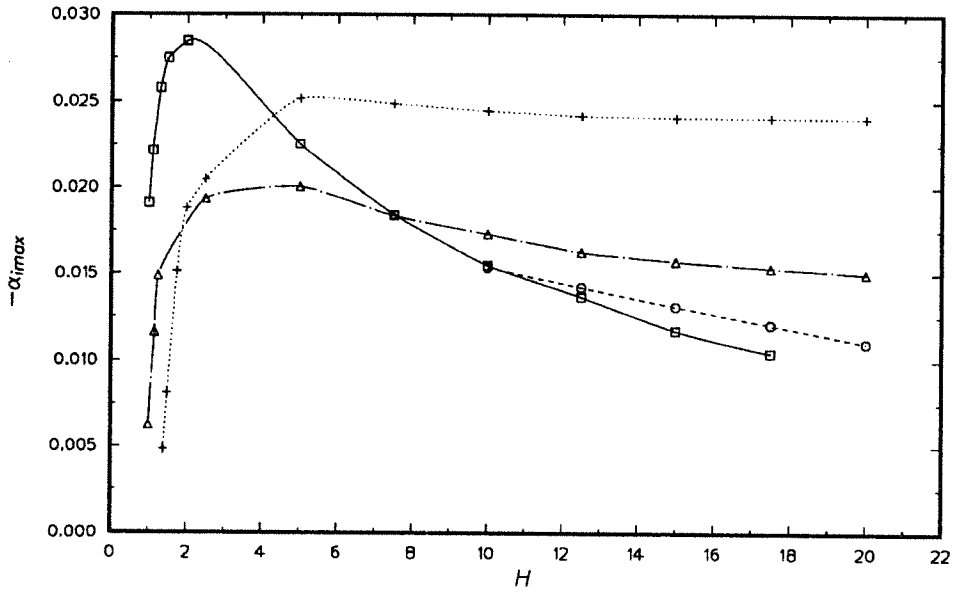

FIGURE 6.6. Maximum amplification rates versus H. m=0, M_1=6, M_2=3, $\bar{T}_2$=1. ▫ , T_{ad}=1, center mode; ○ , T_{ad}=1, slow mode; △ , T_{ad}=4, slow mode; +, T_{ad}=8, slow mode.

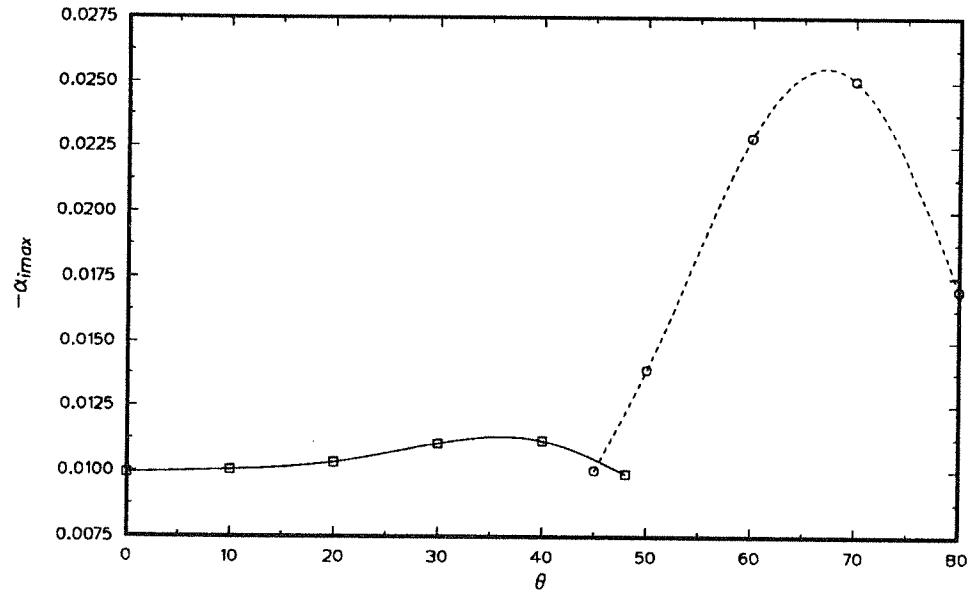

(a)

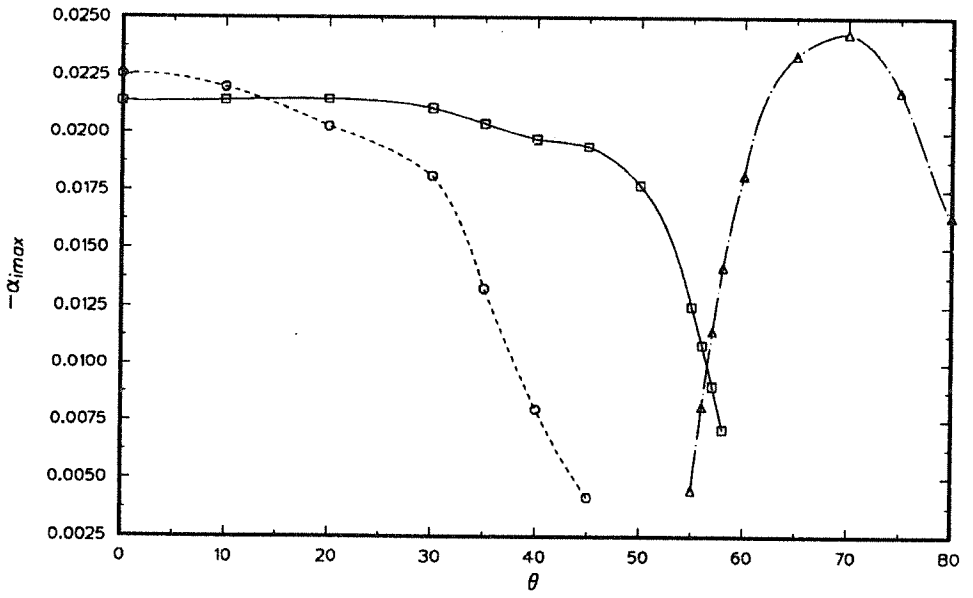

(b)

FIGURE 6.7. Maximum growth rate versus obliqueness angle in partially confined flows at T_{ad}=1. $\bar{T}_2$=1, M_1=6, M_2=3. (a) H=20 (b) H=5. □ , slow mode; ○ , △ , center mode.

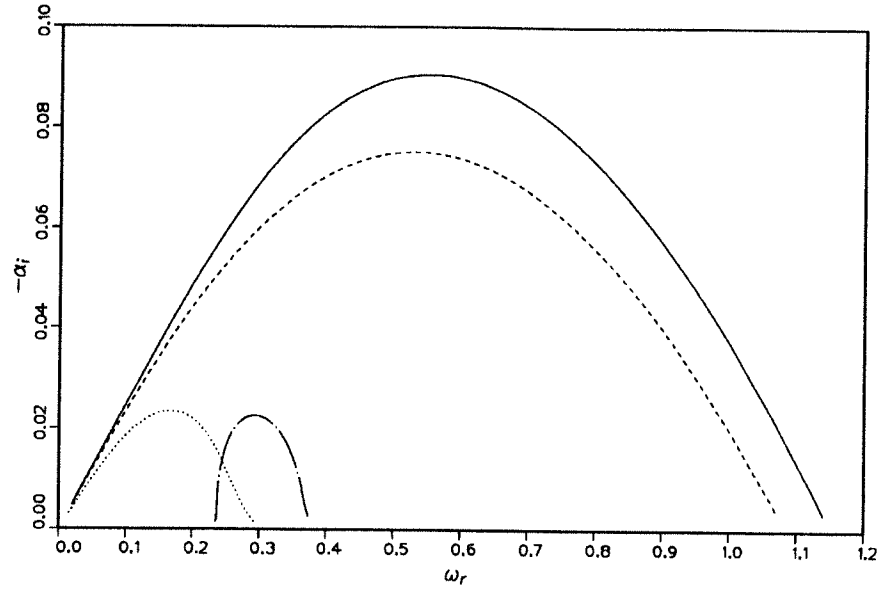

(a)

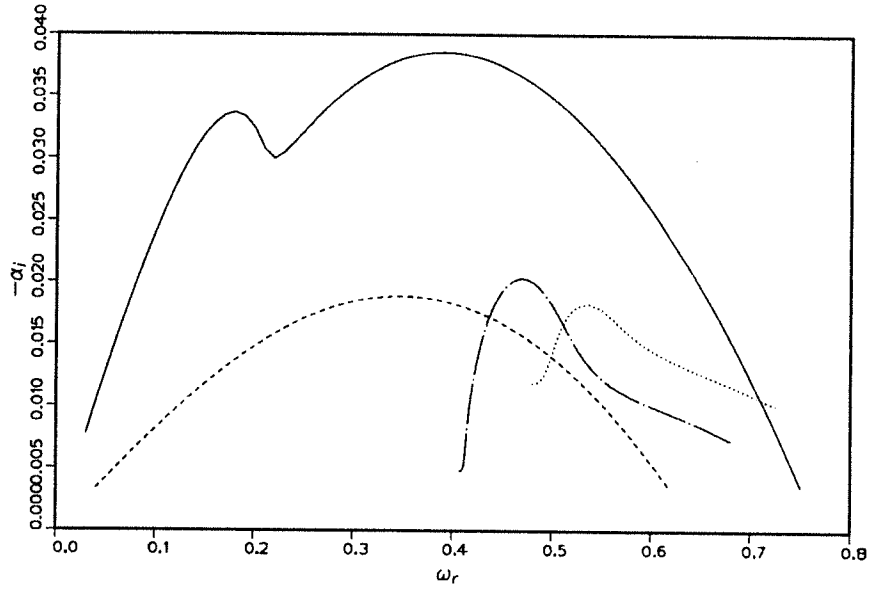

(b)

FIGURE 6.8. Amplification rates in rectangular channel flow for (a) non-reacting (T_{ad}=1) and (b) reacting (T_{ad}=4) flows. $B/2=H=5$, $\bar{T}_2=1$. —— , $M_1=2$, $m=0$; ---- , $M_1=2$, $m=1$; —·— , $M_1=6$, $m=0$; ····· , $M_1=6$, $m=1$.

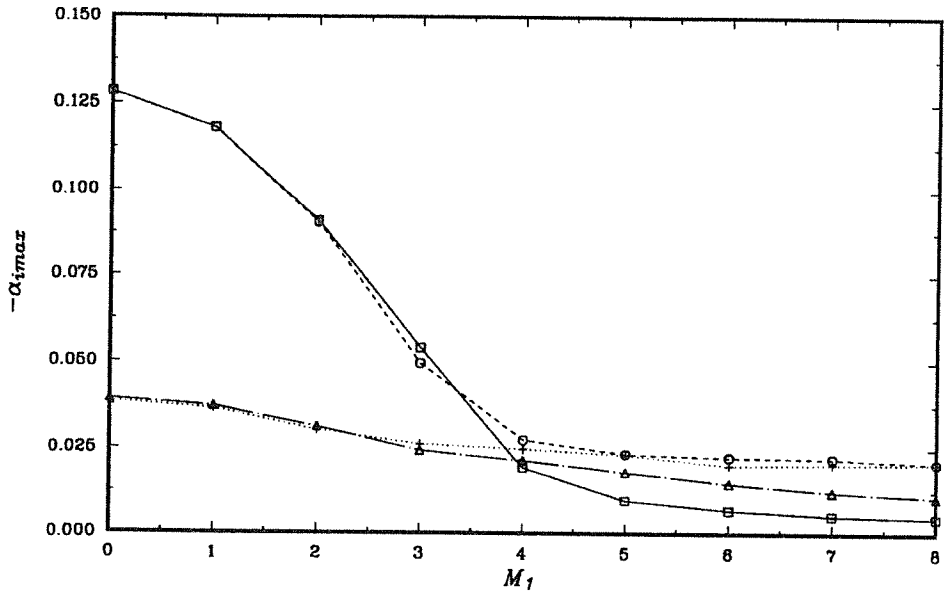

FIGURE 6.9. Maximum amplification rates versus M_1. m=0, H=5, $\bar{T}_2$=1. □ , T_{ad}=1, unconfined; ○ , T_{ad}=1, confined; △ , T_{ad}=4, unconfined; +, T_{ad}=4, confined.

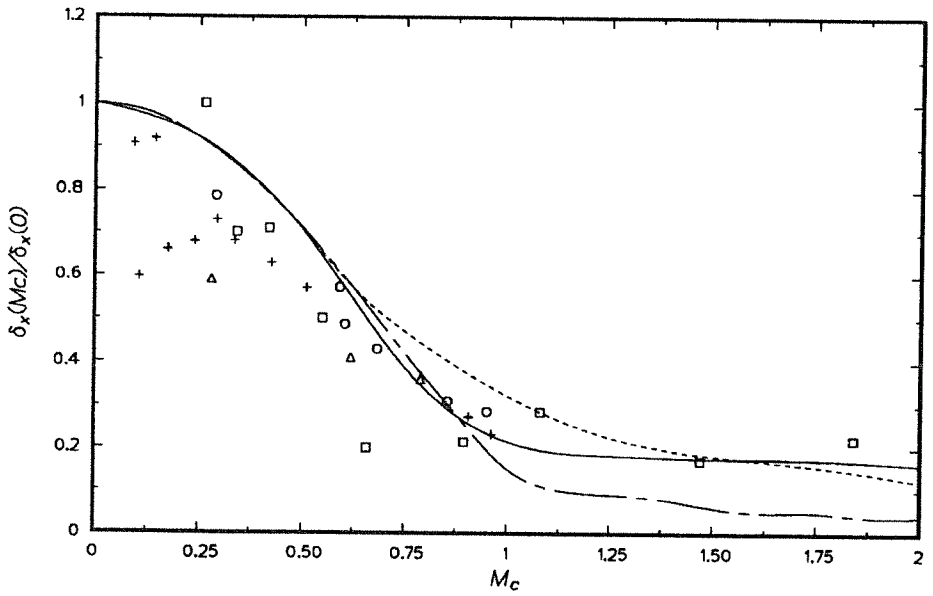

FIGURE 6.10. Comparison of normalized growth rates between theory and experiment. □ , Papamoschou & Roshko [1988]; ○ , Chinzei *et al.* [1986]; △ , Clemens & Mungal [1990]; +, Hall *et al.* [1991]; —— , confined, current; ——— , unconfined, two-dimensional; ---- , unconfined, three-dimensional.

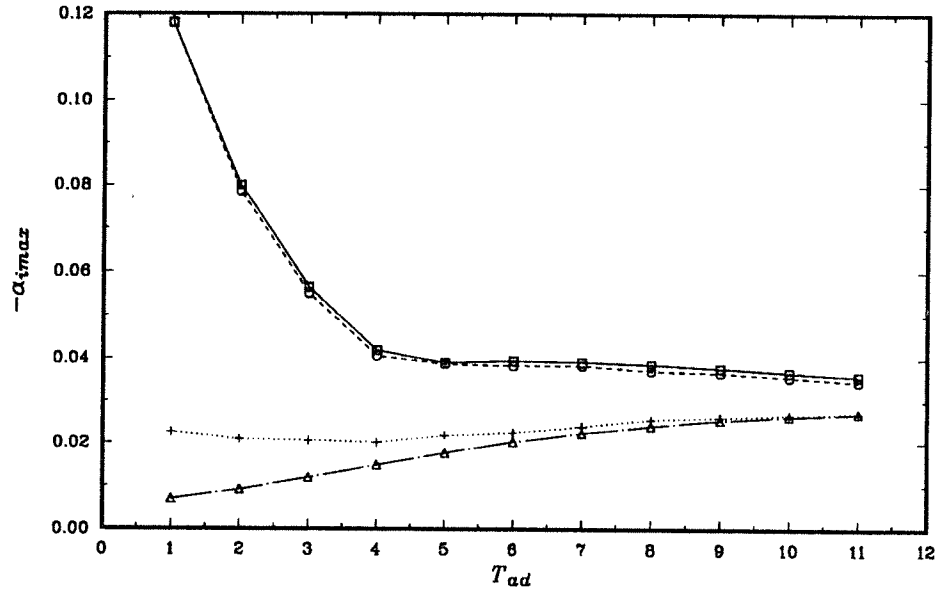

FIGURE 6.11. Maximum amplification rates versus T_{ad}. m=0, H=5, $\bar{T}_2$=1. ▫ , M_1=1, unconfined; ○ , M_1=1, confined; △ , M_1=6, unconfined; +, M_1=6, confined.

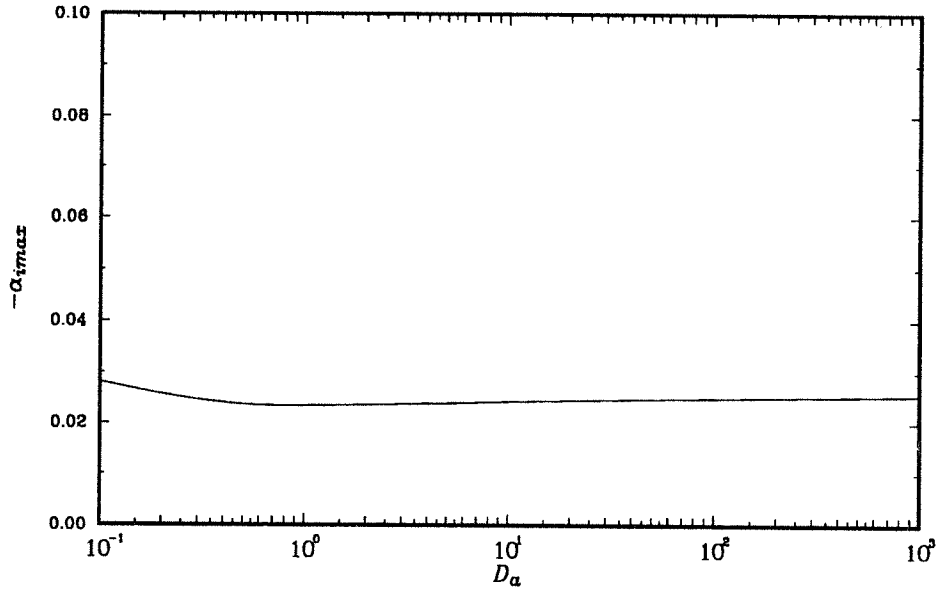

FIGURE 6.12. Maximum growth rate versus Damköhler number. M_1=6 (M_c=1.5), $\bar{T}_2$=1, T_{ad}=4, m=0, H=5.

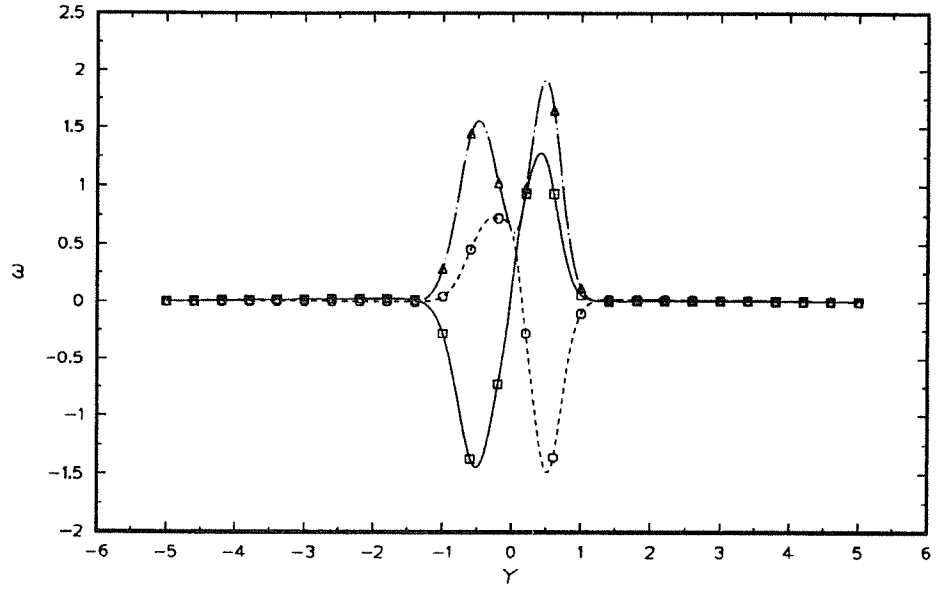

(a)

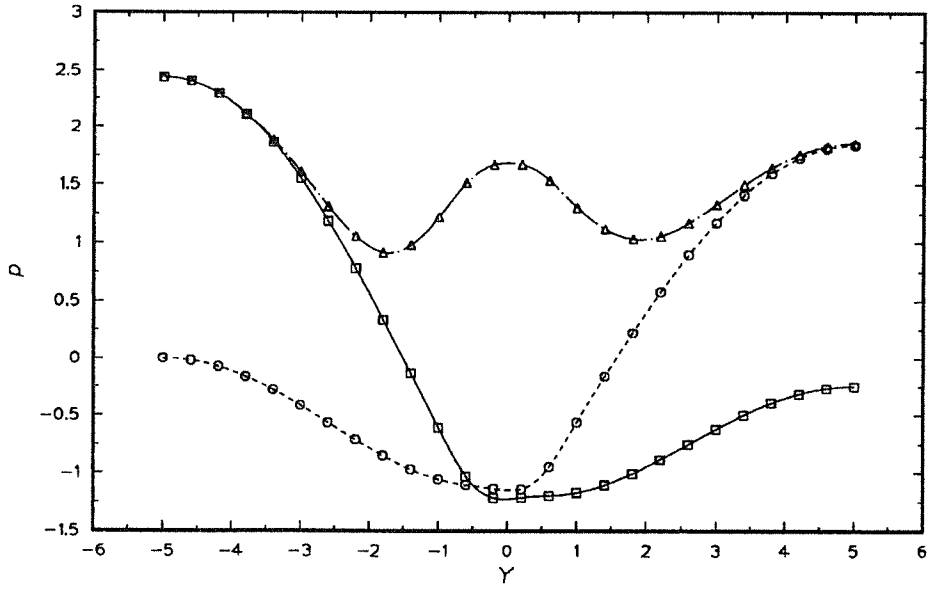

(b)

FIGURE 6.13. Continued.

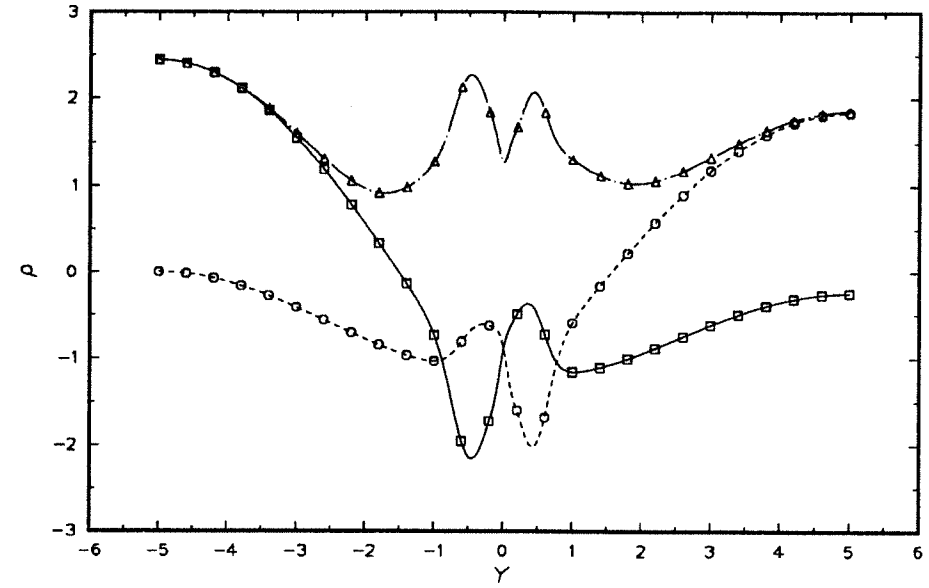

(c)

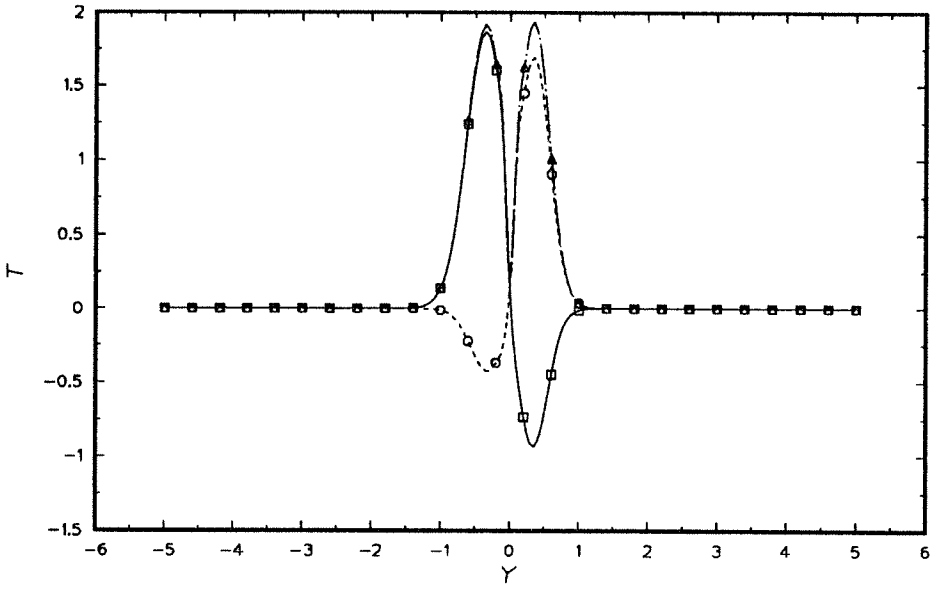

(d)

FIGURE 6.13. Linear eigenfunctions of the non-reacting confined flow (center mode) (a) $\hat{\omega}_z$ (b) $\hat{p}$ (c) $\hat{\rho}$ (d) $\hat{T}$. M_1=6 (M_c=1.5), $\bar{T}_2$=1, T_{ad}=1, m=0, H=5. ▫ , real; ○ , imaginary; △ , absolute.

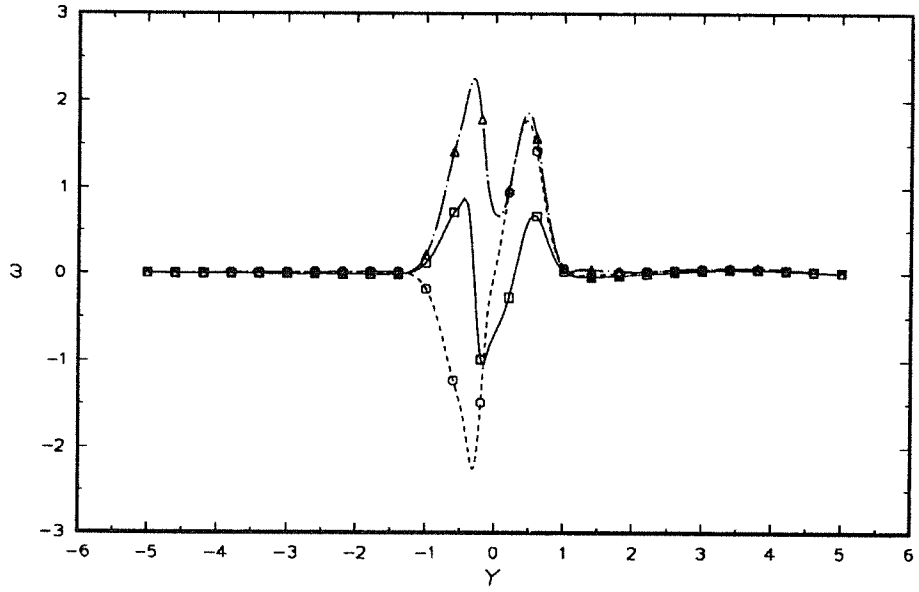

(a)

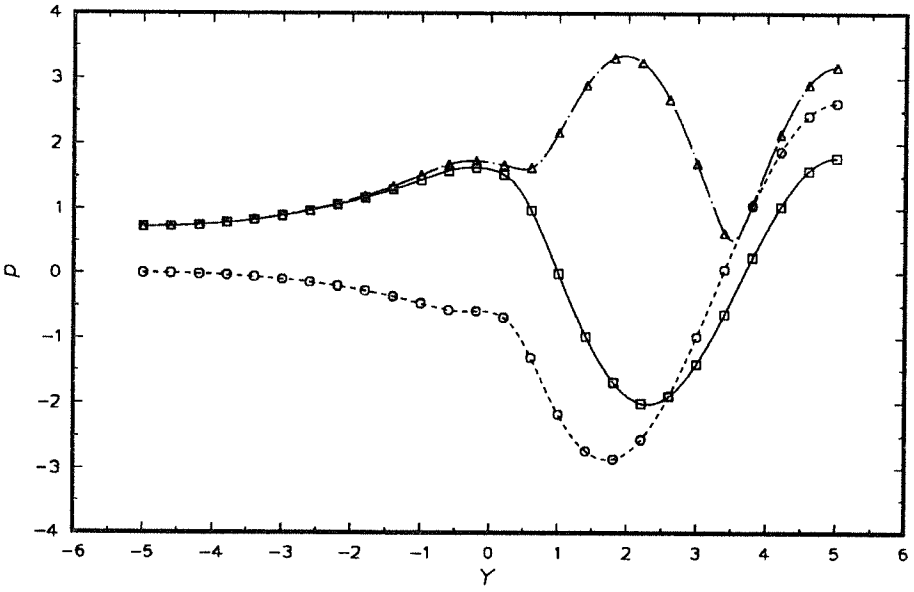

(b)

FIGURE 6.14. Continued.

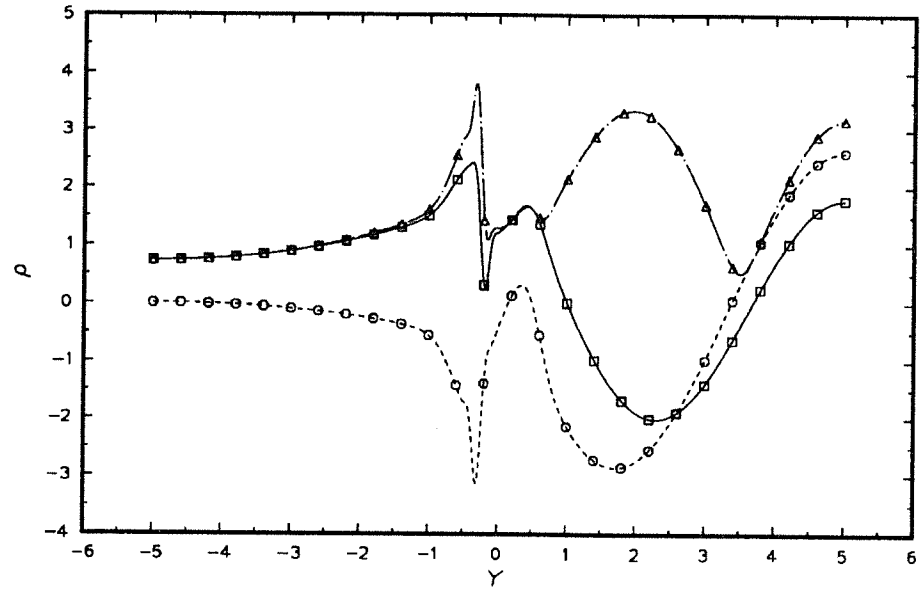

(c)

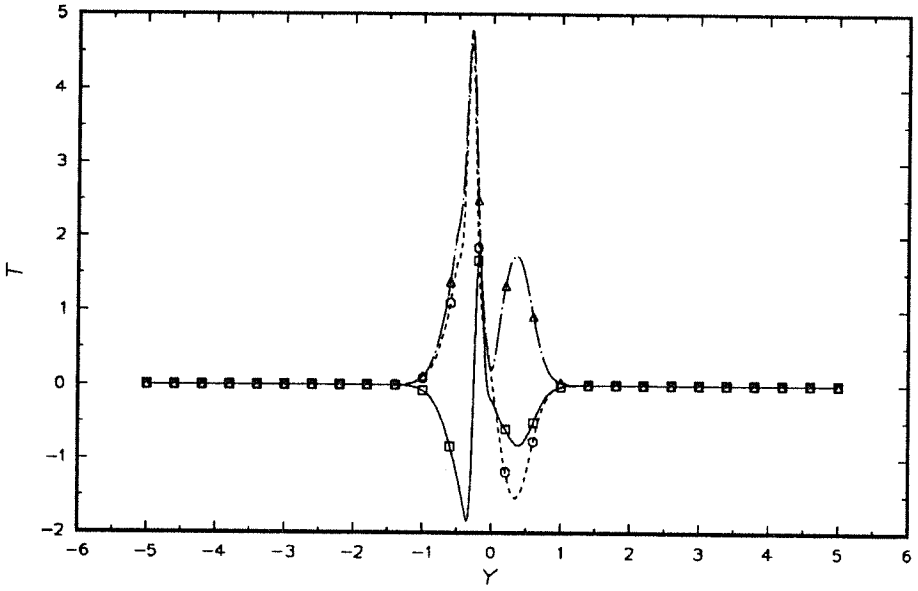

(d)

FIGURE 6.14. Linear eigenfunctions of the non-reacting confined flow (slow mode) (a) $\hat{\omega}_z$ (b) $\hat{p}$ (c) $\hat{\rho}$ (d) $\hat{T}$. M_1=6 (M_c=1.5), $\bar{T}_2$=1, T_{ad}=1, m=0, H=5. □ , real; ○ , imaginary; △ , absolute.

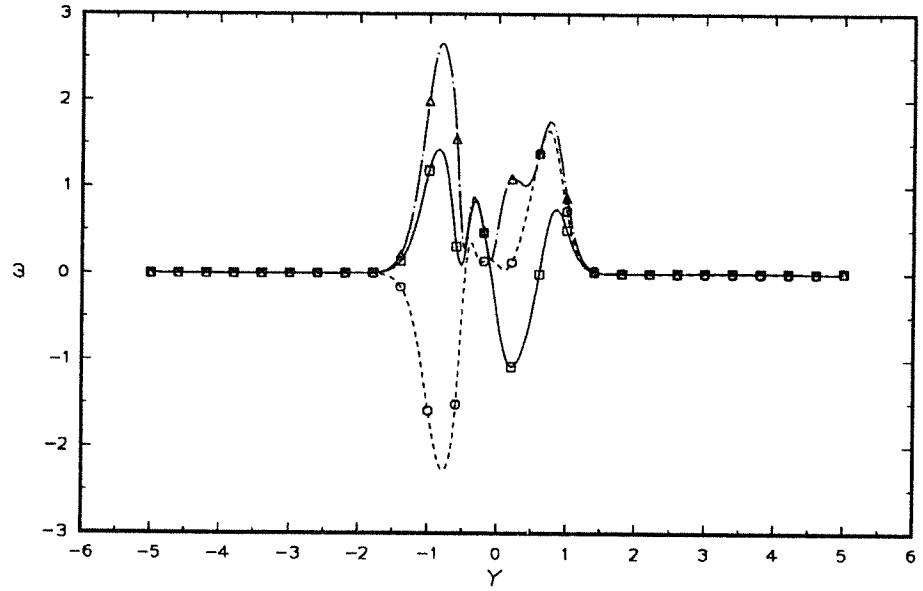

(a)

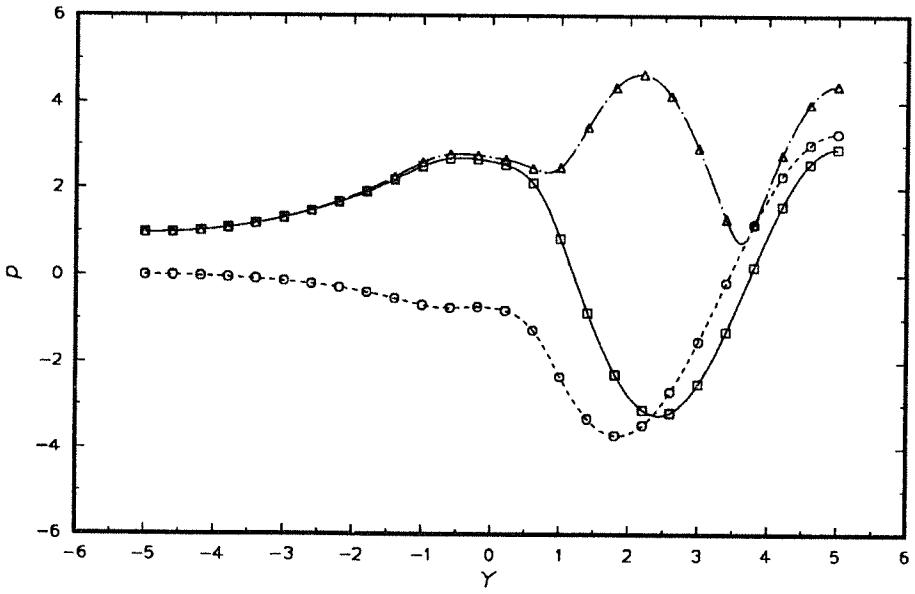

(b)

FIGURE 6.15. Continued.

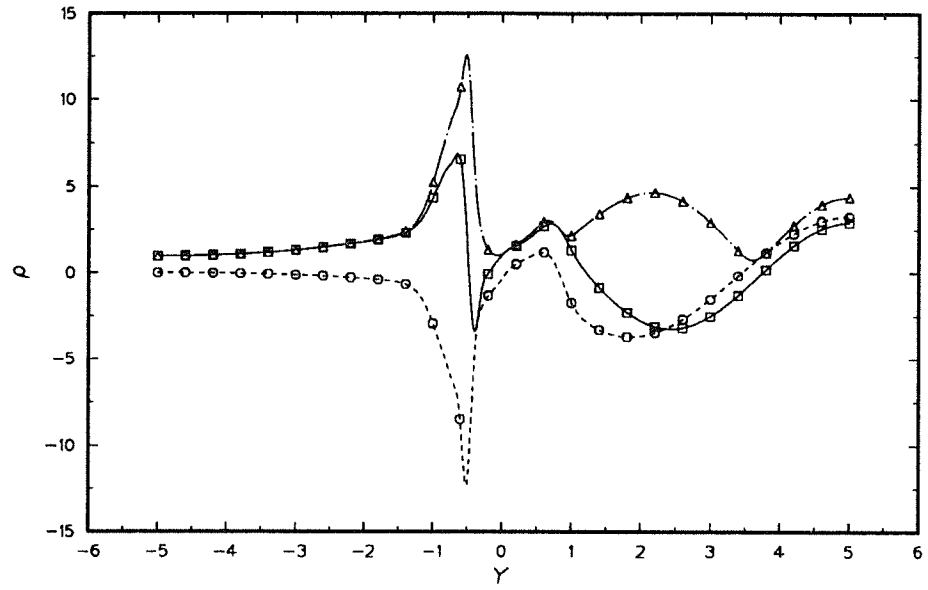

(c)

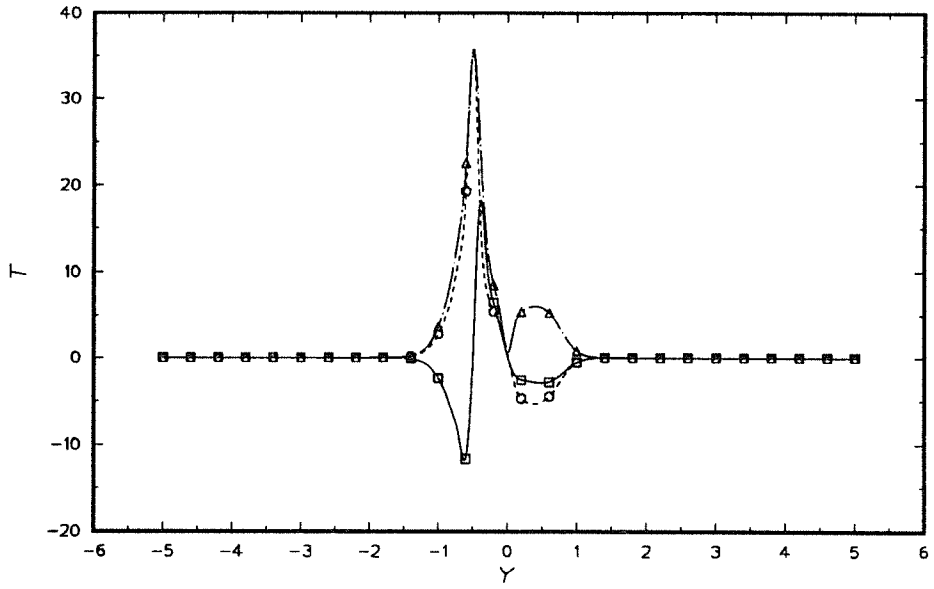

(d)

FIGURE 6.15. Continued.

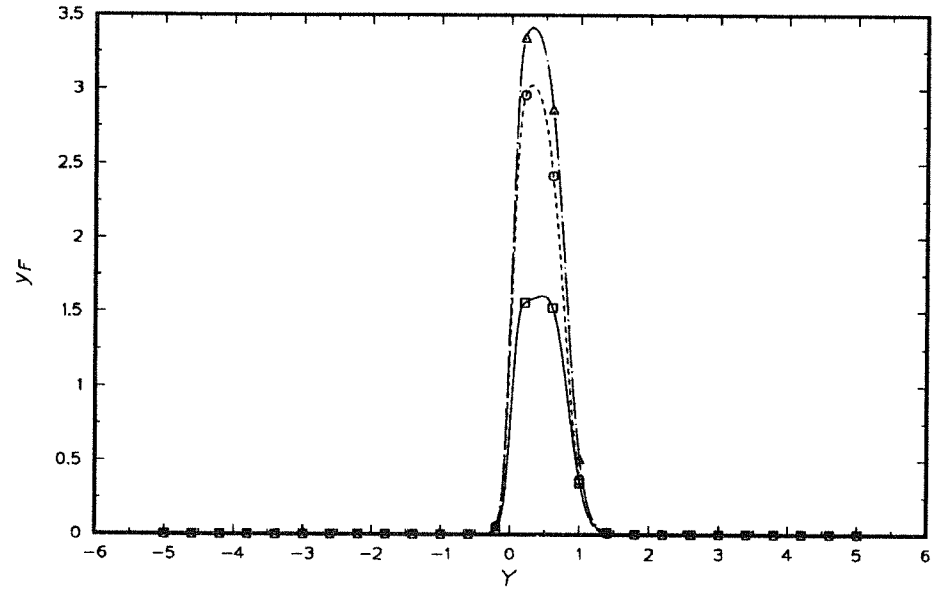

(e)

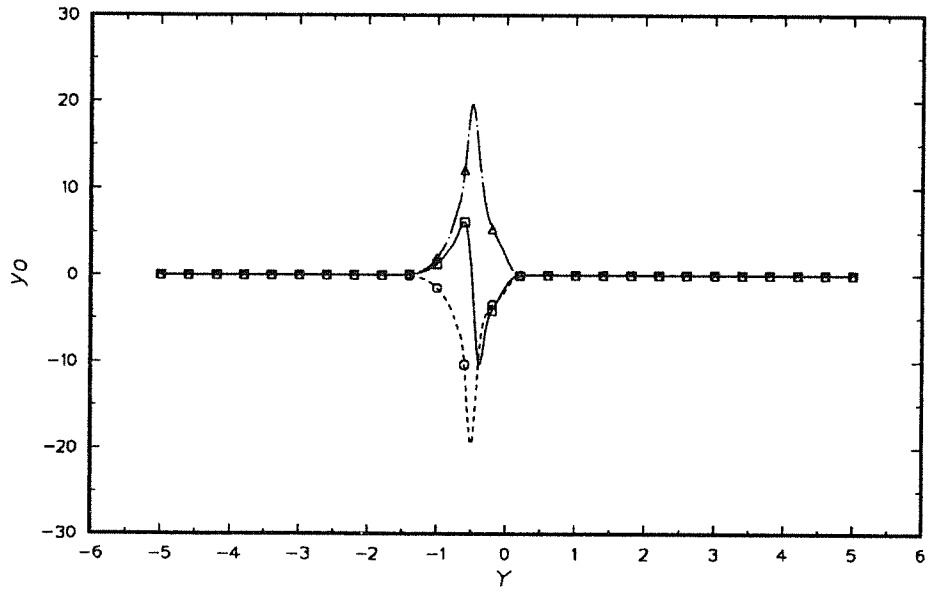

(f)

FIGURE 6.15. Linear eigenfunctions of the reacting confined flow (slow mode) (a) $\hat{\omega}_z$ (b) $\hat{p}$ (c) $\hat{\rho}$ (d) $\hat{T}$ (e) $\hat{y}_F$ (f) $\hat{y}_O$. M_1=6 (M_c=1.5), $\bar{T}_2$=1, T_{ad}=4, m=0, Da=10, H=5. □ , real; ○ , imaginary; △ , absolute.

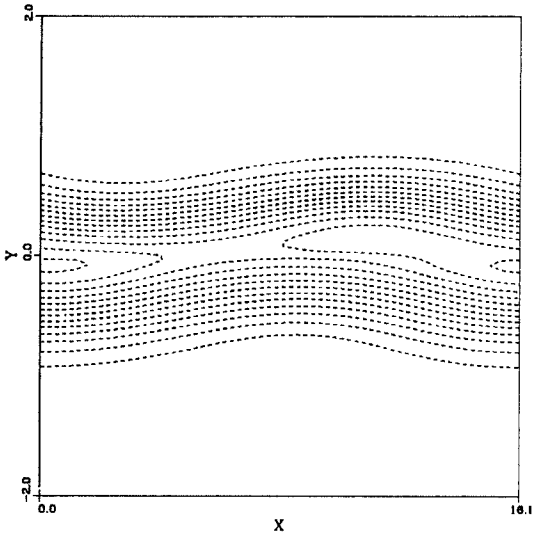

(a) max=$2.51\text{x}10^{-4}$, min=-0.266

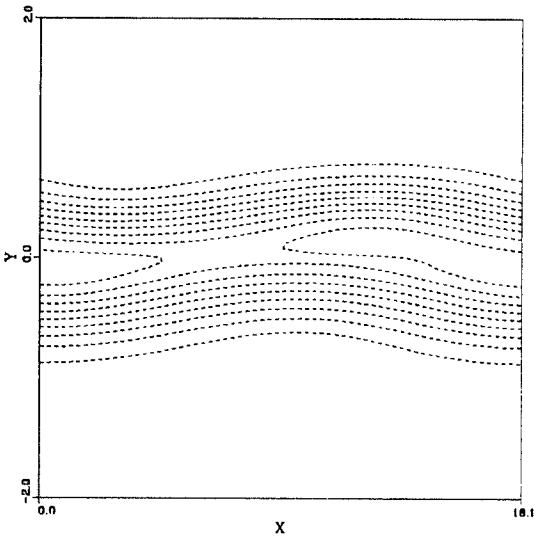

(b) max=$2.46\text{x}10^{-4}$, min=-0.396

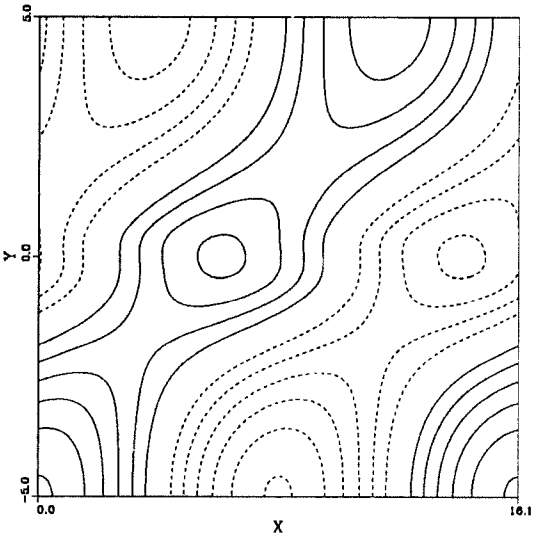

(c) max=1.122, min=0.878

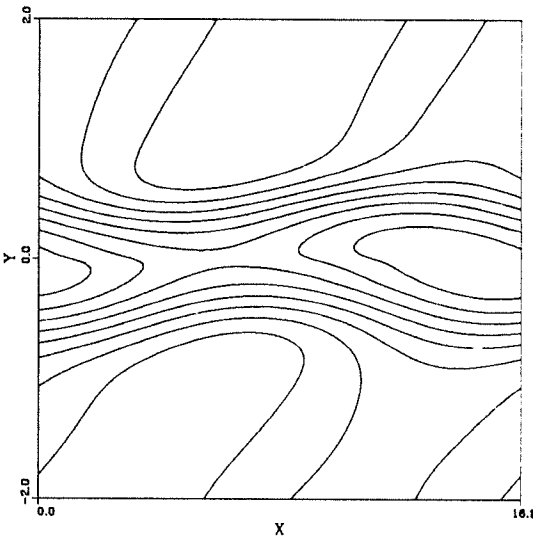

(d) max=1.063, min=0.623

FIGURE 6.16. Continued.

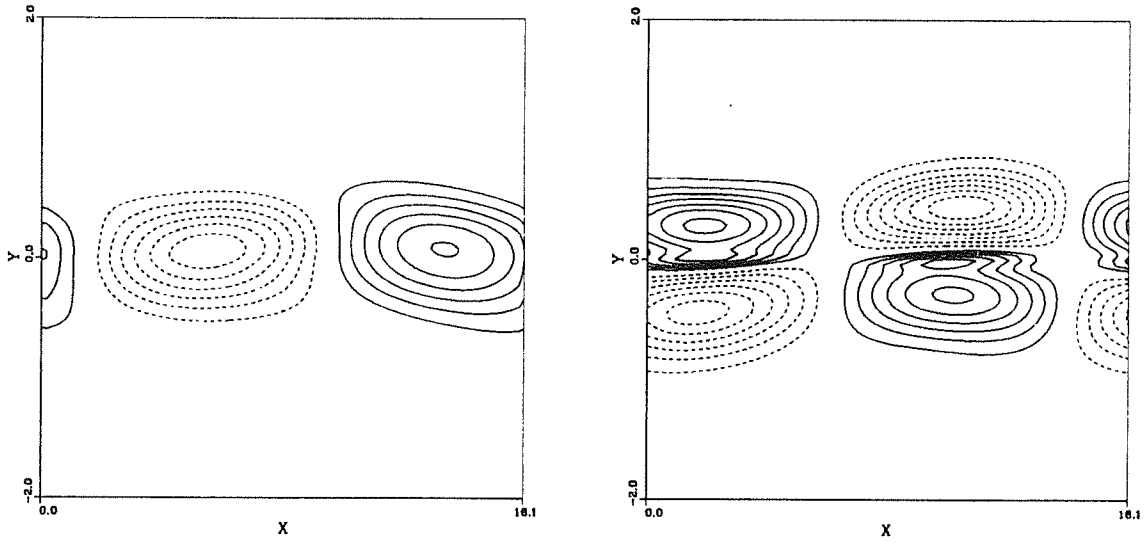

(e) max=2.44x10^{-4}, min=-2.74x10^{-4} (f) max=1.47x10^{-2}, min=-1.57x10^{-2}

FIGURE 6.16. Contour plots from linear eigenfunctions of the non-reacting confined flow (center mode). (a) ω_z (b) ω_z/ρ (c) pressure (d) density (e) dilatation term (f) baroclinic term. M_1=6 (M_c=1.5), $\bar{T}_2$=1, T_{ad}=1, m=0, H=5.

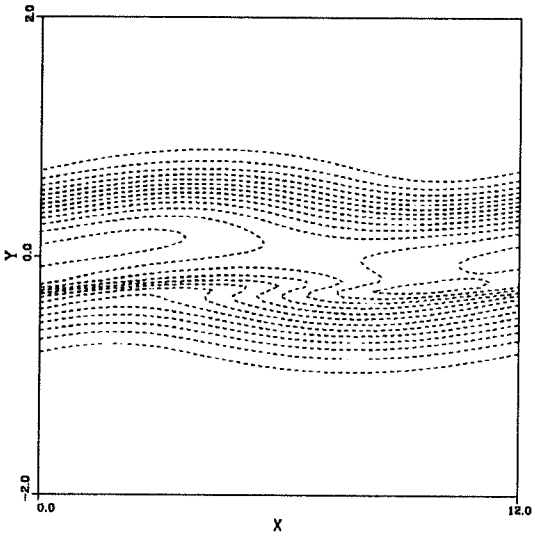

(a) max=$1.11\text{x}10^{-3}$, min=-0.270

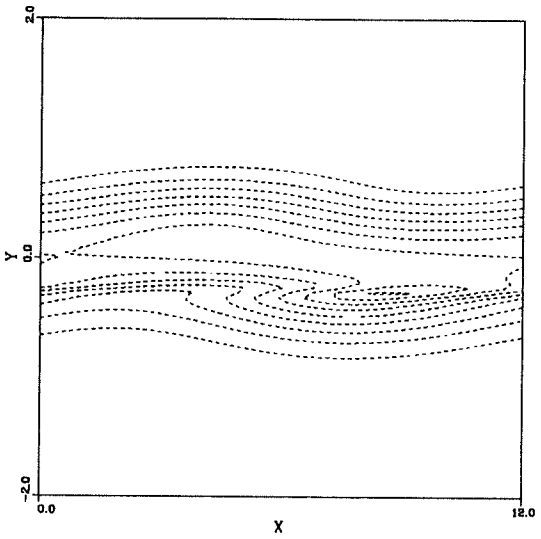

(b) max=$1.12\text{x}10^{-3}$, min=-0.458

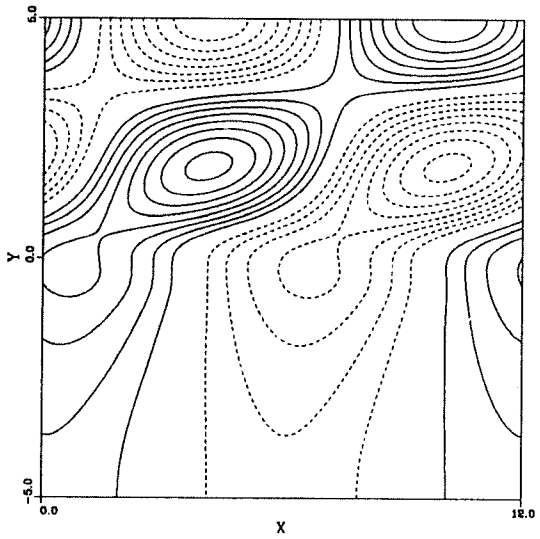

(c) max=1.167, min=0.833

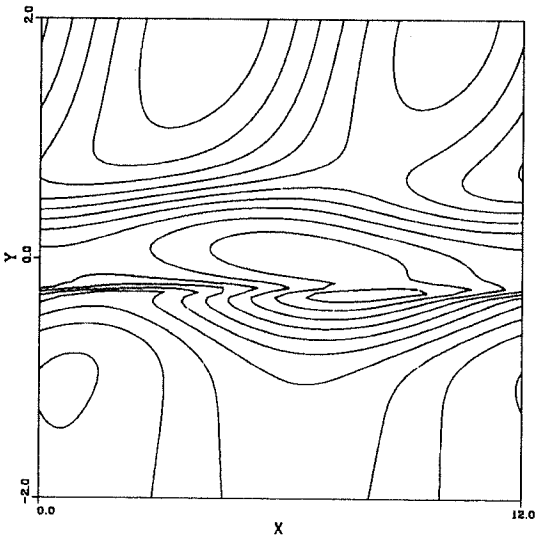

(d) max=1.167, min=0.571

FIGURE 6.17. Continued.

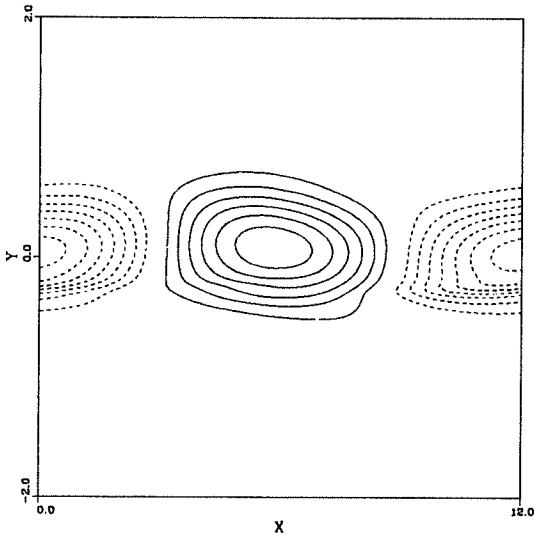

(e) max=3.39x10^{-4}, min=-3.79x10−4

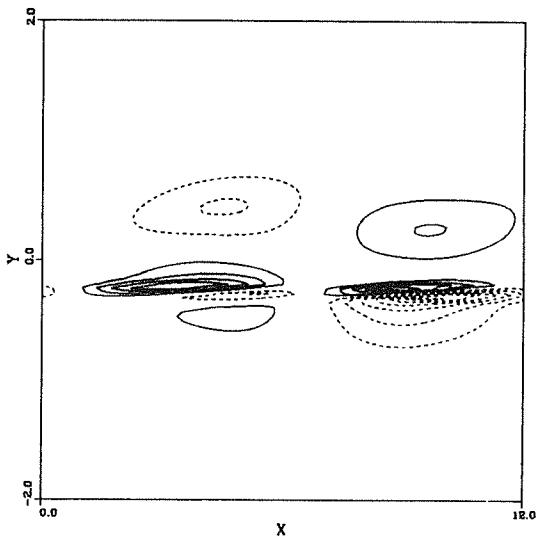

(f) max=5.04x10^{-2}, min=-6.38x10−2

FIGURE 6.17. Contour plots from linear eigenfunctions of the non-reacting confined flow (slow mode). (a) ω_z (b) ω_z/ρ (c) pressure (d) density (e) dilatation term (f) baroclinic term. M_1=6 (M_c=1.5), $\bar{T}_2$=1, T_{ad}=1, m=0, H=5.

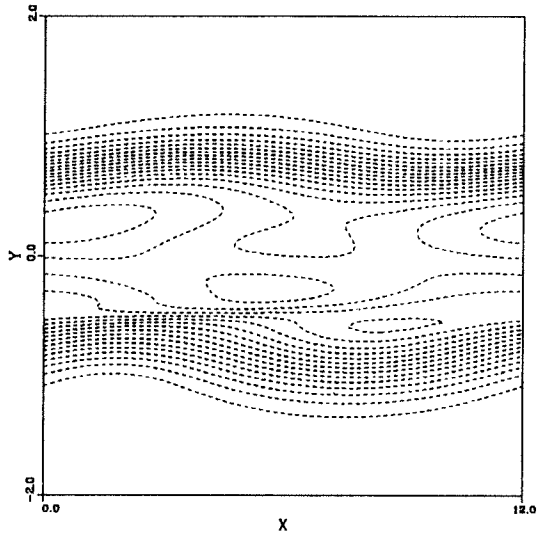

(a) max=2.58x10^{-3}, min=-0.175

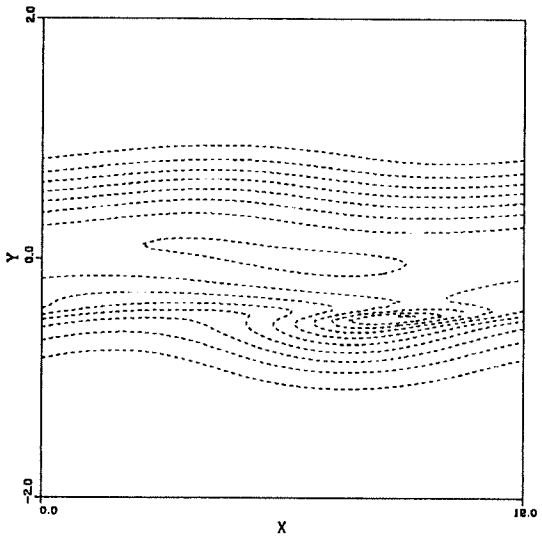

(b) max=2.77x10^{-3}, min=-0.504

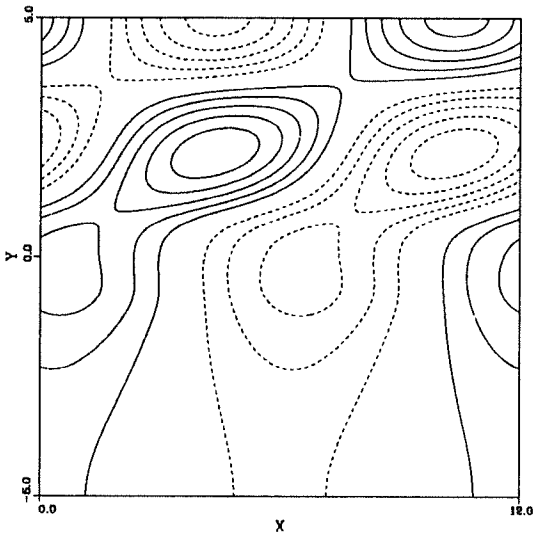

(c) max=1.116, min=0.884

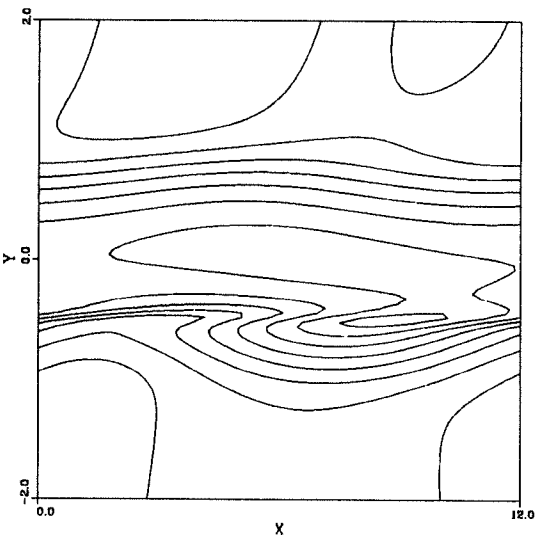

(d) max=1.115, min=0.268

FIGURE 6.18. Continued.

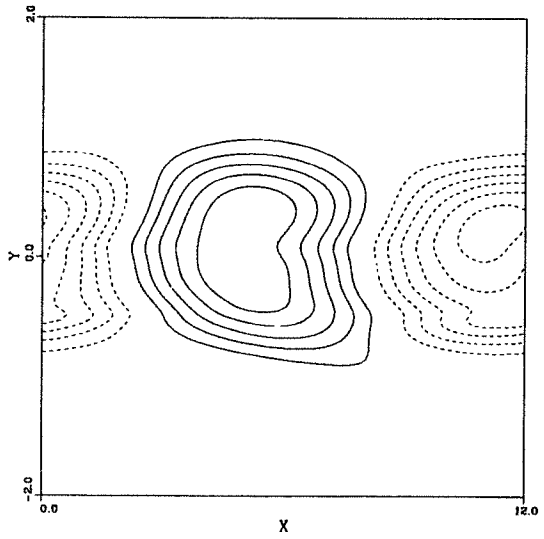

(e) max=1.26x10^{-3}, min=-1.32x10^{-3}

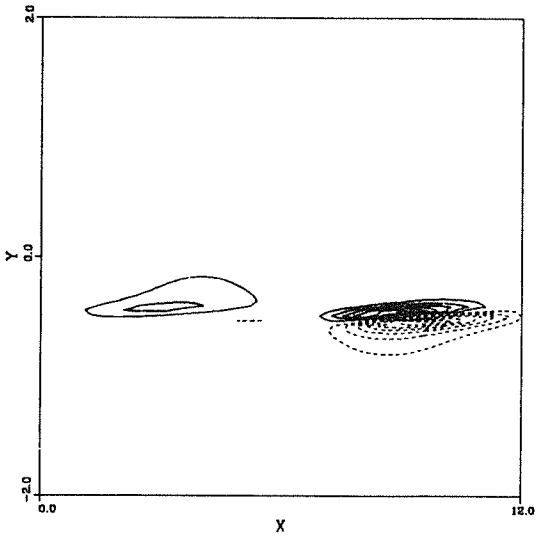

(f) max=0.246, min=-0.293

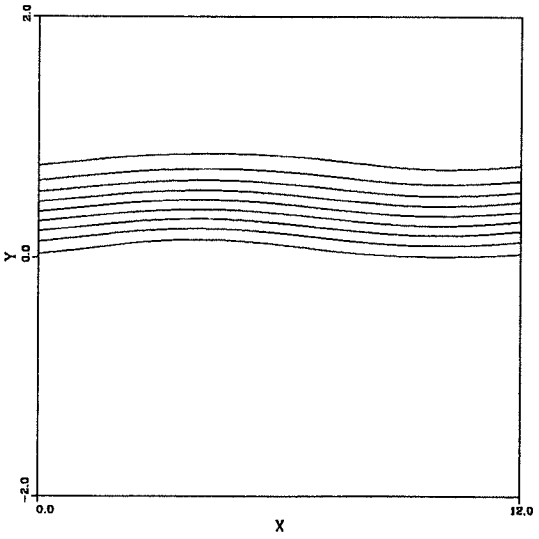

(g) max=1.0, min=0.0

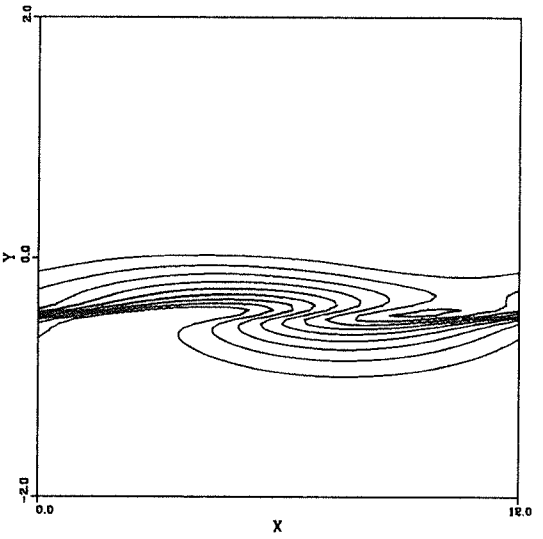

(h) max=1.0, min=0.0

FIGURE 6.18. Contour plots from linear eigenfunctions of the reacting confined flow (slow mode). (a) ω_z (b) ω_z/ρ (c) pressure (d) density (e) dilatation term (f) baroclinic term (g) fuel (h) oxidizer. M_1=6 (M_c=1.5), $\bar{T}_2$=1, T_{ad}=4, m=0, Da=10, H=5.

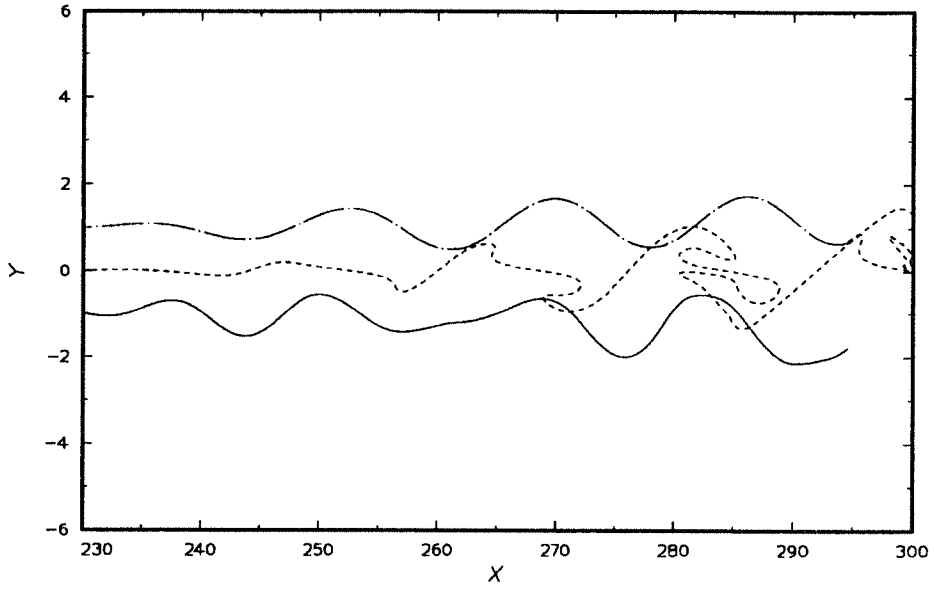

(a)

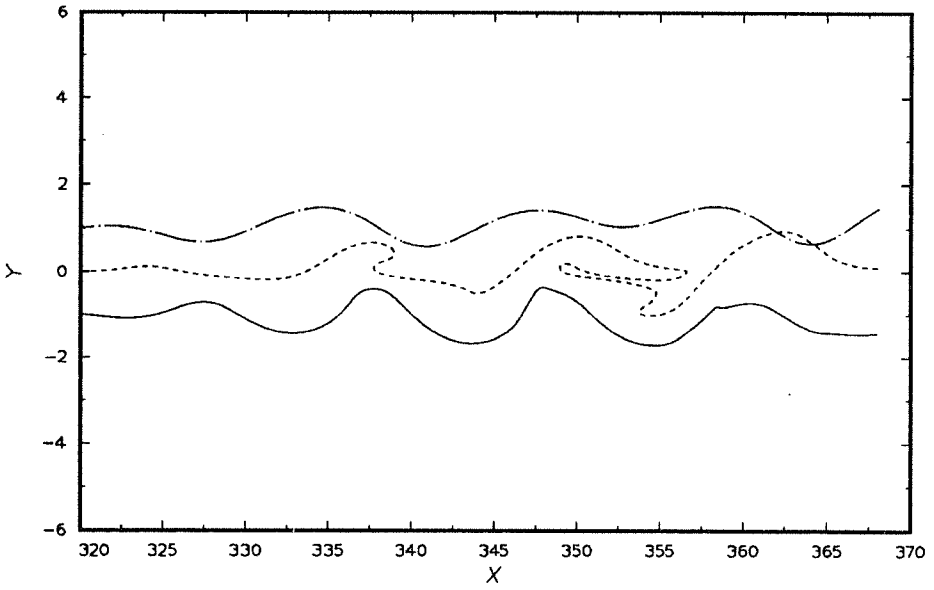

(b)

FIGURE 6.19. Continued.

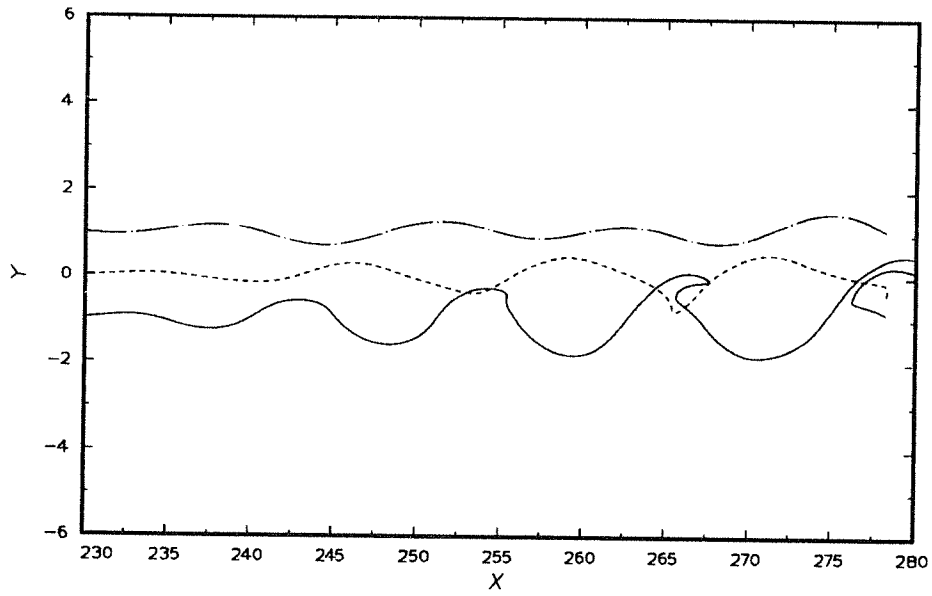

(c)

FIGURE 6.19. Streaklines for the confined shear layers at M_1=6 (M_c=1.5). (a) non-reacting center mode (T_{ad}=1) (b) non-reacting slow mode (T_{ad}=1) (c) reacting slow mode (T_{ad}=4). $\bar{T}_2$=1, m=0, H=5.

Chapter 7

Conclusions and Recommendations

7.1 Conclusions

We have studied the behavior of compressible reacting mixing layers using linear stability analysis. The chemistry model is a single step, irreversible, finite rate reaction between the fuel in the upper stream and oxidizer in the lower stream. We developed an inviscid linear stability theory for compressible reacting flows by including chemical reaction effects. The stability equations were solved by a combination of the shooting and Newton-Raphson methods for a large range of Mach number and heat release. The conclusions are divided into the four main areas: laminar flows, instability of incompressible reacting free shear layers, instability of compressible reacting free shear layers and instability of confined compressible reacting shear layers. For reference, Fig. 7.1 shows the diagram of the most dominant unstable modes with their phase speeds in the isentropic convective Mach number and adiabatic flame temperature plane, and Fig. 7.2 shows the corresponding maximum growth rates.

7.1.1 *Laminar Flows*

The laminar flows were calculated by solving the compressible boundary-layer equations. The results illustrate the structure of laminar diffusion flames. We found that property variation affects the laminar profiles and the stability characteristics considerably; property variations need to be included when there are large temperature differences. The maximum temperature in a laminar reacting mixing layer is almost linear with the adiabatic flame temperature. The normalized product thickness depends strongly on the adiabatic flame temperature at low heat release, but only weakly at high heat release.

The Damköhler number affects the structure of laminar diffusion flames. When the Damköhler number is low ($Da < 2$), it strongly influences the rate of product formation and the growth of the layer thickness; the flow is reaction limited. At a high Damköhler number ($Da > 2$), both rates approach asymptotic values and the growth of the layer is diffusion limited. Compressibility changes the structure of

the laminar layer only slightly when the heat release is high. Free-stream density ratios and equivalence ratios affect the temperature profiles considerably. Ignition, premixed flame, and diffusion flame regimes are found in the laminar reacting mixing layer at high activation energy. At high Mach numbers, ignition occurs earlier due to the higher temperatures in the unburnt gas.

7.1.2 *Instability of the Incompressible Reacting Free Shear Layer*

For the stability study of incompressible flows with density variation, a set of equations valid in the limit of zero Mach number was used. We derived a necessary condition for instability; the condition requires that the angular momentum, not the vorticity, have a maximum in the flow domain. We found new inflectional modes of instability in the outer part of the mixing layer when the heat release is significant. Heat release stabilizes the flow; in particular, it greatly reduces the growth rate of the center mode. The growth rates of the outer modes, which do not exist in the cold flow, are relatively insensitive to heat release. For heat releases typical of combusting flows, the outer modes are more amplified than the center mode. From the eigensolutions of the linear theory, we obtained information about coherent structures in the unstable flow. Both the outer and the center modes have four vorticity maxima per wavelength. The streakline patterns suggest that the outer modes in reacting mixing layers do not cause the flow to roll up in the same way as does the center mode in an incompressible non-reacting mixing layer. Mixing between the fuel and oxidizer is thereby reduced.

The growth rates of instabilities are very sensitive to the mean profiles. Solutions of the boundary-layer equations with variable transport properties are more realistic representations of an actual flow than analytically prescribed functions and provide a better basis for stability analysis.

Increasing Damköhler number is stabilizing at low Damköhler numbers but has little effect at higher Damköhler numbers. At low Damköhler numbers, the direct effect of the chemical reaction on the disturbances is significant and it is important to use consistent Damköhler numbers in stability calculations. At high Damköhler numbers, the density variation caused by chemical reaction in the laminar flow affects the growth rate of the instability much more than chemical reaction during the instability; the flame sheet model is valid in this regime.

The low-speed mixing layer containing high-density gas in the slower stream, is more unstable than the corresponding flow containing uniform- or low-density gas

in the slower stream. Any deviation from stoichiometric conditions destabilizes the flow by reducing the total heat release. For a given adiabatic flame temperature, the fuel-lean case is the most unstable. Finally, two dimensional waves are more amplified than three dimensional ones, although slightly oblique modes may play a role.

7.1.3 *Instability of the Compressible Reacting Free Shear Layer*

In compressible free shear layers, supersonic unstable modes can exist in the absence of a generalized inflection point, provided that there is a region of mean flow supersonic relative to the disturbance phase velocity. The growth rate of the mixing layer drops with increasing Mach number and approaches an asymptotic value at high Mach numbers where the outer modes dominate. Heat release stabilizes low-speed flows but destabilizes high-speed flows. However, the growth rates are small compared to the incompressible cold flow value. The radiative nature of supersonic disturbances, demonstrated by the pressure contours, is one reason for the decreased growth rates. The structure of the dilatational and baroclinic terms suggests that the latter reduces the growth rate of the two-dimensional vorticity. Supersonic disturbances do not mix the reactants very well because they are largely confined to one side of the flow.

For non-reacting supersonic flows at $M_c > 0.6$, the most unstable modes are oblique center modes that are subsonic relative to both free streams. For reacting flows with $T_{ad} > 3$, the most unstable modes are two-dimensional outer modes even at high Mach numbers. The growth rates normalized by the corresponding incompressible growth rates show that the convective Mach number can be used as an overall measure of the effect of compressibility for non-reacting flows but not for reacting-flows.

7.1.4 *Instability of the Confined Compressible Reacting Shear Layer*

For confined supersonic mixing layers, we studied the effect of walls on the stability. Reflection of supersonic disturbances by the walls makes the mixing layer more unstable than the unconfined free shear layer. Decreasing the distance between the walls makes the flow more unstable. Subsonic disturbances are relatively unaffected by the walls. Heat release and Mach number hardly change the maximum growth rates of supersonic disturbances. The growth rates of instabilities in the supersonic mixing layer are very small compared to the corresponding incompressible value. The normalized growth rates for non-reacting flows agree well with experimental results.

The most unstable supersonic disturbances are two-dimensional in rectangular channel flows, but three-dimensional in partially confined flows. The supersonic center mode radiates to both boundaries, whereas the outer modes propagate only to the boundary relative to which they are supersonic. Pressure contours show compression/expansion waves that propagate at the Mach angle. Finally, the reactants are not strongly mixed by supersonic instabilities which mainly disturb one side of the layer.

7.2 Future Work

The present study has produced results concerning the stability of compressible reacting mixing layers. The following topics are suggested for further research:

- Effects of splitter plate:

  Although this work considered established laminar profiles, the flow field right after the splitter tip will be very complicated and be far from clean (cf. Clemens & Mungal [1992]); the flow field will be affected by the recovery temperature and the wake produced by the splitter plate. Inclusion of these effects in laminar profiles will improve the stability study of compressible reacting mixing layers.

- Viscous stability analysis:

  Even though inviscid stability theory is a reliable guide for free shear layers, inclusion of diffusion terms is needed for full understanding of the physics of these flows. In viscous analysis, the center mode might be less unstable than in inviscid analysis due to the increased viscosity in the central portion of the layer but the outer modes might change little because they occur in the outer parts of the layer. Viscous stability analysis can check the above expectation and will also allow the study of the effect of parameters such as the Lewis and Prandtl numbers.

- Other shear flows:

  Although this work considered plane reacting mixing layers, an extension to more complicated flows such as jets and wakes is very important. For these flows, the boundary conditions and asymptotic solutions are different from those in the plane layers. We expect that multiple modes of instabilities similar to the ones found in this work exist in those flows.

- Non-parallel theory:

  In the stability analysis, we assumed parallel flows, neglecting streamwise variation and the small transverse velocity. While this assumption can be tolerated for large-wavenumber disturbances, it is incorrect for small wavenumber disturbances. In addition, reacting mixing layers are not self-similar and the wake formed by trailing edge might alter the mean profiles considerably. Therefore, we need to consider non-parallel effects. The parabolized stability equations might be useful for this purpose.

- Secondary instability analysis:

  We studied the linear instability to small disturbances. In the next stage of transition, the disturbances are still weak and grow exponentially while non-linear distortion of the mean flow profile is negligible. Eventually, the primary instability become fully developed and modifies the base flow. The modified flow can be used as input to secodary instability analysis. Such a study would link the linear and non-linear stages of transition.

- Three-dimensional mean flow (streamwise vortices):

  We studied the parallel reacting mixing layer with velocity vector $\mathbf{V}=(U(y),0,0)$. However, the real mixing layer might have streamwise vortices, which could change the stability characteristics considerably. Thus, we suggest the stability study with three-dimensional flows with $\mathbf{V}=(U,V,W)$ and $\mathbf{V}=\mathbf{V}(y,z)$.

- Non-linear simulation:

  The linear eigenfunctions from the current study can provide initial conditions for direct numerical simulations. Non-linear simulations with two species, including finite reaction rate terms, need to be done to confirm the results of the linear stability study and to see the effects of the heat release on the later development of the reacting mixing layer.

- Reaction model:

  More realistic multistep chemistry models will be useful for comparison with experiments. This will allow the study of such technologically important phenomena as extinction. The study of turbulent diffusion flames, including the ignition, premixed flames and diffusion flames regimes is needed.

- Experiments:

  Experimental measurements of transitional and turbulent compressible reacting flows are lacking. We suggest making more experimental measurements, including the growth rates, three-dimensional behavior and mixing between the fuel and oxidizer. Also, stability analysis of measured experimental profiles will be useful to improve the laminar profiles considered in this work.

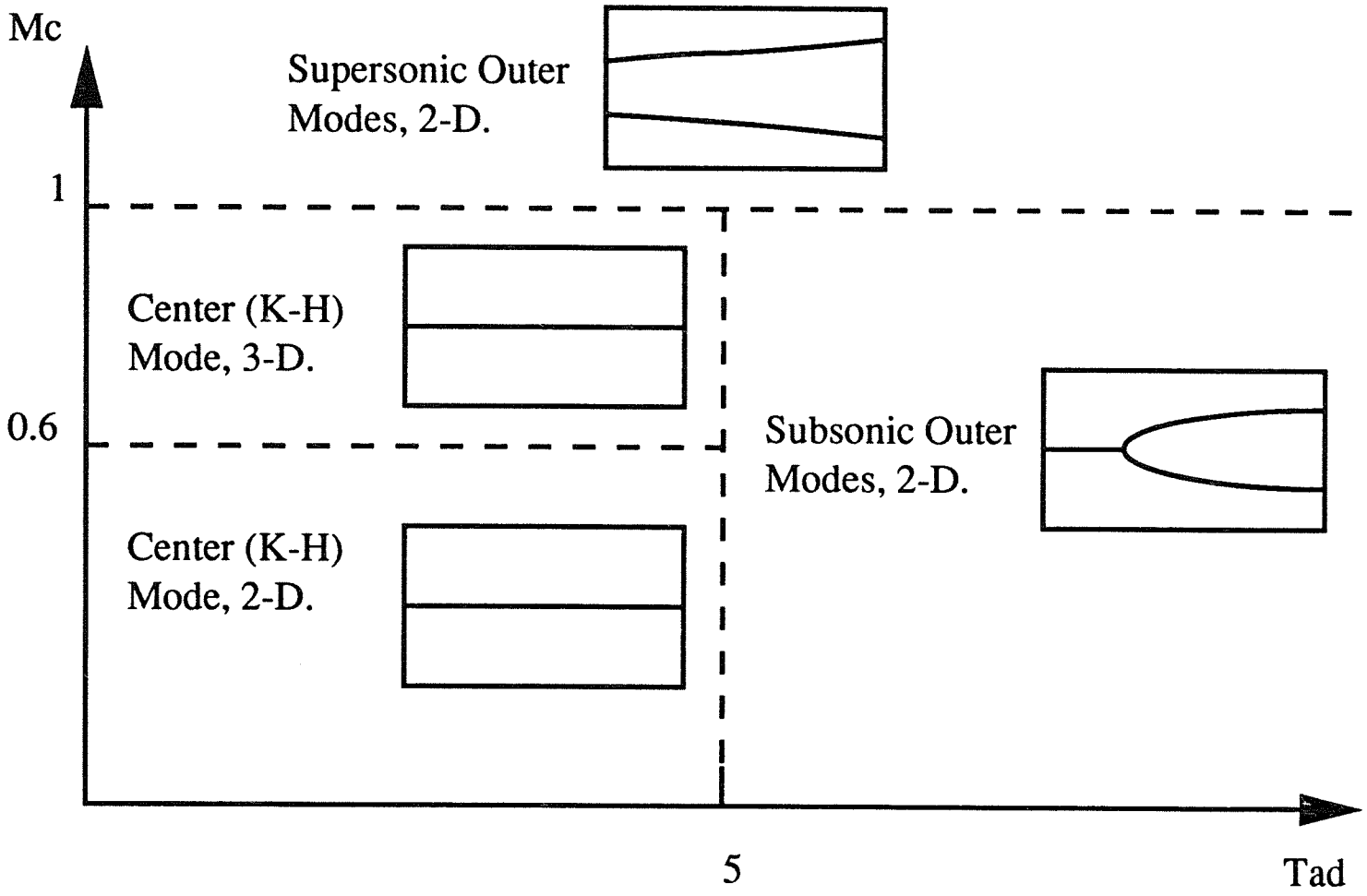

FIGURE 7.1. The most dominant unstable modes with their phase speeds.

$-\alpha_{imax}$

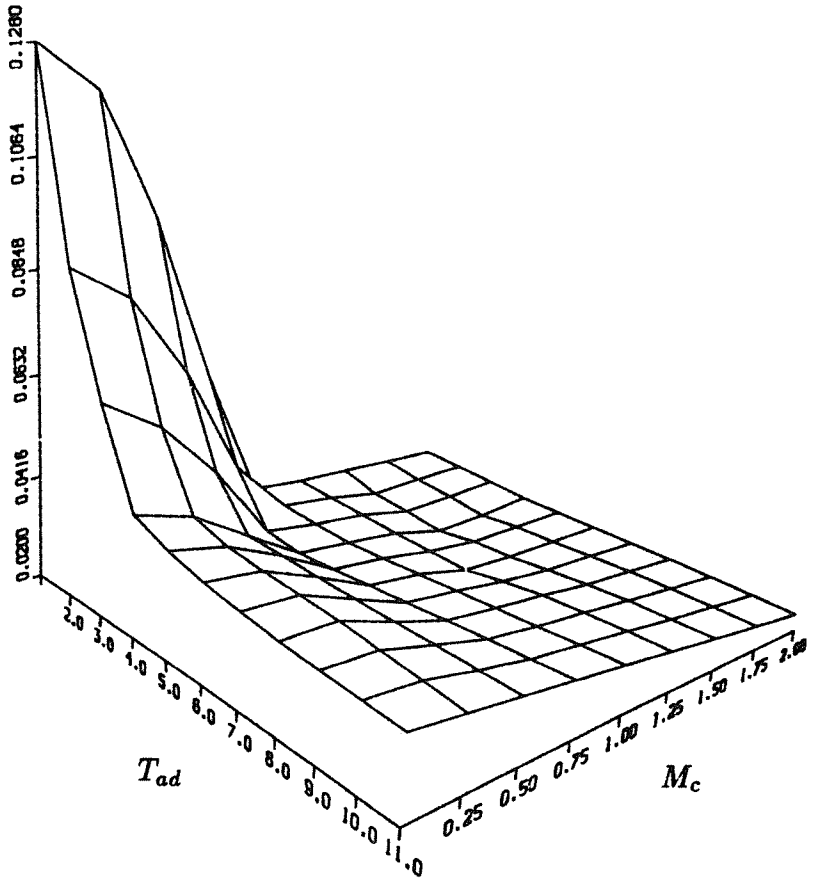

FIGURE 7.2. Maximum growth rates.

Appendix

A.1 Expression for Jacobian $\partial W/\partial\Phi$

The expression for the Jacobian $\partial W/\partial\Phi$, which was used in Sec. 2.2.2, is given.

$$\frac{\partial W}{\partial \Phi} = \begin{bmatrix} 0 & 0 & 0 & 0 & 0 \\ 0 & 0 & 0 & 0 & 0 \\ 0 & 0 & w_{33} & w_{34} & w_{35} \\ 0 & 0 & w_{43} & w_{44} & w_{45} \\ 0 & 0 & w_{53} & w_{54} & w_{55} \end{bmatrix} \tag{A.1}$$

$$w_{33} = Da\frac{Q}{W_F\nu_F}(2\rho - \beta'\rho^2)y_F y_O exp\left[-\beta'\left(\frac{1}{T}-1\right)\right]$$

$$w_{34} = Da\frac{Q}{W_F\nu_F}\rho^2 y_O exp\left[-\beta'\left(\frac{1}{T}-1\right)\right]$$

$$w_{35} = w_{34}\frac{y_F}{y_O}$$

$$w_{43} = -w_{33}\frac{W_F\nu_F}{Q}$$

$$w_{44} = -w_{34}\frac{W_F\nu_F}{Q}$$

$$w_{45} = -w_{35}\frac{W_F\nu_F}{Q}$$

$$w_{53} = w_{43}\frac{W_O\nu_O}{W_F\nu_F}$$

$$w_{54} = w_{44}\frac{W_O\nu_O}{W_F\nu_F}$$

$$w_{55} = w_{45}\frac{W_O\nu_O}{W_F\nu_F}$$

A.2 Expressions for $\hat{A}_j, \hat{B}_j, \hat{C}_j$ and R_j

The expressions for the block matrices and vector used in Sec. 2.2.2 are

$$\hat{A}_j = [A_{mn}]_j, \quad \hat{B}_j = [B_{mn}]_j, \quad \hat{C}_j = [C_{mn}]_j, \quad R_j = [R_m]_j \tag{A.2}$$

$$A_{11} = \frac{\rho''_{j-1}}{\Delta x}$$

$$A_{12} = -\frac{\rho''_{j-1}}{h'_{j-1/2}\Delta\eta}$$

$$A_{13} = \frac{u''_{j-1}}{\Delta x} - \frac{v''_{j-1}}{h'_{j-1/2}\Delta\eta}$$

$$A_{21} = -\frac{\rho_j'' v_j''}{4h_j'\Delta\eta} - \frac{\mu_{j-1/2}}{2Reh_j'h_{j-1/2}'\Delta\eta^2}$$

$$A_{31} = \frac{(\gamma-1)M_1^2\mu_j(u_{j+1}''-u_{j-1}'')}{Re(h_j'\Delta\eta)^2}$$

$$A_{33} = \frac{\rho_j'' v_j'' T_{j-1}''}{4\rho_{j-1}'' h_j'\Delta\eta} + \frac{\kappa_{j-1/2}T_{j-1}''}{2\rho_{j-1}''PrReh_j'h_{j-1/2}'\Delta\eta^2}$$

$$A_{44} = -\frac{\rho_j'' v_j''}{4h_j'\Delta\eta} - \frac{(\rho D)_{j-1/2}}{2ReSch_j'h_{j-1/2}'\Delta\eta}$$

$$A_{55} = A_{44}$$

$$A_{14} = A_{15} = A_{22} = A_{23} = A_{24} = A_{25} = A_{32} = A_{34} = A_{35} = A_{41} = 0$$

$$A_{42} = A_{43} = A_{45} = A_{51} = A_{52} = A_{53} = A_{54} = 0$$

$$B_{11} = \frac{\rho_j''}{\Delta x}$$

$$B_{12} = \frac{\rho_j''}{h_{j-1/2}'\Delta\eta}$$

$$B_{13} = \frac{u_j''}{\Delta x} + \frac{v_j''}{h_{j-1/2}'\Delta\eta}$$

$$B_{21} = \frac{\rho_j'' u_j''}{\Delta x} + \frac{1}{2Reh_j'\Delta\eta^2}\left(\frac{\mu_{j-1/2}}{h_{j-1/2}'} + \frac{\mu_{j+1/2}}{h_{j+1/2}'}\right)$$

$$B_{22} = \frac{\rho_j''(u_{j+1}''-u_{j-1}'')}{4h_j'\Delta\eta}$$

$$B_{23} = \frac{v_j''(u_{j+1}''-u_{j-1}'')}{4h_j'\Delta\eta}$$

$$B_{32} = \frac{\rho_j''(T_{j+1}''-T_{j-1}'')}{4h_j'\Delta\eta}$$

$$B_{33} = \frac{v_j''(T_{j+1}''-T_{j-1}'')}{4h_j'\Delta\eta} - \frac{u_j''T_j''}{\Delta x} - \frac{T_j''}{2\rho_j''PrReh_j'\Delta\eta^2}\left[\frac{\mu_{j-1/2}}{h_{j-1/2}'} + \frac{\mu_{j+1/2}}{h_{j+1/2}'}\right] - \frac{w_{33}}{2}$$

$$B_{34} = -\frac{w_{31}}{2}$$

$$B_{35} = -\frac{w_{35}}{2}$$

$$B_{42} = \frac{\rho_j''(y_{Fj+1}''-y_{Fj-1}'')}{4h_j'\Delta\eta}$$

$$B_{43} = \frac{v_j''(y_{Fj+1}''-y_{Fj-1}'')}{4h_j'\Delta\eta} - \frac{w_{43}}{2}$$

$$B_{44} = \frac{\rho_j'' u_j''}{\Delta x} + \frac{1}{2ReSch_j'\Delta\eta^2}\left[\frac{(\rho D)_{j-1/2}}{h_{j-1/2}'} + \frac{(\rho D)_{j+1/2}}{h_{j+1/2}'}\right] - \frac{w_{11}}{2}$$

$$B_{45} = -\frac{w_{45}}{2}$$

$$B_{52} = \frac{\rho_j''(y_{Oj+1}''-y_{Oj-1}'')}{4h_j'\Delta\eta}$$

$$B_{53} = \frac{v_j''(y_{O_{j+1}}''-y_{O_{j-1}}'')}{4h_j'\Delta\eta} - \frac{w_{53}}{2}$$

$$B_{54} = -\frac{w_{54}}{2}$$

$$B_{55} = \frac{\rho_j''u_j''}{\Delta x} + \frac{1}{2ReSch_j'\Delta\eta^2}\left[\frac{(\rho D)_{j-1/2}}{h'_{j-1/2}} + \frac{(\rho D)_{j+1/2}}{h'_{j+1/2}}\right] - \frac{w_{55}}{2}$$

$$B_{14} = B_{15} = B_{23} = B_{24} = B_{25} = B_{31} = B_{34} = B_{35} = B_{41} = B_{45} = B_{51} = 0$$

$$C_{21} = \frac{\rho_j''v_j''}{4h_j'\Delta\eta} - \frac{\mu_{j+1/2}}{2Reh_j'h'_{j+1/2}\Delta\eta^2}$$

$$C_{31} = -A_{31}$$

$$C_{33} = -\frac{\rho_j''v_j''T_{j+1}''}{4\rho_{j+1}''h_j'\Delta\eta} + \frac{\kappa_{j+1/2}T_{j+1}''}{2\rho_{j+1}''PrReh_j'h'_{j+1/2}\Delta\eta^2}$$

$$C_{44} = \frac{\rho_j''v_j''}{4h_j'\Delta\eta} - \frac{(\rho D)_{j+1/2}}{2ReSch_j'h'_{j+1/2}\Delta\eta}$$

$$C_{55} = C_{44}$$

$$C_{11} = C_{12} = C_{13} = C_{14} = C_{15} = C_{22} = C_{23} = C_{24} = C_{25} = 0$$

$$C_{32} = C_{34} = C_{35} = C_{41} = C_{42} = C_{43} = C_{45} = C_{51} = C_{52} = C_{53} = C_{54} = 0$$

$$R_1 = \frac{2(\rho_j''u_j''+\rho_{j-1}''u_{j-1}'')}{\Delta x}$$

$$R_2 = \frac{\rho_j''u_j''^2}{\Delta x} + \frac{\rho_j''v_j''(u_{j+1}''-u_{j-1}'')}{4h_j'\Delta\eta} + \frac{1}{2Reh_j'\Delta\eta^2}\left[\frac{\mu_{j+1/2}(u_{j+1}''-u_j'')}{h'_{j+1/2}} - \frac{\mu_{j-1/2}(u_j''-u_{j-1}'')}{h'_{j-1/2}}\right]$$

$$R_3 = -\frac{u_j''}{\Delta x} - \frac{\rho_j''v_j''(T_{j+1}''-T_{j-1}'')}{4h_j'\Delta\eta} + \frac{Da\omega_{T_j}''}{2} + \frac{3}{2PrReh_j'\Delta\eta^2}\left[\frac{\kappa_{j+1/2}(T_{j+1}''-T_j'')}{h'_{j+1/2}} - \frac{\kappa_{j-1/2}(T_j''-T_{j-1}'')}{h'_{j-1/2}}\right]$$

$$R_4 = \frac{\rho_j''u_j''y_{F_j}}{\Delta x} + \frac{\rho_j''v_j''(y_{F_{j+1}}''-y_{F_{j-1}}'')}{4h_j'\Delta\eta}$$
$$+\frac{1}{2ReSch_j'\Delta\eta^2}\left[\frac{(\rho D)_{j+1/2}(y_{F_{j+1}}''-y_{F_j}'')}{h'_{j+1/2}} - \frac{(\rho D)_{j-1/2}(y_{F_j}''-y_{F_{j-1}}'')}{h'_{j-1/2}}\right] + \frac{Da\omega_{F_j}''}{2}$$

$$R_5 = \frac{\rho_j''u_j''y_{O_j}}{\Delta x} + \frac{\rho_j''v_j''(y_{O_{j+1}}''-y_{O_{j-1}}'')}{4h_j'\Delta\eta}$$
$$+\frac{1}{2ReSch_j'\Delta\eta^2}\left[\frac{(\rho D)_{j+1/2}(y_{O_{j+1}}''-y_{O_j}'')}{h'_{j+1/2}} - \frac{(\rho D)_{j-1/2}(y_{O_j}''-y_{O_{j-1}}'')}{h'_{j-1/2}}\right] + \frac{Da\omega_{O_j}''}{2}$$

A.3 Coefficients for [RXN1] and [RXN2]

The expressions for the coefficients used in Sec. 3.1 are

$$A = i\bar{\rho}(\alpha\bar{u}-\omega) + Da\,\bar{\rho}^2\bar{y}_O exp\left[-\beta'\left(\frac{1}{\bar{T}}-1\right)\right]$$

$$B = \frac{-i\bar{y}_F'}{(\alpha\bar{u}-\omega)}$$

$$C = Da\,\bar{\rho}^2\bar{y}_F exp\left[-\beta'\left(\frac{1}{\bar{T}}-1\right)\right]$$

$$D = Da\left[\frac{\bar{\rho}^2}{\bar{T}^2}\bar{y}_F\bar{y}_O\beta' - 2\frac{\bar{\rho}^2}{\bar{T}}\bar{y}_F\bar{y}_O\right]exp\left[-\beta'\left(\frac{1}{\bar{T}}-1\right)\right]$$

$$E = 2Da\,\bar{\rho}^2\bar{y}_F\bar{y}_O exp\left[-\beta'\left(\frac{1}{\bar{T}}-1\right)\right]$$

$$F = i\bar{\rho}(\alpha\bar{u}-\omega) + Da\frac{W_O\nu_O}{W_F\nu_F}\bar{\rho}^2\bar{y}_O exp\left[-\beta'\left(\frac{1}{\bar{T}}-1\right)\right]$$

$$G = \frac{-i\bar{y}'_O}{(\alpha\bar{u}-\omega)}$$

$$H = Da\frac{W_O\nu_O}{W_F\nu_F}\bar{\rho}^2\bar{y}_O exp\left[-\beta'\left(\frac{1}{\bar{T}}-1\right)\right]$$

$$I = Da\frac{W_O\nu_O}{W_F\nu_F}\left[\frac{\bar{\rho}^2}{\bar{T}^2}\bar{y}_F\bar{y}_O\beta' - 2\frac{\bar{\rho}^2}{\bar{T}}\bar{y}_F\bar{y}_O\right]exp\left[-\beta'\left(\frac{1}{\bar{T}}-1\right)\right]$$

$$J = E$$

$$K = i\gamma\bar{\rho}(\alpha\bar{u}-\omega) - Da\frac{Q}{W_F\nu_F}\left[\frac{\bar{\rho}^2}{\bar{T}^2}\bar{y}_F\bar{y}_O\beta' - 2\frac{\bar{\rho}^2}{\bar{T}}\bar{y}_F\bar{y}_O\right]exp\left[-\beta'\left(\frac{1}{\bar{T}}-1\right)\right]$$

$$L = -\frac{i\bar{T}'}{(\alpha\bar{u}-\omega)} + \frac{i\bar{\rho}'(\gamma-1)}{\bar{\rho}^2(\alpha\bar{u}-\omega)}$$

$$M = Da\frac{Q}{W_F\nu_F}\bar{\rho}^2\bar{y}_F exp\left[-\beta'\left(\frac{1}{\bar{T}}-1\right)\right]$$

$$N = Da\frac{Q}{W_F\nu_F}\bar{\rho}^2\bar{y}_O exp\left[-\beta'\left(\frac{1}{\bar{T}}-1\right)\right]$$

$$O = i(\gamma-1)(\alpha\bar{u}-\omega) + 2Da\frac{Q}{W_F\nu_F}\bar{\rho}^2\bar{y}_F\bar{y}_O exp\left[-\beta'\left(\frac{1}{\bar{T}}-1\right)\right]$$

References

ANDERSON, D. A., TANNEHILL, J. C. & PLETCHER, R. H. 1984 *Computational Fluid Mechanics and Heat Transfer,* McGraw-Hill, New York.

BIRSH, S. F. & EGGERS, J. M. 1973 A Critical Review of Experimental Data for Developed Free Turbulent Shear Layers. *NASA SP-321,* 11–40.

BLUMEN, W. 1970 Shear Layer Instability of an Inviscid Compressible Fluid. *J. Fluid Mech.* **40**, 769–781.

BOGDANOFF, D. W. 1983 Compressibility Effects in Turbulent Shear Layers. *AIAA Journal* Vol. 22, 1550–1555

BROADWELL, J. E. & BREIDENTHAL, R. E. 1982 A simple model of mixing and chemical reaction in a turbulent shear layer. *J. Fluid Mech.* **125**, 397–410.

BROADWELL, J. E. & MUNGAL, M. G. 1988 Molecular Mixing and Chemical Reaction in Turbulent Shear Layers. *Twenty-Second International Symposium on Combustion,* University of Washington, Seattle, Washington.

BROADWELL, J. E. & MUNGAL, M. G. 1990 Large-Scale Structure and Molecular Mixing. *Phys. Fluids A* **3** (5), 1193–1206.

BROWN, G. L. & ROSHKO, A. 1974 On Density Effects and Large Structure in Turbulent Mixing Layers. *J. Fluid Mech.* **64**, 775–816.

CAIN, A. B., REYNOLDS, W. C. & FERZIGER, J. H. 1981 A Three-Dimensional Simulation of Transition and Early Turbulence in a Time-Developing Mixing Layer. *Report No. TF–14.* Department of Mechanical Engineering, Stanford University, Stanford, California.

CAIN, A. B., FERZIGER, J. H. & REYNOLDS, W. C. 1984 Discrete Orthogonal Function Expansions for Non-uniform Grids Using the Fast Fourier Transform. *J. Comp. Phys.* **56**, 272–286.

CHINZEI, N., MASUYA, G., KOMURA, T., MURAKAMI, A. & KODOU, K. 1986 Spreading of Two-Stream Supersonic Mixing Layers. *Phys. Fluids* **29**, 1345–1347.

CLEMENS, N. T. & MUNGAL, M. G. 1990 Two- and Three-Dimensional Effects in the Supersonic Mixing Layer. AIAA–90–1978. Also to appear in *AIAA Journal* 1992.

DEMETRIADES, A. & BROWER, T. 1990 Experiments on the Free Shear Layer between Two Supersonic Streams. AIAA–90–0710.

DIMOTAKIS, P. E. & BROWN, G. L. 1976 The Mixing Layer at High Reynolds Number: Large-Structure Dynamics and Entrainment. *J. Fluid Mech.* **78**, 535–560.

DIMOTAKIS, P. E. 1986 Two-Dimensional Shear-Layer Entrainment. *AIAA Journal* Vol. 24, 1791–1796.

DRAZIN, P. G. & DAVEY, A. 1977 Shear Layer Instability of an Inviscid Compressible Fluid. Part 3. *J. Fluid Mech.* **82**, 255–260.

ELLIOT, G. S., SAMMY, M. & REEDER, M. F. 1990 Pressure-Based Real-Time Measurements in Compressible Free Shear Layers. AIAA–90–1980.

FJØRTOFT, R. 1955 Application of Integral Theorems in Deriving Criteria of Stability for Laminar Flow and for the Baroclinic Circular Vortex. *Geofys. Publ., Oslo* **17**, No. 6, 1–52.

GANJI, A. T. & SAWYER, R. F. 1980 Experimental Study of the Flowfield of a Two-Dimensional Premixed Turbulent Flame. *AIAA Journal* Vol. 18, 817–824.

GIBSON, C. H. & LIBBY, P. A. 1972 On Turbulent Flows with Fast Chemical Reactions. Part II. The Distribution of Reactants and Products Near a Reacting Surface. *Comb. Sci. Tech.* Vol. 6, 29–35.

GILL, A. E. 1965a A Mechanism for Instability of Plane Couette Flow and of Poiseuille Flow in a Pipe. *J. Fluid Mech.* **21**, 505–511.

GILL, A. E. 1965b Instabilities of "Top-Hat" Jets and Wakes in Compressible Fluids, *Phys. Fluids*, **8**, 1428–1430.

GIVI, P., JOU, W. H. & METCALFE, R. W. 1986 Flame Extinction in Temporally Developing Mixing Layer. *Proc. Twenty-First International Symposium on Combustion*, 1251–1261.

GOEBEL, S. G. & DUTTON, J. C. 1990 Velocity Measurements of Compressible, Turbulent Mixing Layers. AIAA–90–0709.

GREENOUGH, J., RILEY, J., SOESTRISNO, M & EBERHARDT, D. 1989 The Effect of Walls on a Compressible Mixing Layer. AIAA–89–0372.

GROPPENGIESSER, H. 1970 Study on the Stability of Boundary Layers in Compressible Fluids. *NASA TT F–12, 786.*

HALL, J. L., DIMOTAKIS, P. E. & ROSEMANN, H. 1991 Some Measurement of Molecualr Mixing in Compressible Turbulent Shear Layers. AIAA–91–1719.

HELMHOLTZ, H. 1868 Discontinuous Fluid Motions. *Monats. Königl. Preuss. Akad. Wiss. Berlin*, **23**, 215–288.

HERMANSON, J. C. & DIMOTAKIS, P. E. 1989 Effects of heat release in a turbulent, reacting shear layer. *J. Fluid Mech.* **199**, 333–375.

HEIDARINEJAD, G. & GHONIEM, A. F. 1989 Vortex Simulation of the Reacting Shear Layer; Effects of Reynolds and Damköhler number. AIAA–89–0573.

HU, F. Q., JACKSON, T. L. & GROSCH, C. E. 1991 Absolute/Convective Instabilities In a Compressible Mixing Layer with Finite Rate Chemistry. submitted to journal for publication.

HUERRE, P. & MONKEWITZ, P. A. 1985 Absolute and Convective Instabilities in Free Shear Layers. *J. Fluid Mech.* **159**, 151–168.

JACKSON, T. L. & GROSCH, C. E. 1989 Inviscid Spatial Stability of a Compressible Mixing Layer. *J. Fluid Mech.* **208**, 609–637.

JACKSON, T. L. & GROSCH, C. E. 1990a Inviscid Spatial Stability of a Compressible Mixing Layer. Part 2. The Flame Sheet Model. *J. Fluid Mech.* **217**, 391–420.

JACKSON, T. L. & GROSCH, C. E. 1990b Absolute/Convective Instabilities and the Convective Mach Number in a Compressible Mixing Layer. *Phys. Fluids A* **2** (6), 949–954.

JACKSON, T. L. & HUSSANI, M. Y. An Asymptotic Analysis of Supersonic Reacting Mixing Layers. 1988 *Comb. Sci. Tech.* Vol. 57, 129–140.

KELLER, J. O. & DAILY, J. W. 1983 The Effect of Large Heat Release on a Two-Dimensional Mixing Layer. AIAA–83–0487.

KELVIN, L. 1871 Hydrokinetic Solutions and Observations. *Phil. Mag.* (4), **42**, 362–77.

LEES, L. & LIN, C. C. 1946 Investigation of the Stability of the Laminar Boundary Layer in a Compressible Fluid. *NACA Tech. Note* No. 1115.

LELE, S. 1988 Vortex Evolution in Compressible Free Shear Layers. *Workshop on the Physics of Compressible Turbulent Mixing,* Princeton.

LELE, S. 1989 Direct Numerical Simulation of Compressible Free Shear Flows. AIAA-89–0374.

LESSEN, M., FOX, J. A. & ZIEN, H. M. 1965 On the Inviscid Stability of the Laminar Mixing of Two Parallel Streams of a Compressible Fluid. *J. Fluid Mech.* **23**, 355–367.

LESSEN, M., FOX, J. A. & ZIEN, H. M. 1966 Stability of the laminar mixing of two parallel streams with respect to supersonic disturbances. *J. Fluid Mech.* **25**, 737–742.

LIN, C. C. 1955 The Theory of Hydrodynamics Stability. Cambridge University Press.

LIÑAN, A. & CRESPO, A. 1976 An Asymptotic Analysis of Unsteady Diffusion Flames for Large Activation Energies. *Comb. Sci. Tech.* Vol. 14, 95–117.

LOWERY, P. S. & REYNOLDS, W. C. 1986 Numerical Simulation of a Spatially-Developing, Forced, Plane Mixing Layer. *Report No. TF–26.* Department of Mechanical Engineering, Stanford University, Stanford, California.

MACARAEG, M. G. & STREETT, C. L. 1991 Linear Stability of High-Speed Mixing Layers. *Appl. Num. Math.* **7**, 93–127.

MACK, L. M. 1965 Stability of the Compressible Laminar Boundary Layer According to a Direct Numerical Solution. *AGARDograph* **97**, Part I, 329–362.

MACK, L. M. 1975 Linear Stability and the Problem of Supersonic Boundary-Layer Transition. *AIAA Journal* Vol. 13, 278–289.

MACK, L. M. 1984 Boundary-Layer Linear Stability Theory. *Special Course on Stability and Transition of Laminar Flow,* AGARD Report No. 709, 3–1 to 3–81.

MACK, L. M. 1989 On the Inviscid Acoustic-Mode Instability of Supersonic Shear Flows. *Fourth Symp. on Numerical and Physical Aspects of Aerodynamic Flows,* California State University, Long Beach, CA.

MAHALINGAM, S., CANTWELL, B. & FERZIGER, J. H. 1989 Non-Premixed Combustion: Full Numerical Simulation of a Coflowing Axisymmetric Jet, Inviscid and Viscous Stability Analysis. *Report No. TF–43* Department of Mechanical Engineering, Stanford University, Stanford, California.

MANSOUR, N. N., FERZIGER, J. H. & REYNOLDS, W. C. 1978 Large-Eddy Simulation of a Turbulent Mixing Layer. *Report No. TF–11*, Department of Mechanical Engineering, Stanford University, Stanford, California.

MASUTANI, S. M. & BOWMAN, C. T. 1986 The Structure of a Chemically Reacting Plane Mixing Layer. *J. Fluid Mech.* **172**, 93–126.

MCMURTRY, P. A., JOU, W. H., RILEY, J. J. & METCALFE, R. W. 1985 Direct Numerical Simulations of a Reacting Mixing Layer with Chemical Heat Release. AIAA–85–0143.

MENON, S., ANDERSON, J. D. & PAI, S. I. 1984 Stability of a Laminar Premixed Supersonic Free Shear Layer with Chemical Reactions. *Int. J. Engg. Sci.* Vol. 22, No. 4, 361–374.

MICHALKE, A. 1965a On the Inviscid Instability of the Hyperbolic-Tangent Velocity Profile. *J. Fluid Mech.* **19**, 543–556.

MICHALKE, A. 1965b Vortex Formation in a Free Boundary Layer According to Stability Theory. *J. Fluid Mech.* **22**, 371–383.

MONKEWITZ, P. A. & HUERRE, P. 1982 Influence of the Velocity Ratio on the Spatial Instability of Mixing Layers. *Phys. Fluids* **25**, 1137–1143.

MORRIS, P. J. & GIRIDHARAN, M. G. 1991 The Effect of Walls on Instability Waves in Supersonic Shear Layers. *Phys. Fluids A*, **3**, 356–358.

MORKOVIN, M. V. 1988 Guide to Experiments on Instability and Laminar Turbulent Transition in Shear Layers. *NASA-Ames short course.*

MUNGAL, M. G., & DIMOTAKIS, P. E. 1984 Mixing and combustion with low heat release in a turbulent shear layer. *J. Fluid Mech.* **148**, 349–382.

MUNGAL, M. G., & FRIELER, C. E. 1988 The Effects of Damköhler Number in a Turbulent Shear Layer. *Comb. Flame*, **71**, 23–34.

MUNGAL, M. G., HERMANSON, J. C. & DIMOTAKIS, P. E. 1985 Reynolds Number Effects on Mixing and Combustion in a Reacting Shear Layer. *AIAA Journal* Vol. 23, No. 9, 1418—1423.

ROSERS, M. M., & MOSER, R. D. 1989 The Development of Three-dimensional Temporally-evolving Mixing Layers. *Seventh Symposium on Turbulent Shear Flows*, Stanford University, Stanford, California.

OSTER, D., & WYGNANSKI, I. 1982 The Forced Mixing Layer between Parallel Streams. *J. Fluid Mech.* **123**, 91–130.

PAPAMOSCHOU, D. & ROSHKO, A. 1986 Observations of Supersonic Free Shear Layers. AIAA–86–0162

PAPAMOSCHOU, D. & ROSHKO, A. 1988 The Compressible Turbulent Shear Layer: an Experimental Study. *J. Fluid Mech.* **197**, 453–477.

PAPAMOSCHOU, D. 1989 Structure of the Compressible Shear Layers. AIAA–89–0126

PLANCHÉ, O. H. & REYNOLDS, W. C. 1991a Compressibility Effects on the Supersonic Reacting Mixing Layer. AIAA–91-0739.

PLANCHÉ, O. H. & REYNOLDS, W. C. 1991b Direct Simulation of a Supersonic Reacting Mixing-Layer. *Eighth Symposium on Turbulent Shear Flows*, Munich, Germany.

RAGAB, S. A. & WU, J. L. 1988 Instabilities in the Free Shear Layer Formed by Two Supersonic Streams. AIAA–88–0038.

RAYLEIGH, L. 1880 On the Stability, or Instability of Certain Fluid Motions. *Proc. London Math. Soc.* **11**, 57–70.

RILEY, J. J. & METCALFE, R. W. 1980 Direct Numerical Simulation of a Perturbed, Turbulent Mixing Layer. AIAA–80–0274.

SANDHAM, N. D. & REYNOLDS, W. C. 1989 A Numerical Investigation of the Compressible Mixing Layer. *Report No. TF–45*, Department of Mechanical Engineering, Stanford University, Stanford, California.

SANDHAM, N. D. & REYNOLDS, W. C. 1991 Three-Dimensional Simulations of Large Eddies in the Compressible Mixing Layer. *J. Fluid Mech.* **224**, 133–158.

SHAMPINE, L. P. & GORDON, M. K. 1975 Computer Solution of Ordinary Differential Equations. Freeman, San Fransisco.

SQUIRE, H. B. 1933 On the Stability for Three-Dimensional Disturbances of Viscous Fluid Flow between Parallel Walls. *Proc. Royal Soc. of London, Series A* Vol. 142, 621–628.

TAM, K. W. & HU, FANG Q. 1989 The Instability and Acoustic Wave Modes of Supersonic Mixing Layers Inside a Rectangulart Channel. *J. Fluid Mech.* **203**, 51–76.

TOLLMEIN, W. 1935 A General Criterion for the Instability of Laminar Velocity Distributions. *Nachr. Ges. Wiss. Gottingen, Math.-Phys. Klasse*, 79–114

TROUVE, A. & CANDEL, S. M. 1988 Linear Stability of the Inlet Jet in Ramjet Dump Combustor. AIAA–88–0149.

TZUOO, K. S., FERZIGER, J. H. & KLINE, S. J. 1987 Zonal Models of Turbulence and Their Application to Free Shear Flows. *Report No. TF–27*, Department of Mechanical Engineering, Stanford University, Stanford, California.

WALLACE, A. K. 1981 Experimental Investigation of the Effects of Chemical Heat Release in the Reacting Turbulent Plane Shear Layer. Ph.D. thesis. The university of Adelaide.

WHITE, F. M. 1974 *Viscous Fluid Flow*, McGraw-Hill, New York.

WILLIAMS, F. A. 1985 *Combustion Theory*, The Benjamin/Cummings Publishing Company, Inc.

WINANT, C. D. & BROWAND, F. K. 1974 Vortex Paring: the Mechanism of Turbulent Mixing Layer Growth at Moderate Reynolds Number. *J. Fluid Mech.* **63**, 237–255.

ZHUANG, M., KUBOTA, T. & DIMOTAKIS, P. E. 1988 On the Instability of Inviscid, Compressible Free Shear Layers. AIAA–88–3538.

ZHUANG, M., DIMOTAKIS, P. E. & KUBOTA, T. 1990 The Effect of Walls on a Spatially Growing Supersonic Shear Layer. *Phys. Fluids A*, **2**, 599–604.